



universität  
wien

# DISSERTATION

Titel der Dissertation

„Mineralogical, petrological, and geochemical studies of Neoproterozoic Sturtian (750 Ma) and Marinoan (635 Ma) postglacial transition layers in Otavi Group, NW-Namibia“

Verfasserin

Ildikó Gyollai

angestrebter akademischer Grad

Doktorin der Naturwissenschaften (Dr. rer. nat.)

Wien, 2014

Studienkennzahl lt. Studienblatt: A 791 426

Dissertationsgebiet lt. Studienblatt:  
Erdwissenschaften

Betreuerin / Betreuer: Univ.Prof. Dr. Christian Koeberl,  
Wiss. O. Rat Dr. Friedrich Popp



## DEDICATION



**Outcrop of Marinoan platform carbonate (Ombaatjie Fm.) and postglacial cap carbonate (Maieberg Fm., Keilberg Mb.) from Ongongo Area (Photo: F. Popp, 2005)**

This thesis is dedicated to Dr. Márta Polgári.



## PREFACE

This thesis summarizes four years of study at the Department of Lithospheric Research, University of Vienna. The thesis discusses three aspects related to the deglaciation of Neoproterozoic Snowball Earth in NW-Namibia (7 outcrops of Otavi Group):

- 1) Search for impact ejecta in postglacial transition layers (chapter 3);
- 2) Paleoenvironmental reconstruction of Sturtian and Marinoan deglaciation in NW-Namibia (chapter 7);
- 3) Presence of neutrophilic iron-oxidizing bacteria in Sturtian and Marinoan postglacial transition layer and its paleoenvironmental impact (chapter 2, 4, 6).

A co-authored article (Zn isotopic of Marinoan postglacial transition layers) study of related to the thesis project is attached as chapter 5 of the thesis. Manuscripts discussing results of those projects have been submitted for publication in peer-reviewed journals (Communications of the Geology Survey of Namibia, Austrian Journal of Earth Sciences, Carpathian Journal of Earth and Environmental Sciences, Precambrian Research (co-authored), and Central European Journal of Geology).

The thesis also includes a short introduction to Snowball Earth, impact cratering, as well as a brief summary of the methods used in this study (chapter 1) In addition, the CV of the thesis's author includes conference participations, articles, and collaborations related to research project, which is attached to end of thesis.



## ACKNOWLEDGMENTS

This study was supported by the Austrian Academy of Sciences through a grant to Christian Koeberl (International Geological Correlation Program IGCP No. 512, project title: „Search for an extraterrestrial component for triggering Neoproterozoic Snowball Earth aftermath”).

- The samples were collected by Dr. Friedrich Popp, supported by the Geological Survey of Namibia and we are grateful to Director Dr. G. Schneider for her important help regarding field work organization and sample export management.
- I am grateful to the professors and technicians at the University of Vienna who assisted the analytical work „in project of impact research”: Dieter Mader (INAA, IRMS, CL), Susanne Gier (XRD), Lutz Nasdala and Eugen Libowitzky (micro-Raman spectrometry), Sabine Hruby-Nichtenberger (Karbonatbombe), Peter Nagl (XRF) and Patrick McDonald (XRF), to Lidia Pittarello and Ludovic Ferriere (SEM of smear slides of magnetic fractions of postglacial “boundary clays” in NHM). I appreciate the help of the reactor team of the Institute of Atomic and Subatomic Physics, Vienna, with the irradiations.
- I am very grateful to Márta Polgári for help and supervision in topic of geomicrobiology and paleoenvironmental aspects and supporting collaboration with Geochemical and Astronomical Research Institute of Hungarian Academy of Science and Department of Mineralogy, Petrology and Geochemistry at University of Szeged. I am thankful to Raman Laboratory of University Szeged (Krisztián Fintor, Szabolcs Nagy, Elemér Pál-Molnár) to take profile on microbial layers and for good cooperation in submitted microbial articles. Moreover, I am obliged to Zsolt Bendő (EMPA at Dept. of Petrology and Geochemistry, Eötvös University) and Miklós Veres (Raman Labor at Institute of Solid Physics, Institute of Physics of Hungarian Academia of Science) for assistance in measurements of Sturtian oolitic grainstone.
- Last but not least I am grateful to my family, friends and to God for giving me encouragement during the hardest moments of my work.



## ABSTRACT

The aim of this PhD research is to identify the cause of deglaciation of Neoproterozoic Snowball Earth events (Sturtian: 750 Ma, Marinoan: 635 Ma). The research area is located in the Otavi Group, NW-Namibia. The samples were collected by F. Popp in 2009, from post-glacial transition layers (at boundary of glacial diamictite and postglacial cap carbonate), from 3 Sturtian (Copper Mine, Sesfontain-Opuwo, Steilrandberge), and 7 Marinoan (Fransfontain, Bethanis, Tweelingskop, Naraachamspos, Entrance to the South Valley, Khowarib Valley, Warmquelle) outcrops.

Chapter 2 presents microbial record in Sturtian (750 Ma) oolitic grainstone (basal Rasthof Fm.) from Copper Mine studying by mineral spectroscopic methods and back-scattered electron imaging. The bacterial films on ooid shales lived in shallow water environment, and presence of smectite on ooid rim is driven by diagenesis of iron-oxidizing bacteria. The hydrocarbon phases, which are identified by Raman spectroscopy, proves microbial ancient activity.

Chapter 3 presents synsedimentary microbial layering of neutrophilic iron-oxidizing bacteria and cyanobacteria from the boundary of Sturtian Chuos and Rasthof Fm. (Sesfontain-Opuwo and Steilrandberge outcrops). The presence of this microbial community suggests a neutrophilic, suboxic, shallow water environment. The sedimentation of the mineralized biomats can be estimated by life cycle of recent bacteria, considering for length of day and day for Earth historic period. The maximal sedimentation time for 1.45 m microbial laminae is estimated at 385 yrs.

Chapter 4 presents the search for extraterrestrial signatures to test if a meteorite impact triggered deglaciation of Sturtian and Marinoan Snowball Earth. Postglacial transition layers were studied by various analytical methods to find mineralogical signatures, like shock-induced deformation in minerals, high-pressure transformations, shock melts, meteorite mineral fragments (chromium spinels), and geochemical signatures, such as Ir, Cr, Ni, Co enrichments, and Cr-isotopic anomalies. But the studied samples do not contain any unambiguous signature of meteorite impact. However, the samples are highly diluted in carbonate, which contains mostly authigenic phases. For further investigations it is suggested to collect samples that contain more detrital components, or originated from paleocontinents.

Chapter 5 emphasizes Zn, C, and O isotopic study of Marinoan postglacial transition layers and the Profile C2a from Naraachamspos. The differences of C and Zn isotopic fractionation is derived by multiple processes: 1) biogenic metabolism, 2) hydrothermal alteration. The Zn isotopes fractionated originally by hydrothermal alteration, which is modified by biogenic activity. The C isotopic variations are derived by massive inorganic  $\delta^{13}\text{C}$  isotopic reservoir, with minor biologic footprint.

Chapter 6 describes microbial activity in Marinoan postglacial transition layer and basal cap carbonates. The biomats of iron oxidizing bacteria are classified by nutrient source 1) hydrothermal vents (syndimentary microbial layers), 2) bioweathering of iron-bearing minerals, like pyrite, chlorite, 3) microbial coating on clasts (short-term nutrient source or transient suboxic condition). The bioweathering pyrite in Profile C2a was studied by Raman mapping, pyrites were surrounded by lepidocrocite-goethite-hematite alteration zone, containing organic material. The geochemical signature of biogenicity is proofed by enrichment factor of biogenic elements (Cr, Co, Ni, Zn, Rb, U, K, Fe), which have good correlation with petrographic observation of iron-oxidizing bacteria.

Chapter 7 gives a paleoenvironmental reconstruction of deglaciation of Cryogenic Snowball Earth events, including secondary processes, like weathering and diagenesis. The minor role of detrital minerals, the major presence of authigenic phases dismisses fluvial input from continents, which supports a hard Snowball Earth (completely frozen oceans without detrital input). The geochemical signatures and presence of iron-oxidizing bacteria suggests suboxic, brackish, shallow water environment.

The thesis includes two appendices, which contain mineralogy (I) and geochemistry (II) datatables.

## ZUSAMMENFASSUNG

Ziel dieser Doktorarbeit ist die Identifizierung der Ursachen der Deglaziation der neoproterozoischen "Schneeball Erde" Ereignisse ("Sturtian" ~750Ma, "Marinoan" ~635 Ma). Das gearbeitete Gebiet befindet sich in der Otavi-Gruppe, in NW-Namibia. Die Proben wurden im Jahr 2009 von F. Popp gesammelt. Das sind hauptsächlich postglaziale Übergangslagen und Deckkarbonate (cap carbonates) sowie Diamiktite von 3 der Sturtischen (Copper Mine, Sesfontain-Opuwo, Steilrandberge) und 7 der Marinoischen Eiszeit (Fransfontain, Bethanis, Tweelingskop, Naraachampos, Entrance to the South Valley, Khowarib Valley, Warmquelle) zugehörigen Aufschlüssen.

Kapitel 2 präsentiert einen mikrobiellen Beleg für einen sturtischen oolithischen 'Grainstone' (basale Rasthof-Formation bei Copper Mine) mittels mineralspektroskopischen Methoden sowie Rückstreu-Elektronenabbildung an einem Rasterelektronenmikroskop. Die resultierenden Ergebnisse legen nahe, dass sich im Seichtwassermilieu Bakterienfilme an den Ooid-Schiefern bildeten und dass die Anwesenheit von Smektit an den Ooid-Rändern auf dessen diagenetische Bildung durch eisenoxidierende Bakterien hindeutet. Auch die durch Raman-spektroskopie identifizierten Kohlenwasserstoffphasen weisen auf mikrobielle Aktivitäten hin.

Kapitel 3 belegt eine syndimentäre mikrobielle Schichtung durch neutrophilische eisenoxidierende Bakterien und Cyanobakterien an der Grenze zwischen der sturtischen Chuos und der Rasthof Formation (Aufschlüsse Sesfontain-Opuwo und Steilrandberge). Die Anwesenheit dieser mikrobiellen Gemeinschaft deutet ein neutrophilisches, suboxisches Flachwassermilieu an. Die Sedimentationsdauer dieser mineralisierten Biomatten kann mittels der Lebenszyklen rezenter Bakterien abgeschätzt werden, unter Berücksichtigung der bekannten Tages- und Jahreslänge jener Zeit. Die maximale Sedimentationsdauer für die 1,45 m dicken Mikrobenschichten wird daher auf 385 Jahre berechnet.

Kapitel 4 präsentiert die Suche nach extraterrestrischen Signaturen um die Möglichkeit eines Meteoritenimpakts als Ursache der sturtischen und/oder marinoischen Deglaziation zu untersuchen. Dazu wurden die postglazialen Übergangslagen mittels verschiedener Analysemethoden studiert, um sowohl mineralogische Hinweise, wie schock-induzierte Deformationen, Hochdruckumwandlungen, Schockschmelzen, oder meteoritische Mineralfragmente (z.B. Chromspinell) als auch geochemische Signaturen, wie Iridium, Chrom, Nickel und Chrom-Anreicherungen zu finden. Die untersuchten Proben enthielten jedoch keinerlei eindeutigen Hinweise auf ein Impaktereignis. Allerdings stellten sich die Proben als sehr karbonatreich mit hauptsächlich authigenen Phasen heraus. Für weiterführende Untersuchungen in dieser Hinsicht wird für eine Probennahme auf die Suche nach Aufschlüssen aus Ablagerungen mit mehr detritären Komponenten hingewiesen.

Kapitel 5 behandelt Zink-, Kohlenstoff- und Sauerstoffisotopenstudien an der marinoischen postglazialen Übergangslage sowie an einem basalen "cap carbonate"-Profil (C2a, Naraachamspas). Die unterschiedlichen Isotopenfraktionierungen von C und Zn werden auf multiple Prozesse zurückgeführt: 1) biogenem Metabolismus und 2) hydrothermaler Alteration. Die Zn-Isotope fraktionierten originär durch hydrothermale Alteration und danach durch biogene Aktivitäten. Die C-Isotopevariationen werden auf ein massives anorganisches  $\delta^{13}\text{C}$ -Isotopenreservoir zurückgeführt, mit geringen biologischen Einflüssen.

Kapitel 6 beschreibt mikrobielle Aktivitäten in der marinoischen postglazialen Übergangslage und den basalen "cap carbonates". Biomatten aus eisenoxidierenden Bakterien werden nach Nährstoffquellen klassifiziert: 1) hydrothermale Schloten (syndimentäre Mikrobenlagen), 2) Biotische Verwitterung von eisenhaltigen Mineralen wie Pyrit und Chlorit, 3) mikrobieller Überzug an Klasten (kurzzeitige Nährstoffquelle oder vorübergehende suboxische Bedingungen). Im Profil C2a wurden biotisch verwitterte Pyrite mittels Raman-Kartierung untersucht. Die Pyrite sind von einer, organisches Material enthaltenden, Lepidokrokit-Goethit-Hämatit-Alterationszone umgeben. Die Biogenität der geochemischen Signaturen wird mittels Anreicherungsfaktoren biogener Elemente (Cr, Co, Ni, Zn, Rb, U, K, Fe) belegt, welche gut mit den petrographischen Beobachtungen der eisenoxidierenden Bakterien korrelieren.

Kapitel 7 führt eine Paläoumwelt-Rekonstruktion der Deglaziation der cryogenischen Schneeball Erde Ereignisse an, inklusive sedimentärer Prozesse wie Verwitterung und Diagenese. Die geringe Rolle detritischer Minerale und die vorwiegende Präsenz authigener Phasen verwirft den Einfluss fluviatilen Eintrags von den Kontinenten, und könnte damit die Hypothese einer Gesamtvereisung der Ozeane ("hard Snowball Earth") unterstützen. Sowohl die geochemischen Signaturen als auch die Präsenz von eisenoxidierenden Bakterien legen ein suboxisches, brackisches Flachwassermilieu während der Deglaziation nahe.

Die Dissertation inkludiert weiters zwei Appendixes mit den vollständigen mineralogischen (I) und geochemischen (II) Datentabellen.

# TABLE OF CONTENTS

DEDICATION.....	III
PREFACE.....	V
ACKNOWLEDGMENTS.....	VII
ABSTRACT.....	IX
ZUSAMMENFASSUNG.....	XI
TABLE OF CONTENTS.....	XIII
1 Introduction .....	1
1.1 Aim of research project.....	1
1.2 The concept of “Snowball Earth” .....	3
1.2.1 Hypotheses for Neoproterozoic glaciations .....	5
1.2.2 Theories for the deglaciation of “Snowball Earth” .....	8
1.3 Geological background of research area and sample locations .....	9
1.3.1 The break-up of Rodinia and its consequences.....	9
1.3.2 Geological background of the research area .....	12
1.4 Samples .....	16
1.4.1 Lithology of Sturtian postglacial transition layers .....	16
3.1 Lithology of Marinoan post-glacial transition layers.....	18
1.5 Search for extraterrestrial material .....	25
1.6 Methodology.....	27
1.6.1 Sample preparation .....	28
1.6.2 Carbonate measurement with the „Karbonatbombe“ .....	28
1.6.3 Bulk rock mineralogy .....	29
1.6.4 In-situ mineralogical methods.....	32
1.6.5 Bulk rock geochemistry .....	36
1.6.6 In-situ geochemistry .....	42
References .....	47
2 Evidence of microbial activity involved with Neoproterozoic postglacial sediments from the Otavi Group, Namibia: a study of Sturtian oolitic carbonate sandstone with spectroscopic methods .....	57
2.1 Introduction .....	58
2.1.1 Overview.....	58
2.2 Geological background.....	58
2.3 Samples and methods.....	59
2.4 Results.....	60
2.4.1 Petrography .....	60
2.4.2 Microbial structures .....	61
2.4.3 Chemical composition and mineralogy - backscattered electron imaging .....	63
2.4.4 Textural characteristics by cathodoluminescence studies.....	66

2.4.5	Raman spectroscopy.....	68
2.5	Discussion.....	72
2.6	Conclusions.....	73
2.7	Acknowledgements .....	74
2.8	References.....	75
3	Microbially mediated deposition of postglacial transition layers from the Neoproterozoic Otavi Group, Namibia: Evidence of rapid deglaciation after the Sturtian Cryogenic Period ...	77
3.1	Introduction .....	78
3.2	Geological background of sample areas.....	79
3.3	Methods .....	86
3.4	Results.....	86
3.5	Discussion.....	88
3.5.1	Synsedimentary Fe-rich biomat formation .....	88
3.5.2	Diagenesis of Fe-rich biomats .....	94
3.5.3	Constraints on sedimentation rates .....	94
3.6	Conclusions.....	97
3.7	Acknowledgements .....	97
3.8	References.....	99
4	Search for extraterrestrial impact markers in samples from Chuos/Rasthof (Sturtian) and Ghaub/Maieberg (Marinoan) Snowball Earth / Greenhouse transition layers of the Neoproterozoic Otavi Group, Namibia .....	105
4.1	Introduction .....	106
4.2	Geological background.....	109
4.3	Samples and methods.....	111
4.4	Results.....	116
4.4.1	Optical microscopy and XRD: search for shocked quartz .....	116
4.4.2	Geochemistry .....	119
4.5	Discussion.....	127
4.6	Conclusions.....	129
4.7	Acknowledgements .....	129
4.8	References.....	130
5	Zn, C, and O Isotopic Variations Associated with Neoproterozoic Marinoan Glaciations ..	135
5.1	Introduction .....	136
5.2	Materials and Methods.....	139
5.3	Results.....	143
5.4	Discussion.....	146
5.5	Conclusions.....	152
5.6	Acknowledgments .....	152
5.7	References.....	153

6	Paleoenvironment characterization based on microbial activity and geochemical proxies in Marinoan postglacial transition layers (NW-Namibia).....	159
6.1	Introduction .....	160
6.2	Geological background.....	160
6.3	Samples and methods.....	161
6.4	Results.....	165
6.4.1	Petrography of microbial structures.....	165
6.4.2	Raman-mapping measurements .....	168
6.4.3	Geochemistry.....	169
6.5	Discussion.....	173
6.6	Conclusions.....	175
6.7	Acknowledgements .....	175
7	Paleoenvironmental reconstruction, weathering and diagenesis of Neoproterozoic postglacial transition layers: Observation from the Otavi Group/ Namibia.....	179
7.1	Introduction .....	180
7.2	Geological background.....	180
7.2.1	The Congo Cratonic Sedimentary Cover Sequence .....	183
7.2.2	The Otavi Group Research Area .....	184
7.3	Samples and methods.....	190
7.3.1	Samples.....	190
7.3.2	Methods .....	190
7.4	Lithology of Cryogenian postglacial transition layers in Otavi Group.....	191
7.4.1	Sturtian.....	191
7.4.2	Pre-Marinoan .....	192
7.4.3	Marinoan .....	192
7.5	Results of analyses .....	194
7.5.1	Raman Spectroscopy.....	194
7.5.2	Cathodoluminescence studies.....	198
7.5.3	Geochemistry.....	201
7.6	Paleoenvironment .....	205
7.6.1	Paleoredox conditions .....	205
7.6.2	Diagenesis .....	208
7.6.3	Estimation of detrital input .....	211
7.6.4	Weathering.....	215
7.6.5	Microbial structures .....	220
7.7	Conclusions.....	222
7.8	Acknowledgements .....	222
7.9	References.....	223
8	RECAPITULATION .....	229
9	Appendix 1: Mineralogy tables.....	233

---

9.1	Sturtian.....	233
9.2	Marinoan .....	237
9.3	Raman spectroscopy results .....	247
10	Appendix II: Geochemical tables of Sturtian and Marinoan samples following sampling sites .....	251
10.1	Major and rare earth elements.....	252
10.2	Carbon-isotopy.....	267
10.3	Table of CaCO <sub>3</sub> values .....	269
11	CURRICULUM VITAE .....	271

# 1 Introduction

## 1.1 Aim of research project

The initial aim of this PhD project was the search for possible impact ejecta, which might trigger deglaciation of Neoproterozoic Snowball Earth (Sturtian and Marinoan) due to deposition of a large amounts of excavated impact material (shocked rocks and mineral fragments, impact melt rocks, tektites, fire-fall beds, meteorite fragments) released into the atmosphere, causing an ice-albedo changes that lead to a reduction in ice coverage.

The cause and duration of the deglaciation process of Neoproterozoic (Sturtian and Marinoan) Snowball Earth is debated by the scientific community, therefore are currently explained by a variety of climate models. Likewise the precipitation of “cap carbonates”, which are specific sediments indicating the immediate aftermath of the cryogenic periods, has also been explained by a variety of hypotheses: (i) CO<sub>2</sub> supersaturated sea water, because of increased continental weathering and volcanic activity (e.g., Hoffman, 1998); (ii) destabilization of methane clathrates (Kennedy et al., 2001, 2008); and (iii) biogenic carbonate production (e.g., Pruss et al., 2010). The proposed duration of deglaciation ranges from thousand up to millions of years, based on cap carbonate investigations (e.g., Bodiselitsch et al., 2005; Font et al., 2010).

However, this study focuses on straticulate ferruginous-clayish layers, marking the transition from a glacial period towards its aftermath. According to current interpretations, such postglacial boundary layers can be formed by: (i) sedimentation that includes some extraterrestrial dust (Bodiselitsch et al., 2005), (ii) impact ejecta (Koeberl et al., 2007), (iii) weathering of diamictites (Hoffman and Halverson, 2008), or (iv) microbially-induced sediments (e.g., Ferrich biomats, such as Archean BIFs and sedimentary ore deposits, as at Úrkút Bakony Mountains, West Hungary; cf. Polgári et al., 2012).

- (i) Bodiselitsch et al. (2005) found enhanced contents of the siderophile element iridium in Cryogenian postglacial transition layers from the Congo craton, possibly resulting from ice-bounded accumulation of cosmic dust during the “Snowball Earth” period. Indeed, in this case the cosmic dust sedimentation should occur all over the world in Cryogenian postglacial transition layers. Other studies (e.g., Peucker-Ehrenbrink and Hoffman, 2006) found only limited evidence for such extraterrestrial components in transition layers elsewhere.
- (ii) Alternatively, Koeberl et al. (2007) postulated a possible impact event triggering Snowball Earth deglaciation and causing climate change, similar to what happened at the K/Pg boundary.

(iii) - (iv) As studies of the recent polar area imply, ferruginous sediments can be precipitated as biomats beneath the sea ice from sea water, where the source of iron can come from hydrothermal vents or continental weathering incorporated from melt water flow beneath the glaciers (Vincent and Howard-Williams 2000). Concerning the attempt to reconstruct paleoenvironmental conditions, my investigations basically considered the following possible environmental settings: (a) Slushball Earth (presence of continental input during the glaciations; a lower carbonate content of the sediments and a higher amount of detrital minerals would be the result.), or (b) Hard Snowball Earth (absence of detrital minerals). The presence of Gallionella-like synsedimentary Fe-rich biomats in Sturtian and Marinoan postglacial transition layers represents a powerful tool to obtain a paleoenvironmental reconstruction (paleoredox condition, Eh, pH, salinity), combining biogeochemistry and even provide a possibility to estimate the duration of the deglaciation process.

Hence, the task of this study is the search for mineralogical and geochemical signatures of extraterrestrial components, especially shocked minerals (such as planar fractures (PFs) or planar deformation features (PDFs) in quartz grains), chromium-rich spinels, as well as siderophile element anomalies (e.g., Ir, Cr, Co, Ni) compared to upper crustal abundances. Specific attention was straightened on the possible presence of such detrital grain input from older source areas. Last but not least, secondary signatures of an impact event were searched for, such as sedimentological signatures, like synsedimentary tectonic signatures (faults, folds, slumping structures), and clay mineral composition, which may be weathering products of tektites, spherules, and glass droplets.

One of the additional aims of this PhD project is to provide a paleoenvironmental reconstruction for Cryogenian postglacial boundary layers. In particular the provenance and geochemical composition of postglacial diamictite/cap carbonate transition layers and to estimate the paleoenvironmental conditions with respect to glaciomarine sea water composition and sediment accumulation in mineralogical-geochemical aspects. This study proposes possible cap carbonate formation processes and estimates the duration of post-glacial sedimentation via recent analogies.

The samples for this study were collected from post-glacial transition layers on top of the glaciogenic Chuos (Sturtian glaciation) (10 samples) and Ghaub (Marinoan glaciation) formations (63 samples) of the Neoproterozoic Otavi Group in NW-Namibia.

## 1.2 The concept of “Snowball Earth”

Neoproterozoic glaciations of global extent occurred within three succeeding cryogenic periods: 1) the Sturtian (740–647 Ma, type locality South Australia), 2) the Marinoan (660–635 Ma, type locality South Australia), and 3) the Gaskiers (ca. 580 Ma, type locality Avalonian Newfoundland, Canada), each glacial period lasting several million years. The term “Snowball Earth” was introduced by Kirschvink (1992).

The criteria for the definition of “Snowball Earth” glaciations were introduced by Kirschvink (1992) as follows: 1) Synchronous glacial units worldwide, 2) Rapid fluctuations between icehouse and greenhouse stages, 3) Sluggish seawater currents caused by floating ice worldwide on the ocean’s surface. In general, glacial periods were characterized by regressive sea levels and an increasing positive ice - albedo feedback, thus more than half of Earth might have been ice-covered (Budyko, 1966). In Neoproterozoic times the continents were assembled around the Earth’s Equator (Worsley and Kidder 1991) thus, a greater continental effect controlled the global climate) and an increased weathering rate lead to a decrease of  $p\text{CO}_2$ , what might have initiated the “Snowball Earth” cycle (Marshall et al. 1998). In fact, these inputs combined with a decreased oceanic heat transport resulted in the growth of ice cover almost the whole planet’s surface.

Kirschvink (1992) drew attention to the role of plate tectonics with respect to the global climate system, as associated volcanoes pump  $\text{CO}_2$  into the atmosphere and subsequently into the ocean during the Snowball Earth glacial period. The volcanic ash fall resulted in a decrease of the ice albedo effect (reverse ice-albedo feedback) and thus the earth’s ice cover was thinned (Caldeira and Kasting 1992). This process resulted in rapid ice melting and increased weathering by high  $\text{CO}_2$  consumption. In addition, Kirschvink (1992) concluded that a cold planet with tropical continents and polar sea-ice caps would be an unstable situation with rapid fluctuation between icehouse and greenhouse states.

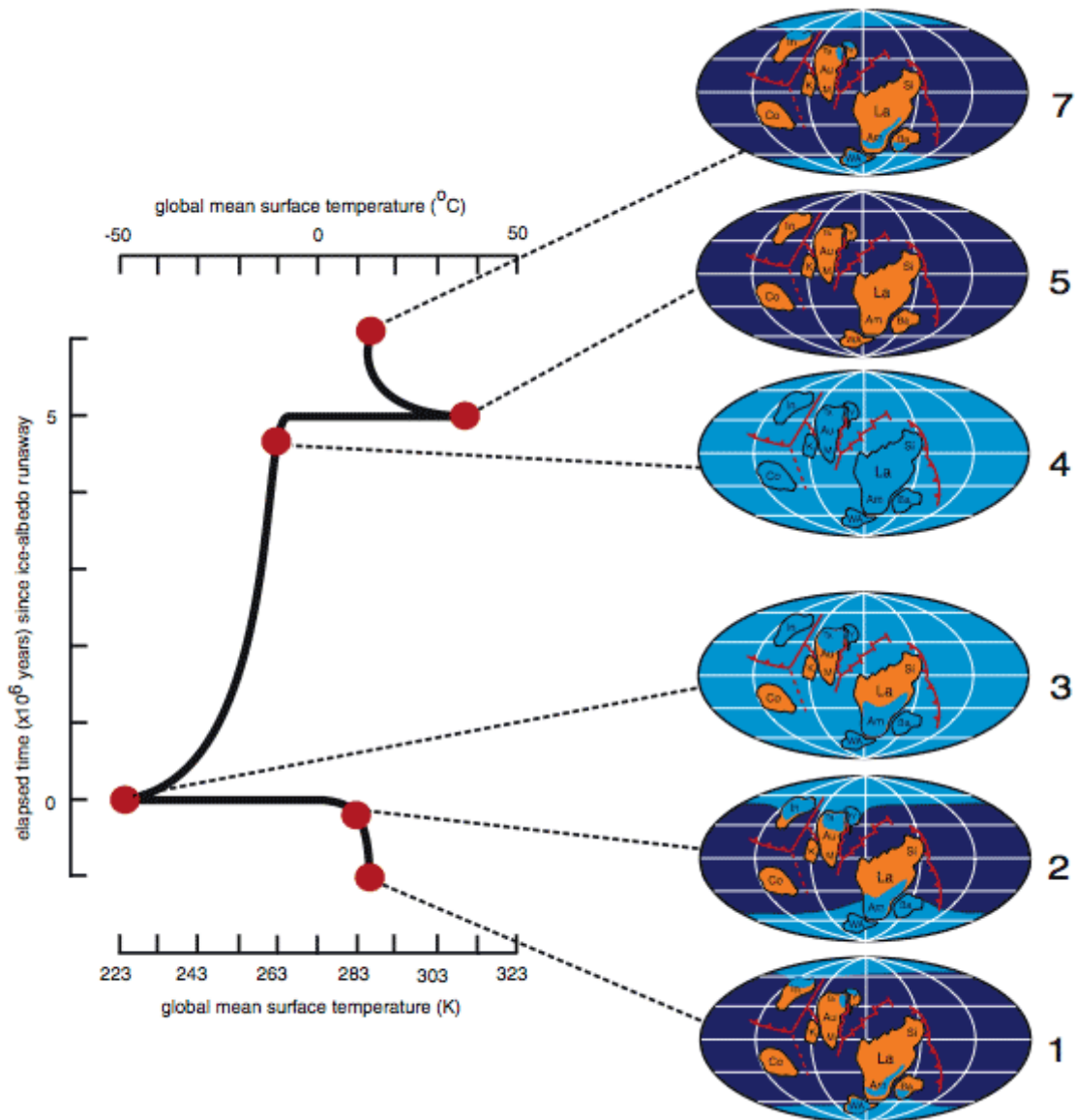


**Figure 1.** Snowball Earth cycle with surface temperature change and paleogeographical setting (from Hoffman et al. 1998).

According to Hoffman and Schrag (2002), “Snowball Earth” glacial diamictites appear in numerous localities around the world (Fig. 1.), for example the Ice Brook Fm. (Canada), Ghaub Fm. (Namibia), Eletina Fm. (Australia) representing the Marinoan cryogenic period, otherwise the Rapitan Fm. (Australia), Chuos Fm. (Namibia) and Sturt Fm. (Australia) representing the Sturtian cryogenic period (Fig. 1., Table 1.).

The age of the Marinoan glaciation is  $635 \pm 1.2$  Ma, which was measured on zircons from the ash bed in the Ghaub Formation by U-Pb geochronology (Hoffman et al., 2004). Different age data come from other Marinoan cryogenic strata, where postglacial black shales have been measured by Re-Os isochrones (for example  $663 \pm 4$  Ma of the Mount Vreelant Fm., NW-Canada;  $599.3 \pm 4.2$  Ma Nantou Fm. in South China;  $592 \pm 14$  Ma of the Olympic Fm., the

Amadeus basin, central Australia; Hoffman and Schrag, 2002, and Hoffman et al. (1996) measured the age of the Chuos Formation at  $746 \pm 2$  Ma by U-Pb dating.

**Table 1.** Neoproterozoic glaciations with paleogeographical setting, BIFs are underlined (Hoffman and Li, 2009).

Paleolocation	Area	Sturtian	Marinoan	Ediacaran (Gaskiers)
Amazon	Alto Paraguay		Puga <u>Urucum</u>	
	Amazonia	<u>Jacadiço Group</u>		
Angola	Northern Namibia	<u>Chuos</u>	Ghaub	
Arabia	Mirbat	Lover Mirbat	unnamed	
	Oman Mntns	Gubrah	Fiq	
Australia	Adelaide	<u>Pualco-Appila</u> <u>Sturt</u>	Elatina	
	Central Australia Kimberley's	Areyonga Walsh	Olympic Landregan	Egan
Avalon	Newfoundland			Gaskiers
Baltica	Oslo			Moelv
	Varanger Peninsula		Smalfjord	Mortensnes
	Urals	<u>Tany</u>		
Congo	West Congo	Lower Tilloid	Upper Tilloid	
	Zambia	Grand Congl.	Petit Congl.	
Kalahari	Gariiep	Kaigas	<u>Numees</u>	
	Witwel-Nauklufft	<u>Blaubekker</u>	Bläaakranz	
Laurentia	Alaska	Upper Tindir		
	British Columbia	Toby	Vreeland	
	Blue Ridge	Konnarock		
	California	Wildrose	<u>Surprise</u>	
	East Greenland	Ulveso	Storeelv	
	East Svalbard	Petrovbreen	Wilsonbreen	
	Idaho	Scout Mountain		
	NW Territories	<u>Rapitan</u>	Stelfox	
	Scotland	Port Askaig	Loch na Cile	
India	Lesser Himalaya		Blaini	
Mongolia	Central Mongolia	Tsagaan Oloom		
	Erzin	<u>Maikhan UI</u>		
Sao Francisco			Macubas	
South China	Guizhou	<u>Chang'an</u>	<u>Nantou</u>	
Tarim	Quruqtah	Baysii	Tereekkan	Hankalchough
West Africa	Taoudeni		Jbéliat	
	Volta		Kodjari	

### 1.2.1 Hypotheses for Neoproterozoic glaciations

The Cryogenian global glaciations were explained by different hypotheses: Hard Snowball Earth (Hoffman, 1998; Hoffman and Schrag, 2002), Slushball Earth (Harland, 1964) Zipper-rift model (Eyles and Januszczak, 2004) and High-tilt Earth (Williams, 2000).

The hard Snowball Earth hypothesis was proposed by Hoffmann et al. (1998) and proposes that sea ice covered oceans as result of runaway ice-albedo feedback with thin or

patchy continental ice caused by the elimination of hydrological cycles. Theoretically, this glacial climate hypothesis was effectively modeled by wind-driven circulation, including vapor, clouds, and ice albedo (Pierrehumbert, 2002, 2005). Hoffman et al. (1998) proposed the abundant precipitation of cap carbonate resulting from intense oceanic alkalinity as intense continental weathering, caused by the post-Snowball extreme greenhouse effect, oversaturated sea water compositions.

Harland (1964) proposed a Slushball Earth hypothesis, which is based on an incompletely frozen Earth during the Cryogenian glaciations, with open water remaining in the equatorial region. This concept was used in the climate model from Hyde et al. (2000). Accordingly, the Slushball Earth has the following assessment criteria:

- (1) Paleomagnetic evidence (Evans, 2000), sedimentary facies (Fairchild, 1993) and distribution of glacial sediments (Hambrey and Harland, 1985).
- (2) Three major glacial units, each indicating a specific cryogenic period identify the sequence of a few discrete glaciations with global influence (e.g., sea-level change or disturbance of the C cycle as manifested by  $\delta^{13}\text{C}$  anomalies; Harland, 1964; Knoll et al., 1986; Kennedy et al., 1998; Halverson, 2006).
- (3) Hydrologic cycle influenced glaciations propose presence of tropic Hadley cells which mean the oceans and rivers of continental area were not completely frozen. (Eyles and Eyles, 1983; Leather et al., 2002).

The high obliquity Earth model was introduced by Williams (1975, 1993, 2000), who suggested high ( $>54^\circ$ ) orbital obliquity to explain low latitude glaciation with strong equatorial seasonality during the Elatina glaciation. According to Laskar et al. (1993) and Williams (1993), the obliquity varied between  $60^\circ$ - $90^\circ$  because of the large lunar forming impact (4.53 Ga) and they postulated a sharp decrease in the orbital obliquity 600 Ma years ago with moderation of seasonal climate cycle.

Williams (1995) suggested  $54^\circ$  obliquity during the Snowball Earth period, which would mean that the glaciation did not start from the poles, but from the equatorial region. Williams (1975) postulated that an even greater obliquity  $54^\circ \leq \epsilon \leq 126^\circ$  was responsible for the low-latitude glaciation in late Precambrian times, which resulted in pronounced global seasonality, weakened climatic zonation allowing warm-water environment and lateritic weathering over wide latitudes binding atmospheric  $\text{CO}_2$ , thus triggering global cooling-down.

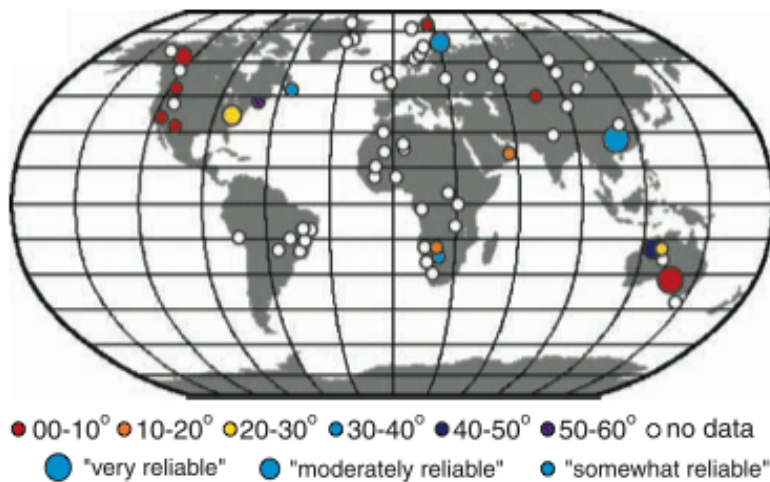


**Figure 2.** Paleoenvironmental distributions of Snowball Earth glaciations (from Evans, 2000).

In Namibia, diamictite sediments from the Sturtian Chuos Fm. were formed at 35° paleolatitude (Christie-Blick et al. 1999), whereas those from the Marinoan Ghaub Fm. formed between 5-10° paleolatitude (Evans, 2000, Fig. 2.).

The “Zipper-rift” hypothesis was introduced by Eyles (1993), who added a sedimentological perspective on the study of glacial facies, arguing for a regional-adiabatic climatic control. Eyles and Januszczak (2004) further developed the Zipper Rift model, postulating first-order control of diachronous tectonic rifting of Rodinia on the occurrence of glacier sediments in rift basins (Fig. 3.). They argue about the significance of cap carbonates in glacial cycles, but suggest clastic re-deposition of diamictites due to the tectonic context. According to Eyles and Januszczak (2004), the Sturtian diamictites (e.g., Chuos Fm. in Namibia) formed during the initial rifting phase of Rodinia (opening of the Paleo-Pacific oceans), whereas Marinoan diamictites (i.e., Ghaub Fm.) might have formed during a second rifting phase, the opening of the Iapetus ocean (Fig. 3.).

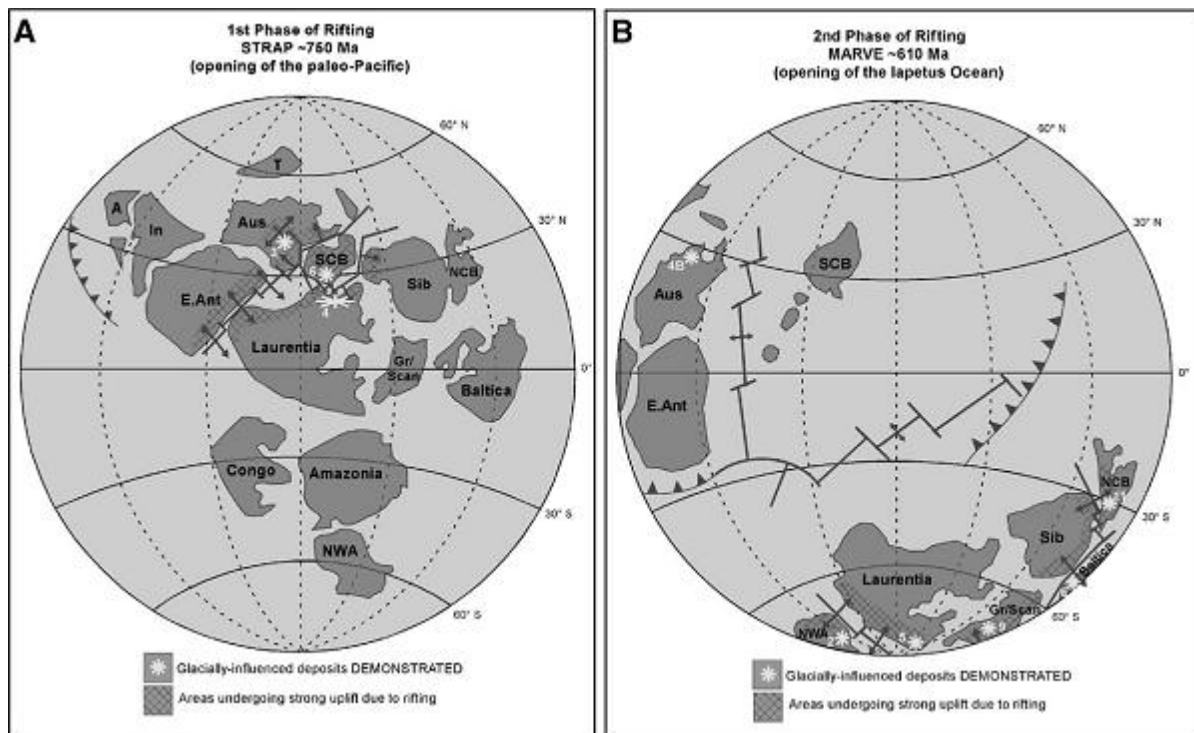


**Figure 3.** Break-up of Rodinia – rifting phase of ocean formations during the Sturtian (Paleo-Pacific Ocean) and Marinoan (Iapetus Ocean) (from Eyles and Januszczak, 2004).

### 1.2.2 Theories for the deglaciation of “Snowball Earth”

The deglaciation of Snowball earth is closely connected with the formation of cap carbonate sediments. The increase in the carbon isotopic ratio indicates cap carbonate formation by high alkalinity of Neoproterozoic oceans due to  $p\text{CO}_2$  (Hoffman, 2001). Fairchild (1993) explained the formation of cap carbonates with reaction of alkaline ions (due to continental weathering) with oversaturated hydrocarbonate ions or with carbonate-rich glacial debris rock powder interaction. Grotzinger and Knoll (1995) related the cap carbonate record to a turnover of a previously stratified ocean.

The following causations for the formation of postglacial cap carbonates are postulated: 1) shutdown of ocean ecosystems for millions of years during Snowball Earth ice ages (Hoffman et al., 1998; Hoffman and Schrag, 2002); 2) destabilization of methane hydrates during deglaciation (extreme  $\delta^{13}\text{C}$  isotopic variation about 40-50‰) (Kennedy et al., 2001). Hoffman et al. (2001) indicated that the carbon isotopic ratio anomaly can be the result of post-glacial sea rise bearing the high alkalinity input required for the  $p\text{CO}_2$  to rise to high levels. The timescales for Cryogenian deglaciations have been derived by climate modeling at thousands to millions of years; e.g., Font et al. (2010) from cap dolostone studies,  $10^3$ - $10^6$  yr,

Hoffman et al. (1998) ( $10^3$ - $10^4$  yr) and Hyde et al. (2000, ice sheet model,  $10^3$  yr), Le Hir et al. (2009, weathering model,  $10^4$ - $10^5$  yr).

Fraiser and Corsetti (2003) discovered structures that formed by microbial (calcify bacterial clumps) and diagenetic processes. Kennedy (1996) assumed cap carbonate precipitation from detrital carbonate debris due to continental weathering during the deglaciation period. Pruss et al. (2010) reported microbial facies (including thinly laminated, slowly lithified mats rolling up into roll-up structures) in the Sturtian Rasthof Formation, considered as signature of potential biogenic provenance of cap carbonate sediments formed below the storm base.

### 1.3 Geological background of research area and sample locations

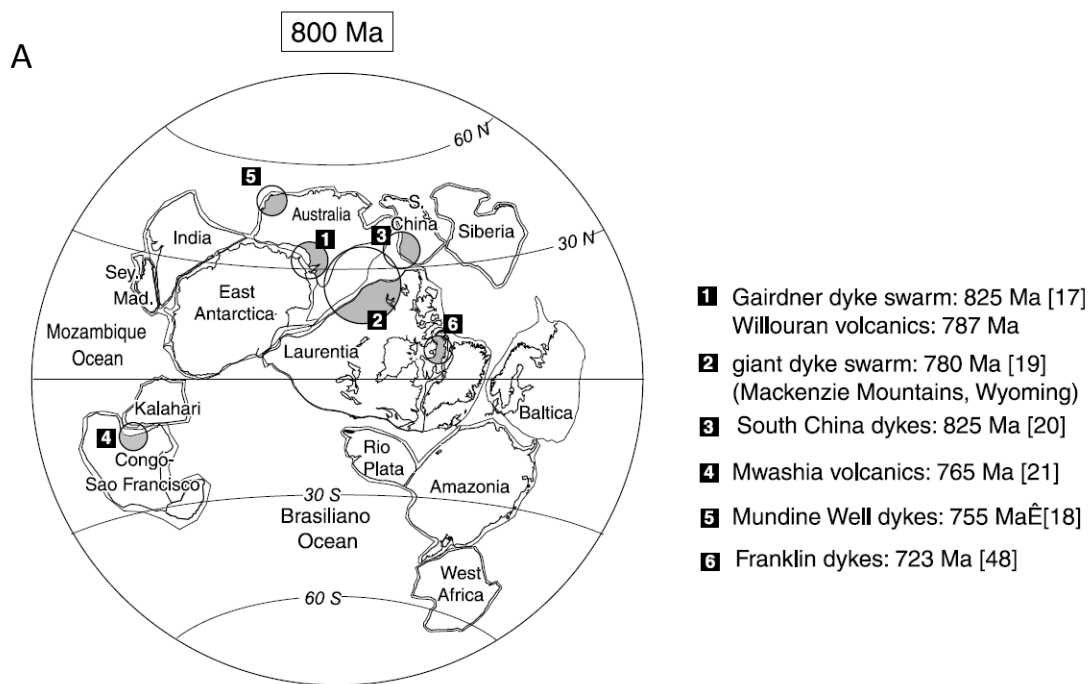
#### 1.3.1 The break-up of Rodinia and its consequences

Li et al. (2004) proposed that Rodinia extended from the equator to the polar regions around 800 Ma ago, followed by rapid  $90^\circ$  rotation around an axis near Greenland and moving to a low latitude position at 750 Ma, meanwhile the supercontinent was fragmented by oceanic spreading between  $40^\circ$ S and  $40^\circ$ N (Meert, 2003). According to Godderis et al. (2003) and Eyles and Januszczak (2004), the Sturtian glaciation (730 Ma) happened diachronous with the break-up of the Rodinia supercontinent which was accompanied by the formation of extensive magmatic provinces between 825 and 755 Ma (e.g., Laurentian basaltic magmatic province at 780 Ma,  $30^\circ$ N paleolatitude). In Australia and South China were even three major magmatic and rifting episodes identified within the Neoproterozoic period (830-700 Ma, 800 Ma, 750-720 Ma; cf. Powell et al., 1994; Li et al., 1995; Wang and Li, 2003; Figs. 3-4.). Godderis et al. (2003) proposed that the presence of large magmatic provinces induced an increase in weathering, which resulted in a decrease of atmospheric  $\text{CO}_2$ , triggering global cooling.

The breakup of Rodinia started  $\geq 750$  Ma (Meert et al., 2001), triggered by tholeiitic magmatism in Australia (825-755 Ma; Wingate et al., 1998, Wingate and Giddings, 2000), northwest Laurentia (Park et al., 1999), South China (Li et al., 1999), and the Congo craton (Key et al., 2001), and rifting between Laurentia and Amazonia Craton (Meert et al. 1999). Alternatively, Li et al. (1999) suggests start of break up Rodinia 850 Ma by rifting of South China-Laurentia-Rio de La Plata in east and Australia-Mawson Craton in west. Godderis et al. (2003) emphasized that mafic rocks lie beneath Sturtian glacial diamictites in Laurentia. The Siberian trap basalt volcanism initiated the opening of the Proto-Pacific ocean and induced a southward drift of Laurentia (Wignall et al., 2001). Torsvik et al. (1996) propose according their paleomagnetic data an enhanced drift with opening of the Proto-Pacific Ocean during the Marinoan suggests a southern location of the continental area. The tropic equato-

rial climate induced high rate weathering of Sturtian fresh flood basalts, maximizing atmospheric oxygen and continental denudation (Godderis et al., 2003). Additionally, Godderis et al (2003) suggests the following paleoenvironmental conditions for the Sturtian Snowball Earth: 1) paleoequatorial location of large basalt provinces caused by rifting of Rodinia and southward drift of Laurentia; 2) rather cool pre-weathering climate; 3) as much as 280 ppm pCO<sub>2</sub> share in air and +0.8°C increase in temperature during the Neoproterozoic glacial periods. Starting ~ 600 Ma ago, the continents (Laurentia, Baltica, Rio de la Plata craton, West Africa, Amazonia craton) drifted towards the southern hemisphere assembling with the Gondwana supercontinent (Meert et al., 2003) via continental collisions building widespread Panafrican orogenic belts (Stern, 1991; Jahn et al., 2001).

Continental rifting in high latitude position and subsequent opening of the Iapetus ocean was approximately diachronous (635 Ma) with (Hartz and Torsvik, 2002), or a later (500 Ma) than the Marinoan glaciations (Cawood et al., 2001). The models for Marinoan glaciations provide the possibility to estimate the effects of orogeny and glacial continental climate (Hyde et al., 1990).



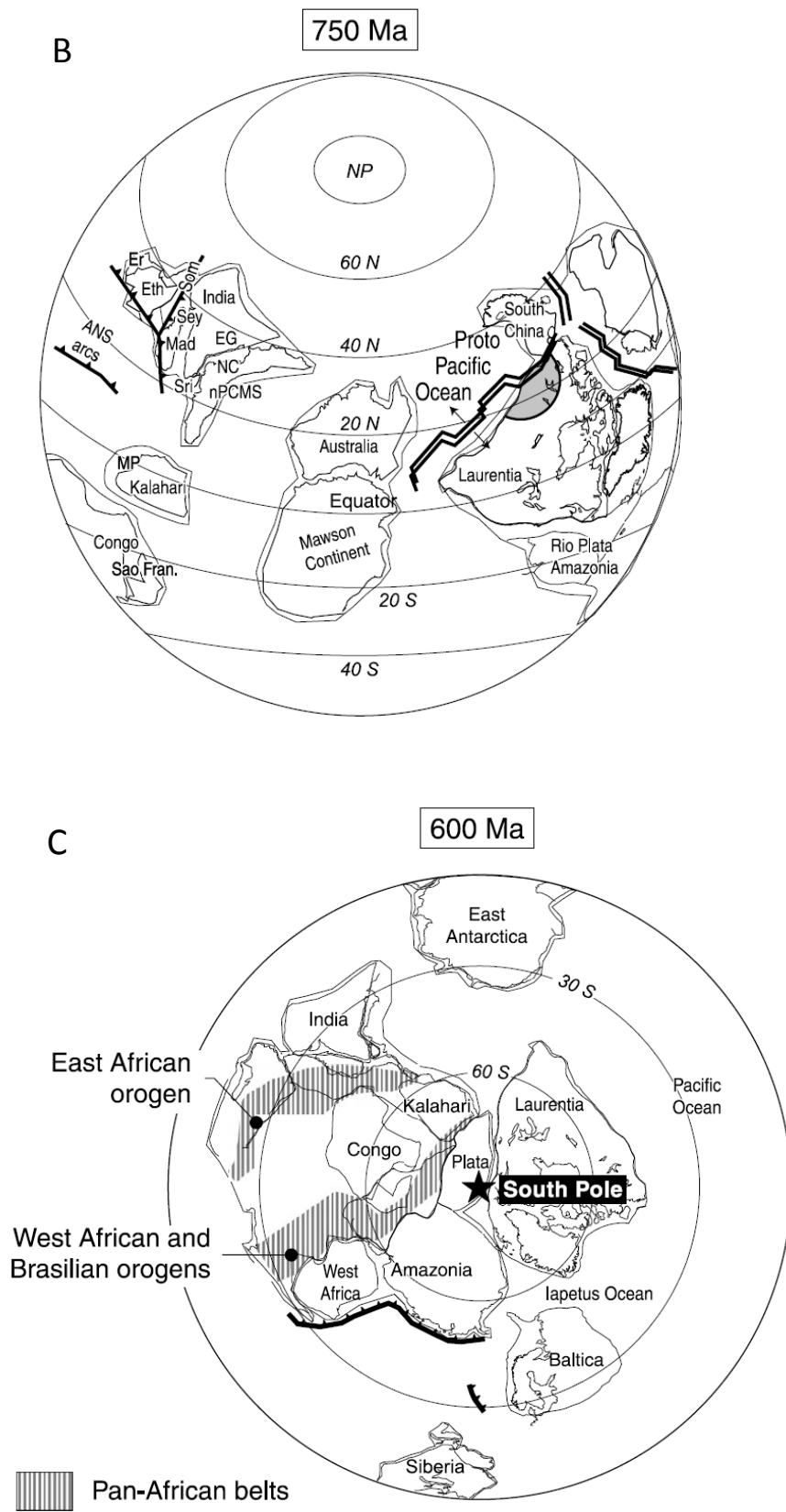


**Figure 4.** Continental reconstruction during the Neoproterozoic ice ages (from Godderis et al., 2003)  
 A: 800 Ma, B: 750 Ma. C: 600 Ma.

Hoffman and Li (2009) favor the assumption that the Sturtian (715 Ma) and Marinoan (635 Ma) glaciations happened at high meridional paleolatitudes. The characteristic, glaciogenic formation of carbonate dominated sediments formed at latitudes around 35°. The large Fe and Fe-Mn (BIF) deposits lay around 35° latitude. (Christie-Blick et al., 1999) Marinoan synglacial cap dolostones decrease in maximum thickness with paleolatitude, whereas the ice retreat polewards. Meridional (N-S) orientation of giant ripples supports zonal wind-driven waves (Hoffman and Li, 2009).

### **1.3.2 Geological background of the research area**

Continental break-up of the Mid-Proterozoic Rodinia Supercontinent produced world-widespread extensional rift systems, followed by the development of passive continental margins. In Namibia the Damara Supergroup, consisting of the Nosib-, Otavi-, Mulden-, Nama-, Witvlei-, and Gariiep Groups, formed during this period in response to Pan-African continental rifting with subsequent oceanic spreading, subsidence, and marine transgression on the West Gondwanaland continent (Porada, 1989). On the Congo Craton initial rifting caused deposition of the Nosib Group siliciclastic sediments; later subsidence and transgression lead to the development of a stable platform where the thick sequence of Otavi Group carbonate dominated sediments accumulated. Subsequent uplift in the northwestern part of the Damara Orogen, caused by the collision of the Kalahari and Rio de la Plata Cratons with the Congo Craton, resulted in deep erosion of Damaran and older rocks (Martin, 1965; Hedberg, 1979; Miller, 1983, Fig. 5.) and the consequent deposition of the Mulden Group as a molasse.

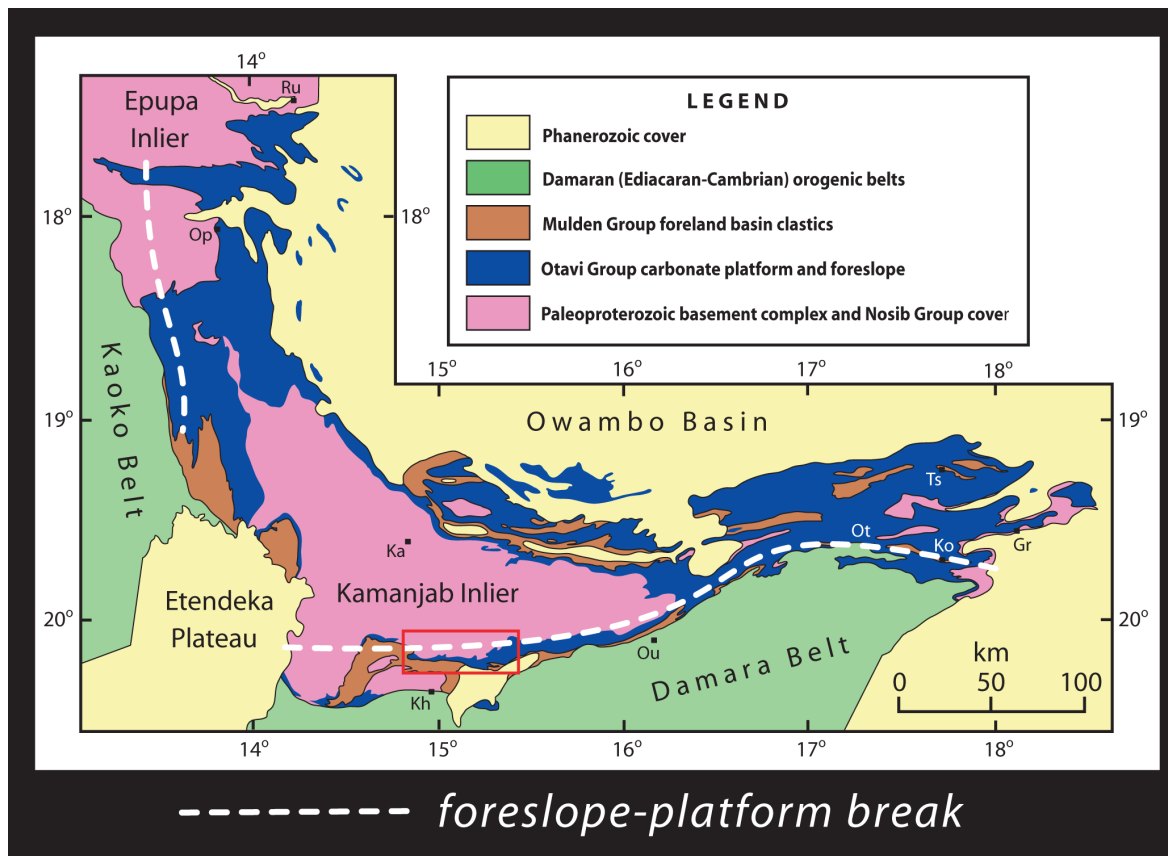


**Figure 5.** Geological map of Otavi belt with tectonic structures (from Hoffman, 2002).

### 1.3.2.1 The Congo Cratonic Sedimentary Cover Sequence

In the late Neo-Proterozoic the Congo Craton was a Bahama-type sea-level carbonate platform of enormous size, accumulating the Otavi Group sediments, which nowadays drape the craton's southern promontory in NW Namibia. The Otavi Group is exposed for ~700 km along strike in the external zone of the Pan-African Damara-Kaoko Belt that rims the Craton (Hedberg, 1979). In NW Namibia the Damara-Kaoko fold belt is defined by a tripartite Neo-Proterozoic succession (Fig. 5.):

- At the base there is the rift-clastic Nosib Group, known to be older than  $756 \pm 2$  Ma (Hoffmann et al., 1996). It consists of conglomerate, arkosic quartzite, and siltstone with minor shale and carbonate. Volcanic rocks are found sporadically within the section (Hedberg, 1979).
- In the middle there is the carbonate-dominated Otavi Group, a succession of Neo-Proterozoic age (~600-760 Ma), which constitutes a typical shelf facies and rests paraconformably or unconformably upon the Nosib Group. The Otavi Group spans the rift-drift transition and succeeding thermal subsidence stage of the Congo Craton's passive margin. The lower Otavi Group (Ombombo Subgroup) contains volcanics dated at  $758 \pm 4$  and  $746 \pm 2$  Ma (Hoffmann et al., 1996).

- The middle Otavi Group (Abeneb Subgroup) is bounded by two discrete intervals of diamictite and associated by glaciomarine deposits, sandwiched by thick carbonate piles. The glaciogenic origin of the older interval (Chuosi Formation) was first documented by Martin (1965a, b) and Hedberg (1975). Later Hoffmann and Prave (1996) lined out the younger glaciogenic interval (Ghaub Formation), covering an erosional surface on top of a carbonate platform sequence (Ombaatjie Formation). The sediments of both glaciogenic periods are overlain by distinct “cap-carbonate” layers, represented by the basal parts of the Rasthof- and respectively Maieberg Formations.

The upper Otavi Group (Tsumeb Subgroup) is a thick and rather monotonous stack of grainstone-dominated cycles of cherty dolomite, deposited during the prolonged drift stage of the Panafrican Damara orogenic cycle.

At the top of the succession the Mulden Group siliciclastic foreland sequence follows a typical molasses facies pile related to the Congo craton’s collision (~630-550 Ma) with the active margin of the Rio de la Plata Craton (Stanistreet et al., 1991; Alkmim et al., 2001). The Mulden Group rests disconformably upon the folded Otavi Group and consists of conglomerate, quartzite, siltstone and shale. Rb-Sr isotopic studies of Mulden Group shales suggest a model depositional age of 550-560 Ma, followed by two distinct low-grade thermal events of regional extent at  $537 \pm 7$  and  $457 \pm 12$  Ma, respectively (Clauer and Kröner, 1979).

### 1.3.2.2 *The termination of the Sturtian glacial period*

Sturtian postglacial transition layers span the uppermost/lowermost portions of the Chuosi/Rasthof Formations. Massive to poorly stratified diamictite is the characteristic lithology of the glaciogenic Chuosi period of sedimentation.

- The **Chuosi Formation** is widely exposed throughout the Northern Platform Area varying both regionally and locally in thickness, being thickest (up to ~1000 m) in paleodepressions and absent on paleohighs (Martin, 1965a, b). Towards the outer Platform edge and foreslope area the diamictite thins virtually to zero. These diamictites are interpreted as originating mainly from glacial marine rain-out deposits, formed close to the grounding line of warm-base ice streams (Hoffmann and Halverson, 2008).
- The upper Chuosi Formation contact is almost invariably sharp and smooth, genetically interpreted as an abrupt flooding surface separating diamictite from deepwater dolomite rhythmite of the basal **Rasthof Formation** that on this part displays no evidence of reworking, subaerial exposure or significant hiatus. Unlike the Marinoan Maieberg cap-carbonate sequence, the Rasthof Formation has no transgressive stage: the deepest water facies are at the bottom of the sequence. This implies that carbonate sedimenta-

tion did not begin until after the glacio-eustatic rise (Hoffmann and Schrag, 2002; Hoffmann and Halverson, 2008).

- The Rasthof Formation, normally 200-400 m thick on the Otavi Platform, has a layer-cake internal stratigraphy comprised of three members termed “abiotic”, “microbial” and “epiclastic” (Hoffmann and Halverson, 2008). The basal abiotic Member of the Lower Rasthof Formation, which is one focus of this work, consists of flaggy, dark gray dolomite and dolomitic limestone, characterized by mm-scale, parallel, turbiditic lamination. Hematite, mobilized from the underlying diamictite, stains the basal few centimeters of the dolomite rhythmite.

### 1.3.2.3 *The termination of the Marinoan glacial period*

Marinoan postglacial transition layers span the uppermost/lowermost portions of the Ghaub/Maieberg Formations. The **Ghaub Formation** is only fragmentary preserved within structural depressions of inner platform areas. It suggests that the western Otavi Platform was the source area for appreciable diamictite accumulations in slope facies areas bordering on the platform edges (Hoffmann and Prave, 1996). The clasts are different types of dolomite and rarely limestones, all apparently derived from the underlying Ombaatjie Formation. Thus, the Ghaub glacial lithofacies are composed almost exclusively of carbonate debris (Hoffmann and Halverson, 2008). Stratigraphic evidence is presented for a single advance and retreat cycle for the Ghaub glaciation; grounded ice existed at the maximum advance leaving characteristic sedimentary features (Domack and Hofmann, 2003).

The **Maieberg Formation** can be subdivided into three members, and it is an up to 400 m thick pile of carbonate sedimentary cycles, which originated in a warm periodic platform facies environment, following the Ghaub glacial period (Hedberg, 1979, SACS 1980). The basal **Keilberg Member** is a “cap dolostone” associated with the sea-level rise attending the Ghaub deglaciation (Kennedy, 1996; Hoffmann and Prave, 1996; Hoffmann and Schrag, 2002). Its characteristic feature is a uniform, 10-15 m thick, pale colored marker bed, which is strongly laminated from bottom to top. Unusual sedimentary textures, featuring vertical “tube-like” appearance, are visible, starting about one meter above the base, in our sample sites. According to Le Hir et al. (2009) these tubes may have been generated due to CO<sub>2</sub> oversaturation and methane outgassing from clathrates (Kennedy et al., 2008). However, Hoffmann and Halverson (2008) instead preferred the hypothesis that the tubes formed in close connection with the growth of compound stromatolites.

## 1.4 Samples

### 1.4.1 Lithology of Sturtian postglacial transition layers

Three sites were sampled from Sturtian post-glacial transition layers for various analyses (Table 2.):

**1.) Site No. 8:** Copper Mine (Fig. 6.) is located within the proximal inner Platform area. A thick pile of conglomerate, altered by Cu-mineralization, is truncated by a 15-m-thick pile of laminated sandstone (samples C9, 10, 11) which is ultimately topped by a 5-m-thick set of dolomite strata. The base of that dolomite layers (sample C8) is probably recording the post-glacial transition sediments in Sturtian times.

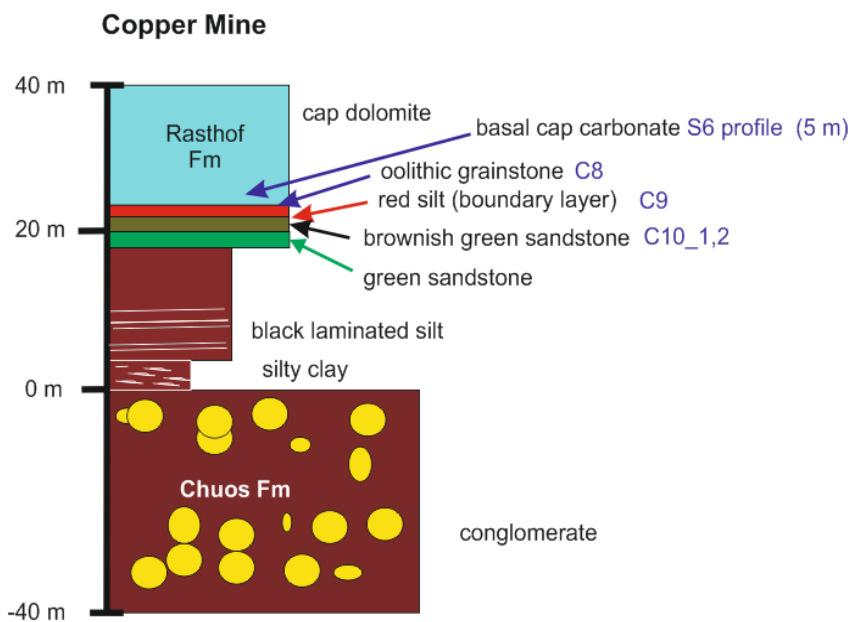


**Figure 6.** Lithological profile of Sturtian glacial deposits from the Otavi platform facies at Copper Mine (19°25'18.43"S, 15° 9'50.90"E) –Road D2680 near Gagarus (F. Popp's field trip data, 2009).

**2.) Site No. 9:** Steilrandberge (Fig. 7.) is located within the Steilrandberge Syncline of the Northern Platform area. Because of its proximal position within the evolving Otavi Platform the diamictites accumulated to an up to 1000 m thick section (Martin, 1965a, b) in Chuos times. Their cap-dolomitic layer (sample C12) is the focus of our interest in this site area:

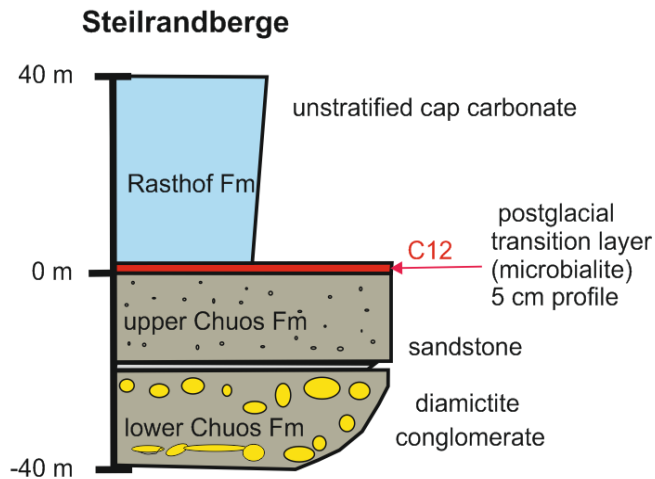


**Figure 7.** Lithological profile of Sturtian glacial deposits from the northern Hoanib shelf at Steilrandberge outcrop (17°47'1.67"S; 13°39'54.10"E) (F. Popp's field trip data, 2009).

**3.) Site No 10:** Sesfontain-Opuwo Road (Fig. 8.) is located within an area of the Northern Platform (Hoanib shelf) which was affected by the tectonic folding of the eastern Kaoko Zone. The diamictites of this site are significantly penetrated by iron-oxide mineralization, which is the source of intensive staining within the basal cap-dolomite transition layers (sample C13).

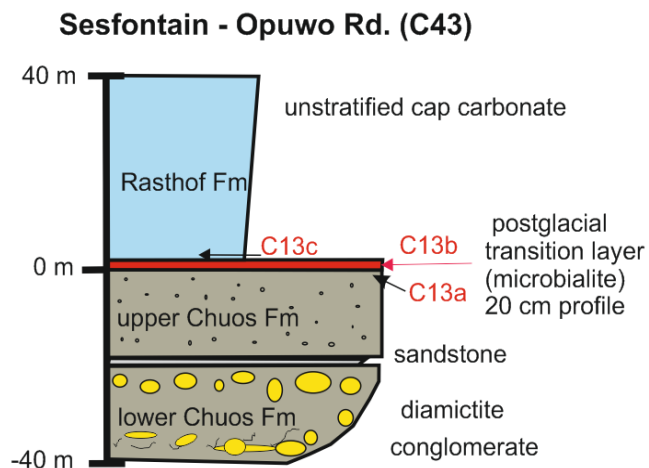


**Figure 8.** Lithological profile of Sturtian glacial deposits from the Hoanib shelf, outcropping at Sesfontain - Opuwo (C43) Rd. (18°46'26.49"S; 13°45'11.24"E). (F. Popp's field trip data, 2009).

**Table 2.** Otavi Group: Samples from Sturtian transition layers.

Site Nr	Sample Nr	Locality	Lithology	Glaciation/Deglaciation Event	Facies
8	Profile S6	Copper Mine	opalized carbonate	Rasthof F.	platform
8	C 8	Copper Mine	red carbonate	Chuoss- Rasthof Fm.	platform
8	C 9	Copper Mine	carbonate-quartzite	Chuoss- Rasthof Fm.	platform
8	C 10_1	Copper Mine	sandstone	Chuoss- Rasthof Fm.	platform
8	C 10_2	Copper Mine	sandstone compact	Chuoss- Rasthof Fm.	platform
8	C 11_1	Copper Mine	black laminated sandstone	Chuoss- Rasthof Fm.	platform
8	C 11_2	Copper Mine	black laminated sandstone	Chuoss- Rasthof Fm.	platform
9	C 12	Steilrandberge	red-brown dolomite	Chuoss- Rasthof Fm.	platform
10	C 13a	Sesfontain-Opuwo Rd	brown sandstone unaltered	Chuoss- Rasthof Fm.	platform
10	C 13b	Sesfontain-Opuwo Rd	red/green sandstone altered	Chuoss- Rasthof Fm.	platform
10	C 13c	Sesfontain-Opuwo Rd	transition zone to carbonate	Chuoss- Rasthof Fm.	platform

### 3.1 Lithology of Marinoan post-glacial transition layers

Seven sites were sampled from Marinoan transition layers for various analyses (Table 3.):

**Site No. 1: Fransfontain** (Fig. 9.) is located at the C35-roadcut north of Fransfontain village. This site is representative for Marinoan **slope facies** deposits of the Fransfontain ridge at the southern edge of the Otavi Platform.

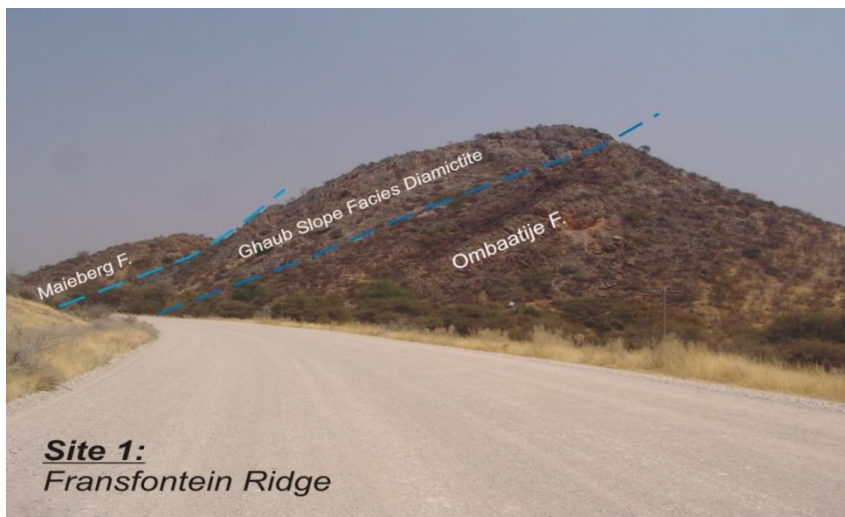


**Figure 9.** Panorama of the Fransfontain ridge showing geological formations (Photo: F. Popp).

The **Ghaub Formation** consists of a 120-m-thick stack of massive to poorly stratified diamictite bodies, rich in ice-rafted debris which is derived almost exclusively from the under-

lying upper Ombaatjie Formation / Franni-aus Member (Hoffman and Halverson, 2008). The upper Ghaub Formation is represented by the **Bethanis Member**, a terminal bedded, fining upward dololomite with outsize clasts deposited together with ice-rafted debris (Hoffmann, 2011).

The base of the **Maieberg Formation** is represented by an equivalent of the **Keilberg Member** (platform area), genetically a post-glacial cap dolostone lying sharply on the Ghaub Formation. Its basal unit is a marly allodapic dolostone (samples C1a, b, c), which is the focus of our interest in this area.

**Site No. 2: Naraachamspos** (Fig. 10.) is located 1.5 km NE from Naraachamspos village. This site takes up a most proximal position at the Fransfontain slope.

The **Ghaub Formation** is composed of a ~55 m thick pile of mixed sandstone, siltstone and poorly stratified diamictite, followed upwards by graded beds of resedimented diamictite debris flow and a terminal, ~2 m thick unit of stratified diamictite (sample C17a, b) with dolomite dropstones up to a meter in size (**Bethanis Member**). It is overlain with an abrupt depositional contact by fine-grained, thin bedded, allodapic dolostone (samples C2, C3, C17c) of the basal **Maieberg Formation** in which outsize clasts are virtually absent. The contact shows no evidence of exposure, reworking or significant hiatus. Low-angle hummocky cross-lamination, stromatolites or tabular structures, ubiquitous in the basal Keilberg cap dolostone on the platform, are absent here. Isopachous cements, filling sheet cracks close to the base of the Maieberg Fm., appear to have formed penecontemporaneously on the sea floor, implying that slope– depth bottom waters were critically oversaturated at least temporally (Hoffman, 2002).

#### Pip's Rock near Naraachamspos

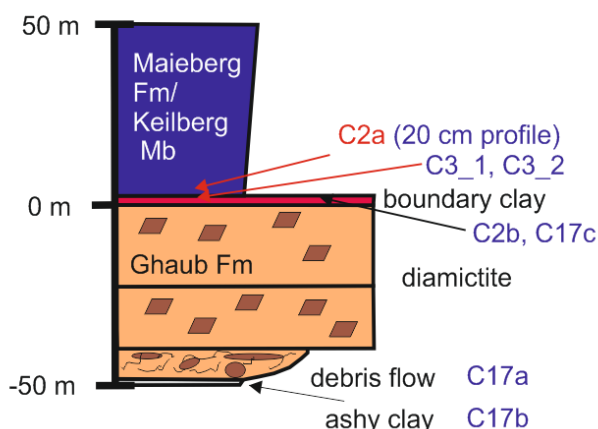


**Figure 10.** Stratigraphic profile of the Otavi slope facies near Naraachamspos, Pip's rock outcrop (20°11'28.74"S; 14°51'4.38"E) (modified after Hoffman, 2002). Position of measured samples is indicated.

**Site No. 3: Tweelingskop** (Fig. 11.) is located on the Huab River near the western edge of the farm Tweelingskop 676 (at Lat. 20°07`S; Long. 14°35`E). This site is representative for Marinoan **outer platform paleokarst facies** deposits of the Huab ridge at the southern edge of the Otavi Platform. Already in pre-glacial times the platform carbonate development of the Ombaatjie **Formation** is marked by a set of strongly retrogradational parasequences in its upper part inclosing a karstic surface (sample C4) consistent with a pre-glacial decline in  $\delta^{13}\text{C}$  of  $\sim 10\text{‰}$  (Hoffman, 2002).

Upwards a 30 m pile of massive, pervasively recrystallized, light gray **dolostone aeolianite** (sample C5) in the place of the **Ghaub diamictite** is present on the Huab ridge. Typical sedimentary structures are aeolian “pinstripe” lamination and large-scale foreset bedding which is oriented consistent with onshore transport by paleowinds. The unit disappears rapidly towards the inner shelf region in the north as well as to the area of a major regional shelf break in the south. Most reasonably this unit represents a cold-desert dune field, developed at the windward edge of the platform, following the sea-level fall associated with the **Ghaub glaciation** (Hoffman, 2002).

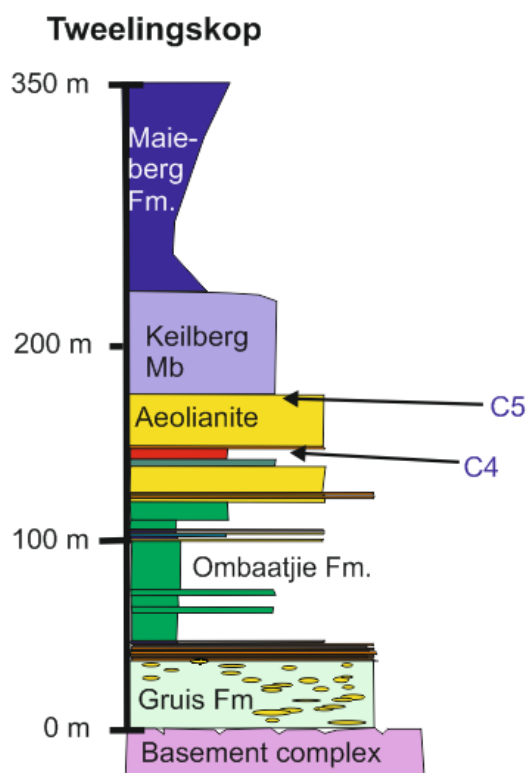


**Figure 11.** Stratigraphic profile of the Huab ridge (Otavi platform edge facies) at Tweelingskop locality (20° 7'13.47"S; 14°35'1.30"E) (modified after Hoffman, 2002).

According to Hoffmann (2002), the overlying cap dolostone of the Maieberg Formation is abiotically laminated within the basal meter, but the rest of the unit is a tube biostrome with the tabular structures invariably standing paleovertical within stromatolites, irrespective of the

primary dip of the stromatolitic lamination. The vertical orientation supports an origin by fluid or gas escape. As the structures do not occur at the base of the unit, the fluid or gas must have been generated within the cap dolostone, rather than from the underlying aeolianite as mentioned in the permafrost-methane hypothesis (Kennedy et al., 2001).

**Site No. 4: Bethanis** (Fig. 12.) is located in the eastern part of farm Bethanis 514, NE from Camp Xaragu. This site is representative for Marinoan **distal slope facies** deposits of the Huab Ridge at the southern edge of the Otavi Platform. The terminal **Ghaub Formation** is a polymictic diamictite (sample C6) of the **Bethanis Member**, which is sharply overlain by a cap dolomite rhythmite (sample C7) of the basal **Karibib Formation**.

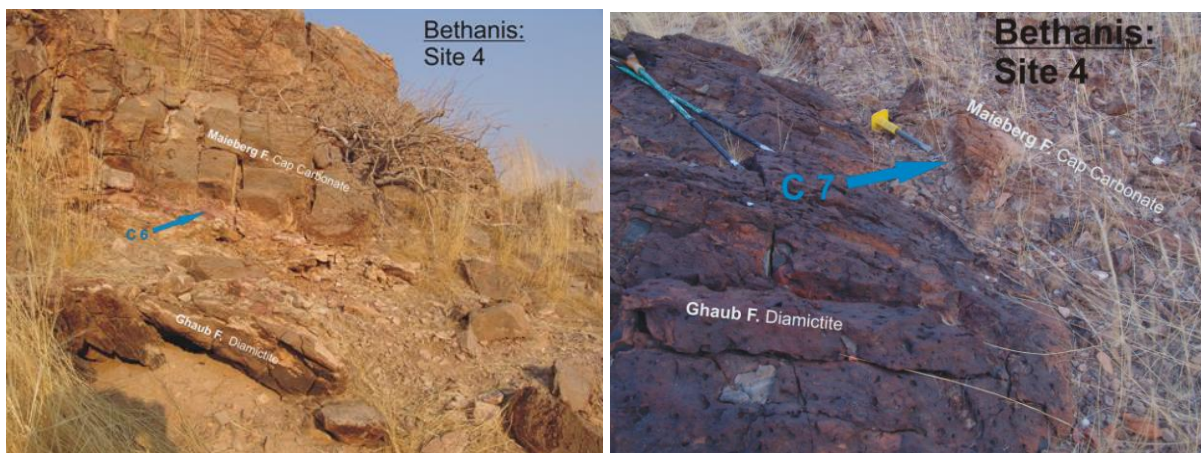


**Figure 12.** Sampling sites from slope facies sediments of the Otavi platform margin at Bethanis. Sample C 6 (20°24'24.00"S; 14°20'13.55"E), sample C 7 (20°24'21.95"S; 14°20'35.06"E) (Photo: F. Popp).

**Site No. 5: Entrance towards SW Valley** (Fig. 13.) is located ~4 km SW from Devede village at the very top end of a traverse following a valley southwesterly directed starting from the road Entrance into the Aap River. This site, embedded in the Panafrican Khowarib fold belt, is representative for Marinoan **inner platform facies** deposits of the western Otavi Platform.

There is a well developed diamictite (C14a) of the Ghaub Formation directly beneath laminated and tubed cap dolostone (C14e and K4) of the basal Maieberg Formation (Keilberg Member). In between there are mm-thin red-green colored transition layers (C14b-d), which was the focus of our interest at this site.

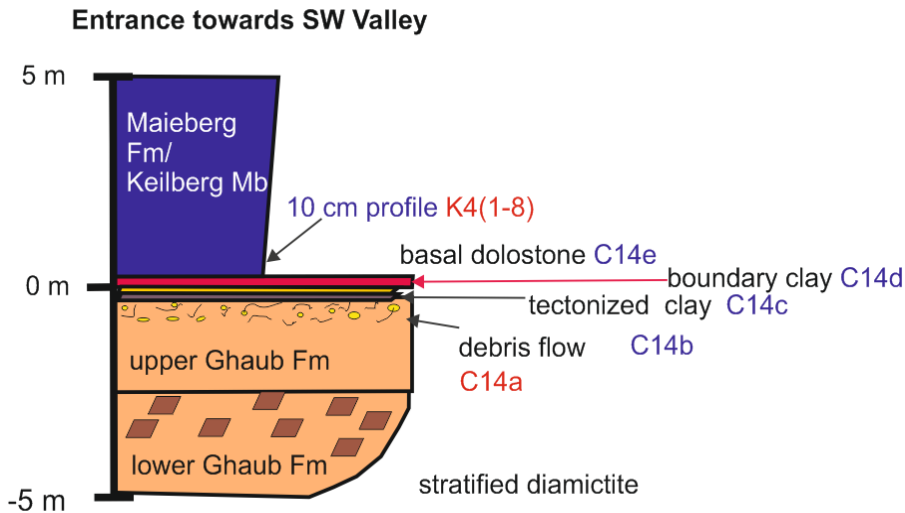


**Figure 13.** Stratigraphic profile of the Otavi platform facies at the very end of the SW Valley from Entrance towards ( $19^{\circ}11'18.40''\text{S}$ ;  $13^{\circ}56'13.39''\text{E}$ ) (after F. Popp, unpublished field data).

**Site No. 6: Khowarib Valley** (Fig. 14.) is located in a northeasterly directed side valley branching from the Hoanib Riverbed ~6 km east of Ombaatjie village. This site is also representative for Marinoan **inner platform facies** deposits of the western Otavi Platform.

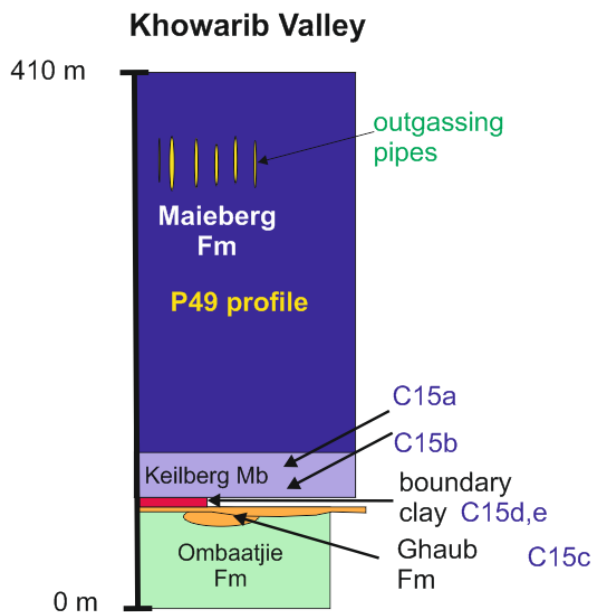


**Figure 14.** Stratigraphic profile of the Otavi platform facies at Khowarib Valley ( $19^{\circ}18'24.52''\text{S}$ ;  $13^{\circ}59'25.57''\text{E}$ ) (modified after Hoffman 2002).

The carbonate diamictite of the **Ghaub Formation** ranges in thickness from 0.1 to 1.5 m showing abrupt lower and upper contacts. The basal meter of the **Keilberg Member** is hummocky cross-laminated pale dolostone (C15a, d). Initiation of tabular sedimentary structures follows across apparently confined within stromatolites, which develop at nodes, expand upwards, and coalesce laterally (Hoffman, 2002).

At the base of the Keilberg Member there are mm-thin red colored transition layers (C15b, c, e), which was the focus of interest at this site.

**Site No. 7:** Ongongo (Warmquelle) (Fig. 15.) is located at the minor road (at S19°08, 5'S; 13°51, 25'E) from Warmquelle to Devede village. This site, also embedded in the Panafrican Khwarib fold belt, and is representative for Marinoan **inner platform facies** deposits in an area, where the Ghaub glaciation left behind an erosional surface within upper strata of the underlying **Ombaatjie Formation**, which directly is overlain by pale cap dolostone of the basal Maieberg Formation (Keilberg Mb.). At the base of the cap dolostone there are partly tectonized transition layers (C16a, b, c and K2), which was the focus of interest at this site.

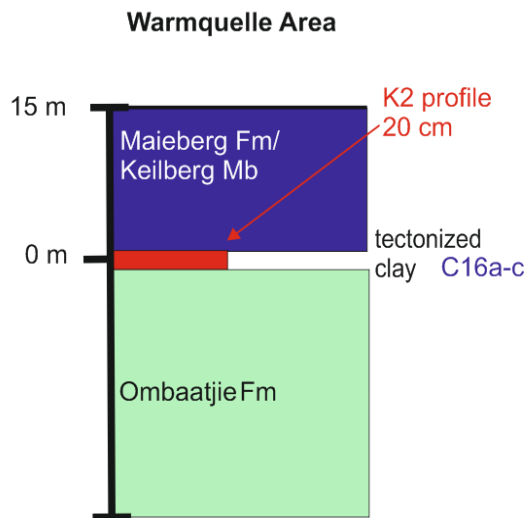


**Figure 15.** Stratigraphic profile of the Otavi platform facies near Ongongo (Warmquelle) (19° 8'35.77"S; 13°51'15.40"E) (after F. Popp, unpublished field trip data).

**Table 3.** Otavi Group: Samples from Marinoan transition layers in Namibia.

Site Nr	Sample Nr	Locality	Lithology	Glaciation/Deglaciation Event	Facies
1	C1a	Fransfontain	allodapic dolostone	Ghaub-Maieberg Fm.	slope
1	C1b	Fransfontain	allodapic dolostone	Ghaub-Maieberg Fm.	slope
1	C1c	Fransfontain	allodapic dolostone	Ghaub-Maieberg Fm.	slope
2	C2a	Naraachamspos	boundary layer	Ghaub-Maieberg Fm.	slope
2	C2b	Naraachamspos	boundary layer	Ghaub-Maieberg Fm.	slope
2	C2c	Naraachamspos	boundary layer	Ghaub-Maieberg Fm.	slope
2	C3_1	Naraachamspos	boundary layer	Ghaub-Maieberg Fm.	slope
2	C3_2	Naraachamspos	boundary layer	Ghaub-Maieberg Fm.	slope
2	C17a	Naraachamspos	tectonic clay	Ghaub-Maieberg Fm.	slope
2	C17b	Naraachamspos	ashy clay	Ghaub-Maieberg Fm.	slope
2	C17c	Naraachamspos	boundary layer	Ghaub-Maieberg Fm.	slope platform
3	C4	Tweelingskop	red dolomite	Ghaub-Maieberg Fm.	edge platform
3	C5	Tweelingskop	aeolianite	Ghaub-Maieberg Fm.	edge
4	C6	Bethanis	red Silt	Ghaub-Maieberg Fm.	distal slope
4	C7	Bethanis	dolomite rhythmite	Ghaub-Maieberg Fm.	distal slope
5	C14a	Entrance to the South Valley	red diamictite	Ghaub-Maieberg Fm.	platform
5	C14b	Entrance to the South Valley	red transition Layer	Ghaub-Maieberg Fm.	platform
5	C14c	Entrance to the South Valley	tectonized clay	Ghaub-Maieberg Fm.	platform
5	C14d	Entrance to the South Valley	red-green boundary clay	Ghaub-Maieberg Fm.	platform
5	C14e	South Valley	basal dolomite	Ghaub-Maieberg Fm.	platform
6	C15a	Khowarib Valley	banded cap-dolomite	Ghaub-Maieberg Fm.	platform
6	C15b	Khowarib Valley	boundary layer	Ghaub-Maieberg Fm.	platform
6	C15c	Khowarib Valley	red boundary clay	Ghaub-Maieberg Fm.	platform
6	C15d	Khowarib Valley	basal cap dolomite	Ghaub-Maieberg Fm.	platform
6	C15e	Khowarib Valley	boundary clay	Ghaub-Maieberg Fm.	platform
7	C16a	Ongongo	sericitized clay	Ghaub-Maieberg Fm.	platform
7	C16b	Ongongo	basal mylonite	Ghaub-Maieberg Fm.	platform
7	C16c	Ongongo	opalized layer	Ghaub-Maieberg Fm.	platform

## 1.5 Search for extraterrestrial material

During a giant meteoric impact the dispersed dust spreads rapidly into the atmosphere and creates a dust layer around the whole globe, resulting in immediate global cooling and interruption of photosynthesis. Catastrophic impacts event of this scale, involving asteroids of about 10 km in diameter, occur on Earth about once every 100 million years (Montanari and Koeberl, 2000). Smaller impact events happen more often. Impacts creating craters of about 100 km in diameter may have global effects.

An impact crater is a depression on the surface of the planetary body, which is caused by an impact event. The crater formation mechanism is divided to three main stages: (i) contact of comet or asteroid with target rock and beginning the compression phase; (ii) excavation stage; and (iii) modification and collapse of the transient crater (e.g., Melosh, 1989; Ivanov and Artemieva, 2002). Impact craters can be classified on Earth according to their morphologies into two main types: 1) simple craters (bowl-shaped craters with up to 4 km diameter); 2) complex craters (central uplift, flat floor, inward collapse; diameters larger than about 4 km).

Different units of crater filling breccias, mixture of shocked and unshocked rock and mineral clasts together with impact melt which slumped in the crater from the walls and crater rim, are good tools for the reconstruction of the crater formation history (Stöffler et al., 2004). There are currently about 183 accepted terrestrial impact structures known according to Impact Crater Database (2013).

Stöffler et al. (1991) classified shock effects in minerals into 6 shock stages. In meteorites olivine and pyroxene are the most abundant mineral phases, in which shock effects can be observed. Whereas in the terrestrial rocks quartz and feldspars are the most important minerals, so impact signatures are observed in these minerals.

*Criteria used for the description of impact structures:*  
(the most important criteria are mineralogical effects and geochemical anomalies – only items no. 1 and 2 below are uniquely characteristic of impact; see, e.g., French and Koeberl 2010)

- 1) The presence of shock metamorphic effects in minerals, especially in quartz and feldspars
- 2) siderophile element anomalies
- 3) petrology: impact breccias
- 4) sedimentology: sedimentary structures in crater formation on marine impacts (Dypvik and Jansa, 2003)
- 5) geophysical methods: magnetic and gravitational anomaly, which describes the crater morphology

Shock metamorphic effects are a term of shock induced changes in the minerals, such as formation of planar microstructures, phase transformations, decomposition, melting and va-

porization of minerals. The shock metamorphic effects occur if the shock P-T regime of adjacent rocks, and minerals are above their Hugoniot elastic limit (HEL; Stöffler, 1972). The HEL of quartz is mostly in the range of 5-8 GPa and 1-10 GPa for almost any types of geological material (Langenhorst and Deutsch, 1994). The shocked rocks are called impactites, which occur in two types: proximal impactites, and distal impactites. Proximal impactites are classified into 1) monomict (occurrence on or below floor of craters; weak or no shock metamorphism), 2) lithic breccia (mineral and lithic casts with absence of cogenetic melts), and 3) suevite (polymict breccia with co-genetic melt) (Stöffler and Grieve 2007). Pseudotachylite is formed by decompression melting of target rocks occurring as irregular dike-like bodies (Vredefort structure, Sudbury; Reimold, 1995; French, 1998). According to Stöffler and Grieve (2007) there are two types of distal impactites: (i) consolidated (tektites and microtektites; (ii) unconsolidated airfall ball beds (Ferriere, 2008). Tektites and microtektites are natural glasses, which are green to black in color, and show variety of shapes which formed by melting of terrestrial surface during the impact event. The microtektites are up to 1 mm in size (Koeberl, 1994). According to Stöffler and Grieve (2007) the airfall beds are pelitic sediment with melt spherules, shocked and unshocked clasts.

In terrestrial rocks, the shock metamorphic features are studied mostly in quartz and feldspar. With increasing shock pressure in minerals appear a variety of shock deformation microstructure: 1) irregular fractures, 2) planar fractures (PFs: greater than 3  $\mu\text{m}$  wide, and are spaced more than 15-20  $\mu\text{m}$  apart; 5-8 GPa shock pressure), 3) planar deformation features (PDFs: 2  $\mu\text{m}$  thick, spaced 2-10  $\mu\text{m}$  apart; shock pressure from 5 to 35 GPa) (for details, see: Stöffler and Langenhorst 1994, Montanari and Koeberl 2000, and French, 1998).

Plastic deformed quartz shows undulatory extinction, which is common in tectonic deformed quartz as well. PDFs have been observed in olivine, pyroxene, amphibole, sillimanite, garnet, apatite and zircon (French, 1998; Langenhorst, 2002). Kink bands have been frequently observed in mica (muscovite, biotite) sometimes in other minerals, such as graphite (Stöffler, 1972) and olivine. Kink-bands form without specific orientation relative to the rational crystallographic planes. Kink-bands in sheet silicates occur in tectonically deformed rocks, and thus cannot be used as diagnostic criteria for the impact origin of a structure. Mechanical twins are mainly observed in pyroxene, amphibole, sphene and ilmenite, and more rarely in plagioclase. These twins appear as sets of parallel bands from submicroscopic to 10  $\mu\text{m}$  in width (Stöffler, 1972). Mosaicism occurs in olivine, pyroxene and feldspar. Little is actually known about shock deformation of calcite, but calcite can develop dense mechanical twins. In general, melting of individual minerals starts at around 50 GPa and around 55-60 GPa 700-800  $^{\circ}\text{C}$  for whole rock melting (Stöffler and Langenhorst, 1994).

Geochemical methods are used to determine the presence of minor traces (usually <1 wt%) of an extraterrestrial component, which can be done by studying the concentrations

and interelement ratios of siderophile elements especially PGEs (Ru, Rh, Pd, Os, Ir, and Pt) and Au, which are several orders of magnitude more abundant in meteorites than in terrestrial upper crustal rocks (e.g., Koeberl et al. 1998). Higher siderophile element content in impact melt can be indicative of the presence of either a chondritic or iron meteoritic component. The often used siderophile elements are Ni, Co, Cr, which of interelemental ratios are effective discriminators. Meteorites have relatively low Re and high Os abundances, hence the Re-Os isotopic system is powerful tool in geochemical identifications of impact events (Koeberl et al., 2002). The Cr isotopic method can provide information regarding the type of projectiles (Koeberl et al., 2002, Montanari and Koeberl, 2000). The geochemical tools in identification of impactites have been used in a variety of studies, such as at the Ries (Morgan et al., 1979), Bosumtwi (Dai et al., 2010), and Chicxulub craters (Koeberl et al., 1994).

## 1.6 Methodology

The mineralogical composition of the samples was studied using the petrographic microscope, X-ray powder diffraction (XRD), cathodoluminescence microscopy (CL), and micro-Raman spectroscopy. Instrumental neutron activation (INAA) and X-ray fluorescence analyses (XRF), as well as analytical electron microscopy (AEM), were used for the geochemical study. Impact signatures were searched for by mineralogical and geochemical methods. Mineralogical signatures of meteorite impact (deformation microstructures in quartz, spherules, tektites, chrome spinels) were searched by optical microscopy, mineral separation, scanning electron microscopy, X-ray powder diffraction. The geochemical signatures related to impact events (e.g., Cr, Ni, Co, Au, and Ir anomalies) were searched with for by instrumental neutron activation analysis. The geochemical specifications relating to paleoenvironmental conditions were obtained by instrumental neutron activation analysis, X-ray fluorescence spectroscopy, isotope ratio mass spectrometry. Iron microbiomats were studied by optical microscopy and micro-Raman spectroscopy.

### 1.6.1 Sample preparation

Samples for bulk rock analysis were crushed manually in polyethylene wrappers, then mechanically in an alumina ceramic jaw crusher, and then powdered with an automatic agate mortar grinder. For in-situ analysis, thin sections were prepared, with the thickness depending on the requirements of each analytical method: 30  $\mu\text{m}$  thick for optical microscopy, 20  $\mu\text{m}$  for cathodoluminescence microscopy, and 60  $\mu\text{m}$  for EMPA measurements. Smear slides of separated polished mineral were prepared for Secondary Electron Microscopy (SEM) to search for extraterrestrial minerals. For the hot cathode cathodoluminescence microscopy carbon coating is required for better imaging. Pressed pellets are required for X-ray diffraction (XRD) and X-ray fluorescence (XRF) trace element analysis. Fused pellets were prepared by a Philips PerIX3 automatic bead machine for XRF major element analysis.

### 1.6.2 Carbonate measurement with the „Karbonatbombe“

Original carbonate content of the material can be estimated by measuring of reacted  $\text{CO}_2$  content of the sample. The dissolution of calcite and aragonite in hydrochloric acid is very rapid (max 2 min.), while the action with dolomite needs longer time (15 min).

The device, which is 25 cm in high, consists of a) a manometer calibrated in % of carbonate content, b) thumbscrew with gasket, c) threaded cap, d) gasket, which fits between the cap and cylinder f), e) 10ml plastic container, threaded Plexiglas cylinder 15.5 cm high (Fig. 16.). 1 gram of dried rock material is put into the cylinder, but previously the plastic container is filled with 5 ml concentrated salt, and then acid is inserted into the cylinder. Then the cap upon the manometer and thumbscrew are mounted and screwed down. If the thumbscrew is tightened, the pressure will increase when the cap is fastened down by decrease in volume within the cylinder (moving of the manometer needle). During that process, the carbonate content of the rock powder reacts with the acid. The carbonate content is calculated from the  $\text{CO}_2$  pressure, where every device has its own calibration table.

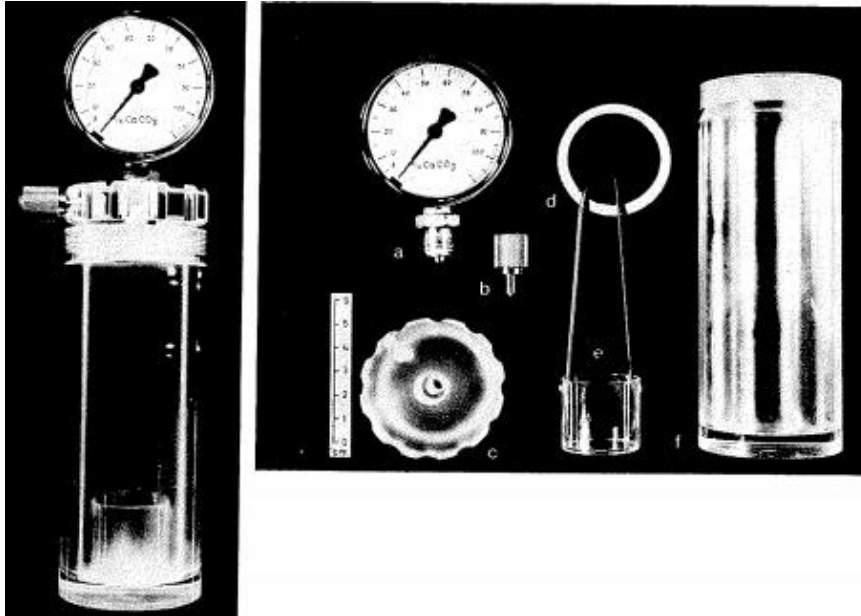


**Figure 16.** “Karbonat-Bombe” (Müller and Gastner, 1971) Legend: a) manometer calibrated for % of  $\text{CaCO}_3$ , b) thumbscrew with gasket, c) threaded cap, d) gasket fitting between cap and cylinder, e) 10ml container of plastic with an A-shaped handle for insertion, f) threaded Plexiglas cylinder that is 15.5 cm high.

### 1.6.3 Bulk rock mineralogy

#### 1.6.3.1 Mineral separation

The collected samples, besides macroscopic description and documentation, were investigated by the following methods. For separation of the minerals, the rock samples were first crushed in a jaw crusher, and then the carbonate was dissolved to separate the detrital minerals. Then the minerals were mesh-separated to different fractions on sedimentological phi scale. Minerals can be separated based on their magnetic properties, which were done by a Frantz isodynamic separator.

The minerals can be classified to three groups based on their magnetic properties: (i) ferro-magnetic, (ii) paramagnetic, and (iii) diamagnetic groups. Ferromagnetic minerals, such as magnetite and pyrrhotite, can be easily separated with a hand magnet. Paramagnetic and diamagnetic minerals are not magnetic, but interact differently with a magnetic field, which can be used for separation in a Frantz Isodynamic Magnetic Separator. The magnetic separator consists of a large electromagnet, through which the mineral mixtures are passed, and are divided near its exit. For separation of minerals, varying strengths of the magnetic field are used.

According to Rosenblum (1958) the Frantz magnetic separation is a free fall method with 20 kg/hour working velocity where the minerals can be separated between 0.6-0.15 mm in

size. The standard angle installation is 20°, which can separate the minerals with higher and average susceptibility. The minerals with very small susceptibilities need a lower site angle installation between 2 and 10° (Table 4.).

**Table 4.** Sample preparation for mineral preparation – details (after Rosenblum, 1958).

<b>A</b>	<b>Site angle 20°</b>			<b>Site angle 5°</b>	
	<b>B</b>	<b>C</b>	<b>D</b>	<b>F</b>	<b>F</b>
<b>Hand magnet</b>	<b>Magnetic on 0.4 A</b>	<b>Magnetic on 0.8 A</b>	<b>Magnetic on 1.2 A</b>	<b>Magnetic on 1.2 A</b>	<b>Nonmagnetic on 1.2 A</b>
pyrrhotite	ilmenite	hornblende	diopside	titanite	zircon
	garnet	hypersthene	tremolite	leucoxene	rutile
	olivine	augite	enstatite	apatite	pyrite
	chromite	actinolite	spinel	andalusite	corundum
	chloritoid	staurolite	light staurolite	monazite	topas
		epidote	muscovite	xenotime	fluorite
		chlorite	zoisite		cyanite
		dark tourmaline	clinozoisite		sillimanite
			light tourmaline		anhydrite
					beryl

About 40 samples from the “C”-series were treated for mineral separation. The larger samples were first crushed with a large jaw crusher at the Department of Geodynamics and Sedimentology (University of Vienna) to 5-cm-sized fragments, than crushed with a smaller jaw crusher at the Department of Lithospheric Research (University of Vienna) to 0.5-1 cm sized fragments. (The smaller samples were small enough to crush only with the smaller jaw crusher). This step is necessary for dissolution of the carbonates, because small fragments are easier to dissolve in the acid than large chips. The carbonates were dissolved in 85% formic acid. The smaller samples were dissolved in plastic cups with 1-2 liters volume, whereas the larger samples were dissolved in a bucket with a volume of 50 liters. The used acid volume was equal to the volume of the samples, and was diluted with water 1:1 ratio of acid and water. The solution time of samples varied between 4 and 14 days. Some samples precipitated in the plastic cups, and thus additional acid had to be used and if that was not enough, vigorous stirring was required. Subsequently the fragments larger than 2 mm in size were removed by sieving with a plastic sieve; the rest of the solution was placed into a larger bucket and diluted with water, and let to be settled for 1-2 days. Later the acid was decanted into another bucket, and the samples were sieved under running water with 300, 160, 63 micrometer-sieves. The fraction of less than 63 micrometers was placed in a large big porcelain dish with water, which was decanted. Then every fraction was dried in an oven for 6-14 hours at about 65-70°C. Finally every fraction was placed into paper bags marked with the sample name and fraction. Each magnetic fraction was studied under a binocular microscope, where the quartz and dark magnetic minerals were picked to plastic vials. These

picked minerals were polished and bedded to epoxy resin to prepare smeared slides. These smeared slides were studied with a scanning electron microscope at the Natural History Museum (Vienna) to search for extraterrestrial minerals (e.g., chrome spinels)

### 1.6.3.2 X-ray powder diffraction (XRD)

This method is the most important to identify the mineral phases from rock samples. For more details about XRD methods, see Jenkins (2000), Scintag Co. (1999), and Langfordy and Loauer (1996). Crystalline materials are characterized by periodic arrangements of atoms, where the unit cell is the basic repeating unit to define a crystal. The crystallographic planes are defined by Miller indices. The diffracting X-rays scatter coherently on the crystal, producing constructive interference from specific angles. Bragg's law is used by modeling of required condition by diffraction:

$$\lambda = 2d_{hkl} \sin \theta$$

Where the X-ray wavelength  $\lambda$  is fixed and the family of planes produces diffraction peak at  $\theta$  angle, and the  $d$  is crystal pattern distance.

The XRD is a suitable method to indentify mineral phases of polycrystalline samples.

The diffractometer consists of an X-ray tube as source of X-rays, monochromator, goniometer, sample holder, and receiving-side optics. The sample holder, the detector arm and associated gearing is referred to as goniometer, working according to Bragg-Brentano parafocusing, where the detector moves as circle to measure the variable crystal plans according to  $2\theta$  angle. The identification of mineral phases can be done manually and by a computer program.

## 1.6.4 In-situ mineralogical methods

### 1.6.4.1 Cathodoluminescence microscopy

Cathodoluminescence is a physical process where the luminescence is produced by bombardment of high-velocity electrons in vacuum. In different materials the luminescence falls in visible range of the electromagnetic spectrum. The advantages and parameters of different cathodoluminescence instruments are listed in Table 5. and are shown in Fig. 17.

**Table 5.** General analytical parameters of different cathodoluminescence microscope types (from Götze and Kempe, 2008).

Parameter	SEM-CL	CL- microscope (OM-CL)	
		Hot cathode	Cold cathode
Sample preparation	Polished sample surface	Polished thin or thick section	Polished sample surface
Detection geometry	Measurement in reflection	Measurement in transmission	Measurement in reflection
Electron beam	Focused, scanning mode	Defocused, stationary mode	
Electron source	Heated filament	Heated filament	Ionized gas
Acceleration voltage	1-40 kV	10-15 kV	10-30 kV
Beam current	0.01-50 nA	0.1-0.5 mA	500-900 $\mu$ A
Vacuum chamber	<10 <sup>-6</sup> bar	<10 <sup>-6</sup> bar	>10 <sup>-6</sup> bar
Optics	Mirror optics	Glass optics	Glass optics
Spectral range	200-1200 nm (UV-IR)	380-1200 nm (VIS_IR)	
Minimal analytical spot diameter	$\leq 1 \mu$ m	$\approx 30 \mu$ m (optical blend)	
Luminescence imaging	Panchromatic (grey levels) or monochromatic	True luminescence colors	
Optical resolution	<1 $\mu$ m	1-2 $\mu$ m	
Possible combination with other signals	SE, BSE, EDX, WDX cooling stage	Polarizing microscopy	

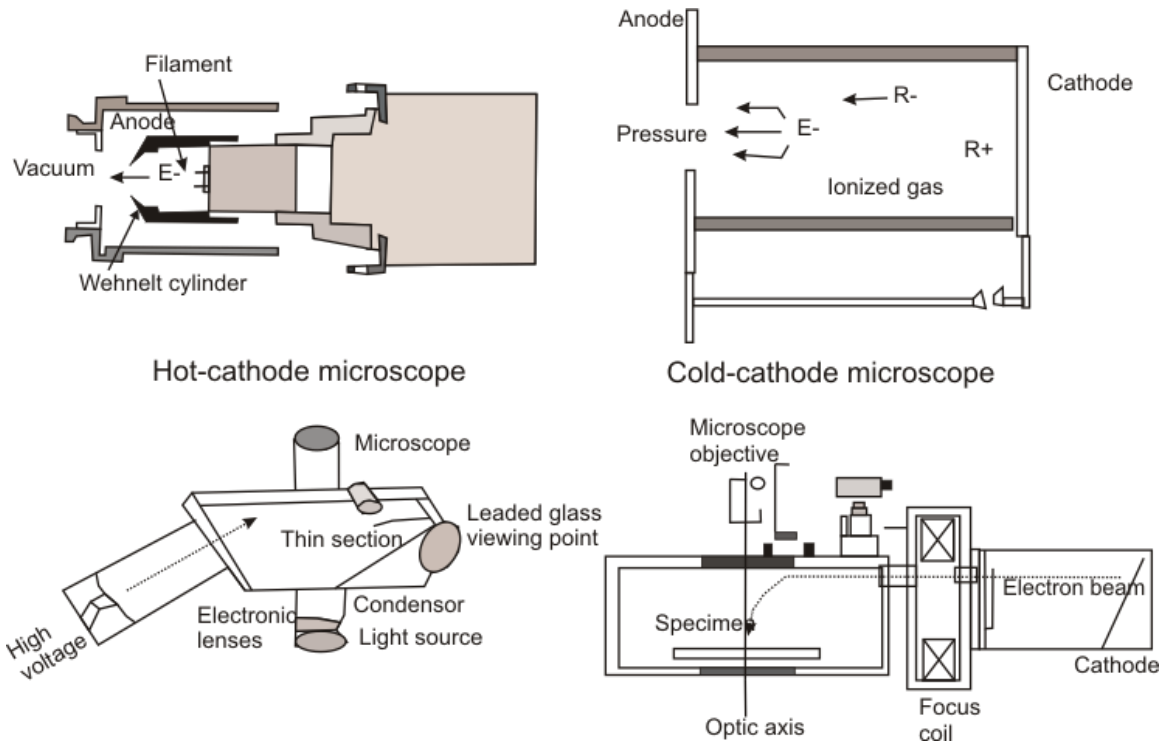


**Figure 17.** Schematic layout of hot cathode and cold cathode microscopes (modified after Götze and Kempe, 2008).

The luminescence in minerals is caused by either the crystal structure defects or the presence of activator atoms in the crystal structure (Houzar and Leichmann, 2003; Fig. 18.). There are three kinds of luminescence: activator-luminescence, sensitized, and quenched. The activator luminescence is often caused by rare earth elements and transition metals.

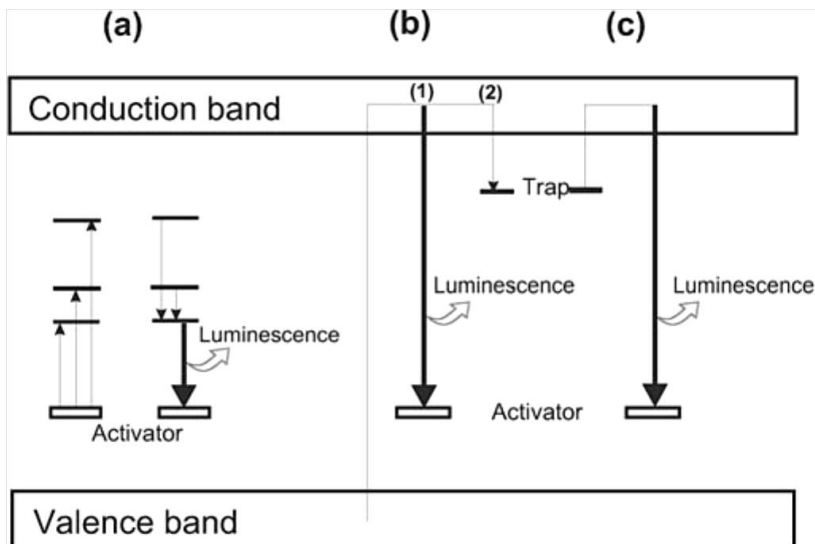


**Figure 18.** Charge transfer and luminescence production processes: a) luminescence emission resulted radiative transitions (e. g., photon absorption), b) excitation of electron from valence band to conduction band resulting luminescence emission with activator (1), or trapping of the electron (2) c) thermoluminescence by an activator (from Götze, 2002).

The sensitizing luminescence is influenced not only by activator elements but also by other processes, such as emission reabsorption, resonance-radiation-less, and non-resonance-radiation-less. The quenching luminescence is caused by luminescence-quenching elements ( $\text{Fe}^{3+}$ ), or due to crystal lattice defects, and thermal quenching.

Cathodoluminescence microscopy is a suitable method in geosciences, like in crystal chemistry (trace elements, internal structures, zoning) and for the reconstruction of geological processes. This method is very useful in impact cratering studies (e.g., Gucsik et al., 2002, shocked zircons: luminescence caused by crystal lattice defects), and in sedimentology, to study diagenetic processes (mineral identifications, chemical composition identifications of cement generations).

The luminescence of calcite and dolomite was studied by Habermann et al. (1998). The principal activator is Mn (which substitutes for Ca) in dolomite and calcite structure, but the Mn can cause luminescence with combination of the REE (mainly  $\text{Sm}^{3+}$ ,  $\text{Tb}^{3+}$  and  $\text{Eu}^{3+}$ ). The most important quencher in carbonates is  $\text{Fe}^{2+}$ . The calcite and dolomite has broad range of luminescence colors ranging from purple to blue, green, white, and orange to red depending on combination of activators and crystal defects. The angular dolomites mostly have dull red (reddish brown), homogenous calcite orange luminescence colors.

Richter et al. (2003) used cathodoluminescence of detrital minerals (zircon, apatite, quartz) as a tool for provenance analysis. The quartz has blue, red yellow, green color caused by mainly crystal defects, whereas activators (Ti, Fe) have minor roles. According to change of luminescence colors, the detrital quartz can be classified into the following categories: blue to violet=plutonic quartz as well as quartz phenocrysts in volcanic rocks, and high-grade metamorphic quartz; red =matrix quartz in volcanic rocks; brown=quartz from regional metamorphic rocks; none or weakly luminescent=authigenic quartz; short-lived green or blue=hydrothermal and pegmatitic quartz.

The intrinsic defects are caused by  $\text{Eu}^{2+}$  and  $\text{Cu}^{2+}$ , the activators are  $\text{Fe}^{3+}$  and REE ( $\text{Sm}^{3+}$ ,  $\text{Dy}^{3+}$ ,  $\text{Eu}^{3+}$ ,  $\text{Tb}^{3+}$ ,  $\text{Nd}^{3+}$ ). In detrital feldspars, five different CL-types of alkali feldspars can be distinguished: a) homogeneous light blue, b) patchy light blue-Prussian blue, c) patchy light blue-light brown, d) homogeneous light brown and e) homogeneous olive-greenish yellow. The luminescence of authigenic feldspars caused by  $\text{Mn}^{2+}$  and  $\text{Fe}^{3+}$  activation in diagenetic to epimetamorphic overprint. The serpentine-kaolinite group has blue luminescent color. Small detrital zircons have yellow luminescent color.

### 1.6.4.2 Raman spectroscopy

Raman spectroscopy is a very good method to identify minerals and identify the change of mineral structures (such as crystal lattice defects, high pressure polymorphs) in thin section. The advantage of this method is that no coating and no sample preparation is required. That is why this method is very good to study rare, small geological samples, such as meteorites. Raman spectroscopy is based on molecular vibrations in the crystal lattice. The disadvantage of the method is that if the sample has high Cr or Fe contents, high fluorescence backgrounds are caused that degrade the quality of the measurements, or the fluorescence drowns out the Raman spectrum (for more details see Nasdala et al., 2004).

The principal interaction of Raman spectroscopy is due to interaction between light and matter. The scattering of light can be characterized as elastic or inelastic (Fig. 19.). The elastic scattering results in no change in the light frequency, whereas the inelastic scattering changes the light spectrum. Consequently the Raman scattering is born of result of interaction of electromagnetic spectrum with vibrations and/or rotations of molecules, resulting in a Raman spectrum of minerals. Brillouin scattering involves transitional motion of molecules, but exist small frequency shifts, where the molecular motions are only discrete energy states. In inelastic Raman scattering the state of molecule is changed: if the scattered light has a lower frequency called Stokes Raman scattering (red shift), if the created photon is more energetic losing vibrational energy, the resulting blue shift is called anti-Stokes scattering. The data are presented as Raman shift wave number in  $\text{cm}^{-1}$ .

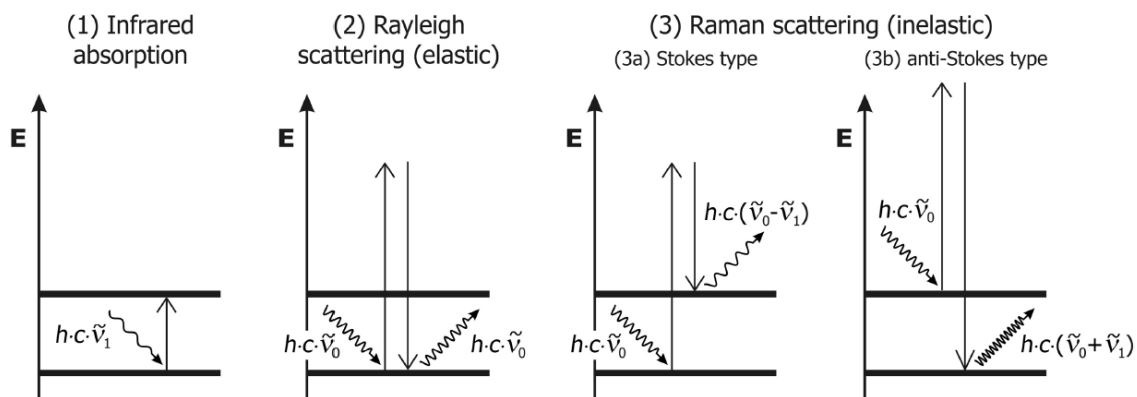


**Figure 19.** Interaction of light and matter: 1) absorbance of light within two vibrational levels, 2) visible light with higher energy difference than energy differences between molecule vibrational states, 3) energy of scattered light either decreased or increased than exciting photon (Raman shift) corresponding energy difference between vibrational levels of the molecule (from Nasdala et al., 2004).

A laser is used as light source, where three kind color lasers can be used for measurement: red He-Ne (632 nm), green Ar (515 nm), and blue Kr (406 nm). The red laser is the best for measuring crystalline phases, but by measuring shocked mineral phases, such as

ringwoodite and maskelynite, the use of blue laser is advised to reduce the high fluorescence background. The laser beam is directed through an optical microscope and focused onto the sample through the objective; the scattered light travels back to the spectrometer through the same objective, and then a charge-coupled device (CCD) detector is used for the measurements (Fig. 20.). In Raman spectroscopy, the wavelength separation is based on the diffraction of light, where the dispersion system consists of a notch (holographic rejection) filter. Alternatively, dispersive double or triple monochromators can be used, which have good spectral resolution, but cause strong light intensity loss.

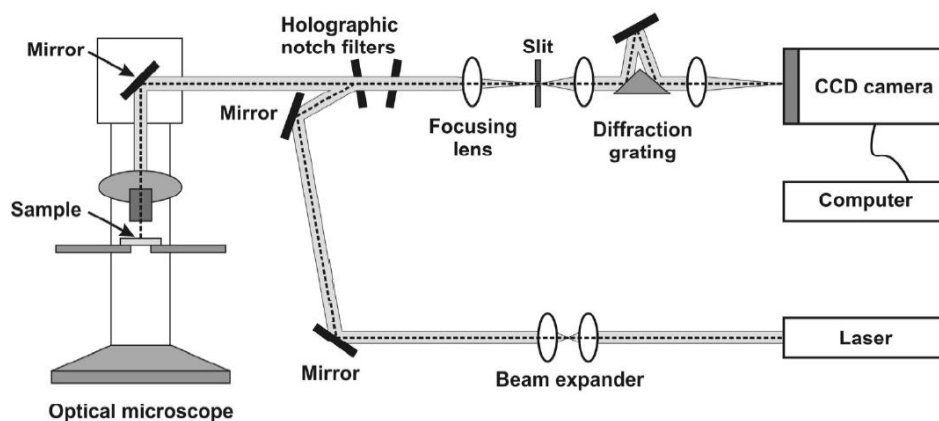


**Figure 20.** Configuration of a confocal micro-Raman spectrometer (from Ferriere, 2008).

## 1.6.5 Bulk rock geochemistry

### 1.6.5.1 Instrumental neutron activation analysis (INAA)

The principle of the method is that the sample is irradiated with neutrons, causing the conversion of stable atoms to radioactive nuclides, followed by the decay by beta and gamma radiation with characteristic energies. The detection of the characteristic decay energies allows to identify the nuclides, and the intensity of the gamma-radiation is correlated with the amount of nuclides. Because the different radioactive isotopes have different half lives, the gamma-spectrum changes with time, which is why the measurements need to be repeated. The short-lived cycles are measured in a first cycle, whereas the longer-lived isotopes are measured in later cycles, when most short-lived isotopes have decayed. The sample spectra are compared to those of international certified rock standards, such as the Allende meteorite (All-1; Smithsonian Institution, Washington DC, USA; Jarosewich et al., 1987), granite (ACE; Centre de Recherche Pétrographique et Géochimique, Nancy, France; Govindaraju, 1989), and Devonian Ohio Shale (SDO-1, United States Geological Survey; Govindaraju, 1989). Nuclear reactors using neutrons from  $^{235}\text{U}$  fission are generally used as neutron sources. Accelerators or radioisotopic emitters can also be used as neutron source.

For details see Koeberl (1993), Mader and Koeberl (2009), and Potts (1987).

### *Analytics*

Samples needed to be crushed and powdered, then 130-160 mg (depending on their expected activity) of each samples were sealed in to plastic capsules (the plastic vials need to be not more than 2/3 full). Each batch contains 17 samples and 3 standards. Then the powdered samples in capsules were irradiated at the Institute of Atomic and Subatomic Physics for 6-8 hours in a 250 kW Triga reactor. Afterwards they were put in a lead container guarding against radiation for 5 days (cooling period). After this cooling period the measurement cycles (Table 4.), following the half life of nuclides, were performed using Canberra coaxial high purity Ge detectors (relative efficiencies of 39.8-45.3 %, energy resolutions of 1.76-1.82 keV) with  $^{1332} \text{ }^{60}\text{Co}$  (Fig. 21., Mader and Koeberl 2009). The first measurement cycle (L1 – Table 6.) is utilized for short half –life (3 days) nuclides (e.g., Na, K, Fe) with duration 60 minutes. Second measurement cycle (L2) were followed by approximately 4 days after L1 (Table 4.) with duration 3 hours. After 6 weeks of irradiation, when every short-life isotopes were decayed, long life isotopes were measured for 12-24 hours for each sample. After measurements of 3 cycles, the achieved spectra were checked for calibration, sample weight, acquisition time, and peak fitting was checked by Genie 2000 Software. The element concentration evaluation was done by PNAA (PC-based Neutron Activation Analysis Software) by peak searching of spectra for each sample. The PNAA data is reported in an Excel output file (in parts per million – ppm). The data are then manually calculated in the Excel file.

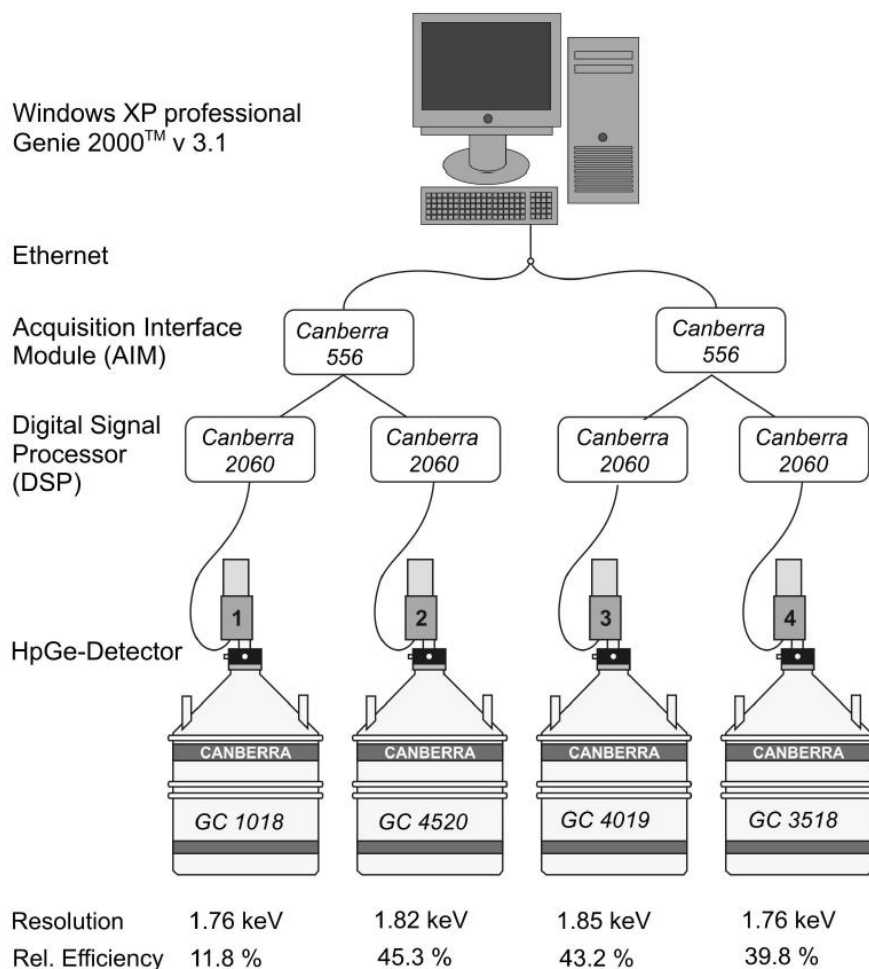


**Figure 21.** Configuration of the INAA lab at the University of Vienna (from Mader and Koeberl 2009).

**Table 6.** Energy lines and half lives from Firestone and Shirley (1996) in Ferriere (2008), “h” for hour, “d” for day, and “y” for year.

Element	Indicator isotope	Energy lines [keV]	Half-life T1/2	Measurement cycle
Na	<sup>24</sup> Na	1368.6	14.96h	L1
K	<sup>42</sup> K	1524.7	12.36h	L1
Sc	<sup>46</sup> Sc	889.3, 1120.5	83.79d	L2, L3
Cr	<sup>51</sup> Cr	320.1	27.70	L2, L3
Fe	<sup>59</sup> Fe	192.3, 1099.2, 1291.6	44.5 d	L2, L3
Co	<sup>60</sup> Co	1173.2, 1332.5	5.27 y	L3
Ni	<sup>58</sup> Ni	810.8	70.82 d	L2, L3
Zn	<sup>65</sup> Zn	1115.5	244.26 d	L3
As	<sup>76</sup> As	559.1	26.32 h	L1
Br	<sup>82</sup> Br	554.3, 776.5	35.30 h	L1
Sr	<sup>85</sup> Sr	514.0	64.84 d	L2, L3
Rb	<sup>86</sup> Rb	1076.6	18.63 d	L2, L3
Zr	<sup>95</sup> Zr	724.2, 756.7	64.02 d	L2, L3
Sb	<sup>124</sup> Sb	1691.0	60.0 d	L3
	<sup>122</sup> Sb	564.1	2.70 d	L1
Cs	<sup>134</sup> Cs	795.8	2.06 y	L3
Ba	<sup>131</sup> Ba	496.3	11.5 d	L2, L3

Element	Indicator isotope	Energy lines [keV]	Half-life T1/2	Measurement cycle
La	<sup>140</sup> La	328.8, 487.0, 1596.2	1.68 d	L1, L2
Ce	<sup>141</sup> Ce	145.4	32.50 d	L2, L3
Nd	<sup>147</sup> Nd	91.1, 531.0	10.98 d	L2
Sm	<sup>153</sup> Sm	103.2	46.27 h	L1, L2
Eu	<sup>152</sup> Eu	121.8, 1408.0	13.54 y	L2, L3
Gd	<sup>153</sup> Gd	97.4, 103.2	241.6 d	L3
Tb	<sup>160</sup> Tb	298.6, 897.4, 966.2, 1178.0	72.3 d	L3
Tm	<sup>170</sup> Tm	84.3	128.6 d	L2, L3
Yb	<sup>175</sup> Yb	282.5, 396.3	4.18 d	L1, L2
	<sup>169</sup> Yb	177.2, 198.0	32.03 d	L1, L2
Lu	<sup>177</sup> Lu	208.4	6.73 d	L1, L2
Hf	<sup>181</sup> Hf	482.2	42.39 d	L2, L3
Ta	<sup>162</sup> Ta	67.7, 222.1, 1221.4, 1231,	114.43 d	L2, L3
Ir	<sup>192</sup> Ir	299.0, 308.5, 316.5, 468.1	73.83 d	L3
Au	<sup>198</sup> Au	411.8	2.70 d	L1
Th	<sup>233</sup> Pa	300.3, 312.2	26.97 d	L2, L3
U	<sup>239</sup> Np	228.2, 277.6	2.36 d	L1

### 1.6.5.2 X-ray fluorescence spectroscopy (XRF)

This method is suitable for analyzing of major (Na, K, Fe, Si, Ti, Al, Mn, Mg, Ca, P) and trace elements (e.g., Cu, Ni, Cr, V, Nb, and Pb, which could be not obtained by INAA). Before XRF analyses, samples have to be dried. For identifying LOD (loss of drying) 5 g of each sample were placed on the oven 110 °C over night, than after cooling (1 hour) were measured their weight after drying. The adsorptive bounds of clay minerals were lost during the drying. During the ignition at 850°C and 1050°C the carbonate content were lost, hence loss ignition is suitable for estimation of carbonate content of each sample. The LOI (Loss on ignition) can be calculated using the following equation:  $LOI = (\text{weight preheated} - \text{weight heated}) * 100 / \text{sample weight}$ . Hence, high LOD corresponds to high clay mineral content, whereas high LOI is common for carbonate rocks.

The X-ray analyzer contains an X-ray tube as X-ray source, which consist of a heated tungsten filament and an anode. The filament emits electrons, which are accelerated on anode and finally focused on tube with high potential difference. The anode produces X-rays from impinged electrons, and the X-rays interact with the sample can eject electrons from inner, K or L shell resulting in fluorescence: the free electron positions are filled by electron from higher electron level accompanying emission of secondary (characteristic X-rays), which are characteristic for each elements. (for details, see Loubser and Verrin, 2008; La Tour, 1989; and Owers and Shalgosky, 1974).

The secondary beams from the sample are collimated and the spectrally dispersed. In the present measurements, the wavelength dispersive (WDS) method was used, where similar to XRD, X-rays are dispersed by diffraction on crystals according to Bragg's law, and these X-rays are collimated again then measured with a detector. Another kind of XRF spectrometer is the energy dispersive (EDS) method, where the detector generates an electric pulse with amplitude proportional to the photon energy for each X-ray photon. The signal is analyzed by a multichannel detector. The WDS method has better detection limits, but that is not simultaneous like the EDS method. The EDS method is also used in SEM analyses, whereas the WDS method is used in electron microprobe analysis (EMPA). For these measurements, a variety of detectors exist:

- 1) Gas ionization detectors have low sensitivity that is why they are used to detect low X-rays.
- 2) Scintillation detectors consist of a NaI crystal doped with Tl atoms; these are used for detecting high-energy X-rays and gamma rays at high sensitivity
- 3) Semiconductor detectors (Li, Si, or Ge) have high resolution and are used in EDS analyses.

### *Analytics*

The XRF measurements were done using a Philips 2400 device with Rh-excitation at the University of Vienna, Department of Lithospheric Research. All of transition layer ("C" samples) samples were measured for trace elements, but only several samples with lower carbonate contents (C1c, C5, C9, C10, C12, C13a-b, C14b-c, C15b-d, C16b-c, C17a) were measured for major element contents. For major element analyses, fused beads were made of fired material (1050°C) and  $\text{Li}_2\text{B}_4\text{O}_7$  flux. For trace element measurements, pressed pellets were produced of mixture 10 g powdered samples and 0.5 ml polyvinyl-alcohol.

International geostandards were used for comparing of signal of sample and establishing the calibration curve for each standard. As the samples included limestone, sandstone, shale, it was necessary to use limestone GSR-6, shale GSR-5, and sandstone GSR4 as standards (international geostandards for X-ray fluorescence are listed in Stork et al., 1987). For data evaluation, the ProTrace software was used. The detection limit was 0.02 wt% for major elements and at the ppm level for trace elements.

### **1.6.5.3 Isotope ratio mass spectrometry (IRMS)**

The Isotope Ratio Mass Spectrometry (IRMS) provides data of isotopic ratios of the elements H, C, N, O, and S. The equipment consists of an ion source, a magnetic sector, and Faraday cup ion detectors. Gas or solid materials are used for ion production. For detailed

information of IRMS, see e.g. Wieser and Brand (1999), Gosh and Brand (2003), Sharp (2006), and Potts (1987). The ions form in the source and are accelerated at electric potential difference from 2000 to 10000 V then those are entered in magnetic field and are separated depending on mass ratio and kinetic energy. The magnetic separator has a trapezoid shape and contains ion source (entrance) and collector (exit) (Fig. 22.).

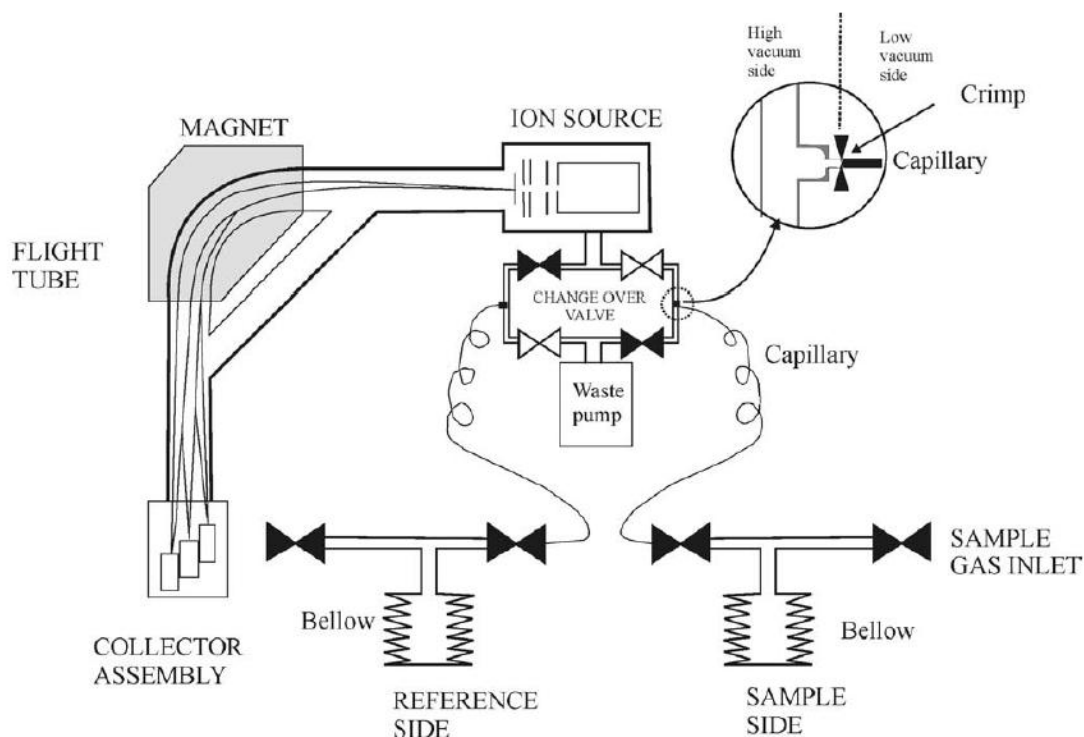


**Figure 22.** Components of gas source spectrometer with dual inlet system (from Gosh and Brand, 2003).

Modern IRMS instruments use a variety of detectors to measure the different ionic currents. There are two ionic sources: thermal ionization (utilized for nanoquantities), electron impact (used for gaseous samples). The Faraday cup detectors measure the most abundant isotopic species and are connected to ground via high Ohmic resistor, which collect ions according to Ohm's law ( $V=IR$ ). The accurate Faraday cup neutralizes the charged particles with electrons. Hence, the Faraday cups are deep graphite boxes with ca. 100 V electric field.

The thermal ionization produces ions by heating sample-coated filaments to temperatures of about 800 to 2000°C. The electron impact sources ionize gases by collisions with transverse electron beams up to 1 mA and 100 eV. This ion source is suitable for isotope abundance measurements of simple gases, such as  $\text{CO}_2$ ,  $\text{N}_2$ ,  $\text{H}_2$ , and  $\text{SO}_2$ . The delta values of stable isotope variations (e.g., C isotopes) are calculated with following equation:

$$\delta^{13}\text{C} = \left[ \frac{(^{13}\text{C}/^{12}\text{C})_{\text{sample}}}{(^{13}\text{C}/^{12}\text{C})_{\text{reference}}} - 1 \right] * 1000$$

The delta values are listed as parts per thousand or permil (‰). The positive  $\delta$  values indicate enrichment of heavier isotope to reference material, whereas negative  $\delta$  values indicated depletion of heavier isotopes to reference.

### *Analytics*

The measurements were obtained with a Carlo Erba Element Analyzer at the Department of Lithospheric Research, University of Vienna, which was coupled to a Micromass Optima stable isotope ratio gas mass spectrometer. The device is built up of two Edwards E2M2 rotary pumps, two Edwards EXT70/ISO63 turbomolecular pumps and one Edwards EXT250/ISO100 turbomolecular pump (down to  $10^{-8}$  mbar). Powdered carbonate samples (K2, K4, P49, C1, C12 profiles, C6, C13c) were put in tin capsules (0.2-0.3 mg). Up to 50 samples were measured for each batches, every sample was measured at least 3 times with a precision between 0.13 and 1.33 %. The following international standards were used: graphite USGS-24 (Coplen et al., 2006) and carbonatite NBS-18 (Verkouteren and Klinedinst, 2004).

## **1.6.6 In-situ geochemistry**

### **1.6.6.1 Scanning electron microscopy (SEM)**

This technique is used to obtain high magnification secondary electron (SE) images for textural and petrographic studies or backscattered electron (BSE) images providing geochemical information, as well as analytical applications involving X-rays (Fig. 23.; for details see: Dunlap and Adaskaveg, 1997; Watt, 1986; Potts, 1987).

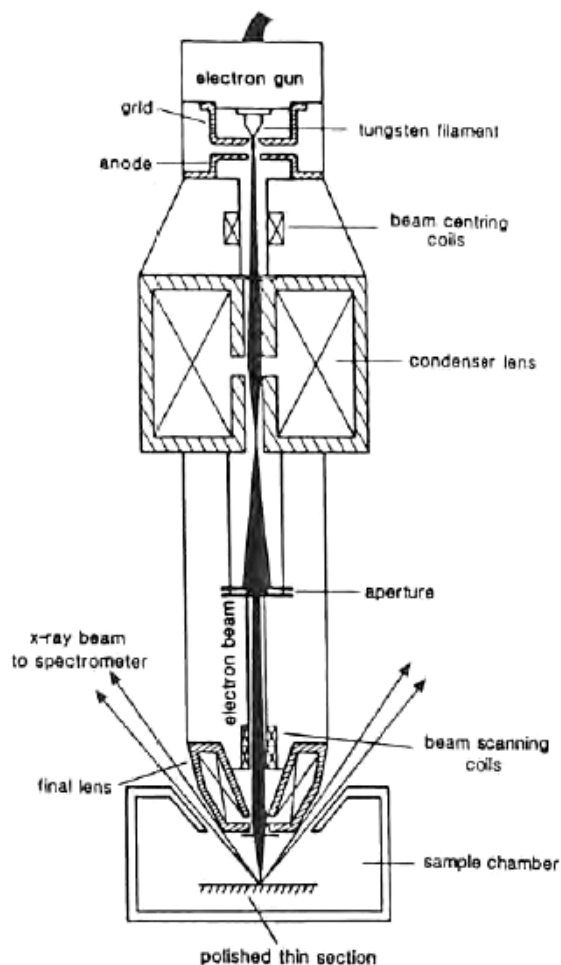


**Figure 23.** Configuration of electron beam in a scanning electron microscope (from Potts, 1987).

A scanning electron microscope consists of electron gun, vacuum system, sample chamber, optical microscope, wave-length dispersive X-ray spectrometer, energy dispersive spectrometer, and detectors (for back scattered electrons, secondary electrons). The electron beam (with an acceleration voltage of 15-30 keV) is emitted from a tungsten electron gun. The beam current is focused by condenser lenses and scanning coils. After passing through the objectives, the primary beam interacts with the specimen by elastic and inelastic scattering producing back-scattered electrons, secondary electron, Auger-electrons, and cathodoluminescence. Secondary electrons (<50 eV) are ejected from the surface layer of ionized atoms of specimen and provide morphological information. The back-scattered electrons produced by elastic interaction of sample, which increase with atomic number ( $Z$ ) giving compositional information. The characteristic X-rays are specific for different elements (selected and counted by X-ray analyzer), allowing the chemical composition to be determined by comparison with reference standards (Fig. 24.).

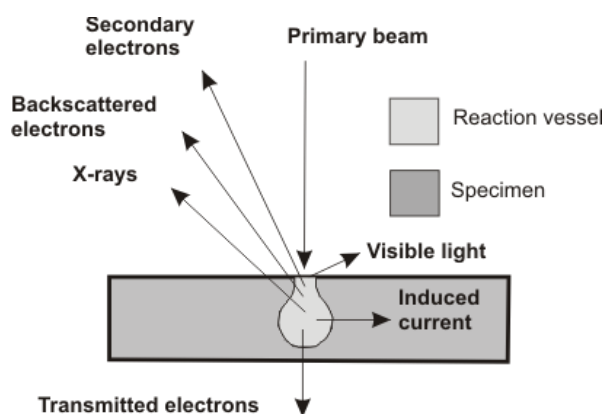


**Figure 24.** Electron-specimen interactions (after Dunlap and Adaskaveg, 1997).

### *Analytics*

Twelve smear slides (C2a, C3\_1-2, C5, C6, C7, C8, C12, C13a-b, C16b, C17a) were prepared of polished grains, which were previously selected under the binocular microscope from each magnetic fraction to search for meteoritic minerals (chrome spinels). The smeared slides were carbon coated for measurements. The analyses were done by JEOL JSM 6400 scanning electron microscope with an energy dispersive X-ray analyzer at the Natural History Museum in Vienna, where back-scattered element images together with electron dispersive X-ray spectrometry (EDX) were used to identify mineral phases. The precision of EDX was 3 rel%, and accuracies 10 rel%. The following elements could be analyzed in EDX mode: Si, Al, Ca, Fe, Mg, K, Na, Ti, Mn, and Cr. The element amounts were recalculated to element oxide contents and normalized to 100 wt%.

#### **1.6.6.2 Electron microprobe analysis (EMPA)**

EMPA is a fast and non-destructive method for quantitative analysis (major elements and some minor elements) of micrometer-sized areas on polished thick section or in thin section samples. The equipment contains electron gun, column/electron optics, optical microscope, vacuum pumps, WDS spectrometers, EDS detector, and SE BSE detector.

The source of electrons is the electron gun which can be thermionic and field emission. Thermionic emission proceeds the electric current passes through heating it, then the electrons leave the wire on high voltage potential nearby the anode. The thermionic emission gun is cheap, but obtains stable current at lower vacuum and lower resolution. The thermionic gun works with either W or LaB<sub>6</sub> filament, where the LaB<sub>6</sub> filament is much brighter. Field emission source is a single crystal shaped to very sharp point and high voltage placed between it and nearby the anode occurring no heating: the electrons can jump the energy barrier to nearby anode. This source is very expensive and occurs in high resolution SEMs.

The minimum beam diameter is produced with condenser lenses to reach stable current with small beam diameter. The lenses are used for focusing the beam and adjusting the current. The beam can be fixed for quantitative point measurement or scanning for imaging.

Vacuum system is very important to avoid the electron interactions with air molecules. For producing vacuum, variable pumps can be used: rough vacuum pumps, diffusion and turbo pumps, ion pumps. The optical microscope is essential to position sample.

The electron beam interacts with the sample by producing X-rays (characteristic X-ray radiation), cathodoluminescence, backscattered electrons, elastically and inelastically scattered electrons, auger electrons, charge collection current and specimen current. This technique allows measuring the composition of mineral phases, not the bulk composition. Because the measurements are on the micrometer scale, small inclusions can be well studied. Images in this instrument can be produced in SE or BSE modes, similarly to scanning electron microscopy. The X-rays can be detected in WDS (wavelength-dispersive) and in EDS (energy dispersive) mode. In WDS method the spectrometer moves step by step, the elements are measured sequential, but this method has a better energy resolution which is better to measure low concentrations. The EDS is more rapid and it is possible to measure the whole spectrum simultaneously. With EDS only the main elements can be measured, but with WDS the minor elements, too. WDS produces better quality results, because the resolution is better than in EDS measurements (Fig. 25.; for details see Watt, 1986; Potts, 1987).

In this work different electron microbeam techniques (scanning electron microscopy, SEM, and electron microprobe, EMP) were used dependent on the type of information (images, mineral phase analysis) that was desired.

### *Analytics*

The electron microprobe analyses for carbon-coated, polished thick section of Sturtian oolitic sandstone (C8 sample) were obtained at the Department of Petrology and Geochemistry, Eötvös University (Budapest), in Hungary. The minerals were determined with BSE and EDX detectors of an Amray 1830 IT/6 electron microscope with EDAX PV9800 EDS detector, a beam current of 1nA and a defocused spot size of 10–50 nm, collection time 100 s. The acceleration voltage was 20 kV. The imaging was done by TESCAN Satallite TS1130 software running on Widows XP system. The surface of sample was carbon-coated in a JEOL-JEE4B vacuum evaporator. The detection limit of the EDS detector is 0.1 wt%, hence major constituents of adjacent minerals could have been measured, but the trace elements could not been detected. Natural and synthetic mineral standards were performed for calibration. The oxide forms of elements were calculated by data processing software.

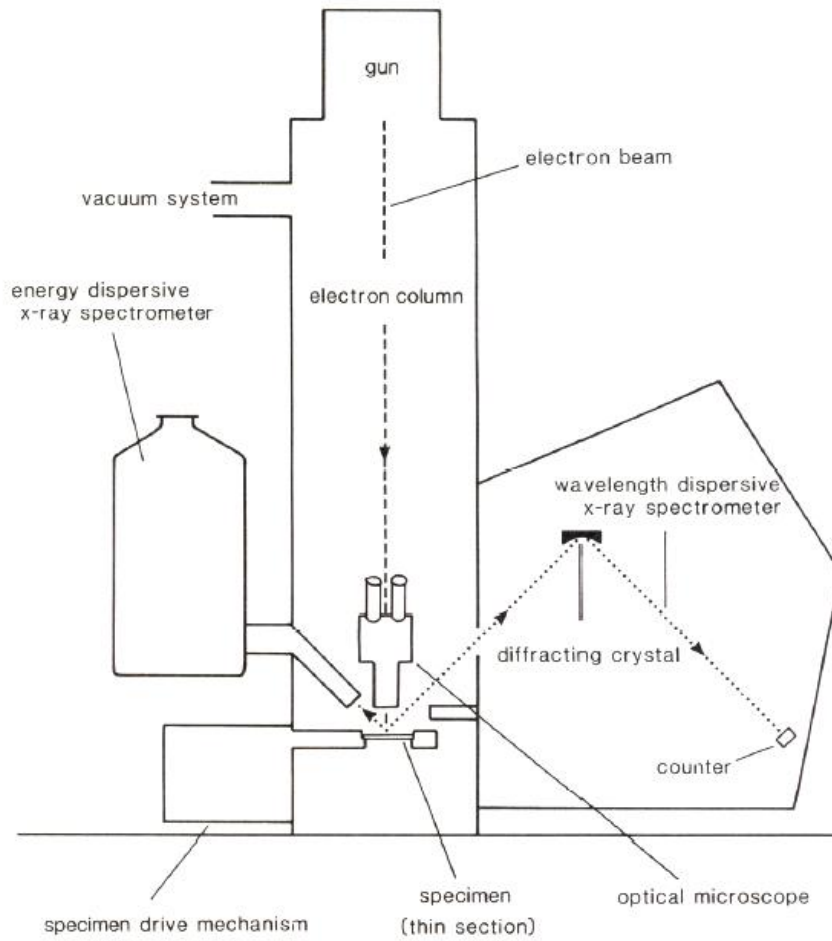


**Figure 25.** Schematic diagram of an electron microprobe (from Potts, 1987).

## References

- Alkmim, F.F., Marshak, S., and Fonseca, M.A., 2001. Assembling West Gondwana in the Neoproterozoic: Clues from the Sao Francisco craton region, Brazil. *Geology*, 29, 319-322.
- Bodiselitsch, B., Koeberl, C., Master, S., and Reimold, W.U., 2005. Estimating duration and intensity of Neoproterozoic Snowball glaciations from Ir anomalies. *Science*, 308, 239-242.
- Budyko, M.I., 1966. Polar ice and climate. Proceedings of Symposium on Arctic heat budget and atmospheric circulation, In: J. O. Fletcher (Ed.), Rand Corp. Memorandum RM-5233-NSF, Santa Monica, California, 3-22
- Caldeira, K. and Kasting, J.F., 1992. Susceptibility of the early Earth to irreversible glaciation caused by carbon dioxide clouds. *Nature*, 359, 226–228.
- Cawood, P.A. and Nemchin, A.A., 2001. Paleogeographic development of the east Laurentian margin: constraints from U-Pb dating of detrital zircons in the Newfoundland Appalachians. *Geological Society of America Bulletin*, 113, 1234-1246.
- Christie-Blick, N., Sohl, L.E., and Kennedy, M.J., 1999. Considering a Neoproterozoic Snowball Earth. *Science*, 284, 1084a.
- Clauer, N. and Kröner, A., 1979. Strontium and argon isotopic homogenization of pelitic sediments during low-grade regional metamorphism: The Pan-African upper Damara sequence of northern Namibia (South West Africa). *Earth and Planetary Science Letters*, 43, 117-131.
- Coplen, T., Brand, W., Gehre, M., Groning, M., Meijer, H., Toman, B., and Verkouteren, R., 2006. New guidelines for delta C-13 measurements. *Analytical Chemistry*, 78, 2439–2441.
- Dai, X., Boamah, D., Koeberl, C., Reimold, W. U., Irvine, G., and McDonald, I., 2010. Bosumtwi impact structure, Ghana: Geochemistry of impactites and target rocks, and search for a meteoritic component. *Meteoritics and Planetary Science*, 40, 1493-1511.
- Domack, E. and Hoffman, P., 2003. Stratigraphic transition into and out of Snowball Glacial: Evidence from the Otavi Platform and Fransfontain slope, Namibia. *Earth Observation System Transcription. American Geoscience Union*, 84/46, Fall Meeting Supplement, Abstract C11B-0819.
- Dunlap, M. and Adaskaveg, J.E., 1997. Introduction to the scanning electron microscope: theory, practice and procedures 1-52, presented by the Facility for Advanced Instrumentation, U.C. Davis, 1997 <https://imf.ucmerced.edu/downloads/semmanual.pdf>
- Dypvik, H. and Jansa, L.F., 2003. Sedimentary signatures and processes during marine bolide impacts: a review. *Sedimentary Geology*, 161, 309–337.

- Evans, D.A.D., 2000. Stratigraphic, geochronological and paleomagnetic constraints upon the Neoproterozoic climatic paradox. *American Journal of Science*, 300, 347–433.
- Eyles, C.H. and Eyles, N., 1983. A glaciomarine model for Upper Precambrian diamictites of the Port Askaig Formation, Scotland. *Geology*. 11, 692–696.
- Eyles, N., 1993. Earth's glacial record and its tectonic setting. *Earth Science Reviews*, 35, 1–248.
- Eyles, N. and Januszczak, N., 2004. 'Zipper-rift': a tectonic model for Neoproterozoic glaciations during the breakup of Rodinia after 750 Ma. *Earth-Science Reviews*, 65, 1–73.
- Fairchild, I.J., 1993. Balmy shores and icy wastes: the paradox of carbonates associated with glacial deposits in Neoproterozoic times. In: *Sedimentology Review 1* (V. P. Wright, ed.), pp. 1–16. Blackwell Scientific Publications, Oxford.
- Ferriere, L., 2008. Shock metamorphism and geochemistry of impactites from the Bosumtwi impact structure: A case study of shock-induced deformations and transformations in quartz and associated methodology. - Ph. D. Thesis, University of Vienna. 279 pp.
- Font, E., Nédélec, A., Trindade, R.I.F., and Moreau, C., 2010. Fast or slow melting of the Marinoan snowball Earth? The cap dolostone record. *Palaeogeography, Palaeoclimatology, Palaeoecology*, 295, 215–225.
- Fraiser M.L. and Corsetti C.A., 2003. Neoproterozoic carbonate shrubs: Interplay of microbial activity and unusual environmental conditions in post-Snowball Earth oceans. *PALAIOS*, 18, 378-387.
- French, B.M., 1998. *Traces of catastrophe: A handbook of shock-metamorphic effects in terrestrial meteorite impact structures*. LPI Contribution #954. Houston, Texas: Lunar and Planetary Institute. 120 pp.
- French, B.M. and Koeberl, C., 2010. The convincing identification of terrestrial meteorite impact structures: What works, what doesn't, and why. *Earth Science Reviews*, 98, 123-170.
- Ghosh, P. and Brand W.A., 2003. Stable isotope ratio mass spectrometry in global climate change research. *International Journal of Mass Spectrometry*, 228, 1–33.
- Godderis, Y., Donnadieu, Y., Nédélec, A., Dupre B., Dessert, C., Grard, A., Ramstein G., and Francois L.M., 2003. The Sturtian 'snowball' glaciation: fire and ice. *Earth and Planetary Science Letters*, 21, 1-12.
- Götze, J., 2002. Potential of cathodoluminescence (CL) microscopy and spectroscopy for the analysis of minerals and materials. *Analytical and Bioanalytical Chemistry*, 374, 703–708.

- Götze, J. and Kempe, U., 2008. A comparison of optical microscope- and scanning electron microscope-based cathodoluminescence (CL) imaging and spectroscopy applied to geosciences. *Mineralogical Magazine*, 72, 909–924.
- Govindaraju, K., 1989. Compilation of working values and sample description for 272 geostandards. - *Geostandards Newsletter*, 13, 1–113.
- Grotzinger, J.P. and Knoll, A.H., 1995. Anomalous carbonate precipitates; is the Precambrian the key to the Permian? *Palaios*, 10/6, 578–596.
- Gucsik, A., Koeberl, C., Brandstätter, F., Reimold, W., U., and Libowitzky, E., 2002. Cathodoluminescence, electron microscopy, and Raman spectroscopy of experimentally shock-metamorphosed zircon. *Earth and Planetary Science Letters*, 202, 495–509.
- Haberman, D., Neuser, R.D., and Richter, D.K., 1998. Low limit of Mn<sup>2+</sup> – activated cathodoluminescence of calcite: state of the art. *Sedimentary Geology*, 116, 13–24.
- Halverson, G.P., 2006. A Neoproterozoic chronology. In: Xiao, S. and Kaufman, A.J. (eds.) *Neoproterozoic Geobiology and Paleobiology*. Springer, New York, 231–271.
- Hambrey, M.J. and Harland, W.B., 1985. The late Proterozoic glacial era. *Palaeogeography, Palaeoclimatology, Palaeoecology*, 51, 255–272.
- Harland, W.B., 1964. Critical evidence for a great Infra-Cambrian glaciation. *Geologische Rundschau*, 54, 45–61.
- Hartz, E.H. and Torsvik, T.H., 2002. Baltica upside down: a new plate tectonic model for Rodinia and the Iapetus Ocean. *Geology*, 30, 255-258.
- Hedberg, R.M., 1975. Stratigraphy of the Ovamboland basin, South West Africa. Ph.D. thesis, Harvard University, Cambridge, 538 p.
- Hedberg, R.M., 1979. Stratigraphy of the Ovamboland basin, South West Africa. *Bulletin Precambrian Research Unit, Cape Town*, 24, 325 pp.
- Hoffman, P.F., 2011. Strange bedfellows: glacial diamictite and cap carbonate from the Marinoan (635 Ma) glaciations in Namibia. *Sedimentology*, 58, 57-119.
- Hoffman, P.F. and Halverson, G.P., 2008. Otavi Group of the western Northern Platform, the Eastern Kaoko Zone and the western Northern Margin Zone. -In: R.McG. Miller [Ed.]: *The Geology of Namibia. - Vol 2: Neoproterozoic to Lower Paleozoic*. Ministry of Mines and Energy, Geological Survey, Namibia 2008, 69-136.
- Hoffman, P.F. and Li, Z.X., 2009. A palaeogeographic context for Neoproterozoic glaciation. *Palaeogeography, Palaeoclimatology, Palaeoecology*, 277, 158-172.
- Hoffmann, K.H., and Prave, A.R., 1996. A preliminary note on a revised subdivision and regional correlation of the Otavi Group based on glaciogenic diamictites and associated cap dolostones. *Communications of the Geological Society of Namibia*, 11, 81-86.

- Hoffman, P.F. and Schrag, D.P., 2002. The snowball Earth hypothesis: testing the limits of global change. *Terra Nova*, 14, 129–155.
- Hoffman, P.F., Hawkins, D.P., Isachsen, C.E., and Bowring, S.A., 1996. Precise U-Pb zircon ages for early Damaran magmatism in the Summas Mountains and Welwitschia Inlier, northern Damara belt, Namibia. *Communications of the Geological Society of Namibia*, 11, p. 47–52.
- Hoffman, P.F., Kaufman, A.J., Halverson, G.P., and Schrag, D.P., 1998. A Neoproterozoic Snowball Earth. *Science*, 281, 1342–1346.
- Hoffman, P.F., Halverson, G.P., Soffer, G., Schrag, D.P., Bowring, S.A., and De Paolo, D.J., 2001. Theme and variations on Neoproterozoic cap-carbonate sequences: signatures of snowball Earth events. *European Geoscience Union; Journal of Conference Abstracts*, 6, 99.
- Hoffmann, P., Condon, D.J., Bowring, S.A., and Crowley J.L., 2004. U-Pb zircon date from the Neoproterozoic Ghaub Formation, Namibia: Constraints on Marinoan glaciations. *Geology*, 32, 817-820
- Houzar, S. and Leichmann, J., 2003. Application of cathodoluminescence to the study of metamorphic textures in marbles from the eastern part of the Bohemian Massif. *Bulletin of Geosciences*, 78, 241–250.
- Hyde, W.T., Kim, K.Y., Crowley, T.J., and North, G.R., 1990. On the relationship between polar continentality and climate: studies with a non-linear energy balance model, *Journal of Geophysical Research*, 95, 18653-18668.
- Hyde, W.T., Crowley, T.J., Baum, S.K., and Peltier, W.R., 2000. Neoproterozoic 'snowball Earth' simulations with a coupled climate/ice-sheet model. *Nature*, 405, 425-429.
- Ivanov, B.A. and Artemieva, N.A., 2002. Numerical modeling of the formation of large impact craters. In: *Catastrophic events and mass extinctions: Impacts and beyond*, edited by Koeberl, C. and MacLeod, K. G. GSA Special Paper #356. Boulder, Colorado: Geological Society of America. pp. 619–630.
- Jahn, B.M., Caby, R., and Monie, P., 2001. The oldest UHP eclogites of the World: age of UHP metamorphism, nature of protoliths and tectonic implications. *Chemical Geology*, 178, 143-158.
- Jarosewich, E., Clarke, R.S.J., and Barrows, J.N., 1987. The Allende meteorite reference sample. - *Smithsonian Contributions to the Earth Sciences*, 27, 1–49.
- Jenkins, R., 2000. X-ray Techniques: Overview *Encyclopedia of Analytical Chemistry*, R.A. Meyers (Ed.) pp. 13269–13288 John Wiley and Sons Ltd, Chichester, 2000.
- Kennedy, M.J., 1996. Stratigraphy, sedimentology and isotopic geochemistry of Australian Neoproterozoic postglacial cap dolostones: deglaciation,  $\delta^{13}\text{C}$  excursions and carbonate precipitation. *Journal Sedimentary Research*, 66, 1050-1064.

- Kennedy, M.J., Runnegar, B., Prave, A.R., Hoffman, K.-H., and Arthur, M.A., 1998. Two or four Neoproterozoic glaciations? *Geology*, 26, 1059–1063.
- Kennedy, M.J., Christie-Blick, N., and Sohl, L.E., 2001. Are Proterozoic cap carbonates and isotopic excursions a record of gas hydrate destabilization following Earth's coldest intervals? *Geology*, 29/5, 443–446.
- Kennedy, M.J., Mrofka D., and von der Borch C., 2008. Snowball Earth termination by destabilization of equatorial permafrost methane clathrate. *Nature*, 453, 642-645.
- Key, R.M., Liyungu, A.K., Njamu, F.M., Somwe, V., Banda, J., Mosley, P.N., and Armstrong, R.A., 2001. The western arm of the Lufilian Arc in NW Zambia and its potential for copper mineralization. *Journal of African Earth Sciences*, 33, 503-528.
- Kirschvink, J.L., 1992. Late Proterozoic low-latitude global glaciation: the Snowball Earth. In: *The Proterozoic Biosphere* (J. W. Schopf and C. Klein, eds.), pp. 51–52. Cambridge University Press, Cambridge.
- Knoll, A.H., Hayes, J.M., Kaufman, A.J., Swett, K., and Lambert, I.B., 1986. Secular variation in carbon isotope ratios from Upper Proterozoic successions of Svalbard and East Greenland. *Nature*, 321, 832–838.
- Koeberl, C., 1993. Instrumental neutron activation analysis of geochemical and cosmochemical samples: A fast and reliable method for small sample analysis. *Journal of Radioanalytical and Nuclear Chemistry*, 168, 47–60.
- Koeberl, C., 1994. Tektite origin by hypervelocity asteroidal or cometary impact: Target rocks, source craters, and mechanisms. In: *Large Meteorite Impacts and Planetary Evolution*, edited by Dressler, B. O., Grieve, R. A. F., and Sharpton, V. L. Geological Society of America Special Paper, 293, 133-151.
- Koeberl, C., Sharpton, V. L., Schuraytz, B. C., Shirey, S. B., Blum, J. D., Marin, L. E., 1994. Evidence for a meteoritic component in impact melt rock from the Chicxulub structure. *Geochimica et Cosmochimica Acta*, 58, 1679-1684.
- Koeberl C., Reimold W.U., Blum J.D., and Chamberlain C.P., 1998. Petrology and geochemistry of target rocks from the Bosumtwi impact structure, Ghana, and comparison with Ivory Coast tektites. *Geochimica et Cosmochimica Acta*, 62, 2179–2196.
- Koeberl, C., Peucker-Ehrenbrink, B., and Reimold, W. U., 2002. Comparison of the osmium and chromium isotopic methods for the detection of meteoritic components in impactites: Examples from the Morokweng and Vredefort impact structures, South Africa. In: *Catastrophic Events and Mass Extinctions: Impacts and Beyond*, edited by Koeberl, C. and MacLeod, K.G., Geological Society of America Special Paper, 356, 607-617.

- Koeberl, C., Ivanov, B.A., and Goodman, B.A., 2007. Impact triggering of the Snowball Earth deglaciation? Bridging the Gap II: Effect of Target Properties on the Impact Cratering Process, Abstracts. LPI Contribution, 1360, 62-63.
- La Tour, T. E., 1989. Analysis of rocks using X-ray fluorescence spectrometry. *The Rigaku Journal*, 6/1, 3-9.
- Langenhorst, F., 2002. Shock metamorphism of some minerals: Basic introduction and microstructural observations. *Bulletin of the Czech Geological Survey*, 77, 265–282.
- Langenhorst, F. and Deutsch, A., 1994. Shock experiments on pre-heated  $\alpha$ - and  $\beta$ -quartz: I. Optical and density data. *Earth and Planetary Science Letters*, 125, 407–420.
- Langfordy, J.I. and Louer D., 1996. Powder diffraction. – *Reports on Progress of Physics*, 59, 131–234.
- Laskar J., Joutel F., and Robutel P., 1993. Stabilization of the Earth's obliquity by the Moon. *Nature*, 361, 615-617.
- Le Hir, G., Donnadieu, Y., Godderis, Y., Pierrehumbert, R.T., Halverson, G.P., Macouin, M., Nedelec, A., and Ramstein G., 2009. The snowball Earth aftermath: Exploring the limits of continental weathering processes. *Earth and Planetary Science Letters*, 277, 453-463.
- Leather, J., Allen, P.A., Brasier, M.D., and Cozzi, A., 2002. Neoproterozoic snowball Earth under scrutiny: evidence from the Fiq glaciation of Oman. *Geology*, 30, 891–894.
- Li, Z.X., Zhang, L., and Powell, C.M., 1995. South China in Rodinia: part of the missing link between Australia–East Antarctica and Laurentia? *Geology*, 23, 407–410.
- Li, Z.X., Li, X.H., Kinny, P.D., and Wang, J., 1999. The break-up of Rodinia: did it start with a mantle plume beneath South China? *Earth and Planetary Science Letters*, 173, 171-181.
- Li, Z.X., Evans, D.A.D., and Zhang, S., 2004. A 90° spin on Rodinia: possible causal links between the Neoproterozoic supercontinent, superplume, true polar wander and low-latitude glaciation. *Earth and Planetary Science Letters*, 220, 409-421.
- Loubser, M. and Verrin, S., 2008. Combining XRF and XRD analyses and sample preparation to solve mineralogical problems. *South African Journal of Geology*, 111, 229-238.
- Mader, D. and Koeberl, C., 2009. Using Instrumental Neutron Activation Analysis for geochemical analyses of terrestrial impact structures: Current analytical procedures at the University of Vienna Geochemistry Activation Analysis Laboratory. *Applied Radiation and Isotopes*, 67, 2100–2103.
- Marshall, H.G., Walker, J.C.G., and Kuhn, W.R., 1988. Long-term climate change and the geochemical cycle of carbon. *Journal of Geophysical Research*, 93/D1, 791-801.

- Martin, H., 1965a. Beobachtungen zum Problem der jung-präkambrischen Glazialen Ablagerungen in Südwestafrika (Observations concerning the problem of the late Precambrian glacial deposits in South West Africa). *Geologische Rundschau*, 54, 115-127.
- Martin, H., 1965b. The Precambrian geology of South West Africa and Namaqualand. *Bulletin of Precambrian Research Unit, Univ. Cape Town*, 159 pp.
- Meert, J.G., 2003. A synopsis of events related to the assembly of eastern Gondwana. *Tectonophysics*, 362, 1–40.
- Meert, J.G. and Powell, C.M., 2001. Assembly and break-up of Rodinia: introduction to the special volume. *Precambrian Research*, 110, 1-8.
- Melosh, H.J., 1989. *Impact cratering – A geological process*. New York: Oxford University Press. 245 p.
- Miller, R.M., 1983. The Pan-African Damara Orogen of South West Africa / Namibia. *Geological Society of South Africa Special Publication*, 11, 431-515.
- Montanari, A. and Koeberl, C., 2000. *Impact stratigraphy: the Italian record*. Lectures notes in Earth Sciences, 93. Heidelberg: Springer Verlag. 364 p.
- Morgan, J.W., Janssens, M.J., Hertogen, J., Gros, J., and Takahashi, H., 1979. Ries impact crater, southern Germany: search for meteoritic material. *Geochimica et Cosmochimica Acta*, 43, 803-815.
- Nasdala, L., Smith, D.C, Kaindl, R. and Ziemann, M.A., 2004. Raman spectroscopy: Analytical perspectives in mineralogical research. *European Mineralogical Union Notes in Mineralogy*, Vol. 6 (2004), Chapter 7, 281–343.
- Owers, M.J. and Shalgosky, H.I., 1974. Use of X-ray fluorescence for chemical analysis. *Journal of Physics E: Scientific Instruments*, 7, 593-603.
- Park, J.K., Buchan, K.L., and Harlan, S.S., 1995: A proposed giant dyke swarm fragmented by the separation of Laurentia and Australia based on paleomagnetism of ca. 780 Ma mafic intrusions in western North America. *Earth and Planetary Sciences Letters*, 132, 129-139.
- Peucker-Ehrenbrink, B. and Hoffman, P. F., 2006. Sedimentary PGE anomalies at Snowball Earth terminations. (abstract) *Geochimica et Cosmochimica Acta*, 70, A488.
- Pierrehumbert, R.T., 2002. The hydrologic cycle in deep-time climate problems. *Nature*, 419, 191–198.
- Pierrehumbert, R.T., 2005. Climate dynamics of a hard Snowball Earth. *Journal of Geophysical Research*, 110, DOI: 10.1029/2004JD005162.
- Polgári, M., Hein, J.R., Tóth, A.L., Pál-Molnár, E., Vigh, T., Bíró, L., and Fintor, K., 2012. Microbial action formed Jurassic Mn-carbonate ore deposit in only few hundred years (Úrkút, Hungary). *Geology*, 40, 903-906.

- Porada, H.R., 1989. Pan-African Rifting and orogenesis in southern to equatorial Africa and eastern Brazil. *Precambrian Research*, 44, 103-136.
- Potts, P.J., 1987. *A handbook of silicate rock analysis*. Glasgow: Blackie. 622 p.
- Pruss, S.B., Bosak, T., McDonald, F.A., McLane, M., and Hoffman, P.F., 2010. Microbial facies in a Sturtian cap carbonate, the Rasthof Formation, Otavi Group, northern Namibia. *Precambrian Research*, 181, 187–198.
- Reimold, W.U., 1995. Pseudotachylite in impact structures – Generation by friction melting and shock brecciation?: A review and discussion. *Earth Science Reviews*, 39, 247–264.
- Richter, D.K., Götte, T. Götze, J., and Neuser R.D., 2003. Progress in application of cathodoluminescence (CL) in sedimentary petrology. *Mineralogy and Petrology*, 79, 127-166.
- Rosenblum, S., 1958. Magnetic susceptibilities of minerals in the Frantz isodynamic separator. – *The American Mineralogist*, 43, 170-173.
- SACS, South Africa Committee for Stratigraphy, 1980. *Stratigraphy of South Africa*. In: Kent L.E. (Comp); Part 1. Lithostratigraphy of the Republic of South Africa, South West Africa/Namibia and the Republics of Bophuthatswana, Transkei and Venda. *Handbook of Geological Survey of South Africa*, 8, 690 pp.
- Scintag Company, 1999. Chapter 7: Basics of X-ray Diffraction, 1-25.
- Stanistreet, I.G., Kukla, P.A., and Henry, G., 1991. Sedimentary basinal response to a Late Precambrian Wilson Cycle: The Damara Orogen and Nama Foreland, Namibia. *Journal of African Earth Sciences*, 13, 41-156.
- Stern, R.J., 1994. Arc assembly and continental collision in the Neoproterozoic East Africa Orogen: implications on the consolidation of Gondwanaland. *Annual Review of Earth and Planetary Sciences*, 22, 319-351.
- Stöffler, D., 1972. Deformation and transformation of rock-forming minerals by natural and experimental shock processes. In: *Behavior of minerals under shock compression*. *Fortschritte der Mineralogie*, 49, 50–113.
- Stöffler, D. and Grieve, R.A.F., 2007. Impactites, Chapter 2.11 In: *Metamorphic rocks: A classification and glossary of terms, recommendations of the International Union of Geological Sciences*, edited by Fettes D. and Desmons J. Cambridge, UK: Cambridge University Press. pp. 82–92, 111-125, and 126-242.
- Stöffler, D. and Langenhorst, F., 1994. Shock metamorphism of quartz in nature and experiment: I. Basic observation and theory. *Meteoritics and Planetary Science*, 29, 155–181.
- Stöffler, D., Keil, K., and Edward, S., 1991. Shock metamorphism of ordinary chondrites. *Geochimica et Cosmochimica Acta*, 55, 3845-3867.

- Stöffler, D., Artemieva, N. A., Ivanov, B. A., Hecht, L., Kenkmann, T., Schmitt, R.-T., Tagle, R.A., and Wittmann, A., 2004. Origin and emplacement of the impact formations at Chicxulub, Mexico, as revealed by the ICDP deep drilling at Yaxcopoil-1 and by numerical modeling. *Meteoritics and Planetary Science*, 39, 1035–1067.
- Stork, A. L., Smith, D.K., and Gill, J.B., 1987. Evaluation of geochemical reference standards by X-ray fluorescence analysis. *Geostandards Newsletter*, 11, 107-113.
- Verkouteren, M.R. and Klinedinst, D.B., 2004. Value assignment and uncertainty estimation of selected light stable isotope reference materials: RMs 8543–8545, RMs 8562–8564, and RM 8566. National Institute of Standards and Technology (NIST) Special Publication 260-149, 59 pp.
- Wang, J. and Li, Z.X., 2003. History of Neoproterozoic rift basins in South China: implications for Rodinia break-up. *Precambrian Research*, 122, 141–158.
- Watt, I.M., 1986. The analytical electron microscope. *Journal of Physics E: Scientific Instruments*, 19, 669-678.
- Wieser, M.E. and Brand, W.A., 1999. Isotope ratio spectrometry using mass spectrometry. – *Mass Spectrometry Applications*, Academic Press, p. 1009.
- Wignall, P.B., 2001. Large igneous provinces and mass extinctions. *Earth Science Reviews* 53, 1-33.
- Williams, G.E., 1975. Late Precambrian glacial climate and the Earth's obliquity. *Geological Magazine*, 112, 441–465.
- Williams, G.E., 1993. History of the Earth's obliquity. *Earth-Science Reviews*, 34, 1-45.
- Williams, G.E., 2000. Geological constraints on the Precambrian history of Earth's rotation and the Moon's orbit. *Reviews of Geophysics*, 38, 37–59.
- Wingate, M.T.D. and Giddings, J.W., 2000. Age and paleomagnetism of the Mundine Well dyke swarm, Western Australia: implications for an Australia-Laurentia connection at 755 Ma. *Precambrian Research*, 100, 335-357.
- Wingate, M.T.D., Campbell, I.H., Compton, W., and Gibson, G.G., 1998. Ion microprobe U-Pb ages for Neoproterozoic basaltic magmatism in south-central Australia and implications for the break-up-of Rodinia, *Precambrian Research*, 87, 135-159.
- Worsley R.T. and Kidder D.L., 1991. First-order coupling of paleogeography and CO<sub>2</sub>, with global surface temperature and its latitudinal contrast. *Geology*, 19, 1161-1164.



## 2 Evidence of microbial activity involved with Neoproterozoic postglacial sediments from the Otavi Group, Namibia: a study of Sturtian oolitic carbonate sandstone with spectroscopic methods

Ildikó Gyollai<sup>1, 2</sup>, Márta Polgári<sup>2</sup>, Miklós Veres<sup>3</sup>, Szabolcs Nagy<sup>4</sup>, Friedrich Popp<sup>5</sup>, Dieter Mader<sup>1</sup>, Christian Koeberl<sup>1, 6</sup>

<sup>1</sup>Department of Lithospheric Research, University of Vienna, Althanstrasse 14, A-1090, Vienna, Austria; <sup>2</sup>Research Centre for Astronomy and Geosciences, Geobiomineralization and Astrobiological Research Group Institute for Geology and Geochemistry, Hungarian Academy of Sciences, 1112 Budapest, Budaörsi út. 45, Hungary; <sup>3</sup>Research Institute for Solid State Physics and Optics of Hungarian Academy of Sciences, Budapest, Hungary; <sup>4</sup>Department of Mineralogy, Geochemistry and Petrology, Szeged University, 6702 Szeged, Egyetem utca 2-6, Hungary; <sup>5</sup>Department of Geodynamics and Sedimentology, University of Vienna, Althanstrasse 14, A-1090, Vienna, Austria; <sup>6</sup>Natural History Museum, Vienna, A-1010, Burgring 7, Vienna, Austria

Corresponding author: Ildiko Gyollai, Department of Lithospheric Research, University of Vienna, Althanstrasse 14, A-1090 Vienna, Austria. E-mail: [gyollai.ildiko@gmail.com](mailto:gyollai.ildiko@gmail.com)

**Article after “minor revision” was re-submitted to “Communications of the Geological Survey of Namibia on 26<sup>th</sup> November 2013, currently it is in press.**

**Abstract** Basal layers from Sturtian postglacial cap carbonate deposits of the Otavi Group, Namibia were studied using various spectroscopic methods in order to define their paleoenvironmental sedimentary conditions, as well as their presumptive micro-fossil record. Deposition of our sample set occurred in shallow water environments during the aftermath of the Sturtian „Snowball Earth” glaciation. Onion-like growth structures related to iron-oxidizing bacteria and cyanobacteria were observed randomly in the interior of ooids and also within micritic matrix material. The Raman spectroscopic detection of various hydrocarbon phases contained in our samples strongly point to bacterial activity involved with sediments allocated to the immediate aftermath of Sturtian „Snowball Earth” glaciations. Backscattered electron imaging and cathodoluminescence microscopy of fine-grained detrital matrix material illustrate a variety of minerals, such as zircon, mica, feldspar, and apatite, all of which indicate detrital input derived from crystalline basement areas. Smectite around the ooids was most probably generated by diagenesis of iron-oxidizing bacterial films.

## 2.1 Introduction

### 2.1.1 Overview

Observational evidence suggests that Planet Earth went through several episodes of global or near-global glaciations during the Late Precambrian Period (Hoffman and Schrag, 2002). The so-called “Snowball Earth” hypothesis states that the Sturtian (~ 750 Ma) and Marinoan (~635 Ma) glaciations were of global extent and may have lasted for several million years (Hoffman et al., 1998). A variation of this hypothesis, called the “Slushball Earth”, assumes intermediate conditions without substantial equatorial sea ice (Harland and Rudwick, 1964). While the “Snowball Earth glaciations” would have ended abruptly in a greenhouse environment, the “Slushball Earth glaciations” ought to be characterized by a slower, gradual deglaciation process (Fairchild and Kennedy, 2007). Concerning the initiation of a global glaciation process a variety of causes have been discussed, including decreased solar luminosity, continental breakup tectonics and the passage of the Solar System through an interstellar cloud (Hoffmann and Schrag, 2002). At this stage, not only the probable cause of the glaciations is unclear, but also the cause and mechanism of deglaciation processes is debated. According to the so-called “Zipper-rift model” (Eyles and Januszczak, 2004) diachronous rifting of the former supercontinent “Rodinia” might have led to a global glaciation, suggesting that some part of the specific diamictites have been formed from turbidity currents. However, our study confirms the existence of distinct ancient areas characterized by specific environmental conditions attended by the Sturtian deglaciation process. Our discovery of fossilized microbial textures is the focus of this study, which attempts to provide evidence of organic material incorporated within these putative microbial remains.

## 2.2 Geological background

Our research area is located in the Neoproterozoic Otavi Group in NW-Namibia. The Otavi Platform formed along the southern fringe of the Congo Craton and abuts on the continental slope facies further South and West (Fig. 1.). Thus, the predominantly calcareous sedimentary successions of the unified Otavi Group were generated in a foreland position relative to the areas of the later Kaoko Belt in the West and to the Damara Belt in the South (Hoffman, 2005). The Otavi Group is subdivided into three subgroups, which are separated from each other by two glaciogenic diamictite units, the lower Chuos Formation and the upper Ghaub Formation (Hoffman, 2005; Hoffmann and Schrag, 2002). The cap carbonates succeeding these subunits might have been generated due to CO<sub>2</sub> oversaturation of the seawater (Le Hir et al., 2008; Kennedy et al., 2008) added by the input of methane outgassing from clathrates (Kennedy et al., 2008).

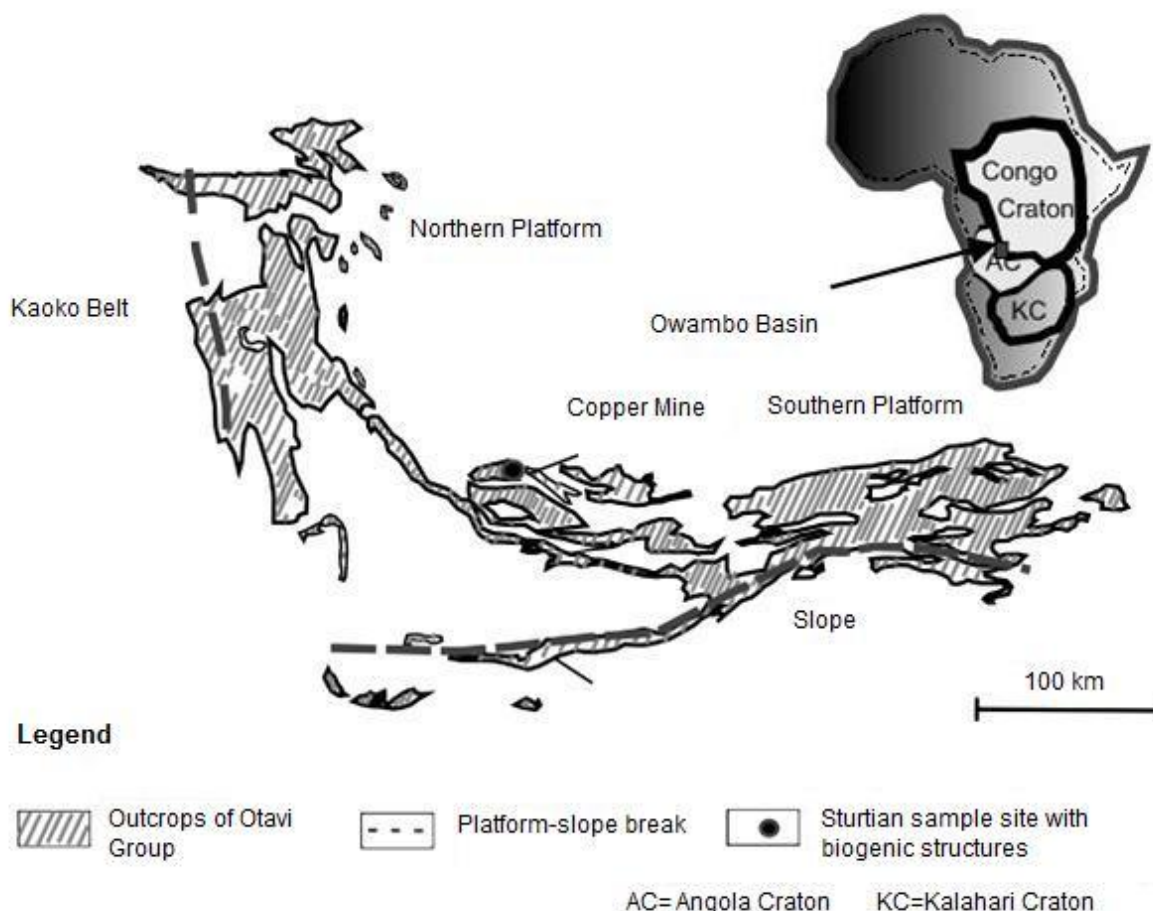


**Figure 1.** Geological map of research area showing sampling site (Copper Mine; 9°25'18.43"S; 15° 9'50.90"E). (Modified after Hoffman, 2005).

### 2.3 Samples and methods

One representative oolitic carbonate sandstone sample (C8=basal layer of the Rasthof Fm.), collected from a distinct Otavi platform facies area was studied at Copper Mine locality (19°25'18.43"S; 15° 9'50.90"E) in NW-Namibia. Macroscopic features show reddish brown-pale red color, grainstone texture with spherical carbonate components, and small quartz pebbles (Fig. 2A.). Four ooid components were measured by micro-Raman spectroscopy in order to identify organic material incorporated within observed microbial structures. Pictured in Fig. 2B is a thin section of our Sturtian oolitic grainstone sample that shows the measured points. The first two investigated components were single cored ooids (oid No. 1 and 2), while the rest have multiple cores (oid No. 3 and 4).

Scanning electron microscopy (SEM) studies were done on a polished thick section of the oolitic sandstone at the Department for Petrology and Geochemistry, Eötvös University, Bu-

dapest, Hungary. Chemical and mineral composition and distribution were determined by an Amray 1830 SEM with an EDAX PV9800 energy dispersive spectrometer detector, using 20 kV accelerating voltage, a beam current of 1nA with a defocused spot size of 10–50 nm and a collection time of 100 s.

The mineral assemblages and textures were also characterized by a NIKON ECLIPSE LV100POL optical microscope at University of Vienna and by a NIKON ECLIPSE 600 at the Institute for Geology and Geochemistry, RCAG, Hungarian Academy of Sciences, Budapest.

Raman spectra were recorded with a Renishaw Rm-2000 Raman spectrometer attached to a Leica DM/LM microscope (785 nm, 8mW laser line) at the Research Institute for Solid State Physics and Optics, Budapest.

Optical cathodoluminescence microscopy on a carbon coated polished thin section was performed with a Lumic HC5-LM system at the Department of Lithospheric Research, University of Vienna, using a beam energy of 14 keV and a beam current of ~0.20 mA. Image acquisitions were done with a KAPPA DX 40 C camera system.

## 2.4 Results

### 2.4.1 Petrography

The studied basal cap carbonate sample (C8) is an oolitic "wackestone" to "packstone" with respect to Dunham's classification on dominant texture (Dunham, 1962) which formed at winnowed inner platform facies (Fig. 2.). Some ooid grains are wrapped with micritic rims generating oncolite sedimentary structures. These oncoids can include one or more cores of different mineralogical composition. In cases of single cored oncoids the composition is micritic, similarly to the matrix of the oncoid. If the oncoids are multicored their composition consists of detrital minerals, like quartz and mica. Recrystallized quartz lenses also occur among the oncoid's cores. The micritic matrix contains mica, quartz, and carbonate. A few clasts are bordered/framed with fibrous mica. Quartz grains coated by sericite indicate very low grade metamorphic reactions. Based on microtexture, the dark micritic rims surrounding cores of dolomitic oncoids are assumed to be of bacterial origin (Fig. 2.).

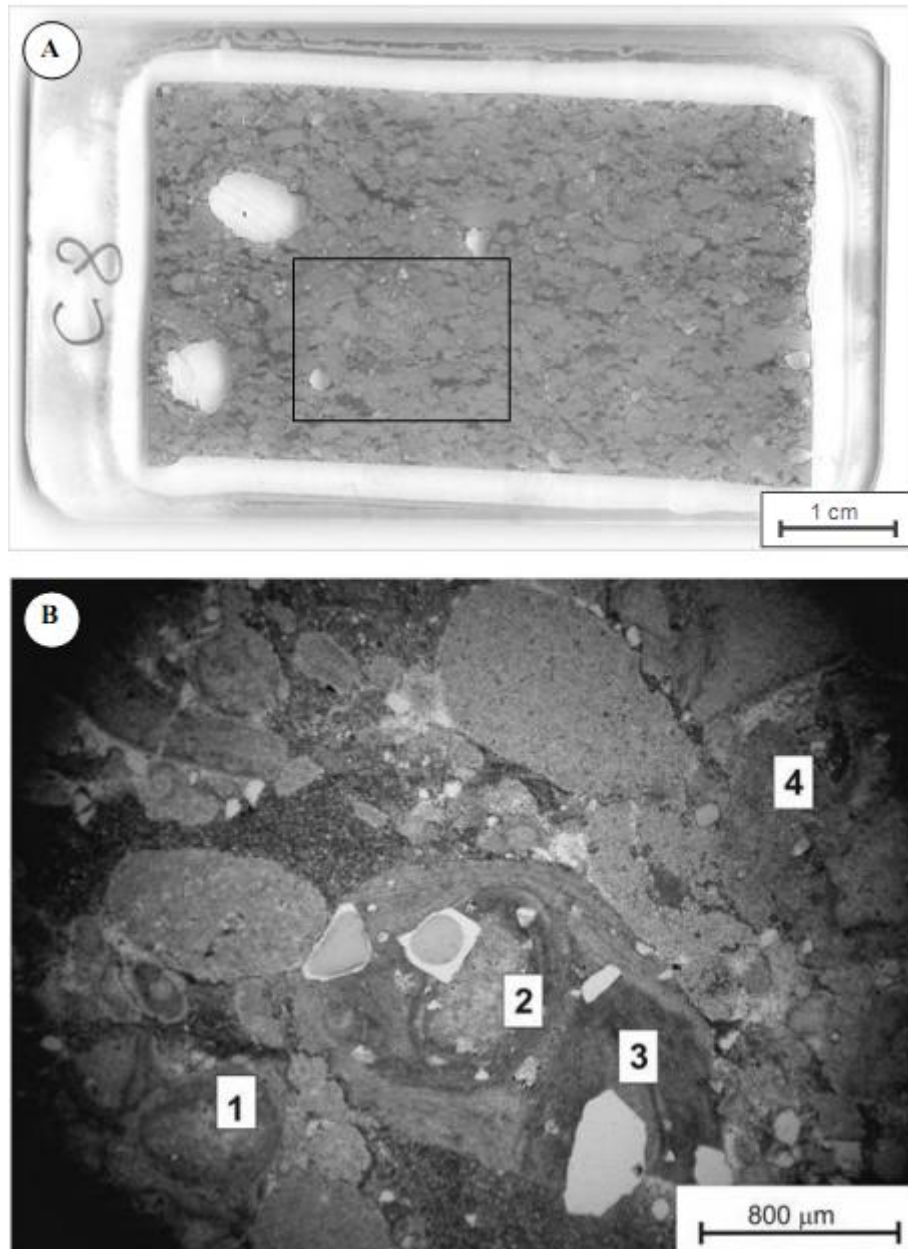


**Figure 2.** Sturtian oolitic grainstone sample. (A) photo of polished section (area of Raman measuring area – picture B is marked by black rectangle), (B) Raman measuring points signed on thin section ("ooids No. 1, 2, 3, 4"; optical microscopic photo, plain polarized light).

#### 2.4.2 Microbial structures

Signs of Fe-oxidizing bacterial activity (FeOB) were observed in sample C8 located at the filamentous rims of the ooids and their onion-shape like internal structures (Fig. 3.). Some supposable coccoidal iron oxidizing bacteria (FeOB) colonies are located perpendicularly to the growth rims of the ooids, being indicative of septum structures. These phenomena indicate that the putative FeOB colonies expanded upon ooid surfaces, and were repeatedly buried by following generations of carbonate films created by metabolism of calcimicrobae

and cyanobacteria (Fig. 4.). Growth sequences of the observed FeOB colonies start randomly onto micritic carbonate nuclei then advancing towards their inner part. Compared to these carbonate nuclei quartz grains often offer a better preservation of this aspect (Fig. 4.). Our samples exhibit mainly coccoidal colonies of FeOB. In general, the observed FeO colonies apparently developed in symbiosis of cyanobacteria and calcimicrobae with diatom-like microorganisms characterized by similar shape and  $\text{SiO}_2$ -bearing frustules incorporated in quartz.

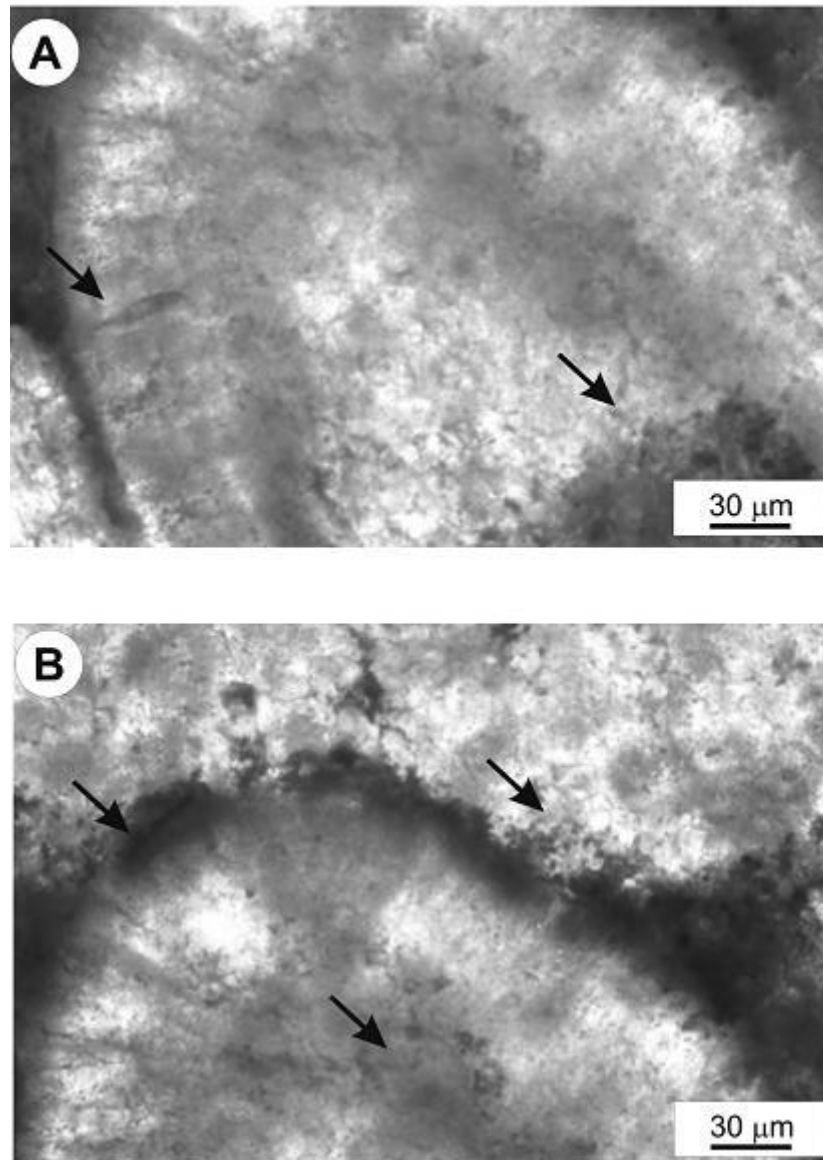


**Figure 3.** FeOB colonies on the surface of ooids and inside along of growth of ooids (in symbiosis with cyanobacteria and calcimicrobae (shown by arrows). (A) FeOB colonies perpendicularly growth inside ooids, (B) FeOB colonies on surface of ooid.

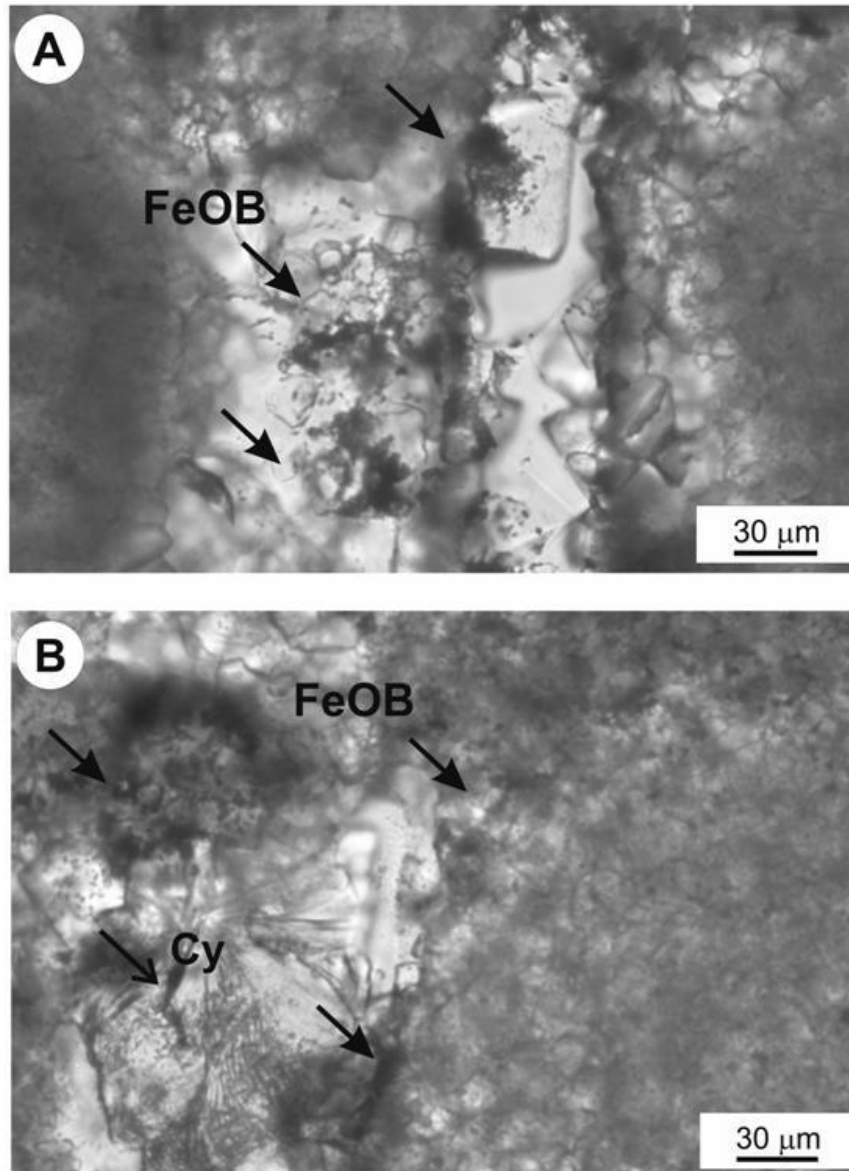
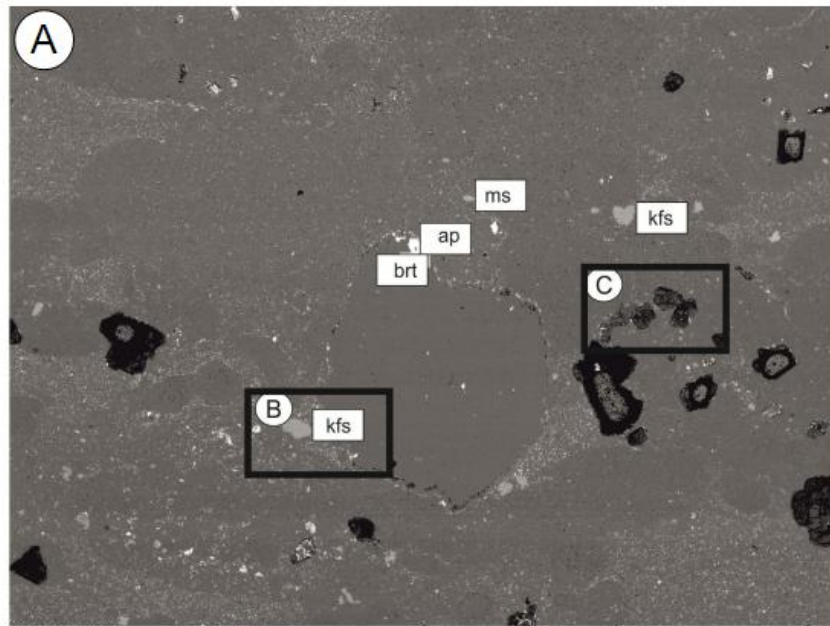


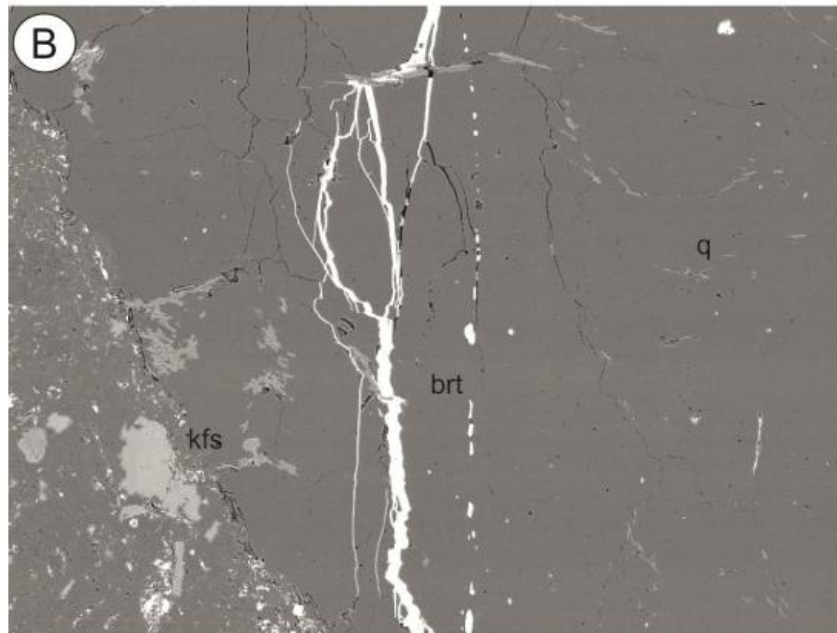
**Figure 4.** FeOB colonies on the surface of quartz pebbles (A) and in symbiosis with oscillatory cyanobacteria (Cy) (B) (shown by arrows).

#### 2.4.3 Chemical composition and mineralogy - backscattered electron imaging

The bulk mineral composition of C8 oolitic packstone is 84 wt.% carbonate, 15 wt.% mica, 5 wt.% quartz and K-feldspar, and 1 wt.% hematite, as determined by optical microscopy. The analyzed ooids No. 1 and 2 have a single dolomite-core, the multi-cored ooid No. 3 consists of dolomite and microcline, and ooid No. 4 has a core of dolomite and quartz. According to SEM-EDS data and back-scattered electron (BSE) images, an analyzed 3 mm sized quartz of the oolitic packstone is surrounded by a rim of fine-grained kaolinite-barite-apatite mineral assemblage. This quartz pebble is crossed by a diagenetic barite vein. The micritic ooids are usually surrounded by a smectite rim, which may contain galenite grains (Fig. 5.).



HV: 20.0 kV      DET: BSE  
 Satellite ©Tescan      DATE: 06/20/12      2 mm



HV: 20.0 kV      DET: BSE  
 Satellite ©Tescan      DATE: 06/20/12      200 um

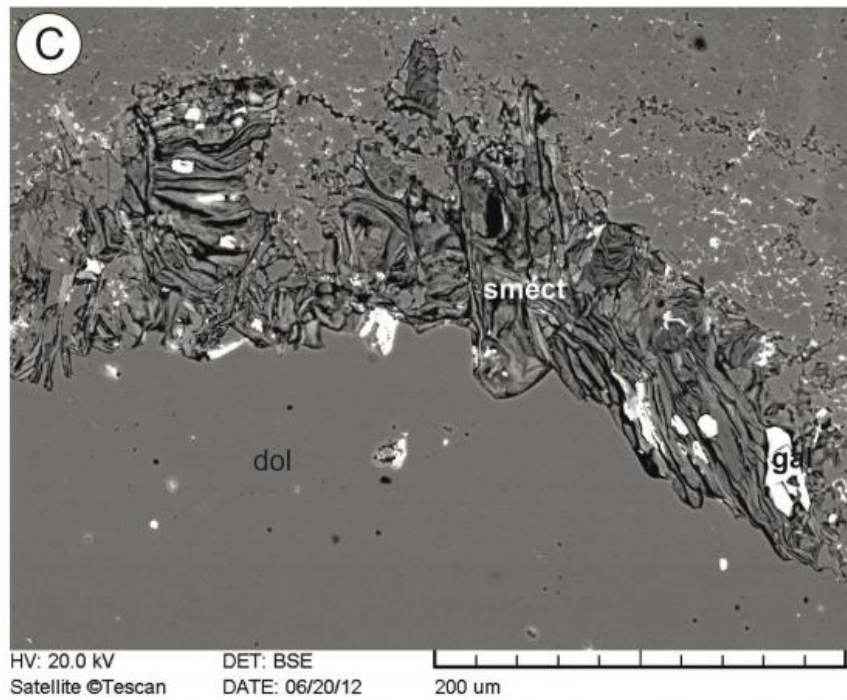


**Figure 5.** Backscattered electron image of an ooid in C8 Sturtian oolitic packstone-wackestone (A); (B) rim of quartz pebble; (C) smectite rim around ooid (Legend: brt=barite, smect= smectite, gal=galenite, kfs=K-feldspar, dol=dolomite, q=quartz, ap=apatite, ms=muscovite (B, C pictures are focused area of picture A, which are marked by black rectangle). Whole scale bar is 2 mm for picture A, and 200  $\mu\text{m}$  for figure B and C.

#### 2.4.4 Textural characteristics by cathodoluminescence studies

The investigated ooid components show zoned luminescence (bright red zones in dull red material; Fig. 6.). Several detrital mineral components can be observed inside the oncoid structure (blue luminescent quartz and feldspar). In general, the carbonate material between oolites has a brighter red luminescent color than the oolites themselves. Bright red luminescent clasts and small grained oolite components with bright red rim occur between larger oolite components (Fig. 7.).

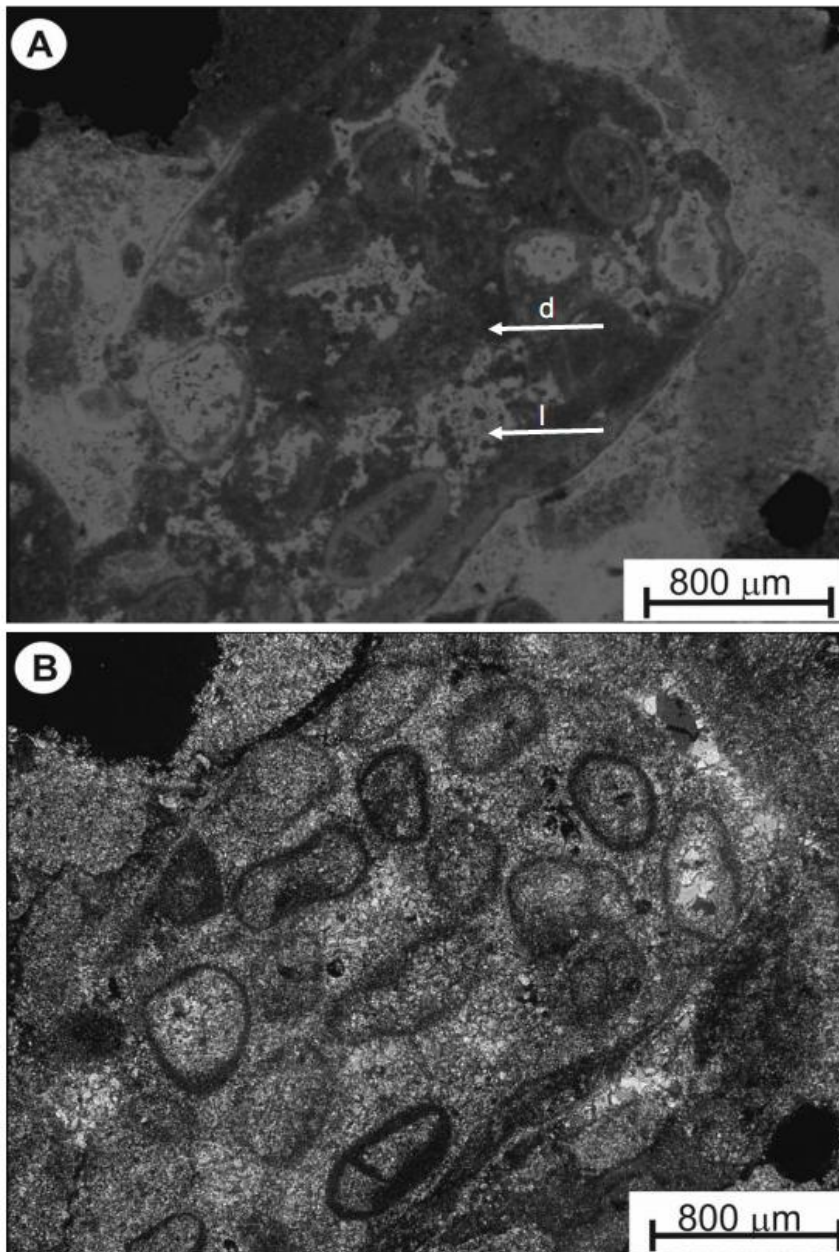


**Figure 6.** Multicore-oncoid where the core is surrounded by fine-grained material (bacterial film). Inside and between the cores, light-luminescent cements are observed (l-arrow), which are filled with small grained oolite components. The dull luminescent part (d-arrow) is built up from/by clayey and carbonaceous material. (A) cathodoluminescent light, (B) plain polarized light.

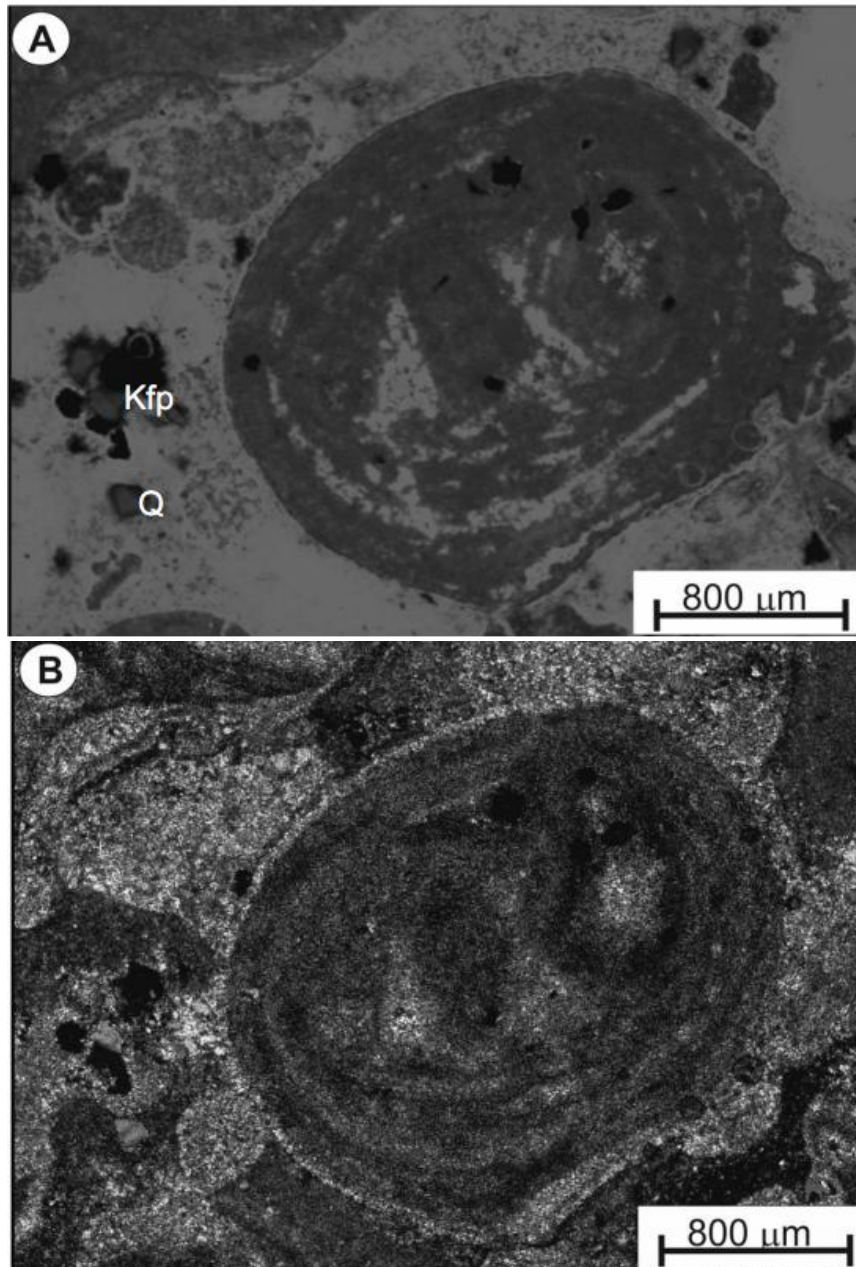


**Figure 7.** Ooids with growth rims, with brighter luminescent color. The middle luminescent grains are quartz (q) and feldspars (kfp) detrital grains (A) cathodoluminescent light, (B) plain polarized light.

### 2.4.5 Raman spectroscopy

The points in our Sturtian oolitic grainstone (“oid No. 1, 2, 3, 4”) thin section that have been measured by Raman spectroscopy are shown in Fig. 2B, and the corresponding Raman vibration data are listed in Table 1.

Ooid No. 1: The spectra are dominated by the narrow bands of dolomite at 178, 300, 723, and 1097  $\text{cm}^{-1}$  (Lewis and Edwards, 2001). Another remarkable feature of the spectra is the broad band in the 1000-2000  $\text{cm}^{-1}$  region, which can be attributed to  $\text{sp}^2$  C=C bonds (up to 1650  $\text{cm}^{-1}$ ) and different carbonyl and cumulated double bonds of the amorphous carbon phase with some oxygen content. Other observable peaks at 1300 and 1450  $\text{cm}^{-1}$  correspond to deformation vibrations of  $\text{CH}_2$  and  $\text{CH}_3$  groups, while the peak at 1402 belongs to asymmetric vibration of  $\text{CH}_2$  and  $\text{CH}_3$  groups. The peak of the carbonyl group can be detected at 1716  $\text{cm}^{-1}$  (Fig. 8A; Table 1A).

Ooid No. 2: The dolomite peaks appear at 173  $\text{cm}^{-1}$ , 298  $\text{cm}^{-1}$ , 725  $\text{cm}^{-1}$  and 1099  $\text{cm}^{-1}$ , respectively. A broad band related to an amorphous carbon phase can be seen in the 1000-2000  $\text{cm}^{-1}$  region. Narrow peaks at 1302 and 1402  $\text{cm}^{-1}$  correspond to vibrations of  $\text{CH}_2$  and  $\text{CH}_3$  groups. The stretching vibration of carbonyl group appears at 1717  $\text{cm}^{-1}$  (Fig. 8B, Table 1B).

Ooid No. 3: The peaks of dolomite appear at 173  $\text{cm}^{-1}$ , 298  $\text{cm}^{-1}$  and 1099  $\text{cm}^{-1}$ , respectively. The peak at 724  $\text{cm}^{-1}$  is of low intensity because of polarization effect. The K-feldspar (microcline) shows minor peaks at 330  $\text{cm}^{-1}$ , 364  $\text{cm}^{-1}$ , and strong vibration of Si-O-Si/Si-O-Al bridges at 475  $\text{cm}^{-1}$ , whereas the most characteristic Raman vibration is centered at 513  $\text{cm}^{-1}$  concerning O symmetric motion in Si-O-Si bridges. The broad amorphous carbon band again appears in the 1000-2000  $\text{cm}^{-1}$  region. Some narrow  $\text{CH}_2$  and  $\text{CH}_3$  vibrations can be detected at 1302 and 1441  $\text{cm}^{-1}$ , together with the peak of C=O stretching vibration at 1710  $\text{cm}^{-1}$  (Fig. 8C, Table 1C).

Ooid No. 4: The peaks of dolomite appear at 299  $\text{cm}^{-1}$  and 1099  $\text{cm}^{-1}$ . The peak at 178  $\text{cm}^{-1}$  overlaps with the band at 199  $\text{cm}^{-1}$ , while the one at 724  $\text{cm}^{-1}$  is affected by the polarization effect. The peaks of quartz appear at 199  $\text{cm}^{-1}$ , 351  $\text{cm}^{-1}$ , 390  $\text{cm}^{-1}$  and 462  $\text{cm}^{-1}$ . The vibrations of  $\text{CH}_3$  and  $\text{CH}_2$  groups are centered at 1296  $\text{cm}^{-1}$ , 1335  $\text{cm}^{-1}$  and 1441  $\text{cm}^{-1}$ . The C=O stretching vibration is at 1710  $\text{cm}^{-1}$ , and a new peak can also be detected that can be attributed to some structural units with cumulated double or triple bonds. Amorphous carbon in the sample causes the broad band in the 1000-2000  $\text{cm}^{-1}$  region (Fig. 8D, Table 1D).

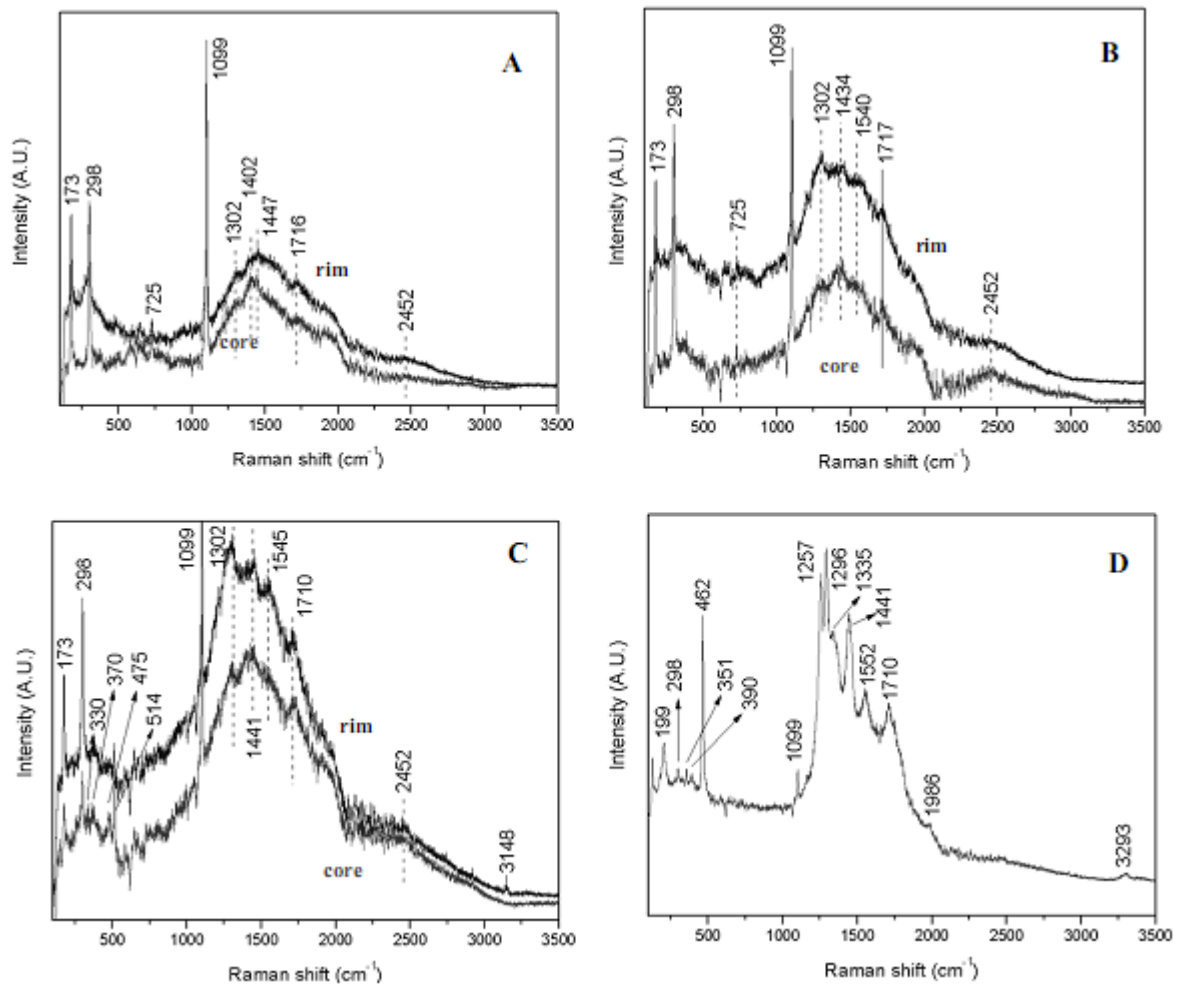


**Figure 8.** Raman spectra of ooid No. 1-4 (for measuring site see Fig. 2B, vibrations are listed in Table 1.). (A) ooid No. 1, (B) ooid No. 2., (C) ooid No. 3, (D) ooid No. 4. Spectra in ooid No.1-3 were measured in core and rim region).

**Table 1.** Mineral and hydrocarbon phases with Raman vibrations in four ooids (A: spectra of ooid No. 1, B: ooid No. 2, C: ooid No. 3, D: ooid No. 4). \*

<b>A</b>			
<b>Standard of dolomite</b>	<b>Hydrocarbon</b>	<b>Ooid 1 core</b>	<b>Ooid 1 rim</b>
178 Eg** T(Ca, Mg, CO <sub>3</sub> )		173 (Dol)	173 (Dol)
300 Eg (T(Ca, Mg, CO <sub>3</sub> ))		298 (Dol)	298 (Dol)
723 Eg v4 symmetric CO <sub>3</sub> deformation		725 (Dol)	725 (Dol)
1097 Ag*** v1 symmetric CO <sub>3</sub> stretching		1099 (Dol)	1099 (Dol)
	1300 CH <sub>3</sub> -CH <sub>2</sub> transverse vibrations of H atoms	1302	1302
	1400 assym. vibrations of CH <sub>3</sub> and CH <sub>2</sub> groups	1402	
1440 Eg v3 asymmetric CO <sub>3</sub> stretching	1450 CH <sub>2</sub> bend	1447	1447
	1710 C=O stretch	1716	1716
	2450 graphite (minor peak)	2452	2452
<b>B</b>			
<b>Standard of dolomite RUFF Database</b>	<b>Hydrocarbon</b>	<b>Ooid 2 core</b>	<b>Ooid 2 rim</b>
178 Eg T(Ca, Mg, CO <sub>3</sub> )		173 (Dol)	173 (Dol)
300 Eg (T(Ca, Mg, CO <sub>3</sub> ))		298 (Dol)	298 (Dol)
723 Eg v4 symmetric CO <sub>3</sub> deformation		725 (Dol)	725 (Dol)
1097 Ag v1 symmetric CO <sub>3</sub> stretching		1099 (Dol)	1099 (Dol)
	1300 CH <sub>3</sub> and CH <sub>2</sub> asym. vibr.	1302	1302
	1430-1450 sp <sup>2</sup> C=C CH <sub>2</sub> and CH <sub>3</sub> group	1434	1434
1440 Eg v3 asymmetric CO <sub>3</sub> stretching	1532 COOH, 1500-1550 sp <sup>2</sup> C	1540	1540
	1710 C=O stretch	1717	1717
	2450 graphite (minor peak)	2452	2452

**C**

Dolomite	Microcline	Hydrocarbon	Ooid 3 core	Ooid 3 rim
178 Eg T(Ca, Mg, CO <sub>3</sub> )			173 (Dol)	173 (Dol)
300 Eg (T(Ca, Mg, CO <sub>3</sub> ))			298 (Dol)	298 (Dol)
	330		330 (mcl)	330 (mcl)
	364		370 (mcl)	370 (mcl)
	475 s Si-O-Si/Si-O-Al		475 (mcl)	475 (mcl)
	513 vs (A.g.)		514 (mcl)	514 (mcl)
723 Eg v4 symmetric CO <sub>3</sub> deformation				
1097 Ag v1 symmetric CO <sub>3</sub> stretching			1099 (Dol)	1099 (Dol)
		1300 asymmetric vibrations of CH <sub>3</sub> and CH <sub>2</sub> group	1302	1302
1440 Eg v3 asymmetric CO <sub>3</sub> stretching		1450 CH <sub>2</sub> bend	1441	1441
		1532-1550 COOH	1545	1545
		1710 C-O stretch	1710	1710
		2450 graphite (minor peak)	2452	2452
		2900-3300 CH stretching vibration		3148

**D**

Standard quartz (Raman) shift) in cm <sup>-1</sup>	Standard of dolomite RUFF Database	Hydrocarbon	Ooid 4
203	178 Eg T(Ca, Mg, CO <sub>3</sub> )		199 (Q)
	300 Eg (T(Ca, Mg, CO <sub>3</sub> ))		298 (Dol)
353			351 (Q)
393.5			390 (Q)
461 vs			462 (Q)
	723 Eg v4 symmetric CO <sub>3</sub> deformation		1099 (Dol)
	1097 Ag v1 symmetric CO <sub>3</sub> stretching		1099 (Dol)
		1000-1275 C-O stretching	1257
		1300 asymmetric vibration of CH <sub>2</sub> -CH <sub>3</sub> group	1296
		1335 amorphous carbon	1335
		1450 CH <sub>2</sub> bend	1441
		1532-1550 COOH	1552
		C=O stretch	1710
		2000 sp <sup>2</sup> C	1986
		3300 C-H stretching of butane	3293

\* Except No. 4, all of ooid specimens were measured at rim and in core. Mineral standards were taken from RUFF database. Hydrocarbon vibrations were interpreted following Kudryavtsev et al., (2001); Kempe et al., (2005); Marshall et al., (2005); Veres et al., (2006). Raman shifts are added in cm<sup>-1</sup>. For measuring site see Fig. 2B, for spectra see Fig. 8A-D.

\*\* Eg: marks minor vibrations in Raman spectrum.

\*\*\* Ag: defines major vibration, which is most characteristic vibration for adjacent phase in Raman spectrum.

## 2.5 Discussion

The Raman spectroscopy is a powerful method to identify organic material as biomarker of microbial structures. Precambrian microfossils were studied using this method by a number of research groups (Kudryavtsev et al., 2001; Kempe et al., 2005; Marshall et al., 2005). The aromatic ring deformation and symmetric breathing is attributed in the 1200-1400  $\text{cm}^{-1}$  range (Mapelli et al., 1999). The peaks of organic material in Precambrian microfossils (e.g., acritarchs) occur around 1600  $\text{cm}^{-1}$ , and there is a group of bands at 1300-1350  $\text{cm}^{-1}$ , with broad peaks belonging to kerogen - aromatic ( $\text{sp}^2$ ) bonded C atoms joined together with peripheral  $\text{sp}^2$  and  $\text{sp}^3$ -bonded hydrocarbons (Kempe et al., 2005). A variety of peaks of apparent C=C aromatic stretching bands at 1600  $\text{cm}^{-1}$ ,  $\text{CH}_3$  terminal groups (1345  $\text{cm}^{-1}$ ), C-H aliphatic stretching (3000-2700  $\text{cm}^{-1}$ ), and C=O vibration (1710  $\text{cm}^{-1}$ ) occur in the hydrocarbon phase (Marshall et al., 2005). In our samples the peak around 1710  $\text{cm}^{-1}$ , related to the carbonyl group, is observed in all the measured ooids, which is similar to the published data of Marshall et al. (2005), while the other reported Raman shifts join the region occupied by the broad band of hydrogenated amorphous carbon phase, the large width of which is caused by the highly disordered character of the sample. This is a remarkable difference compared to the published data mentioned above. In spite of this, some characteristic CH vibrations were observed in form of narrow peaks in the 1300-1450  $\text{cm}^{-1}$  region of our spectra (Fig. 8.).

In general, the Raman spectrum of amorphous carbons consists of a broad band in the 1000-1800  $\text{cm}^{-1}$  region (Dresselhaus and Dresselhaus, 1982; Ferrari and Robertson, 2000; Veres et al., 2006). For visible and near-infrared excitations it is dominated by the characteristic peaks of  $\text{sp}^2$  carbon atoms, since due to resonant processes the Raman scattering on these structural units is a few orders of magnitude higher than that on building blocks consisting of  $\text{sp}^3$  C atoms. The broad band is resulting from superposition of scattering contributions from different structural units and can be divided into several regions. For near infrared excitation used in this study, peaks between 1100-1200  $\text{cm}^{-1}$  and 1400-1500  $\text{cm}^{-1}$  correspond to vibrations of  $\text{sp}^2$  carbon chains (observed mainly in hydrogenated samples), between 1200-1350  $\text{cm}^{-1}$  – to breathing vibrations of  $\text{sp}^2$  carbon rings (this is the so called D band) and above 1570  $\text{cm}^{-1}$  – to stretching vibrations of  $\text{sp}^2$  carbon atoms in rings (the so called G band) (Veres et al., 2006). Features of the broad band observed in our spectra suggest that the amorphous carbon phase in the sample is dominated by  $\text{sp}^2$  (hydro) carbon chains, with relatively minor (graphitic)  $\text{sp}^2$  C ring content (Table 1). This is supported by the narrow peaks assigned to different vibrations of  $\text{CH}_2$  and  $\text{CH}_3$  groups. Components of the broad

band in the  $>1650\text{ cm}^{-1}$  region, together with the carbonyl peak indicate the presence of oxygen in the amorphous carbon structure.

Comparing the broad amorphous carbon bands, ooid No. 2 and 3 have quite similar structure, with somewhat higher graphitic content compared to ooid No. 1 (indicated by the higher intensities in the D and G band regions) (Fig 8A-C, Table 1 A-C). In ooid No. 1 and 2 the narrow hydrocarbon peaks are less intense (Fig 8A-B). These peaks have the highest intensity in the spectrum of ooid No. 4, where the C=O shows also the most pronounced vibration (Fig. 8D, Table 1D).

The observed features of amorphous carbon phases are similar to those found in cryptocrystalline silica varieties with traces of Miocene hydrothermal biomineralization (Müller et al., 2009) and indicate the organic, probably microbial origin of the amorphous carbon phases identified in the sample. Apart from organic matter, mineral components (dolomite, hematite, quartz, feldspar) were also identified by Raman spectroscopy.

The first peak of dolomite ( $178\text{ cm}^{-1}$ ) shifted to  $5\text{ cm}^{-1}$  wave number, and this was overlapped by the quartz band in the spectrum of ooid No. 4 (Table 1D). In ooids No. 3 and No. 4 the  $723\text{ cm}^{-1}$  peak did not appear in the spectra, which is due to a polarization effect (Fig 8C-D, Table 1C-D.). Due to diagenesis and weathering the material was dolomitized and hematitized. A dolomitization process means infiltration of Mg-rich pore water, which changes original microbial carbonate (aragonite, calcite) to dolomite during the diagenesis. Hematite was probably formed by transformation of primary ferrihydrite originated via Fe-oxidizing bacterial activity (Konhauser, 1998). Alternatively, the hematite could be derived by continental weathering (iron-rich matrix) (Hoffman et al., 1998). The smectites around the ooids are derived most probably by diagenesis and/or weathering of microbial structures, whereas galenite formed in a biomineralization process (Erlich, 2010).

## 2.6 Conclusions

A representative sample (C8) was analyzed for its organic geochemistry and mineral composition as well as for its textural characteristics. The presence of amorphous carbon was demonstrated in all of the measured points of the sample. Traces of hydrocarbons and C=O groups were detected, featuring highest concentration in the dolomite-quartz matrix. Ooid 1 and 2 hold light hydrocarbon (with low C number) of the methyl group, whereas ooid 4 contains a more complex hydrocarbon, just like butane.

We consider the hydrocarbons detected in our samples (C8), originated from bacterial (probably cyanobacteria) communities which existed in shallow water environments of the

ancient Otavi platform. Smectite surrounding the ooid grains is most probably derived from diagenesis and/or weathering of microbial films. Numerous peaks attributed to the methyl group might indicate a contribution from methane outgassing and thus indicate the role of rapid global warming after Neoproterozoic “Snowball Earth” glaciations.

## **2.7 Acknowledgements**

This study was supported by the Austrian Academy of Sciences (grant number: IGCP 512). We are grateful to the Geological Survey of Namibia and especially Director Dr. G. Schneider for invaluable help in field work organization and sample export management.

## 2.8 References

- Dunham, R.J., 1962. Classification of carbonate rocks according to depositional texture. In Ham, W.E. (ed.): Classification of carbonate rocks.- Amer. Assoc. Petrol. Geol. Memoir, 1, 108-121.
- Dresselhaus, M.S. and Dresselhaus, G., 1982. Light scattering in graphite intercalation compounds. *Light Scattering in Solids III. Top. App. Phys.*, 51, 3-57.
- Erlich, H. 2010. Biominerals. In: Erlich, H. *Biological Materials of Marine Origin - Biologically-Inspired Systems*, 1, 25-50.
- Eyles, N. and Januszczak, N., 2004. 'Zipper-rift': a tectonic model for Neoproterozoic glaciations during the breakup of Rodinia after 750 Ma. *Earth-Sci. Rev.*, 65, 1-73.
- Fairchild, I.J. and Kennedy, M.J. 2007. Neoproterozoic glaciation in the Earth system. *J. Geol. Soc. London*, 164, 895-921.
- Ferrari, A.C. and Robertson, J., 2000. Interpretation of Raman spectra of disordered and amorphous carbon. *Phys. Rev. B*, 61, 14095–14107.
- Harland, W.B. and Rudwick, M.J.S., 1964. The great Infra-Cambrian glaciation. *Scientific American* 211, 28-36.
- Hoffman, P.F., 2005. 28th DeBeers Alex Du Toit Memorial Lecture (2004): On Cryogenian (Neoproterozoic) ice-sheet dynamics and the limitations of the glacial sedimentary record. *S. Afr. J. Geol.*, 108, 557-576.
- Hoffman P.F. and Schrag D.P., 2002. The Snowball Earth hypothesis: testing the limits of global change. *Terra Nova*, 14, 129-155.
- Hoffman, P.F., Kaufman, A.J., Halverson, G.P., and Schrag, D.P., 1998. A Neoproterozoic snowball Earth. *Science*, 281, 1342-1346.
- Kempe, A., Wirth, R., Altermann, W., Stark, R.W., Schopf, J.W., and Heck, W.M., 2005. Focused ion beam preparation and in situ nanoscopic study of Precambrian acritarchs. *Precambrian Res.*, 140, 36–54.
- Kennedy, M., Mrofka, D., and von der Borch, C., 2008. Snowball Earth termination by destabilization of equatorial permafrost methane clathrate. *Nature*, 453, 642-645.
- Konhauser, K.O., 1998. Diversity of bacterial iron mineralization. *Earth-Sci. Rev.*, 43/ 3–4, 91-121.
- Kudryavtsev, A.B., Schopf, J.W., Agresty, D.G., and Wdowiak T.J., 2001. In situ laser-Raman imagery of Precambrian microscopic fossils. *Proc. Nat. Acad. Sci.*, 98/ 3, 823-826.

- Le Hir, G.; Donnadieu, Y.; Godderis, Y.; Pierrehumbert, R. T., Halverson, G. P., Macouin, M.; Nedelec, A., and Ramstein, G., 2008. The snowball Earth aftermath: Exploring the limits of continental weathering processes. *Earth Planet. Sci. Lett.*, 277, 453-463.
- Lewis, I.R. and Edwards, H., 2001. *Handbook of Raman Spectroscopy: From the Research Laboratory to the Process Line*. Taylor and Francis, 1072 pp.
- Mapelli, C., Castiglioni, C., Zerbi, G. and Mullen, K., 1999. Common force field for graphite and polycyclic aromatic hydrocarbons. *Phys. Rev. B*60, 12710–12725.
- Marshall, C.P., Javaux, E.J., Knoll, A.H., and Walter, A.M., 2005. Combined micro-Fourier transform infrared (FTIR) spectroscopy and micro-Raman spectroscopy of Proterozoic acritarchs: A new approach to palaeobiology. *Precambrian Res.*, 138, 208–224.
- Müller, A., Polgári, M., Gucsik, A., Nagy, Sz., Veres, M., Pál-Molnár, E., Götze, J., Cserhádi, C., Németh, T., and Hámor-Vidó, M., 2009. Cathodoluminescent features and Raman spectroscopy of Miocene hydrothermal biomineralization embedded in cryptocrystalline silica varieties, Central Europe, Hungary. Abstract volume, Conference on Micro Raman Spectroscopy and Luminescence Studies in the Earth and Planetary Sciences, AIP Proceedings CP1163, Micro-Raman Spectroscopy and Luminescence Studies in the Earth and Planetary Sciences (Gucsik A. (ed).), p. 207-218.
- Veres, M., Tóth, S., and Koós, M., 2006. New aspects of Raman scattering in carbon-based amorphous materials. *Diamond and Related Materials*, 17, 1692-1696.

### 3 Microbially mediated deposition of postglacial transition layers from the Neoproterozoic Otavi Group, Namibia: Evidence of rapid deglaciation after the Sturtian Cryogenic Period

Ildikó Gyollai<sup>1,2</sup>, Márta Polgári<sup>3\*</sup>, Krisztián Fintor<sup>4</sup>, Friedrich Popp<sup>5</sup>, Dieter Mader<sup>1</sup>, Elemér Pál-Molnár<sup>4,6</sup>, Szabolcs Nagy<sup>2,4</sup>, Christian Koeberl<sup>1,7</sup>

<sup>1</sup>Department of Lithospheric Research, University of Vienna, Althanstrasse 14, A-1090, Vienna, Austria, <sup>2</sup>Cosmic Materials Research Group, Geobiomineralization and Astrobiological Research Group, Eötvös Loránd University of Budapest, 1117 Budapest, Pázmány Péter Street 1/A, Hungary <sup>3</sup>Research Center for Astronomy and Geosciences, Geobiomineralization and Astrobiological Research Group, Institute for Geology and Geochemistry, Hungarian Academy of Sciences, 1112 Budapest, Budaörsi Street 45, Hungary (e-mail: rodokrozit@gmail.com, \*corresponding author), <sup>4</sup> Department of Mineralogy, Geochemistry and Petrology, Szeged University, 6702 Szeged, Egyetem Street 2, Hungary, <sup>5</sup>Department of Geodynamics and Sedimentology, University of Vienna, Althanstrasse 14, A-1090, Vienna, Austria, <sup>6</sup>MTA-ELTE Volcanology Research Group, H-1117 Budapest, Pázmány P. Street 1/C, Hungary, <sup>7</sup>Natural History Museum, Vienna, A-1010, Burgring 7, Vienna, Austria

**Article was submitted to “Carpathian Journal of Earth and Environmental Sciences” on 10<sup>th</sup> December 2013.**

**Abstract:** Iron-rich postglacial transition layers from early Cryogenian “Snowball Earth” sedimentary environments of the Otavi Group (Namibia) were studied by microtextural high-resolution mineralogical and geochemical methods. Series of Fe-rich biomats (goethite, hematite) were identified, and signs of diverse microbial, filamentous Fe-oxidizing, and cyanobacterial activity were documented for the first time. The matrix mineralogy consists of quartz and dolomite, diverse organic matter, muscovite, apatite, and pyrite. On the basis of mineralized bacterial layering of the Fe-rich biomats, the postglacial transition layers are interpreted to have formed within a few hundred years under suboxic, neutrophilic, shallow, fresh- to brackish-water conditions during an initial rapid deglaciation process from a Neoproterozoic “Snowball Earth” environment. Thus we suggest that the overlying Rasthof cap carbonates, influenced by tectonic subsidence of the region, may also have been deposited within a very short period, comprising the entire deglaciation process.

**Keywords:** Sturtian, Snowball Earth, microbial mats, deglaciation, transition layer, iron-oxidizing bacteria

### 3.1 Introduction

Neoproterozoic glaciations of global extent occurred within three succeeding cryogenic periods: (i) the Sturtian period (720–660 Ma, type location: Sturt valley, South Australia), (ii) the Marinoan period (650–635 Ma, type location: Marino, South Australia) (Arnaud et al., 2011; and references therein) and (iii) the Gaskiers period (ca. 580 Ma, type location: Gaskiers, Newfoundland, Canada), each glaciation lasting several million years (e.g., Kennedy et al., 1998; Bodiselsch et al., 2005). The term “Snowball Earth” was introduced in the year 1992 (Kirschvink, 1992; Hoffman et al., 1998). A variety of hypotheses have been formulated to explain various aspects of the Cryogenian global(?) glaciations (Fairchild and Kennedy, 2007), with the most important being: (i) Hard Snowball Earth (Hoffman et al., 1998; Hoffman and Schrag, 2002), (ii) Slushball Earth (Harland and Rudwick, 1964), (iii) Zipper-rift model (Eyles and Januszczak, 2004) and (iv) High-tilt Earth (Williams, 1975).

Similarities to Paleoproterozoic diamictites are noticeable, e.g., some of the Cryogenian (Sturtian) diamictites are also saturated with iron precipitations. Banded iron ( $\pm$ manganese) formations (BIFs) occur within glacial marine formations in Namibia (Martin, 1964), Australia (Whitten, 1970), Canada (Klein and Beukes, 1993), and Brazil (Klein and Ladeira, 2004; Hoffman et al., 2011).

Large Neoproterozoic Fe and Fe-Mn deposits developed within a paleolatitude range around  $35^\circ$  (Hoffman and Li, 2009) holding a thickness variation from tens to hundreds of meters. These deposits indicate that the ancient glacial deep waters became anoxic, allowing  $\text{Fe}^{2+}$  and  $\text{Mn}^{2+}$  ions supplied by mid-ocean ridge hydrothermal systems to travel widely in solution (Martin, 1964). That dissolved Fe(II) must be oxidized to Fe(III) in order to precipitate as a precursor substance of the BIFs, which could occur wherever oxic waters were supplied (e.g., subglacial meltwater discharges at marine ice grounding lines) or could even be generated by phototrophic bacteria in places of marine environments where ice was cracked or thin (Konhauser et al., 2002; Kappler et al., 2005). These BIF layers were overlain by cap dolostone. The contact between Sturtian glaciogenic deposits, and its cap-carbonates is characteristically singular, smooth, abrupt and conformable (Hoffman et al., 2011), and that is also the case for the parallel-laminated, Fe-rich formations that mark the contact zone at the studied localities.

The paleogeographic rearrangement due to the break-up of Rodinia allowed newly-arranged sea currents to provide an effective source of nutrients, such as Fe and P, to equatorial sea water. As a result, the already existing biodiversity (algae and cyanobacteria) increased and consequently increased the production rate of photosynthetic oxygen (Campbell and Squire, 2010). This process changed the redox state of the ancient oceans and atmos-

phere (Knoll, 2003). Scientists advocate the existence of ice-tolerant biomats during the period of Cryogenian glaciations and compare that with present-day polar ice biota in regions of Antarctica (dominated by, e.g., filamentous cyanobacteria and diatoms; Vincent and Howard-Williams, 2000). The modern-day sea ice biota is dominated by diatoms, and the polar ice shelf communities are dominated by oscillatorian cyanobacteria, a group that is widely distributed in the Archean and Proterozoic fossil records (Vincent et al., 2000; Schopf, 2004).

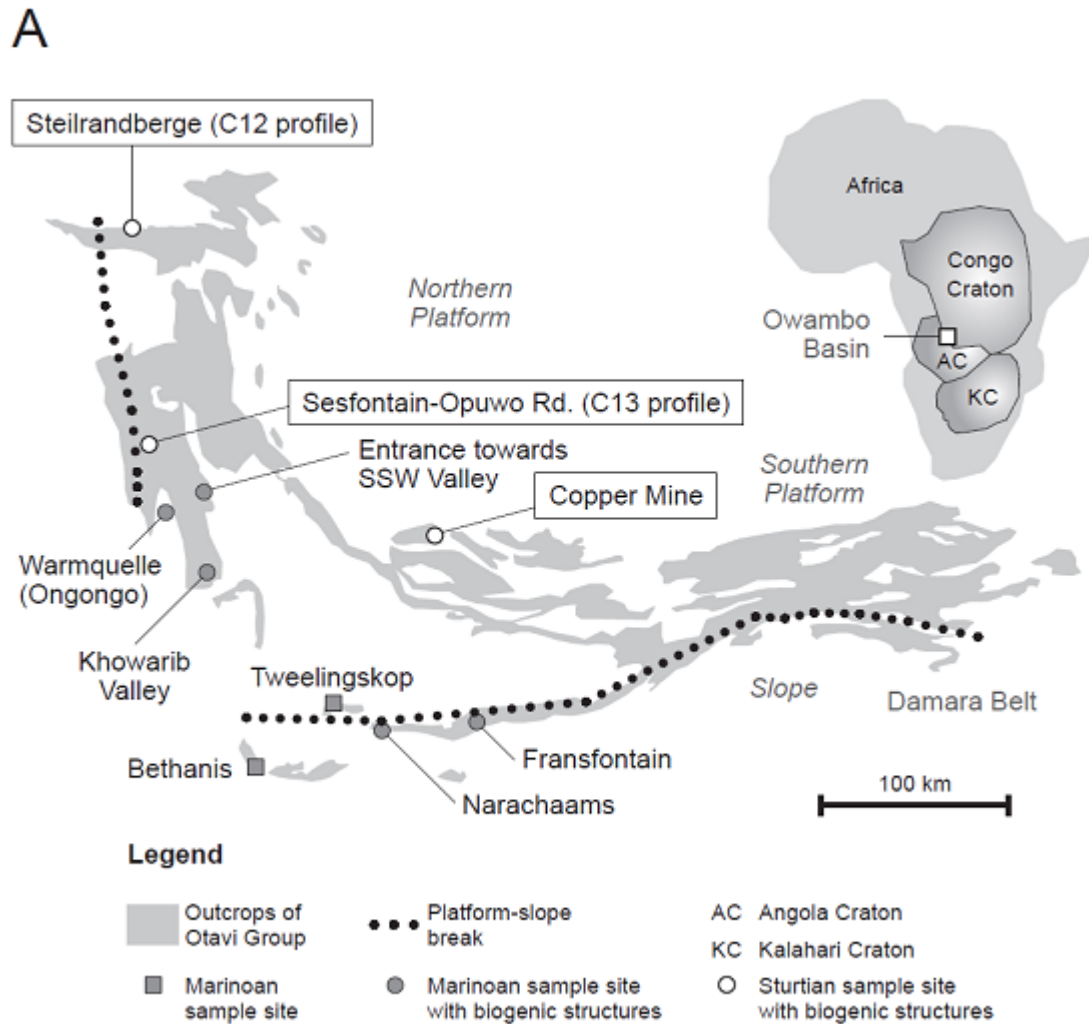
The oldest known microbial mats were discovered in the early Archean (3.2 Ga) Moodies Group, where the organic residue of biomats have biogenic isotopic signatures ( $\delta^{13}\text{C} = -20\text{‰}$ ) closely associated with hematite, goethite and chert (Noffke et al., 2006). Similar structures from the upper Neoproterozoic Nama Group, Namibia, have been described (Noffke et al., 2002). These fossilized biomats, which occur in a higher stratigraphic position (younger occurrence) than our findings, have carpet-like structures and are composed of bacterial cells together with their mucous extracellular polymeric substance (EPS) (Noffke et al., 2003).

We consider the postglacial transition layers (Chuoss Fm. / Rasthof Fm.) of the Namibian Otavi Group as an example of a series of ancient Fe-rich biomats formed at the sediment/water interface. Moreover we emphasize the importance of this mineralized, microbially produced, sedimentary structure system (MMPSS), studied first as microbialite, which offers a novel chance for the estimation of paleoenvironmental conditions and the duration of related sedimentary cycles. Besides we advocate a comparison with rapid, present-day climate change models. Here, we present results and interpretations of our geochemical, microtextural and micromineralogical analysis.

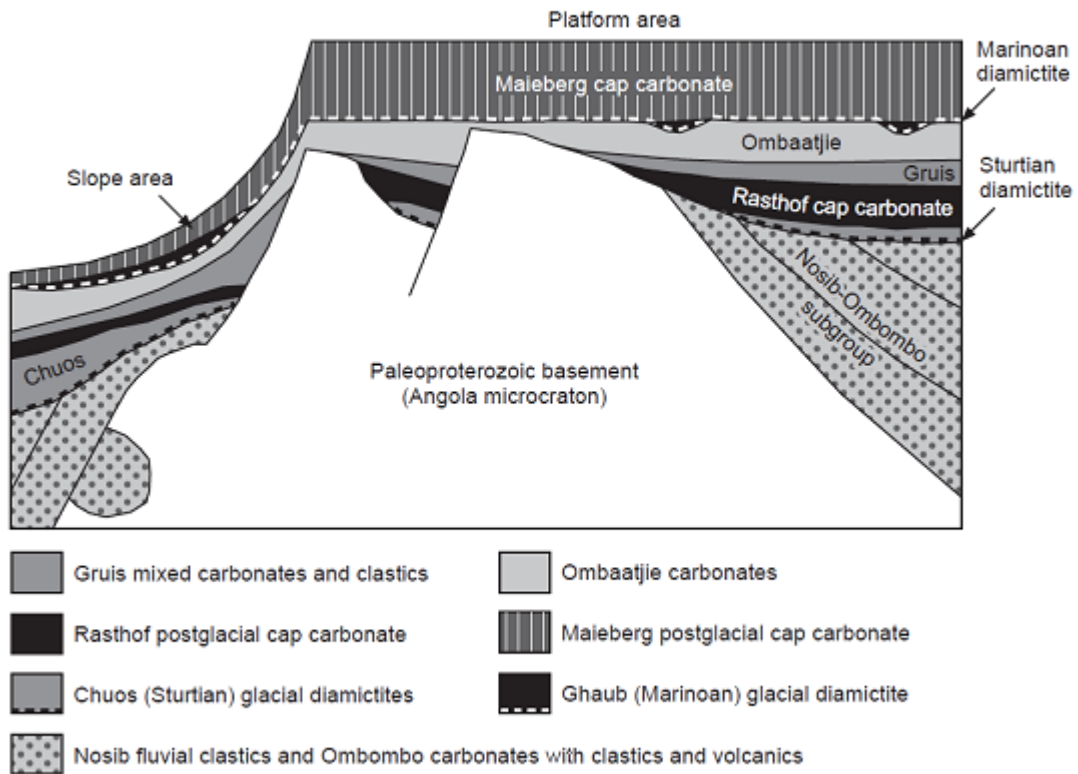
### 3.2 Geological background of sample areas

The Sturtian postglacial transition layer studied here spans the uppermost/lowermost portion of the Chuoss/Rasthof Formation (Fig. 1.). Massive to poorly stratified diamictite is the characteristic lithology of the glaciogenic Chuoss formation, deposited during the initial rifting phase of Rodinia at a paleolatitude around  $35^\circ$  (Christie-Blick et al., 1999; Eyles and Januszczak, 2004). Deposits of the Chuoss Formation are widely exposed throughout the Northern Platform Area, varying both regionally and locally in thickness, being thickest (up to ~1000 m) in paleodepressions and absent on paleo-heights (Martin, 1964). Toward the outer platform edge and foreslope area, the diamictite thins to virtually zero, but accumulates in the foreslope area. The diamictites are interpreted as originating mainly from glacial marine rain-

out deposits formed close to the grounding line of warm-base ice streams (Hoffman and Halverson, 2008).



B



C

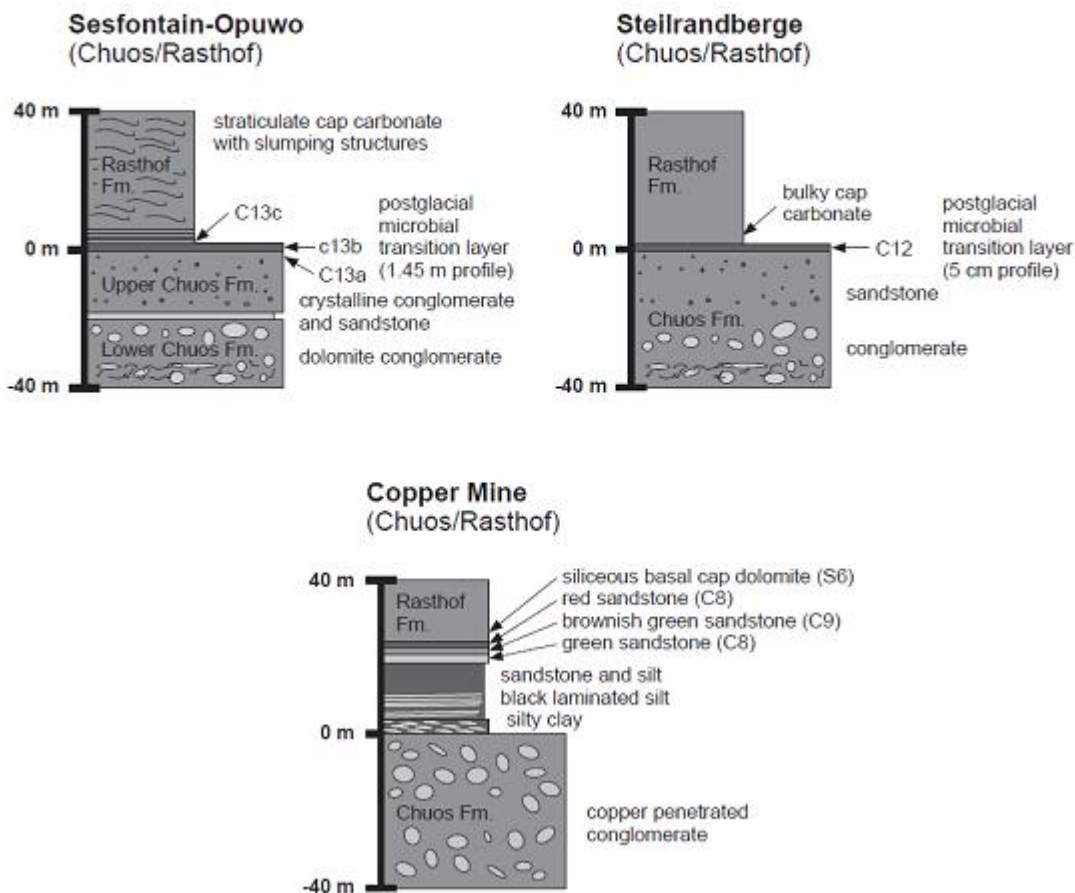


**Figure 1.** Locality map with sampling sites (A) and the stratigraphic development of the Otavi Group (B) (after Hoffman, 2002). (A) The well-developed Fe-rich microbialaminites are located at the Northern Platform (Steilrandberge: C12, Sesfontain-Opuwo: C13). The Marinoan sites contain Fe-rich microstructures only as a single (a few mm) layer within the cap-carbonate. (C) Geological sections of sampling sites, showing postglacial transition layers within upper Chuoss sandstone footwall and Rasthof carbonate hanging wall (after F.Popp's unpublished field data).

At the upper contact of the Chuoss Formation, layers are almost invariably sharp and smooth, being genetically interpreted as an abrupt flooding surface separating the diamictite from the deepwater dolomite rhythmite of the basal Rasthof Formation, which displays no evidence of reworking, subaerial exposure or significant hiatus (Hoffman and Halverson, 2008). However, at our C13 sample locality (Sesfontain-Opuwo Road) the upper part of the Chuoss Formation is composed of siliciclastic, Fe-saturated debris and crystalline pebbles derived from Proterozoic basement source. The outcrop's lower part displays a different composition of carbonate debris- and pebbles eroded from former shelf deposits (Ombombo

Subgroup), hence this depositional trend displays enormous erosive wear of glacier ice in Sturtian times.

The Rasthof Formation, normally 200-400 m thick on the Otavi Platform, has a layer-cake internal stratigraphy comprised of three members termed “abiotic”, “microbial”, and “epiclastic”. The basal “abiotic” member of the Lower Rasthof Formation consists of flaggy, dark gray dolomite and dolomitic limestone, characterized by mm-scale, parallel, turbiditic lamination. Hematite, mobilized from the underlying diamictite, stains the basal few centimeters of the dolomite rhythmite (Hoffmann and Halverson, 2008).

The “microbial” member, which is one focus of this work, may rest directly upon Chuos diamictites in tectonically elevated regions (our samples C13), indicating that the mentioned terms “abiotic” and “microbial” do not represent stratigraphic but facies features. Furthermore, even the “epiclastic” member can be recognized in this tectonically elevated region, thus providing a chance for stratigraphic correlation of time-equivalent facies regions.

Our samples location at Sesfontain-Opuwo Road (Table 1., C13 - 5 samples) stands within an area of the Northern Platform that was affected by tectonic folding of the eastern Kaoko Zone (Fig. 1., Table 1.). At this locality our samples from the transition zone between Chuos diamictites and Rasthof cap carbonates represent the stage of a shallow, fresh- to brackish-water platform-island environment. Field observations indicate that unstratified Chuos diamictites are topped by their own reworked material revealing stratified textures. This trend was detached by the onset of laminated carbonate deposition (based on new field observations by F.P. [2013] in the proximity of the Sesfontain-Opuwo Road locality our C13 samples profile is de facto the lower part of a 1.45 m thick layer). The reworking stage at the diamictite’s top (represented with our samples C13a, b) means that apparently glacial mediated sediment supply ceased (because of vanishing glacier ice) and the sea level increased. Hence the study area was flooded with oversaturated sea water (from upwelling zones) triggering the precipitation of carbonate mud. We consider these specific environmental conditions at the beginning of crustal subsidence/sea level rise being appropriate with respect to the formation of biomats. This assumed glacial transition zone, represented with our samples C13 is obviously stained by iron-saturated fluid migration arising from the underlying Chuos diamictites (iron-oxide mineralization).

Our Steilrandberge locality (Table 1., C12 sample) is situated within the Steilrandberge Syncline of the Northern Platform Area (Fig. 1., Table 1.). Because of its proximal position within the evolving Otavi Platform, the diamictites accumulated reportedly in that area to a thick pile (up to 1000 m) in Chuos times (Hoffman and Halverson, 2008). The transition of these diamictites to a cap-dolomitic layer (sample C12) is the focus of interest in this site.

On the basis of field observations our sample (C12) is a thick bedded, microcrystalline dolomite, indicating its formation within a higher platform-like environment. The sample itself spans the top of the diamictite, as well as the lower part of its cap-carbonate, where it shows signs of diverse putative microbial activity (also Fe-rich forms) from which the most representative presumably microbiolaminite layers are chosen for analysis. Generally, the sampled Fe-rich transition layers (from both the Sesfontain-Opuwo Road and Steilrandberge localities) exhibit continuous and conformable internal parallel laminations hallmarked by sharp basal and upper contacts and variable thickness.

Putative biogenic relicts were also found at our Cooper Mine locality (Table 1., Samples C8, C9, C10). There, intensified debris input (feldspar, quartz, zircon, quartz pebbles, etc.), as well as higher energetic aquatic conditions (oolites), anticipated most likely the development of well stratified Fe-rich layers, but signs of iron-oxidizing bacteria (FeOB) occur as thin biofilms covering ooids and quartz grains. However, the boundary layer of Copper Mine locality (sample C9) does not contain any microbial structures of iron-oxidizing bacteria, hence this iron-rich layer is derived by input of continental weathering, but at the top of diamictite layers (sample C10) FeOB colonies are visible at rims of iron-bearing minerals (e.g., chlorite) originated due to biodegradation. Our samples from the Marinoan postglacial transition layer (Fig. 1.) also exhibit putative microbial structures of iron-oxidizing bacteria (FeOB) and mineral alteration forms, but their preservation state is poor, hence the Marinoan section is not discussed here in detail. As all the studied localities belong to internal platform environments, well-developed biomats may be favored preserved under predominant starving conditions without terrigenous input and a required low energy aquatic system.

**Table 1.** Location and description of samples from Copper Mine (C8-C10), Steilrandberge (C12) and Sesfontain-Opuwo Rd. (C13) localities.

Stratigraphical setting	Sample	Location	Lithology	Mineral composition	Microbial structures
Basal Rasthof Formation	C13c	Sesfontain-Opuwo Road (18°46'26.49"S; 13°45'11.24"E)	Fe-rich microbialite Strong weathering of biogen structures	70 wt% dolomite 30 wt% goethite, hematite, quartz	filamentous (tubular) forms unnamed colonial coccoid cells, and spheroidal unicells
	C8	Copper Mine (9°25'18.43"S; 15° 9'50.90"E)	Oolitic sandstone	carbonate: 75 wt% mica: 8 wt% kali-feldspar: 7 wt% quartz: 10 wt% 5 wt% clay, iron-oxide, zircon, barite	calcification bacterial communities around ooids and oncoids
Chuoss/Rasthof Formation boundary	C12	Steilrandberge (17°47'1.67"S; 13°39'54.10"E)	silt Fe-rich microbialite	70 wt% goethite, hematite, 30 wt% quartz,	filamentous (tubular) forms sheath-enclosed colonial unicells
	C9	Copper Mine (9°25'18.43"S; 15° 9'50.90"E)	Carbonate-quartzite silt	carbonate: 70 wt% iron-oxide: 15 wt% quartz: 10wt% mica: 5wt%	no
	C13b2 C13b1	Sesfontain-Opuwo Road (18°46'26.49"S; 13°45'11.24"E)	Fe-rich microbialite	60-70 wt% goethite, hematite 5-10 wt% dolomite 15 wt% quartz 10 wt% mica	filamentous (tubular) forms unnamed colonial coccoid cells, diatoms (similar to present <i>Navicula</i> ), filamentous cyanobacteria
Chuoss Formation (top)	C13a2 C13a1	Sesfontain-Opuwo Road (18°46'26.49"S; 13°45'11.24"E)	Fe-rich microbialite	50-60 wt% goethite, hematite, 20-30 wt% dolomite, 10 wt% quartz, 5-10 wt% mica	filamentous (tubular) forms unnamed colonial coccoid cells, sheath-enclosed colonial unicells
	C10_2 C10_1	Copper Mine (9°25'18.43"S; 15° 9'50.90"E)	Fine sandstone, segregated terrestrial components in mudstone	carbonate: 40-70 wt% quartz: 10-20 wt% iron-oxide: 10% mica (sericite), chlorite: 5-9 wt% clay: 6 wt% feldspar: 5 wt%	unnamed colonial coccoid cells, sheath-enclosed colonial unicells in recrystallized quartz - filamentous (tubular) forms in iron oxide

### 3.3 Methods

The mineral compositions of the bulk samples were determined by X-ray powder diffraction (XRD) at the University of Vienna. Diffraction data were collected with a Phillips diffractometer (PW 3710, goniometer PW-1820) with CuK $\alpha$  radiation (45 kV, 35 mA), a step size of 0.02 degrees and a counting time of 1 s per step. Minerals were identified using the Joint Committee on Powder Diffraction Standards database (JCPDS, 1980).

Detailed micro-Raman investigation was made on two selected thin sections (C13b2, C13c). A Thermo Scientific DXR Raman Microscope was used, with a 532 nm (green) diode pumped solid-state (DPSS) laser with a Nd-YAG source crystal. Measurements were made under 1.5 mW laser power using a 50x objective lens in confocal mode (confocal aperture 25  $\mu$ m slit). The acquisition time was 1 min and the spectral resolution was  $\sim 2$   $\text{cm}^{-1}$  for each measurement (Szeged University, Hungary). The distance between two measured points was 50  $\mu$ m. Raman spectra acquired for samples were organized into diagrams (n: 1032). 372 spectra were acquired in sample C13b2 and 660 spectra were acquired in sample C13c.

Petrographic structural-textural studies were undertaken using five oriented (bottom and top of sequence position) thin sections using a NIKON ECLIPSE 600 optical petrographic microscope in Budapest, Hungary.

### 3.4 Results

The oriented samples macroscopically resemble series of Fe-rich biomats occurring as millimeter-scale microbiolaminite (Fig. 2A, B). No signs of erosion or any other hiatus were observed in the studied profile. The light and red laminae are variable in thickness and frequency of occurrence; however, they define a more or less regular, millimeter-scale rhythmic lamination in the samples. The thin sections show a fabric-like lacework texture within the very fine-grained dolomite and quartz matrix, described as an interwoven, filamentous meshwork. The range of thicknesses of the mineralized filamentous structures is approximately 1-10  $\mu$ m (Fig. 2C). The filaments are capped by a homogeneous mineral covering, generally goethite and rarely hematite, according to the Raman analyses. Solitary carbonate clusters and quartz matrix material float or are embedded within the laminated matrix without grain-to-grain contact. These intervals show diffuse contacts. The biomats are often so intense that they form an opaque mineralized segment (Fig. 2B). The matrix of the goethite and hematite structures consists of dolomite and/or quartz and organic matter as the main components. Filamentous (tubular) forms of unnamed colonial coccoid cells, sheath-

enclosed colonial unicells and spheroidal unicells also occur in the sections (Fig. 2C). Presence of cyanobacteria support shallow water conditions (Fig. 2C). Bulk sample XRD analyses of six samples indicate dolomite, calcite, goethite, hematite, quartz, and mica (muscovite) as the main minerals.

The distribution of minerals according to profiles was determined based on high-resolution micro-Raman analyses. The main components detected (dolomite, quartz, calcite, goethite, hematite, and carbonaceous material) were used for further investigations. The distribution of carbonaceous material in the samples is inhomogeneous, often occurring as patches. Occasionally, pyrite ( $\mu\text{m}$ -size) with organic matter, apatite, rutile, anatase, quartz (matrix material and very rarely debris), and feldspar (debris-very rare) were also detected. Muscovite occurs in smaller-larger quartz enrichments. Rutile and anatase belong to quartz-rich goethitic parts, whereas apatite occurs in goethite-rich parts of iron stromatolite-like microbial structures. Raman spectra allowed the identification and distribution of microbially mediated minerals (goethite and hematite, formerly ferrihydrite) in samples C13b2 and C13c.

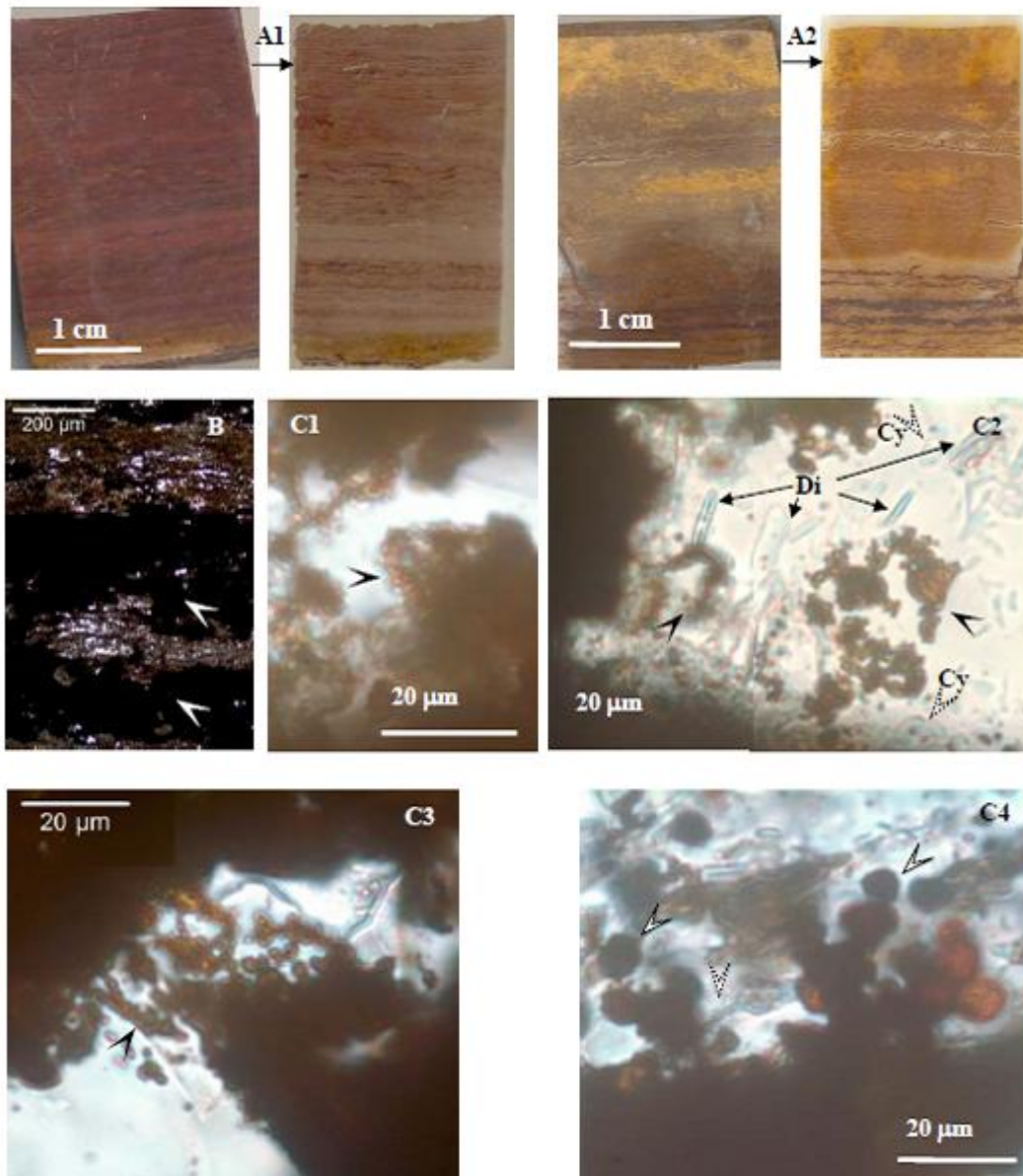
Sample C13b2 reveals a strongly mineralized series of Fe-rich laminae (assumed biomats) in a matrix of quartz and C13c represents the basal transition to the local cap dolomite lithology (Fig. 3). Our calculation of the supposed Fe-biomaat laminae was made by visual counting. Thin section C13b2 represents both thinner (100-200  $\mu\text{m}$ ) and thicker Fe-rich laminae (up to  $\sim 1$  mm, Fig. 3A). The thinner ones are more common. Some biomaat layers contain only goethite or hematite, whereas others contain both minerals. Thicker goethitic biomats occur in the lower part of section 2 and the top of section 3. The abundance of carbonaceous material was not determined in the studied sections, but small patches of organic material are present in the sample. Calcite is rare, mostly occurring in the form of debris material. Visual counting resulted in 100 laminae in the thin section (18.5 mm thick). Using this number, the average thickness of the layers is 185  $\mu\text{m}$  (which we rounded to 200  $\mu\text{m}$  for easier calculations).

The distribution and intensity of the laminae in the C13c thin section is variable (Fig. 3B). The lower part of section 1 shows weak authigenic dolomite formation and very intense Fe-rich biomaat series (less than 3 mm thick). The dolomite precipitation then increased, resulting in less intense mat formation. Irregular intensity changes characterize the biomaat-dolomite formation in the upper part of the thin section. Their thickness variation is approximately 100-200  $\mu\text{m}$  in all sections studied by Raman spectrometry, resulting in 165 laminae within the 33-mm-thick section. Thus we assume an average thickness of 200  $\mu\text{m}$  for this section, too.

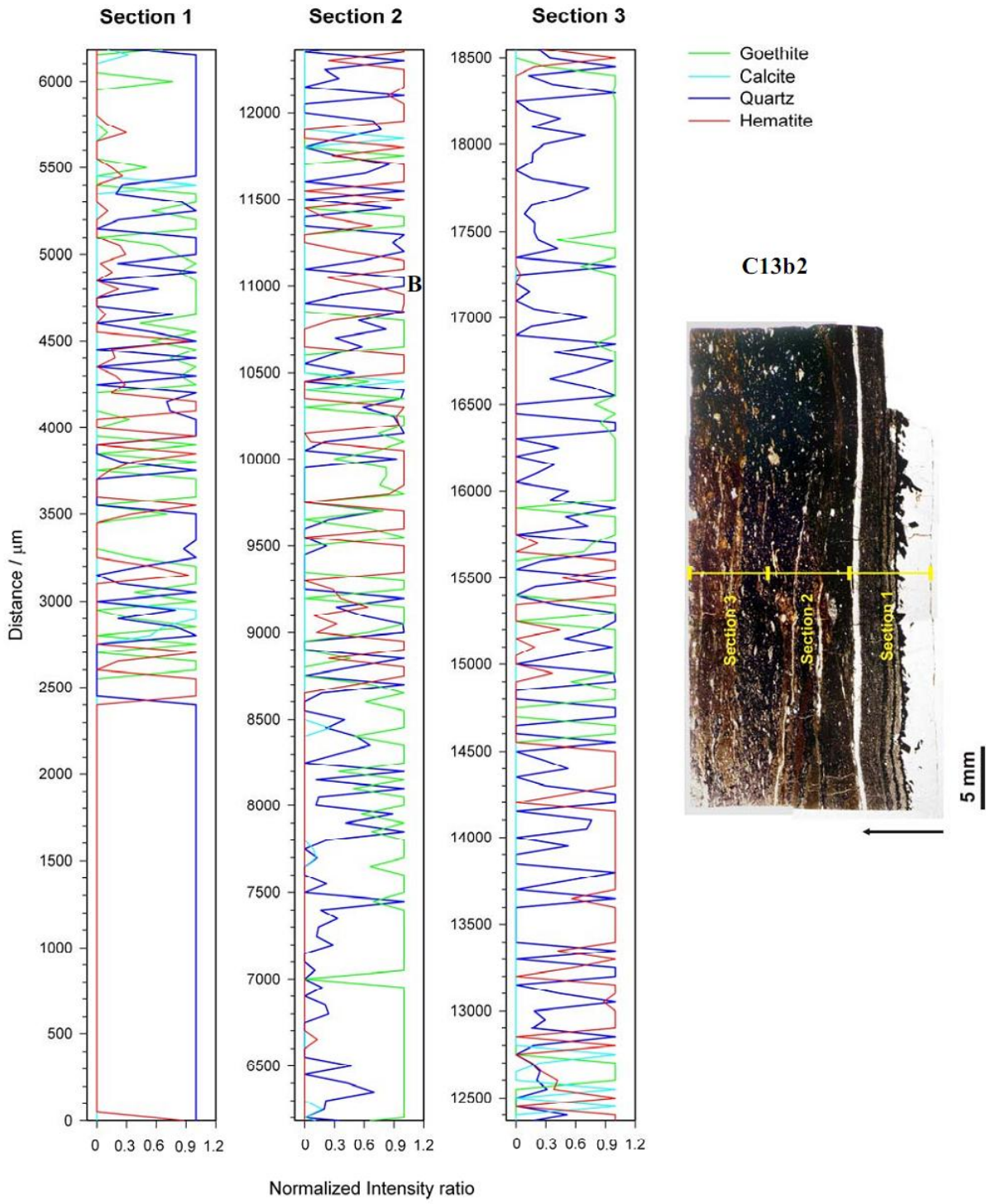
## 3.5 Discussion

### 3.5.1 Synsedimentary Fe-rich biomat formation

The geological record of Neoproterozoic Snowball Earth glaciations in general consists of glacial diamictites, which can contain and/or can be followed by a postglacial transition layer, at its basis rich in Fe/Fe-Mn oxide-clay, and finally covered by thick cap carbonate (Hoffman et al., 2011, e.g., Doushantuo Fm. (China), Rapitan Group (Canada), Jacadigo Group, Brazil). This widespread cap carbonate formations are well studied and microbial contribution in their genesis is generally accepted (Fraiser and Corsetti, 2003). Contrary, only rare information can be found on microbial mediation of the Fe-rich postglacial transition layer (Pruss et al., 2010). In our sections the Sturtian diamictites are followed by Fe-oxide-rich postglacial transition layers and identifying it for the first time as a fossilized biomat is a basically new observation. This study does not support the previously suggested hypotheses, including: (i) leaching/weathering product of diamictite (Hoffman et al., 1998; Hoffman and Schrag, 2002); (ii) extraterrestrial a) extraterrestrial dust (Bodiselsch et al., 2005), b) impact ejecta (Koeberl et al., 2007); (iii) chemical sediments a) ferrous vs. euxinic anoxia, b) subglacial, sulphate-rich ferrous waters and c) localization of oxidative titration (Hoffman et al., 2011). Optical microscopic investigations (textural and mineralogical) confirmed that our Sturtian transition layer of Steilrandberge (C12) and Sesfontain-Opuwo (C13) sections are not weathered or condensed ones. A condensed section contains non-depositional surfaces, and on that surfaces some erosional features, or, e.g., in case of microbial activity (which occurs at the sediment/water contact zone) would end in a dense border, because with time, open spaces are filled with minerals. Weathered sections would contain altered minerals; clay minerals also indicate diagenesis and/or alteration, but in the studied sections they do not occur, thus the samples do not show any indication of weathering. In the case of our samples, authigenic mineralization took place together with microbial mineralization (quartz and carbonate) which suggest a special type of accumulation. Microbes living in the solution (aquatic environment) were mineralized and matrix minerals were precipitated in intimate connection with microbes, which preserved in a very fine structure (authigenic mineralization). The complex microtextural features (filamentous forms with inner globular fine texture) also exclude inorganic chemical precipitation (Liesegang banding).



**Figure 2.** Polished sample and thin section photos showing Fe-rich biomat structures (goethite and hematite) for different representative samples (C12; C13a1, C13b1, C13b2, C13c) and magnifications (the density of the biomats is variable). (A1-A2) Photos of polished surfaces of samples and thin sections, arrows show from polished surfaces to thin sections; (A1) sample C13c, (A2) C12; (B) Section of Fe-rich biomat, thin section photo, 1N, sample C12, arrows show opaque mineralized segments; (C1-C4) Fe-rich mineralized filamentous (tubular) microbial forms (black arrows), unnamed colonial coccoid cells, spheroidal unicells, sheath-enclosed colonial unicells (white arrows), (C1) -sample C12, (C2) C13a1, (C3) C13b2, (C4) C13b1; Di on C2 indicates silica-bearing fossils; Cy indicate cyanobacteria; the matrix material is quartz, dolomite and hydromuscovite, thin section photos, 1N.



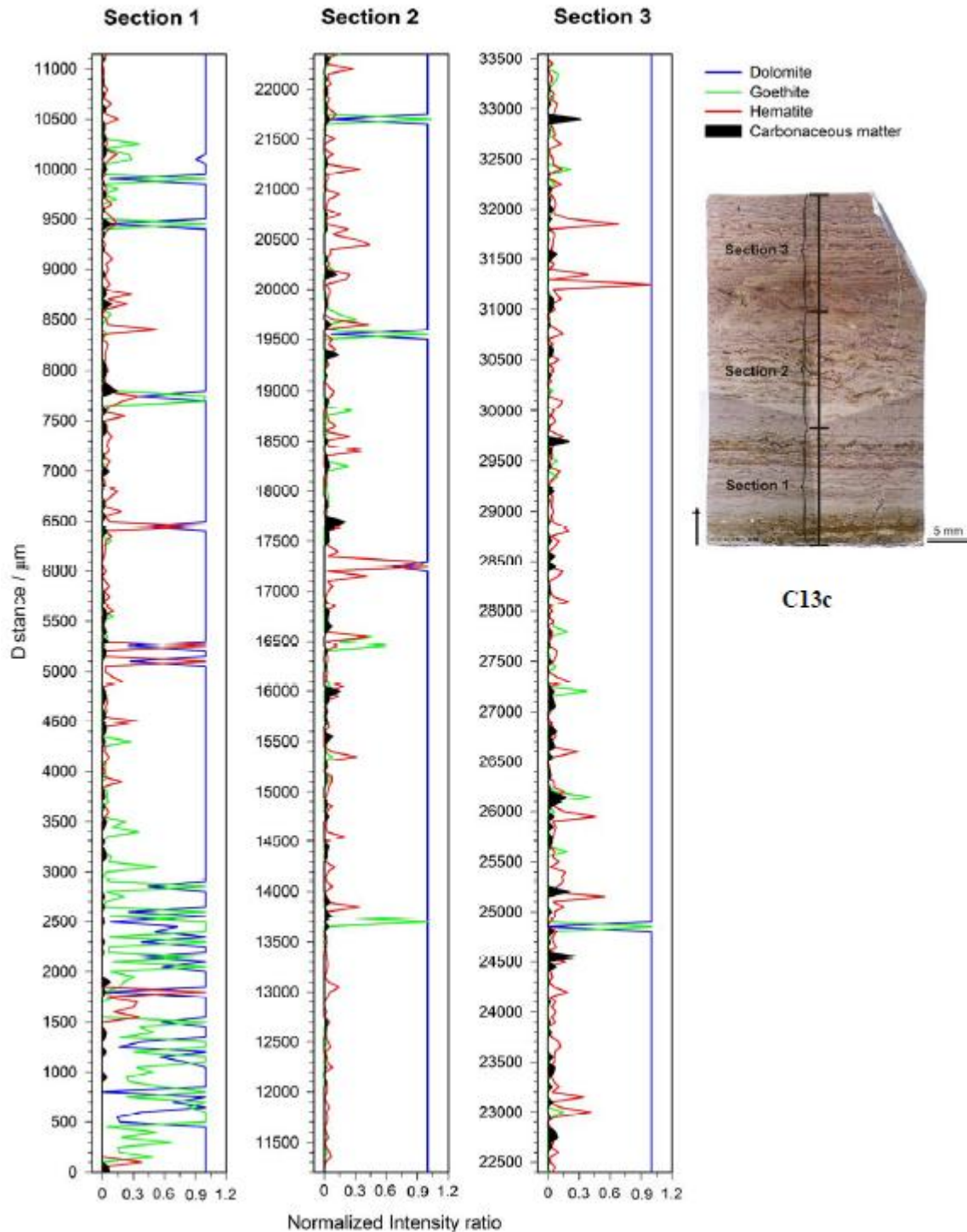


**Figure 3.** Composite images of C13b2 (A) and C13c (B) oriented thin sections with bands (1-3) of Raman microscopy measurements. The distance between two measured points is 50  $\mu\text{m}$ ; Diagrams of relative peak height ratio vs the analytical spot number of each of the 6 phases along the Raman scanned section of the C13b2 and C13c thin sections. Intensity ratios are normalized to the highest peak for each spectrum. The following Raman bands were used for normalization: goethite:  $390\text{ cm}^{-1}$ ; hematite  $\sim 225\text{ cm}^{-1}$ ; quartz:  $\sim 463\text{ cm}^{-1}$ ; carbonaceous matter:  $\sim 1586\text{ cm}^{-1}$ ; dolomite:  $1097\text{ cm}^{-1}$ ; calcite:  $1088\text{ cm}^{-1}$ . Number of total Raman spectra: 372 (C13b2) and 660 (C13c).

In the vicinity of our sample localities the sedimentary environment was dominated by a continental rift setting giving rise for a considerable topographic relief above and below sea-level locally holding domains, with fresh- to brackish-water. We consider that transportation and deposition of massive diamictite material required powerful media such as glacier ice or melt-water rivers, both providing tight influence concerning the water composition within that regions. The reported iron-rich straticulate sedimentary structures formed temporally representing initial sea ice deglaciation as a consequence of melting glaciers. We assume that a photosynthetic zone existed during the formation of the mentioned postglacial transition layer, which may have been rich in cyanobacterial activity at the sediment/water interface. This environmental assessment is suggested by the observed organic matter distribution in the measured sections of Sturtian transition layers from Sesfontain-Opuwo and Steilrandberge localities and by diverse putative microbial textures, among them features of Fe-free filamentous microbes (Fig. 2C). First of all, we study only the case of the above-mentioned Fe-rich biomat formation for the purpose of their paleoenvironmental interpretation. Then we try to estimate the time necessary for the upgrowth, as it is supposed that MMPSS play an important role in paleoenvironmental considerations.

The basic aim is to confirm the existence of Fe-oxidizing bacteria forming Fe-rich biomats in the samples. The presence of Fe-rich biomats is indicated by textural evidence (Fig. 2C), homogeneous Fe precipitation along the filaments that build a 3D network, which is a robust biosignature (Chan et al., 2011). Understanding the biochemistry of biomat formation is key for determining the type of Fe-rich biomats that may have been involved with the formation of the samples lithology and thus are defining the suspected environmental conditions. There are four types of microbial metabolism that can oxidize  $\text{Fe}^{2+}$  forming Fe-oxide minerals (Konhauser, 1998). The first type of the microbial Fe(II) metabolisms is acidophilic and oxic, the occurrence of which in shallow fresh- to brackish-water conditions is unlikely. A second type of microbial Fe(II) metabolism is driven by light, anoxic/anaerobic, and neutrophilic (photoferrotroph); a condition that is not supported by the mineralogy. The third type is suboxic/anaerobic, where neutrophilic  $\text{NO}_3$  reducers coupled with Fe(II) oxidizers probably contributed to the biochemical milieu, but morphological features do not support this metabolism as main process in biomat formation. The formation conditions were thus most likely governed by the fourth type, namely suboxic and neutrophilic *Gallionella*-like Fe-oxidizing microbes. Non-enzymatic reactions provide an indirect role for bacteria in the oxidation of Fe. As a result of microbial activity, chemical conditions (Eh, pH) are changed in the vicinity of the cells, favoring the chemical oxidation of Fe. Non-Fe-oxidizing microbes may have been the sole microbiota involved in mat formation. The main difficulty with this scenario, however, is the uniformity of the Fe lacework structures throughout the section, which would not be expected to form from inorganic processes.

Thus, two types of Fe-rich biomats are considered as possibilities for what we observe in our samples, all of which are neutrophilic and consistent with shallow fresh- to brackish-water conditions: (1) *Gallionella*-like microbial neutrophilic microaerobic Fe<sup>2+</sup>-oxidizing bacteria with photosynthetic metabolism (Konhauser, 1998); (2) *Gallionella*-like non-photosynthetic neutrophilic microaerobic microbial Fe<sup>2+</sup>-oxidizing bacteria (Hallbeck and Pedersen, 1990; Konhauser, 1998). Of the two types of microbial Fe<sup>2+</sup> oxidation, photosynthetic metabolism produces a daily rhythmicity with growth only during daylight. Biomat growth at the sediment/water interface would have been in competition with authigenic sediment formation. Alternatively, non-photosynthetic microbial Fe<sup>2+</sup>-oxidizing bacteria can also produce rhythmic developmental stages via existing as free-living Fe<sup>2+</sup>-oxidizing bacteria in the lag and log phases, and stalk formation (Fe-rich biomat) during the stat phase under optimal conditions.\*

For *Gallionella*-like freshwater and *Mariprofundus*-like marine types, 1–3 weeks (7–21 days) of whole microbial population growth is reported based on laboratory experiments, and natural observations (Hallbeck and Pedersen, 1990; Chan et al., 2011; Polgári et al., 2012). Microbial mats always form at the sediment/water interface or very close to it (within a few cm), and this fact excludes that these microbial mats formed long after the sediments were deposited; thus they are synsedimentary formations that have important roles in paleoenvironmental interpretation. The Raman spectra indicate the presence of organic matter in the goethite-hematite lacework (Raman shifts at 1000-2000 cm<sup>-1</sup>); even though the data are not diagnostic regarding the exact type of organic matter (biomarkers), a biogenic origin of our samples is supported. The microtextural evidence and the fine-grained authigenic dolomite support a suboxic and neutrophilic environment. Debris did not dilute the sediments, and Fe precipitation in mats via redox interfaces can be excluded based on textural evidence (Gerdes, 2007). Increasing biomat condensation and 3D mats relate to sediment starvation (lower intensity of authigenic mineralization; Gerdes, 2007). Starving sedimentary conditions are supported by authigenic carbonate (dolomite) formation, in which debris (quartz, feldspar) is rare. Starving conditions support the formation of well-developed mats generally within 1-3 weeks (Gerdes, 2007), which support our interpretation. Authigenic dolomite formation is supported by a fresh- or brackish-water environment (marine sulfate inhibits the binding of Mg to carbonate) and slightly negative  $\delta^{13}\text{C}$  values because of the organic matter-rich environment. The dolomite precipitation most likely occurred via microbial mediation (Hoffman et al., 2011). The carbonate is Fe-free, which supports the lack of diagenetic Fe

---

\* Microbial population growth phases are the following: (i) *lag phase*: bacterial adaptation; (ii) *log* (logarithmic) *phase*: a period characterized by cell doubling with exponential growth; (iii) *stationary (stat) phase*: the growth rate slows as a result of nutrient depletion and accumulation of toxic products; (iv) *decline (dec) phase*: closes the growth period (exponential death phase), bacteria succumb to their own wastes (but endospores survive), and the cycle starts again (Novick, 1955; Zwietering et al., 1990).

reduction as a main process. Locally very fine-grained pyrite in quartz was observed together with organic matter and most likely formed by decay from the sulphur in organic matter. Annual, seasonal rhythmicity can be excluded because the weather conditions during biomat formation were in the freezing to just thawing range.

### 3.5.2 Diagenesis of Fe-rich biomats

According to the diagenesis of Fe-rich biomats, the microbes produce poorly ordered ferrihydrite as a primary mineral, which transforms to more ordered minerals, such as goethite or hematite, within a few months or years via dissolution-dehydration processes (Konhauser, 1998; Schwertmann and Cornell, 2007). The main Fe oxide mineral in the filaments of our samples is goethite, but Raman analyses indicate that hematite also occurs. The fossilized Fe-rich biomats were rapidly and extensively encrusted by authigenic minerals, such as dolomite and silica, similarly to what has been reported by Baele et al. (2008). The amorphous silica can easily transform into more stable minerals, such as cristobalite, tridymite, and quartz (Herdianita et al., 2000). Silica precipitation is derived by either the destruction of organic complexes or the transformation of ferrihydrite (Baele et al., 2008). Apatite can be precipitated under a pH of 7-8 and occurs in micrometer-sized crystals in the silica-rich part of BIFs. Similar apatite occurrences were noted in our samples, based on Raman analyses. Muscovite (hydromuscovite) is common in the studied samples and was most likely formed by the diagenesis of cyanobacteria filaments in Fe-rich microbialites by the leaching of biofilm alkali (Na, K, Al, Mg) (Ewers, 1983).

The organic matter was preserved in the sediment because of the (i) intense authigenic carbonate and Fe oxide mineralization and (ii) the absence of oxidizing agents in the matrix material (absence of Fe reduction because of the stabilization of primary ferrihydrite). The maturation degree of the organic matter is variable in the samples. The sediment formed under suboxic conditions, which later did not turn anoxic. The microbial Fe oxidation ended toward the onset of cap carbonate precipitation, which most likely is due to (i) the elimination of the Fe supply and (ii) the change from suboxic to oxic conditions.

### 3.5.3 Constraints on sedimentation rates

So far the timescales for Cryogenian deglaciations have been only specifically abiogene-targeted in climate modeling up to thousand and million years:  $10^4$ - $10^5$  yr (Hoffman et al., 2007),  $10^3$  yr (Hyde et al., 2000),  $10^4$ - $10^5$  yr (Le Hir et al., 2009; Font et al., 2010). In contrast, longer deglaciation times ( $10^5$ - $10^6$  yr) were proposed by, e.g., Trindade et al., (2003); and Raub et al. (2007). The above-mentioned models are based on meteorological simulations,

abiogenic precipitation of cap carbonate, geochemical studies, or weathering processes. We propose that cap carbonates as a whole formed after the main deglaciation process and the Fe-rich microbialites emerging at their basis in the studied localities represent the immediate beginning of the deglaciation process. Below the Fe-rich biomat layer is the uppermost part of a diamictite unit, which is thought to be deposited from glacier ice or meltwater flows in the course of an entire glacial stage during the Cryogenian period, but in any case the onset of these layers marks the cessation of glacially mediated sedimentation processes. The continuously overlying formation is a ~40-m-thick pile of cap-carbonate, which did start with freshwater to brackish environmental conditions at its very base, but now alter to marine conditions caused by an increasing sea level due to the input of melting inland glacier ice. We suggest that the assumed biogenic-mediated deposition of layers represent distinct chronological periods, thus our results may help with the (local) estimation of postglacial sedimentation rates.

Recent iron-rich biomat formations beneath the sea ice (*Gallionella* with diatoms, and cyanobacteria) at the Earth's polar regions may be a clue that iron favoring biomats possibly have formed during the deglaciation after each glacial stage of the Snowball Earth's period (Vincent and Howard-Williams, 2000). Nevertheless, deglaciation histories suggest that Sturtian and Marinoan ice sheets disappeared rapidly (Hoffman et al., 1998). Based on recent analogs and accumulation rate studies on the Marinoan cap carbonate, the deglaciation took place over a period of several thousand years (Castanier et al., 2009; Font et al., 2010; Hoffman et al., 2011).

In case of our Sturtian postglacial transition layer samples, microbial layers (series of Fe-rich biomats) were used for the estimation of sedimentation rates at the very beginning of an environmental change due to vanishing sea-glacier ice. Assuming that biomineralization occurs only during some phases of microbial growth, the microbial layering can be used as a time scale (Polgári et al., 2012). Our samples display Fe-rich laminations, suggesting FeOB activity during their deposition. On the other hand, the proposed FeOB occurrence indicates that we need to consider microbial characteristics, such as microbial population growth cycles (in the form of mineralized microbial layering).

The proposed *Gallionella*- or *Mariprofundus*-type Fe-oxidizing bacteria form stalks (filamentous form) (Fe-rich biomats - biomineralization) only during the stat phase of microbial growth cycle and under optimal conditions, producing rhythmic developmental stages via existing, free-living Fe<sup>2+</sup>-oxidizing bacteria (without mineralization) in the lag and log phases. The mineralized horizons of the Fe-rich biomat represent distances in the sediment that can be measured on micrometer to millimeter scales, explaining how the mineralogical/geochemical composition of these layers can be converted into chronological information. In the layers we consider only the Fe-oxide phase resulting from biomineralization in our cal-

culations. We did not find any evidence for annual lamination, such as rhythmic debris contribution or other mineralogical differentiation. Microbial activity cycles are of much shorter duration (only minutes, days, weeks).

The laminations visible in our samples comprise Fe-rich mineralized parts and less or non-mineralized parts following each other. Naturally, the laminae are not regular in any physical, mathematical, or chemical sense, because many factors influence the microbial metabolism and the 3D filamentous network, but macroscopically they show rhythmicity on a mm-scale. Measuring the length of the mineralized and non-mineralized laminae, the number of laminae can be counted in the studied layer, which is ca. 1.45 m thick in the proximity of the C13 locality, thus providing a basis for our calculations.

The lamina thicknesses in the two measured sections are similar on average (200  $\mu\text{m}$ ). Extrapolating the lamina frequency to the whole postglacial transition layer (1.45 m), the estimated number of laminae is 7,250.

The Fe-oxidizing bacterial activity could be driven by light (supported by shallow water conditions) as photosynthetic metabolism; hence the laminae could represent a daily cycle, and, thus represent a minimum estimation for the sediment accumulation of the 1.45-m-thick postglacial transition layer of 7,250 days (18 years). In the Neoproterozoic period the length of years was 400-430 days and the length of days was 22 hours (Williams, 2000), but here we use an average 400 days/year and 22 hours/day.

Otherwise the maximum estimation is a three-week (21 days) duration of the microbial population growth period of non-photosynthetic Fe-oxidizing bacteria, giving a total of 152,250-days (381 years) required for the accumulation of our 1.45 m thick section. Even at the upper range of our estimate, this is a very rapid timescale for deglaciation as represented by the thin Fe-rich postglacial transition layer, and about one tenth of even the shorted estimate mentioned above ( $10^3$  yr, Hyde et al., 2000). The postglacial transition layer does not show evidence for erosion or another hiatus, or other annual or seasonal rhythmicities that could be explained by long-lasting freezing-melting conditions.

At our C13 locality the 1.45-m-thick pile of microbially mediated layers are concordantly overlain by 4 m of thin-bedded planar grain flow deposits. Their successive hanging wall grain flow deposits exhibit sedimentary slumping structures within a ~ 40-50 m thick rock sequence. We suggest that this observed sedimentary trend was caused by a gradual, tectonically mediated subsidence of the region. Consequently the environmental conditions of the mentioned microbial layers formation may have been explained by beginning of cap carbonate formation and deglaciation duration. Cap carbonates are generally divided in lower cap dolostone and an upper cap limestone (e.g., James et al., 2001, Hoffman and Schrag, 2002), which implies a non-uniform process of cap carbonate deposition. We propose that the studied putative biolites represent the onset of deglaciation, i.e., the rapid floating sea-ice

collapse in the initial deglaciation phase. There are indications that the Cryogenian glaciations had not much disastrous influence on biota (e.g., Gaidos et al., 1999; Olcott et al., 2005; Corsetti et al., 2006; Moczyłowska, 2008). The refugia for life during Snowball Earth glaciations are still debated, but photosynthetic life might have survived in some ice-free areas (e.g., Le Heron, 2012) or on/in ice as photosynthesis in several meter thick permanently ice-covered Antarctic lakes is known (e.g., Hawes and Schwarz 1999). Melting of sea-ice does not induce sea-level rise and would give microbial organisms the opportunity to growth on hard substrate. Former biofilms under thin ice locations and cryoconites (McMenamin, 2004 and references therein) could now flourish on the continental shelf areas or inland seas. According to Kasemann et al. (2010), the paleoenvironmental conditions during the Sturtian were different from those of the Marinoan; i.e., no extreme pH of the ocean and no elevated  $p\text{CO}_2$  at the glaciation and deglaciation time, providing adequate conditions for neutrophilic microbial mats. The duration of continental ice deglaciation, or melting of ground ice, which would have diminished microbial induced sedimentation layers, is not constrained by our study.

### 3.6 Conclusions

We present the first identification of mat forming filamentous Fe-oxidizing bacteria in the Sturtian postglacial transition layer. The existence of Fe-oxidizing bacterial mats suggests a basically different paleoenvironment (suboxic, neutral) than what was considered for similar widespread Fe-microbialites earlier (anoxic, photoferrotroph, acidophilic microbes). The Sturtian (sea-ice) deglaciation process happened extremely rapidly during deposition of this very thin but important transition layer (few hundred years) based on mineralized bacterial layering.

These results allow comparisons with other Sturtian and Marinoan Fe-bearing layers of variable geological settings and also concerning the paleoenvironmental conditions and the duration of the transition layers formation. It is proposed that the Fe-bearing transitional layer represents the beginning of the deglaciation period. At other localities it can give information on the duration of the formation of Fe-bearing layers.

### 3.7 Acknowledgements

This research was supported by the Geological Survey of Namibia, for which we are extremely grateful. We acknowledge Director Dr. G. Schneider for her important help related to field work organization and sample export management. We are grateful to colleagues at the University of Vienna who assisted with the analytical work, especially Susanne Gier (XRD),

Peter Nagl (XRF), and Patrick McDonald (XRF). We appreciate the help of the reactor team of the “Atominstitut”, Vienna, with the irradiations. This study was supported by the Austrian Academy of Sciences through a grant to CK (International Geological Correlation Programme IGCP No. 512).

### 3.8 References

- Arnaud, E., Halverson, G.P., Shields-Zhou, G., 2011. Chapter 1 The geological record of Neoproterozoic ice ages. Geological Society, London, Memoirs, 36/1, 1-16.
- Baele, J.-M., Bouvain, F., De Jong, J., Matielli, N., Papier, S., Prat, A., 2008. Iron microbial mats in modern and Phanerozoic environments. Proc. Soc. Phot. Instr. Eng., 7097, 70970N-70970N-12.
- Bodiselič, B., Koeberl, C., Master, S., Reimold, W.U., 2005. Estimating duration and intensity of Neoproterozoic Snowball glaciations from Ir anomalies. Science, 308, 239-242.
- Campbell, I.H., Squire, R.J., 2010. The mountains that triggered the Late Neoproterozoic increase in oxygen: The second great oxidation event. Geochim. Cosmochim. Acta, 74, 4187-4206.
- Castanier, S., Le Métayer-Levrel, G., Perthuisot, J.-P., 2009. Ca-carbonates precipitation and limestone genesis — the microbiogeologist point of view. Sedim. Geol., 126, 9-23.
- Chan, C.S., Fakra, S.C., Emerson, D., Fleming, E.J., Edwards, K.J., 2011. Lithotrophic iron-oxidizing bacteria produce organic stalks to control mineral growth: implications for biosignature formation. Multidisciplinary Journal of International Society for Microbial Ecology, 5, 717-727.
- Christie-Blick, N., Sohl, L.E., Kennedy, M.J., 1999. Considering a Neoproterozoic Snowball Earth. Science, 284, 1087-1087.
- Corsetti, F. A., Olcott, A. N., Bakermans, C., 2006. The biotic response to Neoproterozoic snowball Earth. Palaeogeogr., Palaeoclimat., Palaeoecol., 232, 114-130.
- Ewers, W.E., 1983. Chemical Factors in the Deposition and Diagenesis of Banded Iron-Formation, in: A.F. Trendall and R.C. Morris (Eds.), Developments in Precambrian Geology, Vol. 6, Iron formation: Facts and Problems. Elsevier, pp. 491-512.
- Eyles, N., Januszczak, N., 2004. "Zipper-rift": a tectonic model for Neoproterozoic glaciations during the breakup of Rodinia after 750 Ma. Earth-Sci. Revs., 65, 1-73.
- Fairchild, I.J., Kennedy, M.J., 2007. Neoproterozoic glaciation in the Earth System. J. Geol. Soc. Lond., 164, 895-921.

- Font, E., Nédélec, A., Trindade, R.I.F., Moreau, C., 2010. Fast or slow melting of the Marinoan snowball Earth? The cap dolostone record. *Palaeogeogr., Palaeoclim., Palaeoecol.*, 295, 215-225.
- Fraiser, M.L., Corsetti, F.A., 2003. Neoproterozoic carbonate shrubs: interplay of microbial activity and unusual environmental conditions in post-Snowball Earth oceans. *Palaios*, 18, 378-387.
- Gaidos, E.J., Neelson, K.H., Kirschvink J.L., 1999. Life on ice-covered oceans. *Science*, 284, 1631-1633.
- Gerdes, G., 2007. Structures left by modern microbial mats in their host sediments. In: Schieber, J., Bose, P.K., Eriksson, P.G., Banerjee, S., Sarkar, S., Altermann, W., Cătușeanu, O. (Eds.) *Atlas of Microbial Mat Features Preserved within the Siliciclastic Rock Record*. Elsevier, pp. 5-38.
- Hallbeck, L., Pedersen, K., 1990. Culture parameters regulating stalk formation and growth rate of *Gallionella ferruginea*. *J. Gen. Microbiol.*, 136, 1675-1680.
- Harland, W.B., Rudwick, M.J.S., 1964. The great infra-Cambrian ice age. *Scientific American*, 211, 28-36.
- Hawes, I., Schwarz, A.M., 1999. Photosynthesis in an extreme shade environment: benthic microbial mats from Lake Hoare, a permanently ice-covered Antarctic lake. *J. Phycol.*, 35/3, 448-459.
- Herdianita, N.R., Browne, P.R.L., Rodgers, K.A., Campbell, K.A., 2000. Mineralogical and textural changes accompanying ageing of silica sinter. *Miner. Deposita*, 35, 48-62.
- Hoffman, P.F., 2002. Carbonates bounding glacial deposits: Evidence for Snowball Earth episodes and greenhouse aftermaths in the Neoproterozoic Otavi Group of northern Namibia. *Excursion Guide, 16th International Sedimentological Conference, Auckland Park, South Africa*, 39 pp.
- Hoffman, P.F., Halverson, G.P., 2008. Otavi Group of the western Northern Platform, the Eastern Kaoko Zone and the western Northern Margin Zone. In: Miller R.M. and Becker, T. (Eds.) *The Geology of Namibia: Neoproterozoic to lower Palaeozoic*. Vol. 2, *Geological Survey of Namibia (Windhoek)*, pp. 69-136.
- Hoffman, P.F., Li, Z.-X., 2009. A palaeogeographic context for Neoproterozoic glaciation. *Palaeogeogr., Palaeoclim., Palaeoecol.*, 277, 158-172.

- Hoffman, P.F., Schrag, D.P., 2002. The snowball Earth hypothesis: testing the limits of global change. *Terra Nova*, 14, 129-155.
- Hoffman, P.F., Kaufman, A.J., Halverson, G.P., Schrag, D.P., 1998. A Neoproterozoic Snowball Earth. *Science*, 281, 1342-1346.
- Hoffman, P.F., Halverson, G.P., Domack, E.W., Husson, J.M., Higgins, J.A., Schrag, D., 2007. Are basal Ediacaran (635 Ma) post-glacial "cap dolostones" diachronous? *Earth Planet. Sci. Lett.*, 258, 114-131.
- Hoffman, P.F., Macdonald, F.A., Halverson, G.P., 2011. Chemical sediments associated with Neoproterozoic glaciation: iron formation, cap carbonate, barite and phosphorite. *Geological Society, London, Memoirs*, 36, 67-80.
- Hyde, W.T., Crowley, T.J., Baum, S.K., Peltier, W.R., 2000. Neoproterozoic "snowball Earth" simulations with a coupled climate/ice-sheet model. *Nature*, 405, 425-429.
- James, N.P., Narbonne, G.M., Kyser, T. K., 2001. Late Neoproterozoic cap carbonates: Mackenzie Mountains, northwestern Canada: precipitation and global glacial meltdown. *Can. J. Earth Sci.*, 38, 1229-1262.
- Joint Committee on Powder Diffraction Standards database (JCPDS), 1980.
- Kappler, A., Pasquero, C., Konhauser, K.O., Newman, D.K., 2005. Deposition of banded iron formations by anoxygenic phototrophic Fe(II) -oxidizing bacteria. *Geology*, 33, 865-868.
- Kasemann, S.A., Prave, A.R., Fallick, A.E., Hawkesworth, C.J., Hofmann, K.H., 2010. Neoproterozoic ice ages, boron isotopes, and ocean acidification: Implications for a snowball Earth. *Geology*, 38, 775-778.
- Kennedy, M.J., Runnegar, B., Prave, A.R., Hoffmann, K.-H., Arthur, M.A., 1998. Two or four Neoproterozoic glaciations? *Geology*, 26, 1059-1063.
- Kirschvink, J.L., 1992. Late Proterozoic low-latitude glaciations. In: Schopf, J.W. (Ed.) *The Proterozoic Biosphere*. Cambridge University Press, Cambridge, 51-52.
- Klein, C., Beukes, N.J., 1993. Sedimentology and geochemistry of the glaciogenic late Proterozoic Rapitan Iron-Formation in Canada. *Econ. Geol.*, 88, 542-565.
- Klein, C., Ladeira, E.A., 2004. Geochemistry and mineralogy of Neoproterozoic banded iron-Formations and some selected, siliceous manganese formations from the Urucum District, Mato Grosso Do Sul, Brazil. *Econ. Geol.*, 99, 1233-1244.

- Koeberl, C., Ivanov, B.A., Goodman, J., 2007. Impact-induced deglaciation of the Snowball Earth? AGU Fall Meeting Abs., #U22A-08. Bibliographic Code: 2007AGUFM.U22A.08K.
- Konhauser, K.O., 1998. Diversity of bacterial iron mineralization. *Earth-Sci. Revs.*, 43, 91-121.
- Konhauser, K.O., Hamade, T., Raiswell, R., Morris, R.C., Ferris, F.G., Southam, G., Canfield, D.E., 2002. Could bacteria have formed the Precambrian banded iron formations? *Geology*, 30, 1079-1082.
- Knoll, A.H., 2003. The geological consequences of evolution. *Geobiology*, 1/1, 3-4.
- Le Heron, D.P., 2012. The location and styles of ice-free 'oases' during Neoproterozoic glaciations with evolutionary implications. *Geosciences*, 2, 90-108.
- Le Hir, G., Donnadiou, Y., Godd ris, Y., Pierrehumbert, R.T., Halverson, G.P., Macouin, M., N d lec, A., Ramstein, G., 2009. The snowball Earth aftermath: Exploring the limits of continental weathering processes. *Earth Planet. Sci. Lett.*, 277, 453-463.
- Martin, H., 1964. Beobachtungen zum Problem der jung-Pr kambrischen glazialen Ablagerungen in S dwestafrika. *Geol. Rundsch.*, 54, 115-127.
- McMenamin, M.A.S., 2004. Climate, paleoecology and abrupt change during the Late Proterozoic: A consideration of causes and effects. In: Jenkins, G.S., McMenamin, M.A.S., McKay, C.P., Sohl, L. (Eds.) *The Extreme Proterozoic: Geology, Geochemistry, and Climate*. American Geophysical Union, Washington, D C., *Geophys. Monogr. Series*, 146, 215-229.
- Moczydłowska, M., 2008. The Ediacaran microbiota and the survival of Snowball Earth conditions. *Precamb. Res.*, 167, 1-15.
- Noffke, N., Knoll, A.H., Grotzinger, J.P., 2002. Sedimentary controls on the formation and preservation of microbial mats in siliciclastic deposits: A case study from the upper Neoproterozoic Nama Group, Namibia. *Palaios*, 17, 533-544.
- Noffke, N., Gerdes, G., Klenke, T., 2003. Benthic cyanobacteria and their influence on the sedimentary dynamics of peritidal depositional systems (siliciclastic, evaporitic salty, and evaporitic carbonatic). *Earth-Sci. Revs.*, 62, 163-176.

- Noffke, N., Eriksson, K.A., Hazen, R.M., Simpson, E.L., 2006. A new window into Early Archean life: Microbial mats in Earth's oldest siliciclastic tidal deposits (3.2 Ga Moodies Group, South Africa). *Geology*, 34, 253-256.
- Novick, A., 1955. Growth of Bacteria. *Ann. Rev. Microbiol.*, 9, 97-110.
- Olcott, A.N., Sessions, A.L., Corsetti, F.A., Kaufman, A.J, Oliviera, T. F., 2005. Biomarker evidence for photosynthesis during Neoproterozoic glaciation. *Science*, 310, 471-474.
- Polgári, M., Hein, J.R., Tóth, A.L., Pál-Molnár, E., Vigh, T., Bíró, L., Fintor, K., 2012. Microbial action formed Jurassic Mn-carbonate ore deposit in only a few hundred years (Úrkút, Hungary). *Geology*, 40, 903-906.
- Pruss, S.B., Bosak, T., Macdonald, F.A., McLane, M., Hoffman, P.F., 2010. Microbial facies in a Sturtian cap carbonate, the Rasthof Formation, Otavi Group, northern Namibia. *Precamb. Res.*, 181, 187-198.
- Raub, T.D., Evans, D.A.D., Smirnov, A.V., 2007. Siliciclastic prelude to Elatina–Nuccaleena deglaciation: lithostratigraphy and rock magnetism through the base of the Ediacaran system. In: Vickers-Rich, P., Komarower, P. (eds) *The Rise and Fall of the Ediacaran Biota*. Geological Society, London, Special Publications, 286, 53-76.
- Schopf, J.W., 2004. Earth's earliest biosphere: status of the hunt. In: Eriksson, P.G., Altermann, W., Nelson, D.R., Mueller, W., Catuneanu, O. (Eds.) *The Precambrian Earth: Tempos and Events*. *Developments in Precambrian Geology*, Elsevier, pp.516-538.
- Schwertmann, U., Cornell, R.M., 2007. *Iron Oxides in the Laboratory: Preparation and Characterization*. Wiley-VCH, 188 pp.
- Trindade, R.I.F., Font, E., D'Agrella-Filho, M.S., Nogueira, A.C.R., Riccomini, C., 2003. Low-latitude and multiple geomagnetic reversals in the Neoproterozoic Puga cap carbonate, Amazon craton. *Terra Nova*, 15, 441-446.
- Vincent, W.F., Howard-Williams, C., 2000. Life on Snowball Earth. *Science*, 287, 2421-2421.
- Vincent, W.F., Gibson, J.A.E., Pienitz, R., Villeneuve, V., Broady, P.A., Hamilton, P.B., Howard-Williams, C., 2000. Ice shelf microbial ecosystems in the high Arctic and implications for life on Snowball Earth. *Naturwissenschaften*, 87, 137-141.
- Whitten, G.F., 1970. The investigation and exploration of the Razorback Ridge iron deposits. *Geol. Surv. South Austr., Rep. Invest.*, 33, 151 pp.

Williams, G.E., 1975. Late Precambrian glacial climate and the Earth's obliquity. *Geol. Mag.*, 112, 441-465.

Williams, G.E., 2000. Geological constraints on the Precambrian history of Earth's rotation and the Moon's orbit. *Rev. Geophys.* 38, 37-59.

Zwietering, M.H., Jongenburger I, Rombouts F.M, van Riet T.K., 1990. Modeling of the bacterial growth curve". *Appl. Envir. Microbiol.*, 56, 1875-1881.

## 4 Search for extraterrestrial impact markers in samples from Chuos/Rasthof (Sturtian) and Ghaub/Maieberg (Marinoan) Snowball Earth / Greenhouse transition layers of the Neoproterozoic Otavi Group, Namibia

Ildikó Gyollai<sup>1,2,3</sup>, Dieter Mader<sup>1</sup>, Márta Polgári<sup>3\*</sup>, Friedrich Popp<sup>4</sup>, Christian Koeberl<sup>1,5</sup>

<sup>1</sup>Department of Lithospheric Research, University of Vienna, Althanstrasse 14, 1090 Vienna, Austria, e-mail: [gyildi@gmail.com](mailto:gyildi@gmail.com); <sup>2</sup>Cosmic Materials Research Group, Eötvös Loránd University of Budapest (ELTE), Pázmány Péter sétány 1/A, 1117 Budapest, Hungary; <sup>3</sup>Research Center for Astronomy and Geosciences, Geobiomineralization and Astrobiological Research Group, Institute for Geology and Geochemistry, Hungarian Academy of Sciences, Budaörsi út 45, 1112 Budapest, Hungary, e-mail: [rodokrozit@gmail.com](mailto:rodokrozit@gmail.com); <sup>4</sup>Department of Geodynamics and Sedimentology, University of Vienna, Althanstrasse 14, 1090 Vienna, Austria, e-mail: [friedrich.popp@univie.ac.at](mailto:friedrich.popp@univie.ac.at); <sup>5</sup>Natural History Museum, Vienna, Burgring 7, 1010 Vienna, Austria e-mail: [christian.koeberl@univie.ac.at](mailto:christian.koeberl@univie.ac.at),

\*Corresponding author: M. Polgári ([rodokrozit@gmail.com](mailto:rodokrozit@gmail.com))

**Keywords:** Snowball Earth, impact event, Neoproterozoic, boundary layer

**Article was submitted to “Austrian Journal of Earth Sciences” on 5<sup>th</sup> December 2013.**

**Abstract:** At least two global Neoproterozoic (Cryogenian) glaciation events (“Snowball Earth”) occurred 710 Ma (Sturtian) and 630 Ma (Marinoan) ago, where the oceans were either completely frozen or at most a few small open water oases remained. Neither the cause of the onset of the glaciations, their extent and duration, nor the cause for the deglaciations, are currently understood. In this study we try to follow up earlier studies by our group that indicated the presence of an extraterrestrial signature in rock units that mark the transition between the glacial diamictites and the overlying cap carbonates. Earlier results indicated that during the prolonged glaciation only extraterrestrial dust accumulated and the amount of dust can be used as proxy for the duration of the glaciation. This study deals with the suggestion that a large-scale impact event might have triggered the deglaciation. The problem of the climatic effects of large impact events is not clear, as previously a Chicxulub-scale impact was suggested to induce global freezing, but it is possible that an impact event may cause rapid deglaciation. Here we discuss the search for impact signatures using mineralogical and geochemical methods in samples from the Chuos/Rasthof (Sturtian) and Ghaub/Maieberg (Marinoan) postglacial transition at the Neoproterozoic Otavi Group (Namibia). We performed geochemical analyses on whole-rock samples spanning the range from underlying glacial

diamictite to overlying cap carbonate in an effort to search for impact related signatures; in addition, mineral separations were done on selected samples to study detrital minerals. However, no geochemical and mineralogical signatures, such as an enrichment in siderophile element abundances or the presence of Cr-spinells or shocked minerals were found in our samples. Thus, there is no clear indication that an impact event was involved in the formation of the studied transition layers.

#### 4.1 Introduction

Neoproterozoic glaciations of global extent occurred within three different cryogenic periods: 1. the Sturtian (740–647 Ma, type location South Australia), 2. the Marinoan (660–635 Ma, type location South Australia) and 3. the Gaskiers (ca. 580 Ma, type location Avalonian Newfoundland, Canada), with the duration of each glaciation being estimated at several million years. The Snowball Earth hypothesis was introduced by Kirschvink (1992). The different global glaciations have been attempted to be explained by a variety of hypotheses, such as the (i) Hard Snowball Earth (Hoffman, 1998; Hoffman and Schrag, 2002); (ii) Slushball Earth (Harland, 1964); the (iii) Zipper-rift model (Eyles and Januszczak, 2004); and (iv) high-tilt Earth (Williams, 2000).

(i) The Hard Snowball Earth hypothesis postulates total sea ice coverage of oceans with thick dynamic continental ice sheets, fed by sublimation of deep tropical sea ice (Hoffman et al., 1998; Donnadieu et al., 2003; Pollard and Kasting, 2004), with a temperature of  $-50^{\circ}\text{C}$  (Hoffman and Schrag, 2002) and with rapid deglaciation via an extreme greenhouse state (Hoffman et al., 1998, Kennedy et al., 2008).

(ii) The Slushball Earth model proposes milder conditions without substantial equatorial sea ice and with following slower deglaciation (Harland and Rudwick, 1964).

(iii) The Zipper-rift Earth model supports climatic control of tectonic events based on occurrence of glacier sediments in rift basins during diachronous rifting of Rodinia (Eyles and Januszczak, 2004).

(iv) High tilt model is based on high obliquity related (greater than  $54^{\circ}$ ) Cryogenian glaciations, which developed firstly at low latitudes characterized by extreme seasonality (Williams, 1975, 2000).

Bodiselitsch et al. (2005) noted the presence of anomalously elevated contents of the element iridium in samples from the Sturtian and Marinoan diamictite/cap carbonate boundary layers at the Congo Craton and proposed that this anomaly reflects cosmic dust deposition during the glaciation phase; furthermore, these authors used the abundance of Ir (and other

siderophile elements) in the boundary layer to estimate the duration of the glaciations, based on a steady-state accumulation of extraterrestrial dust. However, studies from other locations in the Canadian Cordillera and in Namibia have yielded ambiguous results. Peucker-Ehrenbrink and Hoffman (2006) noted slightly elevated abundances of osmium and a decrease in the  $^{188}\text{Os}/^{187}\text{Os}$  isotopic ratio in samples from two continuously sampled profiles at the end of the Marinoan glaciation in Namibia (Otavi Platform) and the northern Canadian Cordillera (Mackenzie Mts), where a 2-12 cm thick clay layer separates glacial diamictite from post-glacial cap dolomite. On the other hand, further analyses of additional samples, and re-analysis of a split of the Congo Craton sample, by Waters et al. (2009, 2010) failed to find significant platinum-group element (PGE) anomalies, but conformed the Os isotopic trend. They also noted that samples with higher Os concentrations have less radiogenic Os, which is consistent with binary mixing between terrestrial and extraterrestrial Os. This either means that the Ir anomaly found by Bodiselitsch et al. (2005) is not global or not of purely extraterrestrial origin.

Hence, Koeberl et al. (2007) proposed a possible alternative explanation, namely that the Ir anomaly was the result of an impact event. One of the two goals of the present project is to investigate if it is conceivable that a large-scale impact event might have triggered the deglaciation. The problem of the climatic effects of large impact events is not clear, as previously a Chicxulub-scale impact was suggested to induce global freezing.

In terms of cratering rates, it is statistically plausible that the impact of a ~5 km diameter asteroid occurs during a “snowball period” with duration of several million years. Most probable is an impact into the ice-covered ocean. In such a case a vapor plume with a total mass of several times  $10^{15}$  kg will rise up and then collapse over the atmosphere, creating a transient “hot spot”. The more indirect consequences may include a global enrichment of the upper atmosphere with water vapor, dust and sea salt particles (in the case of an impact into the ocean). Photochemical reactions should be taken into account for a further climatic modeling. At this point the trial simulations do not allow a conclusion if an impact of a realistic magnitude could cause deglaciation of a Snowball Earth. More detailed work, based on the initial studies reported by Koeberl et al. (2007), is still necessary.

One of the goals of this study was, therefore, to search for evidence of an impact event in samples from the transition between the glacial diamictites and the overlying cap carbonates. The recognition of geological structures and ejecta layers on Earth as being of impact origin requires the detection of either shock metamorphic effects in minerals and rocks, and/or the presence of a meteoritic component in these rocks. The presence of shock metamorphic

effects constitutes confirming evidence for impact processes. In nature, shock metamorphic effects are uniquely characteristic of shock levels associated with hypervelocity impact.

A wide variety of shock metamorphic effects have been identified. The most common ones include planar microdeformation features, optical mosaicism, changes in refractive index, birefringence, and optical axis angle, isotropization (e.g., formation of diaplectic glasses), and phase changes (high pressure phases; melting). Planar microstructures are the most characteristic expressions of shock metamorphism and occur as planar fractures (PFs) and planar deformation features (PDFs). The presence of PDFs in rock-forming minerals (e.g., quartz, feldspar, or olivine) provides diagnostic evidence for shock deformation, and, thus, for the impact origin of a geological structure or ejecta layer (see, e.g., Stöffler and Langenhorst, 1994; Montanari and Koeberl 2000, French and Koeberl, 2010; Glass and Simonson, 2013; and references therein).

Another way to determine the impact origin of crater rocks or ejecta is by confirming the presence of a meteoritic component in these rocks. Apart from studying meteorite impact craters, information can also be gained from the study of impact ejecta. Geochemical methods have been used to determine the presence of the traces of such an extraterrestrial component. In the absence of actual meteorite fragments, it is necessary to chemically search for traces of meteoritic material that is mixed in with the target rocks in breccias and melt rocks. Meteoritic components have been identified for just fewer than 50 of the more than 180 impact structures that have so far been identified on Earth. The presence of a meteoritic component can be verified by measuring abundances and interelement ratios of siderophile elements, especially the platinum group elements (PGE), which are much more abundant in meteorites than in terrestrial upper crustal rocks. Often the content of the element iridium is measured as a proxy for all PGEs, because it can be measured with the best detection limit of all PGEs by neutron activation analysis. For more detailed information on this topic, see, e.g., Koeberl (1998), Koeberl et al. (2012), and references therein.

Our research area, Otavi Group in NW Namibia is near to the area studied by Bodiselitsch et al. (2005), the Congo Craton. Hence, we undertook a search for impact signatures in samples from the Sturtian and Marinoan “boundary clay” similar to those found in distal impact ejecta, such as the Late Eocene or the Cretaceous/Paleogene boundary (cf. Montanari and Koeberl, 2000).

## 4.2 Geological background

The research area is located in the Neoproterozoic Otavi Group in NW-Namibia (Fig. 1). The Otavi Platform formed along the southern fringe of the Congo Craton and abuts on the continental slope further south and west. Thus its predominantly calcareous sedimentary successions, unified as Otavi Group, are located in a foreland position relative to the Kaoko Belt in the west and the Damara Belt in the south (Hoffman, 2002, 2005; Fig. 1., 2.). The Otavi Group is subdivided into three subgroups, which are separated from each other by two glaciogenic diamictite units, the lower Chuos Formation and the upper Ghaub Formation (Hoffmann, 2002, 2005; Fig. 2.).

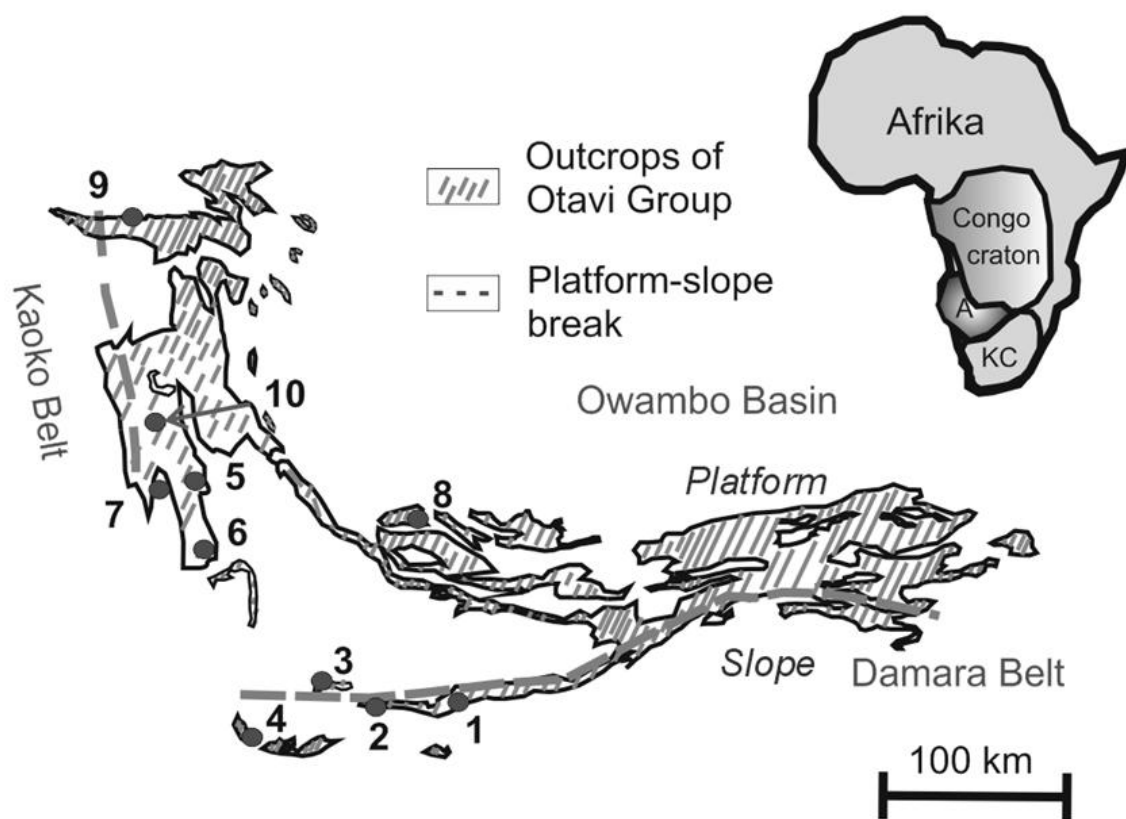


**Figure 1.** Geological map of Otavi group outcrops showing sampling sites of Sturtian and Marinoan postglacial transition layers (modified after Hoffman, 2002). The sampling sites are marked by numbers: 1 = Fransfontain, 2 = Naraachaspos, 3 = Tweelingskop, 4 = Bethanis, 5 = Entrance to the South Valley, 6 = Khowarib Valley, 7 = Ongongo (Warmquelle), 8 = Copper Mine, 9 = Steilrandberge, 10 = Sesfontain-Opuwo Rd. The collected samples are listed in Table 1. including their lithology and facies.

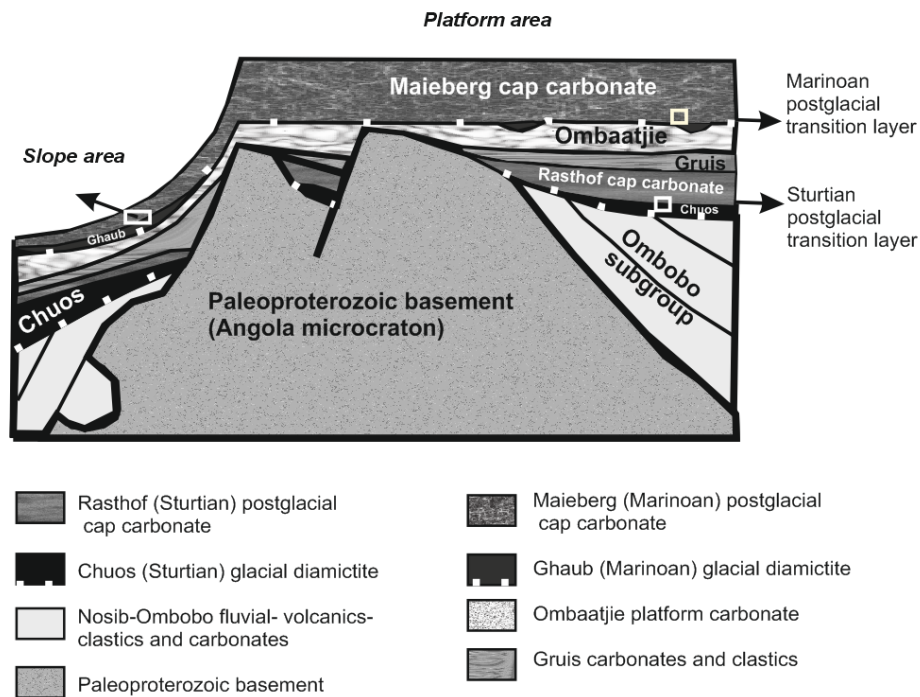


**Figure 2.** Geological cross section of Otavi Group (modified after Hoffman, 2005). Marinoan postglacial transition layer: sampling sites 1-7; Sturtian postglacial transition layer: sampling sites 8-10 (see Table 1. and Fig. 1. for details).

Continental break-up of the Mid-Proterozoic Rodinia Supercontinent produced world-widespread extensional rift systems followed by the development of passive continental margins. On the Congo Craton initial rifting caused deposition of siliciclastic sediments (conglomerate, arkosic quartzite, and siltstone with minor shale and carbonate, Hedberg, 1979); later subsidence and transgression lead to the development of a stable Bahama-type sea-level carbonate platform of enormous size, where the thick sequence of Otavi Group carbonate dominated sediments accumulated.

The middle Otavi Group is bounded by two discrete intervals of diamictite and associated by glaciomarine deposits, sandwiched by thick carbonate piles. The glaciogenic origin of the older interval (Chuos Formation) was first documented by Martin (1965) and Hedberg (1975). Later Hoffmann and Prave (1996) lined out the younger glaciogenic interval (Ghaub Formation), covering an erosional surface on top of a carbonate platform sequence (Ombaatjie Formation). The sediments of both glaciogenic periods are overlain by distinct “cap-carbonate” layers, represented by the basal parts of the Rasthof- and respectively Maieberg Formations. The upper Otavi Group (Tsumeb Subgroup) is a thick and rather monotonous

stack of grainstone-dominated cycles of cherty dolomite, deposited during the prolonged drift stage of the Panafrican Damara orogenic cycle.

### 4.3 Samples and methods

Our samples were collected from postglacial transition layers on top of the glaciogenic Chuos Fm. (Sturtian) (6 bulk samples and 7 subsamples – total 10 from 3 locations) and Ghaub Fm. (Marinoan) (11 bulk samples and 3 profiles – total 62 samples from 7 locations) of the Neoproterozoic Otavi Group in NW-Namibia (Fig. 1., Table 1. AB). The methods used in the study of the individual samples are given in Table 2.

**Table 1.** Locality of sample sites and sample description of Ghaub (Marinoan) Fm. (A) and Chuos (Sturtian) Fm. (B)

A Site No.*	Sample No.	Sub samples	Locality	GPS Data	Lithology	Glaciation/Deglaciation Event	Facies
1	C 1	C 1a	Fransfontain	20°11'59.06"S; 15° 0'58.68"E	allodapic dolostone	Ghaub-Maieberg Fm.	slope
1		C 1b	Fransfontain	"	allodapic dolostone	Ghaub-Maieberg Fm.	slope
1		C 1c	Fransfontain	"	allodapic dolostone	Ghaub-Maieberg Fm.	slope
2	C 2	C 2a	Naraacham spos	20°11'27.68"S; 14°51'4.42"E	boundary layer	Ghaub-Maieberg Fm.	slope
2		C 2b	Naraacham spos	"	boundary layer	Ghaub-Maieberg Fm.	slope
2		C 2c	Naraacham spos	"	boundary layer	Ghaub-Maieberg Fm.	slope
2	C 3	C 3_1	Naraacham spos	20°11'28.74"S; 14°51'4.38"E	boundary layer	Ghaub-Maieberg Fm.	slope
2		C 3_2	Naraacham spos	"	boundary layer	Ghaub-Maieberg Fm.	slope
2	C 17	C 17a	Naraacham spos	no data	tectonic clay	Ghaub-Maieberg Fm.	slope
2		C 17b	Naraacham spos	no data	ashy clay	Ghaub-Maieberg Fm.	slope
2		C 17c	Naraacham spos	20°11'28.00"S; 14°51'2.76"E	boundary layer	Ghaub-Maieberg Fm.	slope
3	C 4		Tweelingskop	20° 7'13.47"S; 14°35'1.30"E	red dolomite	Ghaub-Maieberg Fm.	platform edge
3	C 5		Tweelingskop	20°7'13.82"S; 14°35'1.71"E	aeolianite	Ghaub-Maieberg Fm.	platform edge
4	C 6		Bethanis	20°24'24.00"S; 14°20'13.55"E	red Silt	Ghaub-Maieberg Fm.	distal slope
4	C 7		Bethanis	20°7'13.47"S; 14°35'1.30"E	dolomite rhythmite	Ghaub-Maieberg Fm.	distal slope
5	C 14	C 14a	Valley Entrance	S 19°11'18.40"S; 13°56'13.39"E	red diamictite	Ghaub-Maieberg Fm.	platform
5		C 14b	Valley Entrance	S "	red transition Layer	Ghaub-Maieberg Fm.	platform
5		C 14c	Valley Entrance	S "	tectonized clay	Ghaub-Maieberg Fm.	platform

A Site No.*	Sample No.	Sub samples	Locality	GPS Data	Lithology	Glaciation/Deglaciation Event	Facies
5		C 14d	Valley Entrance	S “	red-green boundary clay	Ghaub-Maieberg Fm.	platform
5		C 14e	Valley Entrance	S “	basal dolomite	Ghaub-Maieberg Fm.	platform
5	Profile K4	K4-01-08 (8)	Valley Entrance	S “	basal dolomite	Ghaub-Maieberg Fm.	platform
6	C 15	C 15a	Khowarib Valley	19°18'24.52"S; 13°59'25.57"E	banded cap-dolomite	Ghaub-Maieberg Fm.	platform
6		C 15b	Khowarib Valley	“	boundary layer	Ghaub-Maieberg Fm.	platform
6		C 15c	Khowarib Valley	“	red boundary clay	Ghaub-Maieberg Fm.	platform
6		C 15d	Khowarib Valley	“	basal cap dolomite	Ghaub-Maieberg Fm.	platform
6		C 15e	Khowarib Valley	“	boundary clay	Ghaub-Maieberg Fm.	platform
6	Profile P49	P49-01-18 (15)	Khowarib Valley	“	basal cap dolomite	Ghaub-Maieberg Fm.	platform
7	C 16	C 16a	Ongongo (Warmquelle)	19°8'35.77"S; 13°51'15.40"E	sericitized clay	Ghaub-Maieberg Fm.	platform
7		C 16b	Ongongo (Warmquelle)	“	basal mylonite	Ghaub-Maieberg Fm.	platform
7		C 16c	Ongongo (Warmquelle)	“	opalized layer	Ghaub-Maieberg Fm.	platform
7	Profile K2	K2-01-11 (11)	Ongongo (Warmquelle)	“	basal cap carbonate	Ghaub-Maieberg Fm.	platform

B Site No.*	Sam-ple No.	Sub sam-ples	Locality	GPS Data	Lithology	Glacia-tion/Deglaciation Event	Facies
8	C 8		Copper Mine	19°25'18.43" S; 15° 9'50.90"E	red car- bonate	Chuos- Rasthof Fm.	platform
8	C 9		Copper Mine	"	carbonate- quartzite	Chuos- Rasthof Fm.	platform
8	C 10	C 10_1	Copper Mine	"	sandstone	Chuos- Rasthof Fm.	platform
8		C 10_2	Copper Mine	"	sandstone compact	Chuos- Rasthof Fm.	platform
8	C 11	C 11_1	Copper Mine	"	black lam- inated sandstone	Chuos- Rasthof Fm.	platform
8		C 11_2	Copper Mine	"	black lam- inated sandstone	Chuos- Rasthof Fm.	platform
9	C 12		Steilrandber- ge	17°47'1.67"S ; 13°39'54.10" E	red-brown dolomite	Chuos- Rasthof Fm.	platform
10	C 13	C 13a	Sesfontain- Opuwo Rd	18°46'26.49" S; 13°45'11.24" E	brown sandstone unaltered	Chuos- Rasthof Fm.	platform
10		C 13b	Sesfontain- Opuwo Rd	"	red/green sandstone altered	Chuos- Rasthof Fm.	platform
10		C 13c	Sesfontain- Opuwo Rd	"	transition zone to carbonate	Chuos- Rasthof Fm.	platform

\*For site number localities see Fig. 1.

The mineralogical composition of our samples was studied using the petrographic microscope, X-ray powder diffraction (XRD), cathodoluminescence microscopy (CL), and micro-Raman spectroscopy at the University of Vienna. Instrumental neutron activation analysis (INAA) and X-ray fluorescence (XRF) spectrometry, as well as analytical electron microscopy (AEM), were used for the geochemical study.

XRD data were collected at with a Phillips-diffractometer (PW 3710, goniometer PW-1820), CuK $\alpha$  radiation (45 kV, 35 mA), step size of 0.02 degrees, and counting time of 1 s per step. Minerals were identified using the Joint Committee on Powder Diffraction Standards database (JCPDS, 1980).

A Renishaw RM1000 confocal edge filter-based micro-Raman spectrometer with 20 mW, 632.8 nm He-Ne laser excitation system, and thermoelectrically cooled charged coupled device array detector was used at the Institute of Mineralogy and Crystallography, University of Vienna for identification of some mineral phases. For identification of different generations of

carbonate cement and origin of quartz a Lumic HC5-LM CL-microscope was used. The acceleration voltage applied on the tungsten filament in the electron gun is 14 kV; the beam current can be varied from about 0.05 to 0.4 mA, depending on the examined material.

INAA was used for the determination of the contents of major and trace elements, from which some were selected for this study (Cr, Co, Ni, Au, and Ir). For this purpose, approximately 150 mg of each of the powdered samples were weighed and sealed in small polyethylene vials, as well as about 60–100 mg of three of the following international rock standards: the carbonaceous chondrite Allende (Smithsonian Institution, Washington DC, USA; Jarosewich et al., 1987), the granite AC-E (Centre de Recherche Pétrographique et Géochimique, Nancy, France; Govindaraju, 1989), and the Devonian Ohio shale SDO-1 (United States Geological Survey; Govindaraju, 1989). These capsules were irradiated in the 250 kW Triga Mark II reactor at the Atominstut (Institute of Atomic and Subatomic Physics) of the Technical University of Vienna for 6–8 h at a thermal neutron flux of about  $1.7 \cdot 10^{12} \text{ n cm}^{-2}\text{s}^{-1}$ . Three measurements cycles, according to the half-lives of the nuclides, were done using high purity germanium detectors with relative efficiencies of about 40 to 45 % and energy resolutions of 1.76 – 1.82 keV at 1332 keV ( $^{60}\text{Co}$ ), respectively. For further details of the INAA measurements, see Mader and Koeberl (2009).

XRF analyses were done using a Philips PW 2400 sequential X-ray spectrometer equipped with a Rh-excitation source (Department of Lithospheric Research, University of Vienna), where the contents of the main elements and some selected trace elements were measured and considered in this study. The specimens were ground in an electric agate mill, homogenized, dried at 110 °C and fired at 950 °C to determination of water content and loss on ignition. For XRF analyses, fused beads were produced consisting of a 1:5 mixture of fired sample material and flux ( $\text{Li}_2\text{B}_4\text{O}_7$ ).

Polished smeared slides were carbon-coated and examined at the Department of Mineralogy, Natural History Museum, Vienna (Austria) on a JEOL JSM 6400 scanning electron microscope (SEM) equipped with an energy-dispersive X-ray (ED) analyzer.

Because of high carbonate content, the detrital minerals were diluted in carbonate. The samples were solved in formic acid to remove carbonate minerals to study detrital minerals. The detrital phase were then sieved, where the fractions between 63-400 micrometer fractions were studied under binocular microscope to search for shocked quartz, impact spherules, and chromium spinels. Chrome spinels are magnetic minerals, and thus the different fractions of each sample were subjected to magnetic separation using a Frantz Isodynamic magnetic separator. Within magnetic fractions, magnetites and pyrites were determined according to their crystal shape. The identity of some rounded magnetic grains (C3\_2, C17a,

C7) could not be determined under the binocular microscope; thus thick sections were prepared for SEM-EDS studies. The clay fraction was measured by XRD.

**Table 2.** Methods used for sample characterization

Sample Nr*	Pet-ro-graphy	C L	Ra man	XR D	XR D clay	XRF (major elements)	XRF (trace elements)	INA A	INA A clay	Mineral separation (decarbonatized sieved fractions)	SEM/EDX
C 1a				X	X		X	X	X	X	
C 1b		X		X	X		X	X	X	X	
C 1c	X			X		X	X	X			
C 2a	X	X	X	X	X		X	X	X	X	
C 2b				X	X		X	X	X	X	
C 2c				X	X		X	X	X	X	
C 3_1	X			X	X		X	X	X	X	
C 3_2	X	X		X	X		X	X	X	X	
C 4	X		X	X		X	X	X			X
C 5	X	X		X	X	X	X	X	X	X	
C 6	X			X	X		X	X	X	X	
C 7	X			X	X		X	X	X	X	
C 8	X	X		X	X		X	X	X	X	
C 9	X			X	X	X	X	X	X	X	X
C 10_1	X			X	X	X	X	X	X	X	
C 10_2	X			X	X	X	X	X	X	X	
C 11_1	X			X	X			X			
C 11_2	X			X	X			X			
C 12	X		X	X	X	X	X	X	X	X	
C 13a	X			X	X	X	X	X	X	X	X
C 13b	X		X	X	X	X	X	X	X	X	X
C 13c	X			X	X		X	X	X	X	X
C 14a	X	X		X	X		X	X	X	X	
C 14b				X	X	X	X	X	X	X	
C 14c				X	X	X	X	X	X	X	
C 14d	X			X	X		X	X	X	X	
C 14e				X	X		X	X	X	X	
C 15a	X										
C 15b				X	X	X	X	X	X	X	
C 15c				X		X	X	X			
C 15d	X	X		X		X	X	X			
C 15e	X			X		X	X	X	X	X	X
C 16a				X		X	X	X			
C 16b	X			X		X	X	X	X	X	X
C 16c	X			X		X	X	X	X	X	X
C 17a				X		X	X	X	X	X	X
C 17b				X			X	X	X	X	X
C 17c	X	X		X			X	X	X	X	X
Profile K2 (11)	X			X				X			
Profile K4 (8)	X			X				X			
Profile P49 (15)	X			X				X			

\* Legend:CL=cathodoluminescence microscopy, XRD=X-ray powder diffraction, XRF=X-ray fluorescence, INAA=instrumental neutron activation analysis, SEM/EDS=scanning electron microscopy – energy dispersive X-ray spectroscopy)

## 4.4 Results

### 4.4.1 Optical microscopy and XRD: search for shocked quartz

As some of the most important mineralogical indicators of shock metamorphism are PFs and PDFs in quartz (cf. Stöffler and Langenhorst, 1994; French and Koeberl, 2010), we studied 60 thin sections and 12 smear slides by optical microscopy, and found mostly carbonate minerals in both the diamictite and the boundary layers. The diamictites were composed of either fine-grained or micritic-clayish matrix material with carbonate clasts of various size. The Sturtian and Marinoan transition layers are dominated by clayish material containing authigenic minerals (hematite, sericite), but a few samples contain also a low amount (5 vol%) of detrital minerals (feldspar, mica). Coarse grained detrital mineral phases from some Sturtian basal carbonate layers are partly enclosed within the cores of oncoids (C8 sample at Copper Mine), indicating shallow water depositional conditions.

The Marinoan transition deposits from Naraachamspos (sample C2a) contain thin diamictite layers composed of coarse-grained quartz, calcite, twinned K-feldspar (orthoclase, microcline, and albite) and kink-banded mica. No shock deformation features were observed within the quartz grains but regional tectonic deformation is distinctly and visibly.

The basal cap carbonate layer from the Bethanis location (sample C7) also contains coarse detrital mineral grains, especially chlorite and quartz. Several chlorite minerals were kinked, but quartz grains do not display any signature of shock deformation. The matrix of Sturtian and Marinoan postglacial layers is mostly fine-grained material, where the quartz grains occur as secondary phase, such as cement among synsedimentary structures (C3), and as fracture-filling material (e.g., K2, K4, P49). Several diagenetic generated carbonate grains from Marinoan postglacial transition deposits (samples K4 and K2) contain dense, differently oriented deformation lamellae systems (Fig. 3) which is genetically assigned to regional tectonics in connection with foreland thrust faults of the Panafrican Kaoko Belt.

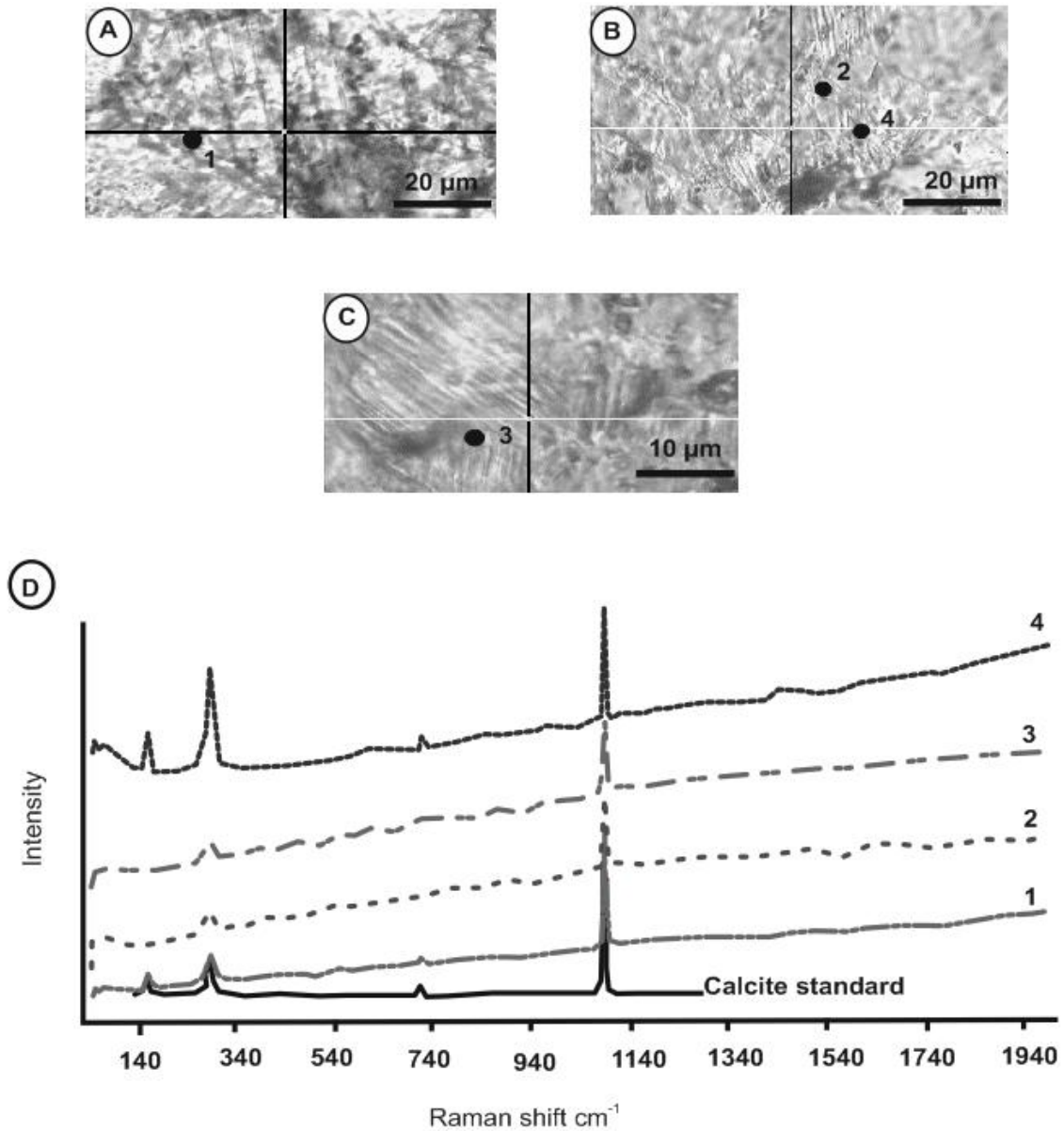
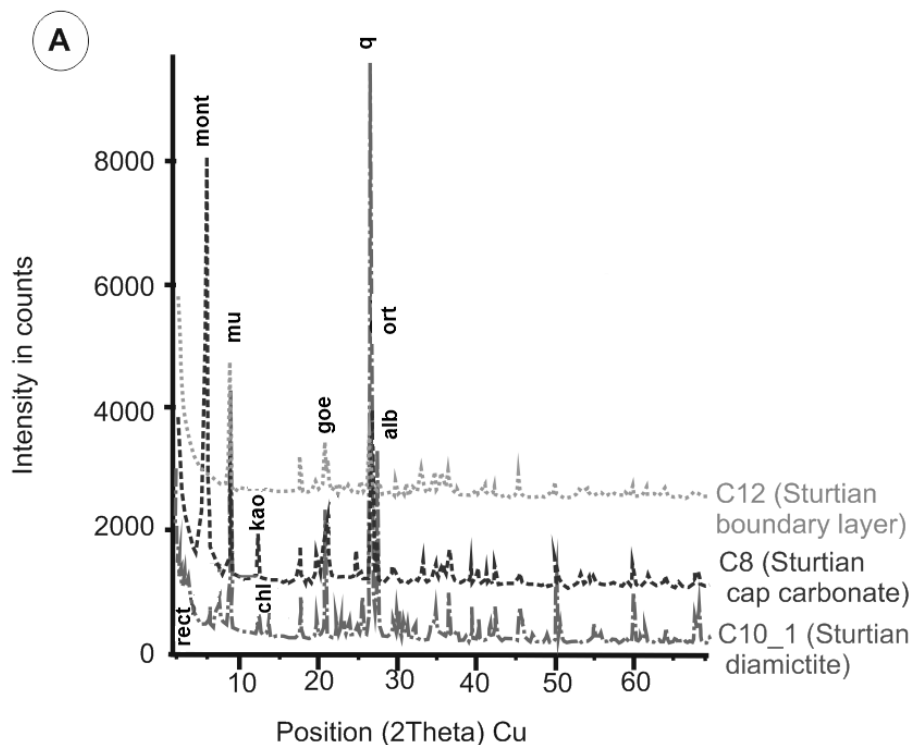


**Figure 3.** Raman spectra and thin section photos of K2-1 and K4-1 samples. The Raman spectra are marked by numbers (1-4), and measuring points are shown on thin section photos (plain polarized lights). (A) normal mechanical twins in K4-1 sample; (B) the mechanical twins are crossed by dense, dislocation-like lamellae system of K2-1 sample; (C) dense, dislocation-like lamellae system with two orientations in calcite grain in K4-1 sample; (D) Raman spectra of calcites. All of Raman spectra show high background line because of fluorescence. In spectra (2) and (3) (near to dislocation-like lamella system), the minor peaks disappeared, but main vibration peaks are not shifted to other wave number indicating no phase transition but disturbance in crystal lattice.

CL microscope studies were used to distinguish authigenic from detrital quartz and also to determine other detrital minerals. We also searched for shock deformation lamellae in quartz grains using the CL-procedure, but did not find any characteristic signatures (e.g., Boggs et al., 2001; Hamers and Drury, 2011). In our CL studies, quartz assemblages don't show any luminescence color, what is indicative for a diagenetic origin of the quartz in the Sturtian and Marinoan postglacial transition layers. Quartz sigmaclasts, indicating a NW orientated strain component of the assigned Panafrican tectonics were observed in very basal Marinoan cap carbonate layers from Naraachamspos (profile C2a). Quartz lenses are clearly of diagenetic origin as it is indicated by their lack of luminescence colour

Some Marinoan samples, such as the diamictite from Tweelingskop, have high quartz contents, and the cap carbonate from Naraachamspos also contains quartz lenses. These samples also have no luminescence color, again indicating a diagenetic origin of the quartz. At Tweelingskop locality *öleanit* was deposited instead of glacial diamictite, but due to diagenesis the original quartz grains are completely recrystallized (no luminescence color, grain fabric)

In the EDS spectra, the presence of Fe and Si was noted, indicating hematite-magnetite precipitations which are coating quartz grains. Chrome spinells were not noted in the XRD spectra of the clay fractions; only feldspars (albite, orthoclase), quartz, muscovite, hematite, goethite and clay minerals, such as chlorite, smectite, and kaolinite, were found (Fig. 4AB).



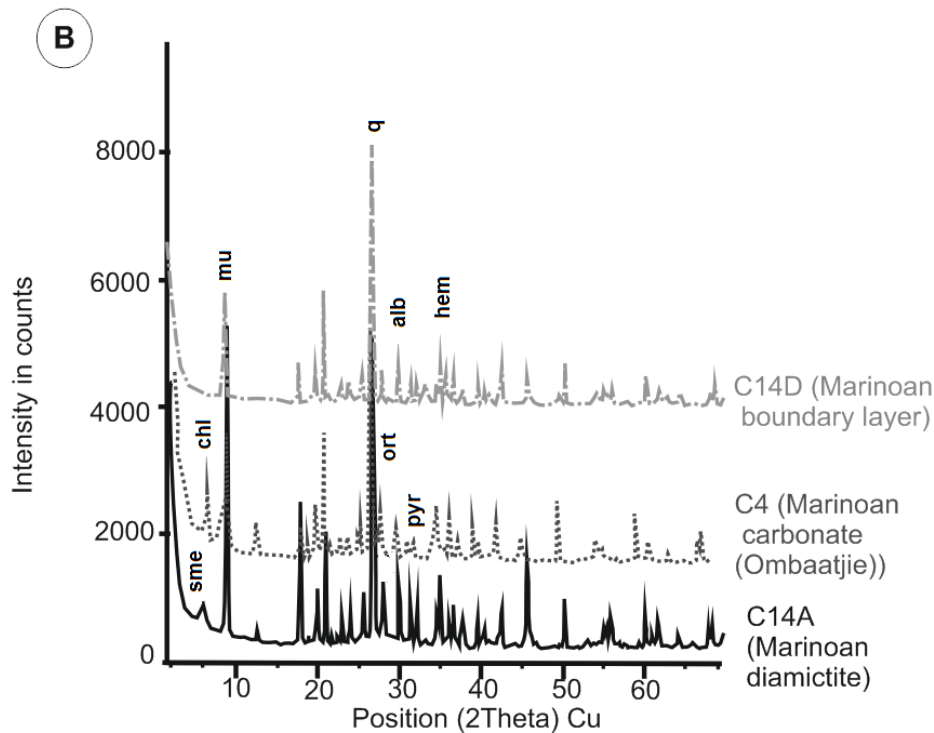


**Figure 4.** Selected XRD spectra of Sturtian (A) and Marinoan (B) stratigraphic sections after dissolving carbonate with formic acid. All of presented Sturtian and Marinoan layers contain quartz (q) and muscovite (mu). (A) Sturtian top diamictite (C10\_1) contain different clay mineral phases (montmorillonite (mont), chlorite-chl, rectorite-rect, kaolinite-kaol), which are derived by clay minerals. Sturtian postglacial transition layer (C8, C12) contains goethite (goe) and feldspar (alb, ort). The Marinoan transition layers (B) contain hematite (hem) (C14), smectite (sme) (C14a), feldspar (alb, ort) (C4, C14d) pyrite (pyr) and chlorite (chl) (C4).

#### 4.4.2 Geochemistry

The most important geochemical signature of a meteoritic component is enrichment in the contents of siderophile elements (and other related elements that are also enriched in meteorites) in ejecta samples compared to contents in the average upper continental crust (see above). In our analyses, the contents of the elements Cr, Ni, and Co do not show any significant enrichment. The abundances of Ir were all below the detection limit with INAA (1-2.5 ppb).

The Ni/Cr and Co/Cr ratios for the transition layer samples from Naraachamspos (C2a-c, C17a, C3-1-2) Sesfontain-Opuwo (C13a-b) and Steilrandberge (C12, C12a, Bethanis (C6), Entrance to the SW-Valley (C14 b, d1, e) are near or higher than values for the upper conti-

mental crust (Rudnick and Gao, 2003) for both of bulk rock samples and their clay fractions after dissolving the carbonate (Fig. 5.).

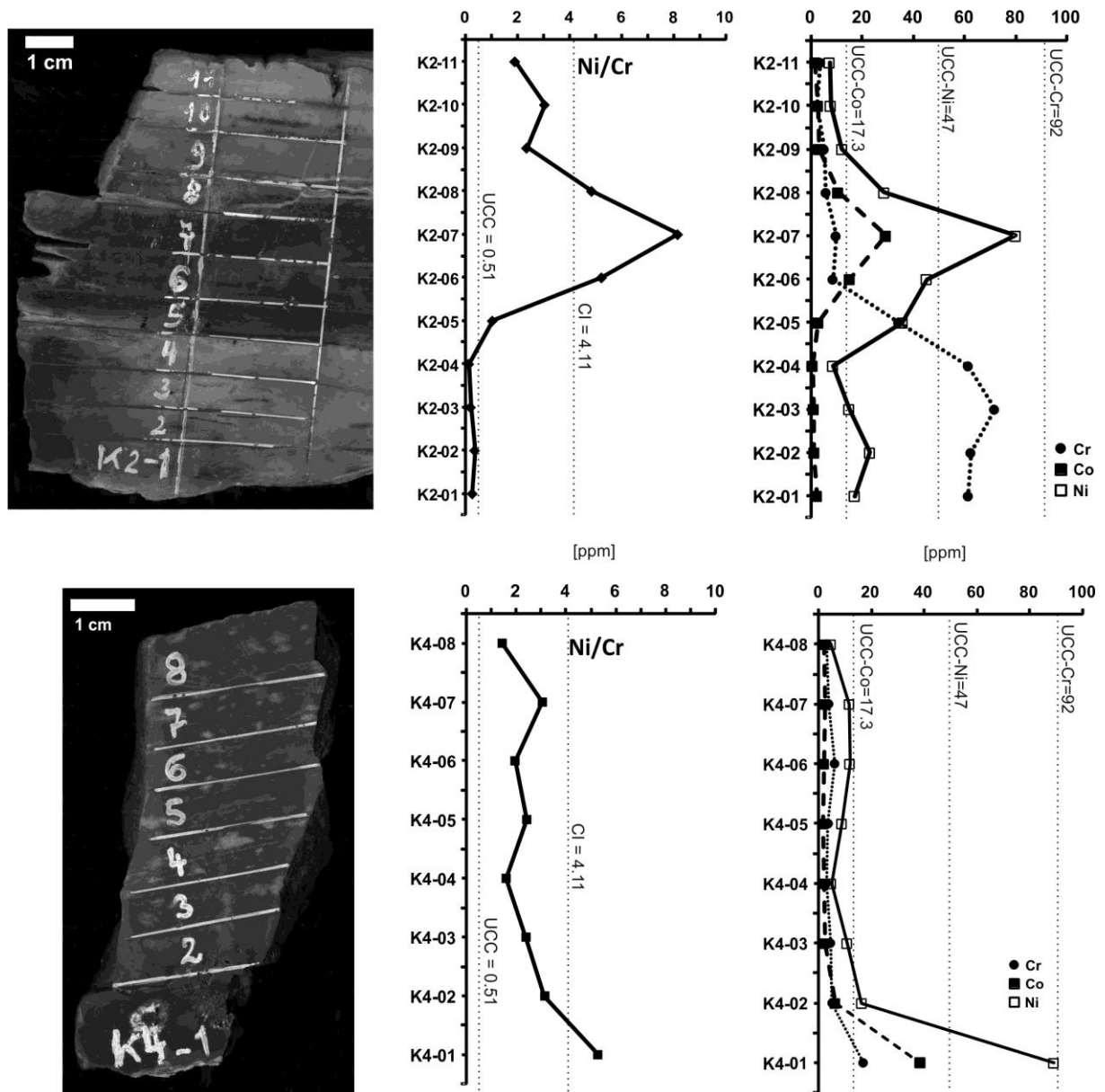


**Figure 5.** Cr-Ni-Co values and Ni/Cr ratio profiles of Marinoan cap carbonate profile from Warmquelle (K2) and Entrance of South Valley (K4). The boundary layers are slightly enriched in Ni/Cr ratio, and Ni, Cr, Co values compared to upper continental crust (Rudnick and Gao, 2003) but the Ni/Cr ratio of samples K4-01, K2-06, K2-07, K2-08 is higher than that of chondritic meteorites (Henderson and Henderson, 2009), not indicating the presence of a meteoritic component.

**Table 3.** Major and trace element contents for post-glacial transition samples from Namibia.

Legend: G= Ghaub Fm., G/M = Ghaub/Maieberg boundary, M= Maieberg Fm., C=Chuosi Fm., C/R= Chuosi/Rasthof boundary, R= Rasthof Fm., O=Ombaatjie Formation Clay fractions are marked by "T". LOI = loss on ignition. "n.d." = not determined. The Ir content is below the detection limit for all samples (1-2.5 ppb). -- = some of the major element contents were not determined.

**A) Marinoan transition layers**

Location Strat. setting wt. % / sample	Fransfontain			Tweelingskop		Bethanis	
	M C 1a	G/M C 1b	G/M C 1c	O C 4	G C 5	G/M C 6	M C 7
SiO <sub>2</sub>	n.d.	n.d.	27.5	n.d.	62.2	n.d.	n.d.
TiO <sub>2</sub>	n.d.	n.d.	0.43	n.d.	0.05	n.d.	n.d.
Al <sub>2</sub> O <sub>3</sub>	n.d.	n.d.	7.00	n.d.	0.37	n.d.	n.d.
Fe <sub>2</sub> O <sub>3</sub>	0.38	1.42	2.56	1.33	14.2	0.94	3.48
MnO	n.d.	n.d.	0.19	n.d.	0.06	n.d.	n.d.
MgO	n.d.	n.d.	22.6	n.d.	7.95	n.d.	n.d.
CaO	n.d.	n.d.	36.0	n.d.	12.7	n.d.	n.d.
Na <sub>2</sub> O	0.02	0.02	0.03	0.02	0.09	0.06	0.37
K <sub>2</sub> O	0.18	1.02	1.74	0.74	0.03	0.75	1.81
P <sub>2</sub> O <sub>5</sub>	n.d.	n.d.	0.28	n.d.	0.30	n.d.	n.d.
LOI	45.9	40.4	35.3	45.4	17.0	41.3	29.4
Total	--	--	99.3	--	98.0	--	--
<b>ppm</b>							
Cr	7.22	15.0	25.8	14.4	9.27	14.1	30.8
Co	1.32	5.43	7.20	2.14	3.50	4.03	6.82
Ni	7.1	47.1	67.7	7.1	20.9	34.3	53.9
Au (ppb)	<0.2	0.2	0.2	<0.5	<0.4	<0.2	0.1

Location Strat. setting wt. %	Naraachamspos							
	G C 2a1-T	G/M C 2b-T	G/M C 2c-T	G/M C 3_1-T	G/M C 3_2-T	G C 17a-T	G/M C 17b-T	M C 17c-T
Fe <sub>2</sub> O <sub>3</sub>	1.55	3.74	1.62	2.61	3.04	2.88	2.28	2.23
Na <sub>2</sub> O	0.41	0.14	0.79	0.07	0.07	0.09	0.07	0.09
K <sub>2</sub> O	3.83	7.71	6.64	7.89	6.91	8.48	7.22	7.82
<b>ppm</b>								
Cr	56.0	232	120	131.	93.0	129	98.3	89.1
Co	15.8	33.2	17.0	16.4	26.9	2.11	1.64	6.98
Ni	115	250	184	241	192	112	131	98.2
Au (ppb)	0.37	<1.4	<0.7	<1.1	<1	<1.1	<0.92	<0.6

Location Strat. setting wt. % /sample	Naraachamspos							
	G C 2a	G/M C 2b	G/M C 2c	G/M C 3_1	G/M C 3_2	G C 17 a	G/M C17 b	M C17 c
SiO <sub>2</sub>	n.d.	n.d.	n.d.	n.d.	n.d.	64.0	n.d.	n.d.
TiO <sub>2</sub>	n.d.	n.d.	n.d.	n.d.	n.d.	0.91	n.d.	n.d.
Al <sub>2</sub> O <sub>3</sub>	n.d.	n.d.	n.d.	n.d.	n.d.	16.2	n.d.	n.d.
Fe <sub>2</sub> O <sub>3</sub>	1.90	2.66	1.68	3.76	14.21	2.5	2.33	2.19
MnO	n.d.	n.d.	n.d.	n.d.	n.d.	0.03	n.d.	n.d.
MgO	n.d.	n.d.	n.d.	n.d.	n.d.	4.87	n.d.	n.d.
CaO	n.d.	n.d.	n.d.	n.d.	n.d.	3.36	n.d.	n.d.
Na <sub>2</sub> O	0.42	0.13	0.20	0.06	0.07	0.19	0.07	0.07
K <sub>2</sub> O	1.60	2.76	1.75	6.33	7.23	6.18	5.25	3.61
P <sub>2</sub> O <sub>5</sub>	n.d.	n.d.	n.d.	n.d.	n.d.	0.34	n.d.	n.d.
LOI	35.9	27.6	34.1	11.7	9.38	6.80	11.7	24.8
Total	--	--	--	--	n.d.	98.6	n.d.	n.d.
<b>ppm</b>								
Cr	20.2	65.4	35.4	94.1	110	191	88.5	41.4
Co	18.2	32.7	16.9	40.7	56.9	2.93	7.04	14.0
Ni	93.0	132	128	172	257	48.2	82.1	63.6
Au (ppb)	<1.0	<1.1	<0.9	0.5	<0.9	<0.7	0.3	<0.9

Location Strat. setting wt. %/ sample	Entrance of South Valley						
	G C 14a	G/M C 14b	G/M C 14c	G/M C 14d	G/M C 14d1	G/M C 14d2	M C 14e
SiO <sub>2</sub>	n.d.	24.0	52.9	n.d.	n.d.	n.d.	n.d.
TiO <sub>2</sub>	n.d.	0.40	0.63	n.d.	n.d.	n.d.	n.d.
Al <sub>2</sub> O <sub>3</sub>	n.d.	6.93	13.5	n.d.	n.d.	n.d.	n.d.
Fe <sub>2</sub> O <sub>3</sub>	1.86	3.08	2.48	2.35	17.1	1.55	2.98
MnO	n.d.	0.02	n.d.	n.d.	n.d.	n.d.	n.d.
MgO	n.d.	24.2	8.52	n.d.	n.d.	n.d.	n.d.
CaO	n.d.	38.6	15.5	n.d.	n.d.	n.d.	n.d.
Na <sub>2</sub> O	0.04	0.22	0.16	0.09	0.03	0.09	0.04
K <sub>2</sub> O	1.53	1.81	5.11	8.65	1.64	8.89	0.50
P <sub>2</sub> O <sub>5</sub>	n.d.	0.24	0.24	n.d.	n.d.	n.d.	n.d.
LOI	36.3	43.9	17.4	4.3	n.d.	n.d.	42.6
Total	n.d.	99.4	98.9	n.d.	n.d.	n.d.	n.d.
<b>ppm</b>							
Cr	32.4	5.08	44.8	71.3	26.2	71.7	12.2
Co	3.79	3.28	5.93	4.83	62.2	4.87	12.2
Ni	26.7	6.5	43.2	75.0	139	51.8	27.8
Au (ppb)	0.5	<0.3	<0.5	1.1	0.8	<0.6	0.3

Location Strat. setting wt. %	Entrance of S Valley					
	G C 14a-T	G/M C 14b-T	G/M C 14c-T	G/M C 14d-T	M C 14e-T	
Fe <sub>2</sub> O <sub>3</sub>	3.04	2.80	2.00	18.3	11.5	
Na <sub>2</sub> O	0.10	0.08	0.09	0.08	0.06	
K <sub>2</sub> O	8.78	5.93	8.54	6.89	1.73	
<b>ppm</b>						
Cr	158	133	111	65.4	32.4	
Co	4.39	7.80	6.47	49.2	22.5	
Ni	122	97.5	128	206	109	
Au (ppb)	<0.8	0.7	<0.8	0.9	0.7	

Location Strat. setting wt. % / sample	Khowarib Valley					Warmquelle		
	G/M C 15b	G/M C 15c	M C 15d	G/M C 15e	M C 15e1	G C 16a	G/M C 16b	M C 16c
SiO <sub>2</sub>	31.6	28.2	55.8	n.d.	n.d.	39.0	19.3	80.7
TiO <sub>2</sub>	0.34	0.35	0.67	n.d.	n.d.	1.14	0.25	0.48
Al <sub>2</sub> O <sub>3</sub>	6.44	5.97	13.4	n.d.	n.d.	20.6	4.36	8.68
Fe <sub>2</sub> O <sub>3</sub>	1.43	1.65	3.36	2.06	0.47	7.31	2.30	2.07
MnO	n.d.	0.01	0.01	n.d.	n.d.	n.d.	0.02	n.d.
MgO	15.9	24.7	9.34	n.d.	n.d.	4.89	28.5	1.63
CaO	39.8	35.36	10.7	n.d.	n.d.	14.8	44.2	1.14
Na <sub>2</sub> O	0.16	0.19	0.14	0.03	0.02	0.23	0.11	0.14
K <sub>2</sub> O	2.29	1.98	5.73	3.81	0.35	8.46	0.42	3.29
P <sub>2</sub> O <sub>5</sub>	0.79	0.65	0.35	n.d.	n.d.	0.36	0.15	0.26
LOI	32.6	35.6	15.4	27.4	44.8	14.4	39.9	2.95
Total	98.8	99.0	99.5	n.d.	n.d.	96.9	99.7	98.4
<b>ppm</b>								
Cr	26.9	24.6	73.7	40.0	3.42	151	25.3	59.8
Co	3.38	2.60	6.69	11.6	2.68	9.68	3.49	0.75
Ni	11.3	23.1	40.2	34.6	<19	62.9	18.3	11.7
Au (ppb)	<0.3	<0.4	<0.6	<0.9	<0.4	<0.9	0.6	0.2

Location Strat. setting wt. %	Fransfontain		Tweelingskop		Bethanis		Khowarib Valley		Warmquelle	
	M C 1a-T	G/M C 1b-T	O C 4-T	G C 5b-T	G/M C 6-T	M C 7-T	G/M C 15b-T	G/M C 15e-T	G/M C 16b-T	M C 16c-T
Fe <sub>2</sub> O <sub>3</sub>	1.85	3.31	3.77	3.62	5.70	7.95	3.04	14.2	2.57	4.48
Na <sub>2</sub> O	0.10	0.13	0.21	0.03	0.29	0.80	0.07	0.07	0.08	0.06
K <sub>2</sub> O	6.61	8.14	3.98	0.21	1.34	2.98	7.78	10.2	5.19	3.57
<b>ppm</b>										
Cr	95.9	84.4	110	16.8	23.1	86.7	127	68.1	87.0	70.3
Co	13.0	12.5	5.39	2.19	7.95	21.0	7.54	9.30	4.37	2.00
Ni	147	288	55.1	16.1	78.1	275	49.5	81.2	96.2	48.8
Au (ppb)	2.3	<1	0.4	0.2	<0.8	<0.9	<0.9	0.8	1.6	0.6

**B) Sturtian transition layer**

Strat. setting wt. %/ sample	Copper Mine				Steilrandberge		Sesfontain-Opuwo		
	R	C/R	C	C	C/R	R	C	C/R	R
	C 8	C 9	C 10_1	C 10_2	C 12	C 12a	C 13a	C 13b	C 13c
SiO <sub>2</sub>	n.d.	67.3	61.9	68.1	29.7	n.d.	46.5	47.4	n.d.
TiO <sub>2</sub>	n.d.	0.62	0.61	0.72	0.19	n.d.	0.39	0.65	n.d.
Al <sub>2</sub> O <sub>3</sub>	n.d.	9.26	12.0	14.6	2.72	n.d.	3.65	6.72	n.d.
Fe <sub>2</sub> O <sub>3</sub>	1.74	12.0	2.02	2.56	25.4	0.62	42.1	32.3	1.61
MnO	n.d.	b.d.l.	b.d.l.	b.d.l.	b.d.l.	n.d.	0.01	0.04	n.d.
MgO	n.d.	0.98	7.48	0.53	1.32	n.d.	1.16	1.30	n.d.
CaO	n.d.	1.53	6.47	1.78	34.3	n.d.	1.28	5.60	n.d.
Na <sub>2</sub> O	0.05	0.20	0.21	0.24	0.13	0.05	0.13	0.14	0.01
K <sub>2</sub> O	<0.4	5.94	7.53	9.03	0.93	0.16	1.27	2.39	0.10
P <sub>2</sub> O <sub>5</sub>	n.d.	0.21	0.20	0.22	0.09	n.d.	0.18	0.57	n.d.
LOI	35.8	2.93	11.1	1.68	25.2	42.9	7.28	7.23	45.7
Total	--	97.8	98.4	97.8	94.8	--	96.7	97.1	--
<b>ppm</b>									
Cr	8.52	66.2	61.0	74.3	15.2	4.57	26.4	37.6	11.3
Co	4.42	5.96	3.16	3.75	4.90	1.72	17.4	34.4	1.65
Ni	21.2	25.9	30.2	28.0	25.4	3.33	147	38.7	4.23
Au (ppb)	<0.5	0.4	0.4	<0.7	16.7	0.9	1.7	0.9	0.2

Location Strat. setting wt. %	Copper Mine				Steilrandberge	Sesfontain-Opuwo		
	R	C/R	C	C	C/R	C	C/R	R
	C 8-T	C 9-T	C 10-1-T	C 10_2-T	C 12-T	C 13a-T	C 13b-T	C 13c-T
Fe <sub>2</sub> O <sub>3</sub>	11.9	11.8	2.35	5.15	48.1	36.7	30.1	20.7
Na <sub>2</sub> O	0.04	0.10	0.12	0.11	0.08	0.24	0.03	0.03
K <sub>2</sub> O	2.04	7.04	8.93	9.69	3.04	2.05	2.81	3.29
<b>ppm</b>								
Cr	47.4	114	73.0	150	61.1	46.9	50.8	53.8
Co	18.8	6.31	3.85	9.37	12.8	16.5	24.4	23.5
Ni	59.4	95.4	40.2	63.2	67.8	146	72.5	173
Au (ppb)	0.7	0.6	<0.6	0.6	36.7	3.2	1.0	2.9

**C) Marinoan cap carbonates - profile**

Location		Warmquelle profile										
Strat. setting		M	M	M	M	M	G/M	G/M	G/M	M	M	M
wt. %		K2-01	K2-02	K2-03	K2-04	K2-05	K2-06	K2-07	K2-08	K2-09	K2-10	K2-11
Fe <sub>2</sub> O <sub>3</sub>		1.32	1.33	1.04	0.62	4.38	3.39	3.22	1.17	0.59	0.55	0.36
Na <sub>2</sub> O		0.07	0.07	0.07	0.07	0.05	0.03	0.03	0.02	0.02	0.02	0.02
K <sub>2</sub> O		3.11	3.23	3.51	3.57	2.97	0.65	0.45	0.35	0.27	0.18	0.19
LOI		n.d.	5.66	4.74	2.98	5.38	39.4	42.8	44.3	45.8	46.5	46.5
<b>ppm</b>												
Cr		61.5	62.5	71.8	61.5	34.3	8.63	9.80	5.89	5.17	2.53	3.8
Co		2.31	1.29	1.02	0.57	2.84	15.1	29.3	10.6	3.02	2.72	1.73
Ni		17.1	23.1	15.0	8.6	35.8	45.2	80.0	28.6	12.2	7.7	7.3
Au (ppb)		0.3	<0.4	<0.4	<0.3	0.2	<0.4	<0.4	<0.2	<0.2	0.1	0.1

Location		Entrance of South Valley Profile									
Strat. setting		G/M	G/M	M	M	M	M	M	M	M	M
wt%		K4-01	K4-02	K4-03	K4-04	K4-05	K4-06	K4-07	K4-08		
Fe <sub>2</sub> O <sub>3</sub>		9.05	2.22	0.48	0.44	0.45	0.47	0.50	0.45		0.45
Na <sub>2</sub> O		0.03	0.03	0.03	0.02	0.03	0.03	0.03	0.03		0.03
K <sub>2</sub> O		0.26	0.19	0.28	0.26	0.27	0.34	0.34	0.34		0.28
LOI		n.d.	45.4	45.9	46.0	45.8	43.6	46.0	45.8		45.8
<b>ppm</b>											
Cr		16.9	5.22	4.54	3.05	3.68	6.10	3.85	3.30		3.30
Co		38.5	6.45	2.39	2.01	1.88	2.20	2.41	2.06		2.06
Ni		89.1	16.5	11.1	4.9	8.9	11.9	11.8	4.7		4.7
Au (ppb)		0.4	2.3	0.3	<0.2	0.1	<0.2	<0.2	<0.2		<0.2

Location		Khowarib Valley profile							
Strat. setting		M	M	M	M	M	M	M	M
wt. %		P49-01	P49-02	P49-03	P49-04	P49-05	P49-06	P49-07	
Fe <sub>2</sub> O <sub>3</sub>		0.21	0.16	0.15	0.15	0.19	0.19	0.15	
Na <sub>2</sub> O		0.02	0.01	0.02	0.02	0.02	0.02	0.01	
K <sub>2</sub> O		0.22	0.21	0.17	0.11	0.16	0.12	0.14	
LOI		n.d.	46.4	46.5	46.6	46.6	46.6	46.5	
<b>ppm</b>									
Cr		3.40	2.22	1.89	1.93	1.74	2.05	1.52	
Co		1.56	1.37	1.32	1.44	1.62	1.61	1.24	
Ni		5.8	3.5	5.4	6.8	6.6	7.3	3.7	
Au (ppb)		<0.2	<0.2	<0.2	<0.2	<0.2	<0.2	<0.1	

Location		Khowarib Valley profile								
Strat. setting		M	M	M	M	M	M	M	M	M
wt. %		P49-08	P49-09	P49-11	P49-12	P49-13	P49-14	P49-16	P49-18	
Fe <sub>2</sub> O <sub>3</sub>		0.16	0.16	0.15	0.18	0.19	0.17	0.18	0.18	
Na <sub>2</sub> O		0.02	0.02	0.01	0.01	0.01	0.01	0.02	0.01	
K <sub>2</sub> O		0.19	0.16	0.14	0.13	0.13	0.13	0.13	0.13	
LOI		46.4	46.4	46.3	46.4	46.5	46.3	46.5	46.5	
<b>ppm</b>										
Cr		1.80	1.68	1.59	1.63	1.58	1.57	2.50	1.54	
Co		1.11	1.08	1.10	1.21	1.21	1.12	1.38	1.14	
Ni		4.8	5.1	3.3	4.4	3.4	4.9	4.9	3.4	
Au (ppb)		<0.2	0.1	<0.1	<0.1	<0.1	<0.2	<0.2	<0.2	

## 4.5 Discussion

Koeberl et al. (2007) suggested that the impact of an asteroid onto the ice-covered planet might lead to a deglaciation of the Snowball Earth, although details remained open. Thus a search for possible evidence of any impact ejecta debris in post-glacial transition layers would be one possibility to find evidence for such a hypothesis. However, no impact crater or impact ejecta have been detected, which formed during the Snowball Earth glaciation or deglaciation. However, several impact craters have been dated near the Cryogenian Period, but their ages are not very accurately known (Strangways  $646 \pm 42$ , Söderfjärden  $\sim 600$ , Beaverhead  $\sim 600$ , Saarijärvi  $> 600$ , Jänisjärvi  $700 \pm 5$  million years old; cf. Earth Impact Database, 2013). In addition, all these craters are relatively small, from 6 to 60 km diameter.

In a search to confirm the Ir anomalies detected by Bodiselitsch et al. (2005) at other locations, Peucker-Ehrenbrink and Hoffman (2006) indeed detected higher Os concentrations with a lower than crustal radiogenic Os isotopic component for Marinoan postglacial transition layers in Canadian Cordillera, revealing a possible mixture of terrestrial and extraterrestrial Os. But Waters et al. (2009, 2010) measured platinum group element (PGE) abundances and Re-Os isotope systematics of two continuous Marinoan deposits from the Otavi Platform and Hoanib Shelf basin in northwestern Namibia and found mostly crustal-level Os concentrations for both sections (5.0-74 ppt), with a lack of significant anomalies. One sample from the Hoanib Shelf basin is an exception, with an Os concentration of 0.7 ppb. In their analyses, osmium concentrations vary inversely with sediment accumulation rates, and samples with higher Os concentrations have less radiogenic Os, which is consistent with binary mixing between terrestrial and extraterrestrial Os, similar to what was found by Peucker-Ehrenbrink and Hoffman (2006). Nevertheless, no distinct and unambiguous PGE or Os isotope signal was found, making a global presence of an extraterrestrial anomaly in Sturtian and Marinoan postglacial transition layers less likely.

As noted above, impact ejecta should contain evidence of shock metamorphism or the geochemical or mineralogical signature of an extraterrestrial component (cf. Montanari and Koeberl, 2000; Gabrielli et al., 2006; Cavosie et al., 2010; French and Koeberl, 2010; Koeberl et al., 2012). Our postglacial boundary layer samples do not contain any high pressure phases, chrome spinels, or geochemical impact signatures (Table 3., Figs. 3-5.). In ejecta layers, the shocked minerals should be a primary phase, and not have formed by secondary processes, such as diagenesis. Quartz, feldspar, and muscovite were identified as detrital minerals in our samples, with feldspar grains starting to be altered to kaolinite. Several locations, Naraachamspos (Marinoan) (C3\_1, C3\_2) and Copper Mine (Sturtian) (C8) contain coarser fragments of detrital minerals (quartz pebble -3 mm, feldspar - 0.1 mm), which contain nei-

ther shock lamellae (PDF) and planar fractures (PF), nor high pressure phases. In general, the quartz occurs as a secondary fracture filling phase, and no PDFs occur. However, the mica and chlorite contain kink bends, but these can be formed by metamorphism due normal tectonic regime. Little is known about shock deformation of calcite (e.g., Huson et al., 2009), but calcite can develop dense mechanical twins, which was noted in a few calcite grains in K2\_1 and K4\_1 sample (Fig. 3.). Differently oriented dense deformation lamellae in carbonate occur in heterogeneous stress field at the time of deformation in sedimentary rock, so enhanced twin lamellae/mm in calcite probably indicate increased shear stress. Sigmaclasts were observed in Marinoan postglacial basal cap carbonate (profile C2a), which can be explained by normal tectonic pressure. The PGE abundances (e.g., Ir, Os) are below the detection limit (below 400 ppb for Os, and below 2.5 ppb for Ir) of INAA for our Sturtian and Marinoan postglacial transition layers. It might of course be possible that any signature is in the sub-ppb range for Ir and Os; but the determination of such low abundances was beyond the scope of the present work. For a more detailed geochemical study, the PGE abundances in the clay fraction and of separated montmorillonites might be needed, as well as Os or Cr-isotope data. In our samples the Cr, Co, Ni abundances were near (Marinoan: C3\_1, C3\_2, C17a-b, C2a-b, Sturtian: C9, C10) or below to the upper crustal values (Rudnick and Gao, 2003) (especially postglacial cap carbonates), and thus do not indicate any geochemical signature of impact ejecta (Table 3.). Chrome spinels, as an impact marker mineral, also could not be identified in the silt fraction or in the coarser fraction with binocular microscopy and SEM-EDS analyses.

Several Sturtian (C8, C10 from Copper Mine) and Marinoan (C14a, b-c –Entrance to the Southern Valley) postglacial boundary layers contain smectite-rich clays (smectite, chlorite, rectorite kaolinite). Smectite rich-clays can be formed by weathering of impact ejecta and fireball layer deposits (Ferrel and Dypvik, 2003). However, the smectite in our samples are derived from diagenesis and/or weathering of iron biomats or leaching, based on microtextural evidence (Gyollai et al. in prep.). Thus, no unambiguous geochemical or mineralogical signature has been observed for meteoritic impact in Sturtian and Marinoan postglacial transition layers in Otavi Group, NW-Namibia.

*Thus we can summarize our observations in two different ways:*

- (1) there might have been an impact event at the end of one or both Snowball Earth glaciation periods, but no direct evidence is visible in our samples, at least not at the search level. Some impact marker minerals might have been altered to clay minerals (smectite, rectorite, fine-grained chlorite), but this is not confirming evidence of an impact event. The weathering of mineral fragments of meteorite minerals is a rapid process within the marine

environment, where geochemical signatures can be changed due to diagenesis and weathering. Bodiselitsch et al. (2005) found Ir anomalies in samples from near to our research area, which did not appear at other locations of Neoproterozoic Snowball glaciations, making the “cosmic dust deposition” hypothesis difficult to confirm elsewhere. If an Ir anomaly occurs only at one outcrop of a marine stratigraphic section (Congo Craton – Bodiselitsch et al. 2005), a nearby marine impact could be postulated. But again, similar results would be expected at least within the same region. Only some admixture of extraterrestrial material was indicated in samples from this region by the analyses of Waters et al. (2009, 2010), but our samples did not provide evidence for any significant extraterrestrial component; however, a small component might still exist, as our geochemical analyses had rather high detection limits. Nevertheless, no impact ejecta materials, such as shocked minerals, were found either.

- (2) There was no meteorite impact, and the minor Cr, Co, Ni enrichment was derived by iron-biomats or hydrothermal vents. The smectites are derived from diagenesis and/or weathering of iron biomats or leaching. The microtectonical and synsedimentary structures are derived by turbidite flow of rift basin, or post depositional tectonic processes or anchimetamorphosis during the diagenesis.

## 4.6 Conclusions

The lack of unambiguous mineralogical and geochemical signatures does not provide immediate support for any meteorite impact-induced deglaciation of the Sturtian and Marinoan glaciations. Other signatures, such as kinked mica, have normal tectonic origin. The smectite-rich boundary layers might include the signature of a marine impact, but the main component most likely formed by weathering of volcanic ash.

## 4.7 Acknowledgements

We are grateful to Peter Nagl (XRF), Lutz Nasdala, Eugen Libowitzky (micro-Raman Spectroscopy), and Susanne Gier (XRD), Lidia Pittarello and Ludovic Ferriere (SEM) for help in lab work and helpful discussions. This study was supported by the Austrian Academy of Sciences through a grant to C.K. (International Geological Correlation Program IGCP No. 512, project title: „Search for an extraterrestrial component for triggering Neoproterozoic Snowball Earth aftermath”). We are grateful for support by the Geological Survey of Namibia and its Director Dr. G. Schneider with relation to field work organization and sample export management. We appreciate the help of the reactor team of the Institute of Atomic and Subatomic Physics, Vienna, with the irradiations.

## 4.8 References

- Bodiselič, B., Koeberl, C., Master, S. and Reimold, W.U., 2005. Estimating duration and intensity of Neoproterozoic Snowball glaciations from iridium anomaly. *Science*, 308, 239-242.
- Boggs, S., Jr., Krinsley, D. H., Goles, G. G., Seyedolali, A. and Dypvik, H., 2001. Identification of shocked quartz by scanning cathodoluminescence imaging. *Meteoritics and Planetary Science*, 36, 783-791.
- Cavosie, A.J., Quintero, R.R., Radovan, H.A. and Moser, D.E. 2010. A record of ancient cataclysm in modern sand: Shock microstructures in detrital minerals from the Vaal River, Vredefort Dome, South Africa. *Geological Society of America Bulletin* 122, 1968–1980.
- Donnadieu, Y., Fluteau, F., Ramstein, G., Ritz, C. and Besse, J., 2003. Is there a conflict between the Neoproterozoic glacial deposits and the snowball Earth interpretation: an improved understanding with numerical modeling. *Earth and Planetary Science Letters*, 208, 101-112.
- Dypvik, H. and Jansa, L. F., 2003. Sedimentary signatures and processes during marine bolide impacts: a review. *Sedimentary Geology*, 161, 309–337.
- Earth Impact Database: <http://www.passc.net/EarthImpactDatabase/index.html>, accessed September 29, 2013.
- Eyles, N. and Januszczak, N., 2004. “Zipper-rift”: a tectonic model for Neoproterozoic glaciations during the breakup of Rodinia after 750 Ma. *Earth-Science Reviews*, 65, 1–73.
- Ferrell, R.E., Jr., and Dypvik, H., 2003. The mineralogy of the Exmore beds – Chickahominy Formation boundary section of the Chesapeake Bay impact structure revealed in the Eyreville core, in Gohn, G.S., Koeberl, C., Miller K.C., and Reimold, W.U., eds. *The ICDP-USGS Deep Drilling Project in Chesapeake bay Impact structure: Results from Eyreville Core Holes: Geological Society of America Special Paper 458*, 723 -746.
- Ferrière, L., 2008. Shock metamorphism and geochemistry of impactites from the Bosumtwi impact structure: A case study of shock-induced deformations and transformations in quartz and associated methodology. PhD Thesis, University of Vienna, 297 pp.
- French, B.M. and Koeberl, C., 2010. The convincing identification of terrestrial meteorite impact structures: What works, what doesn't, and why. *Earth-Science Reviews*, 98, 123–170.

- Gabrielli, P., Plane, J.M.C., Boutron, C.F., Hong, S., Cozzi, G., Cescon, P., Ferrari, C., Crutzen, P.J., Petit, J.R., Lipenkov, V.Y. and Barbante, C. 2006. A climatic control on the accretion of meteoric and super-chondritic iridium–platinum to the Antarctic ice cap. *Earth and Planetary Science Letters*, 250, 459–469.
- Glass, B.P. and Simonson, B.M., 2013. *Distal Impact Ejecta Layers. A Record of Large Impacts in Sedimentary Deposits*. Springer, Heidelberg, 716 pp.
- Hamers, M.F. and Drury, M.R., 2011. Scanning electron microscope-cathodoluminescence (SEM-CL) imaging of planar deformation features and tectonic deformation lamellae in quartz. *Meteoritics and Planetary Science*, 16, 1814-1831.
- Harland, W.B., 1964. Critical evidence for a great Infra-Cambrian glaciation. *Geologische Rundschau*, 54, 45–61.
- Harland, W.B. and Rudwick, M.J.S., 1964. The great infra-Cambrian ice age. *Scientific American* 211, 28-36.
- Hedberg, R.M., 1975. *Stratigraphy of the Owamboland basin, South West Africa*. - Ph.D. thesis, Harvard University, Cambridge.
- Hedberg, R.M., 1979. *Stratigraphy of the Owamboland basin, South West Africa*. *Bulletin of Precambrian Research Unit, Cape Town*, 24, 325 pp.
- Henderson, P. and Henderson, G., 2009. *The Cambridge Handbook of Earth Science Data*. Cambridge University Press, Cambridge, UK, 286 p.
- Hoffman, P.F., 2002. Carbonates bounding glacial deposits: Evidence for Snowball Earth episodes and greenhouse aftermaths in the Neoproterozoic Otavi Group of northern Namibia. *IAS Field Excursion Guidebook, 16th International Geology Congress, Rand Africaans Univ., Johannesburg, S-Africa*, 39 pp.
- Hoffman, P.F., 2005. 28th DeBeers Alex. Du Toit Memorial Lecture, 2004. On Cryogenian (Neoproterozoic) ice-sheet dynamics and the limitations of the glacial sedimentary record. *South African Journal of Geology*, 108, 557-576.
- Hoffman, P. F. and Schrag, D. P., 2002. The Snowball Earth hypothesis: testing the limits of global change. *Terra Nova*, 14, 129-155.
- Hoffman, P. F., Kaufman, A. J., Halverson, G. P. and Schrag, D. P., 1998. A Neoproterozoic Snowball Earth. *Science*, 281, 1342–1346.

- Hoffmann, K.-H., and Prave, A.R., 1996. A preliminary note on a revised subdivision and regional correlation of the Otavi Group based on glaciogenic diamictites and associated cap dolostones. *Communications of the Geological Society of Namibia*, 11, 81-86.
- Huson, S. A., Foit, F. F., Watkinson, A. J. and Pope, M. C., 2009. Rietveld analysis of X-ray powder diffraction patterns as a potential tool for the identification of impact-deformed carbonate rocks. *Meteoritics and Planetary Science*, 44, 1695–1706.
- Jarosewich, E., Clarke, R.S.J., and Barrows, J.N., 1987. The Allende meteorite reference sample. *Smithsonian Contributions to the Earth Sciences*, 27, 1–49.
- Kennedy, M.J., Mrofka D., and von der Borch C. (2008): Snowball Earth termination by destabilization of equatorial permafrost methane clathrate. – *Nature*, 453, 642-645.
- Kirschvink, J.L., 1992. Late Proterozoic low-latitude global glaciation: the Snowball Earth. In: J.W. Schopf and C. Klein (eds.), *The Proterozoic Biosphere* (, Cambridge University Press, Cambridge, pp. 51–52.
- Koeberl, C., 1998. Identification of meteoritic components in impactites. - In: Grady, M.M., Hutchison, R., McCall, G.J.H. and Rothery, D.A. (editors): *Meteorites: Flux with Time and Impact Effects*. Geological Society London Special Publication, 140, pp. 133-153.
- Koeberl, C., Ivanov, B.A. and Goodman, B.A., 2007a. Impact triggering of the Snowball Earth deglaciation? Bridging the Gap II: Effect of Target Properties on the Impact Cratering Process, Abstracts of the conference held September 22-26, 2007 in Saint-Hubert, Canada. Lunar and Planetary Institute Contribution No. 1360, pp. 62-63.
- Koeberl C., Ivanov, B.A., and Goodman J., 2007b. Impact-induced deglaciation of the Snowball Earth? *EOS Trans. American Geophysical Union* 88(52), Fall Meet. Suppl., Abstract U22A-08.
- Koeberl, C., Claeys, P., Hecht, L., and McDonald, I., 2012. Geochemistry of impactites. *Elements*, 8, 37-42.
- Mader, D. and Koeberl, C., 2009. Using Instrumental Neutron Activation Analysis for geochemical analyses of terrestrial impact structures: Current analytical procedures at the University of Vienna Geochemistry Activation Analysis Laboratory. *Applied Radiation and Isotopes*, 67, 2100–2103.

- Martin, H., 1965. Beobachtungen zum Problem der jung-präkambrischen glazialen Ablagerungen in Südwestafrika (Observations concerning the problem of the late Precambrian glacial deposits in South West Africa). *Geologische Rundschau*, 54, 115-127.
- Montanari, A. and Koeberl, C., 2000. Impact stratigraphy: the Italian record. *Lectures Notes in Earth Sciences*, 93, Heidelberg: Springer Verlag. 364 pp.
- Peucker-Ehrenbrink, B. and Hoffman, P. F., 2006. Sedimentary PGE anomalies at Snowball Earth terminations. (abstract). *Geochimica et Cosmochimica Acta*, 70, A488.
- Pollard, D. and Kasting, J.F., 2004. Climate-ice sheet simulations of Neoproterozoic glaciation before and after collapse to Snowball Earth. In: Jenkins, G.S., McMenamin, M.A.S., McKey, C.P., and Sohl, L. (eds.) *The Extreme Proterozoic: Geology, Geochemistry, and Climate*. Geophysical Monograph 146, American Geophysical Union, Washington, DC., pp. 91-105.
- Rudnick, R.L., and Gao, S., 2003. Composition of the Continental Crust. In: R.I. Rudnick (ed.), *Treatise on Geochemistry*, 3, Elsevier, pp.1-64.
- Stöffler D. and Langenhorst F., 1994. Shock metamorphism of quartz in nature and experiment: I. Basic observations and theory. *Meteoritics*, 29, 155-181.
- Waters, C., Peucker-Ehrenbrink, B., and Hoffman, P.F., (2010). Platinum group element and Re-Os isotope systematics of Cryogenian glacial terminations. (abstract) *Geochimica et Cosmochimica Acta*, 74, A1117.
- Waters, C., Peucker-Ehrenbrink, B., and Hoffman, P.F., 2009. Platinum group element and Re-Os isotope systematics of Cryogenian glacial terminations. (abstract) American Geophysical Union, Fall Meeting 2009, abstract #U13A-0047.
- Williams, G.E., 1975. Late Precambrian glacial climate and the Earth's obliquity. *Geological Magazine*, 112, 441–465.
- Williams, G.E., 2000. Geological constraints on the Precambrian history of Earth's rotation and the Moon's orbit. *Reviews of Geophysics*, 38/1, 37-59.



## 5 Zn, C, and O Isotopic Variations Associated with Neoproterozoic Marinoan Glaciations

Maxwell M. Thiemens<sup>1,2\*</sup>, Robina Shaheen<sup>3</sup>, Ildiko Gyollai<sup>4</sup>, Kenneth Chong<sup>3</sup>, Friedrich Popp<sup>5</sup>, Christian Koeberl<sup>4,6</sup>, Mark H. Thiemens<sup>3</sup>, Frederic Moynier<sup>1</sup>

<sup>1</sup>Department of Earth and Planetary Sciences, Washington University in Saint Louis, 1 Brookings Drive St. Louis, MO 63130, <sup>2</sup>Institut für Planetologie, Wilhelm-Klemm-Str. 10 48149 Münster, Germany,

<sup>3</sup>Department of Chemistry, University of California, San Diego, 9500 Gilman Drive # 0356 La Jolla, CA 92093-0356, <sup>4</sup>Department of Lithospheric Research, University of Vienna, Althanstrasse 14, A-1090

Vienna, Austria <sup>5</sup>Department of Geodynamics and Sedimentology, University of Vienna, Althanstrasse 14, A-1090 Vienna, Austria, <sup>6</sup>Natural History Museum, Burgring 7, A-1010 Vienna, Austria

\*Corresponding Author: e-mail: [mthie\\_03@uni-muenster.de](mailto:mthie_03@uni-muenster.de)

Main Address: 1

Current Address: 2

Phone: +49 251 83-3349 6 Ext: 39708

**Article was submitted to “Precambrian Research” on 15<sup>th</sup> February 2014.**

**Abstract :** We report a multi-isotopic oxygen (O), carbon (C), and zinc (Zn) analysis of Otavi group samples from northern Namibia that belong to the Marinoan glaciation of the Cryogenian period (850-635 Myr). The  $\delta^{18}\text{O}$  (standardized to the Vienna Pee Dee Belemnite, V-PDB) carbonate composition indicates that the samples were largely unaltered. Measurement of the  $\delta^{13}\text{C}$  (standardized to V-PDB) finds an offset between calcite and dolomite, presumably due to changes in depositional chemistry. This study represents the first comparison between C, O, and Zn isotopic compositions in these carbonates.

At  $\delta^{66}\text{Zn}$  values of 0.45 ‰ (JMC Lyon standard), a significant CIE (Carbon Isotope Excursion) was observed (at  $\delta^{13}\text{C} = -6$  ‰) with some Zn and C isotope ratio covariations near  $\delta^{13}\text{C}$  values of -3 per mil. The differences in the variation of the two isotope systems require multiple processes. As the  $\delta^{13}\text{C}$  composition varies whereas  $\delta^{66}\text{Zn}$  remains constant, two reservoirs are required to account for the observations. As large Zn isotopic fractionations typically require biological processes (*e.g.*, metabolic), the data imply that the process when Zn isotopic composition varies is different from the process which fractionates C isotopes, where a biological effect would be implausible due to the massive inorganic C, nutrient devoid reservoir. Zinc that is sourced from hydrothermal vents will also be isotopically light, requiring both Zn and C isotopes to differentiate the hydrothermally fractionated Zn from biological sources. We find the hydrothermally fractionated Zn to be the dominant source of Zn in the car-

bonates, although some sample sites could have been modified by post-depositional biological activity.

**Keywords:** Zinc, Carbon, Oxygen, Marinoan, Namibia

## 5.1 Introduction

The Snowball Earth or Cryogenian period precedes one of the greatest diversifications of life on Earth, ending the so-called "boring billion" wherein biology remained relatively stagnant, and the study of what led to these key events and what occurred during them has been well summarized (Sumner et al., 1987; Hoffman et al., 1998, 2007). The basic Snowball Earth hypothesis holds that the positioning of continents at low latitudes could induce a positive feedback effect because of greatly enhanced silicate weathering, leading to worldwide glaciations as drawdown of the atmospheric CO<sub>2</sub> reservoir causes decreased IR radiative forcing, weakened Hadley cell heat transfer, with concomitant growth of ice caps, a decrease of planetary albedo, and a net decrease of temperature the thermal conditions. The result is runaway thermal effects and the oceans freezing solid, or nearly so (e.g., Baum and Crowley, 2001; Evans, 2000; Evans et al., 2000; Hyde et al., 2000; Kirschvink 1992; Marshall et al., 1988; Warren et al., 2002; Worsley and Kidder 1991).

With the biosphere and hydrosphere (silicate weathering) removed from the classical carbon cycle, only the lithosphere/atmosphere interaction remains active, until a buildup of atmospheric CO<sub>2</sub> levels to 0.12 bar from outgassing (assuming a planetary albedo of 0.6) ultimately thawing the glaciers (Caldeira and Kasting, 1992; Kirschvink, 1992; Walker et al., 1981). The global correlation of  $\delta^{13}\text{C}$  of Marinoan carbonates reflects the scale of the event. With the short residence time of oceanic carbon massive global events on rapid time scales (~10 kyr) must have occurred to produce the observed synchronicity (Kaufman et al., 1992; Kump and Arthur, 1999; Veizer et al., 1999). The  $\delta^{13}\text{C}$  composition of the carbonates is presumed to be buffered against diagenetic effects due to their large carbon reservoir size, rendering it a relatively robust isotope system for its preservation (Veizer et al., 1999). The Neoproterozoic geological record contains  $\delta^{13}\text{C}$  changes of >10 ‰, the largest of which bracket the global glacial events (Jacobsen and Kaufman, 1999; Walter et al., 2000). These excursions begin with a steep decline in  $\delta^{13}\text{C}$  prior to glacial onset, with a  $\delta^{13}\text{C}$  of  $-6 \pm 1$  ‰ in the Cap Carbonates, the same value as hydrothermal CO<sub>2</sub> from mid-ocean ridges (Brasier and Shields, 2000; Hoffman et al., 1998; Hoffman and Schrag, 2002; Kaufman and Knoll, 1995; Kaufman et al., 1997). Measurement of organic  $\delta^{13}\text{C}$  from the same deposits reveals a tracking of the inorganic isotopic values with  $\delta^{13}\text{C}_{\text{org}}$  values reaching a low of -33 ‰ (Summons and Hayes, 1992).

With post glacial carbonate formation being particularly high due to the quantity of CO<sub>2</sub> brought into the oceans, low δ<sup>13</sup>C values should persist even with climatic recovery (Hoffman and Maloof, 1999; Hoffman and Schrag, 2002). There is an extended input time period given the large amount of CO<sub>2</sub>, though the actual timeline of carbonate formation is still poorly constrained.

The measurement of δ<sup>18</sup>O in carbonates provides insight and measure of properties, such as temperature, reservoir exchange and relative sizes, and sources (Jaffres et al., 2007; Veizer et al., 1999). The oceans' δ<sup>18</sup>O is modeled to have been ~13 ‰ (V-PDB) during the Neoproterozoic (Jaffres et al., 2007), with a steady climb to the uncharacteristically high δ<sup>18</sup>O of -3 ‰ seen after the Marinoan glaciations. Shields (2005) and Hoffman et al. (2007) hypothesize that these values reflect the admission of glacial melt water into the surface ocean, though it may also be the consequence of a massive carbon reservoir in oceanic deepwater that transfers to the sedimentary record.

Precise measurements of isotopic ratios of non-traditional stable isotopes through the multi-collection inductively-coupled-plasma mass-spectrometry (MC-ICP-MS) such as Zn opens the possibility of new insights to the glacial events as it may identify sources and time-scales differently than oxygen and carbon. Zn has five stable isotopes and exhibits a small range in isotopic composition of terrestrial rock samples (Chen et al., 2013). This is largely a combination of its high atomic mass and single available valence state. The main processes affecting the Zn isotope composition are evaporation/condensation processes, adsorption (organic and inorganic), diffusion, and biological translocation (Cloquet et al., 2008). It is traditionally expressed in the δ<sup>x</sup>Zn notation:

$$\delta^x\text{Zn} = \left[ \frac{\left( \frac{X_{\text{Zn}}}{^{64}\text{Zn}} \right)_{\text{sample}} - \left( \frac{X_{\text{Zn}}}{^{64}\text{Zn}} \right)_{\text{JMC-Lyon}}}{\left( \frac{X_{\text{Zn}}}{^{64}\text{Zn}} \right)_{\text{JMC-Lyon}}} \right] \times 1000$$

with x=66, or 68.

Zinc is a key nutrient for organisms, where it is used in protein synthesis and membrane activities (e.g., Welch et al., 1982; Frassinetti et al., 2006). Zinc has a residence time of 51 kyr in modern oceans, and 99% of the dissolved Zn found in seawater is bound to organic ligands (Bruland, 1989). Zinc isotopes have a very homogeneous composition in terrestrial rocks, with a typical isotopic composition of δ<sup>66</sup>Zn ranging between 0.2 to 0.4 ‰ in igneous rocks (Herzog et al., 2009; Paniello et al., 2012, Chen et al. 2013) and up to 0.70 ‰ in some

sedimentary rocks and ores (Albarede, 2004). The  $\delta^{66}\text{Zn}$  values of hydrothermal systems generally match those of basalts, unless there is significant sulfide subsidence and input, in which case the deposited Zn will become isotopically heavier (John et al., 2008). Zinc isotope abundances are unfractionated at pH less than 5.5, but can vary in the pH range of 5-8 (Pons et al., 2013). Pons et al. (2013) discuss the maximum  $\delta^{66}\text{Zn}$  values correlating to Zn binding with phosphates, another potential source for the heavy Zn signal. The isotopic composition defines the biogenic and authigenic sediments, as heavy Zn leaves the system with the formation of phosphate.

Natural samples with isotopically light Zn (negative  $\delta^{66}\text{Zn}$ , down to -0.90%) are uncommon, and the largest variation occurs in biological materials (e.g., cells) (John et al., 2007; Moynier et al., 2009a; Weiss et al., 2005), consistent with energetically favorable preferential uptake of light isotopes by biological activity and participation via catalytic reactions. The process is highly energy selective, producing an isotopic between different Zn species (Fujii et al., 2011; Pons et al., 2013). Pichat et al. (2003) found that  $\delta^{66}\text{Zn}$  variations in recent carbonates (from the last 175 ky) were correlated with biological productivity in the rock record. In the modern ocean, Zn tends to be isotopically light in the surface ocean and becomes heavier at greater oceanic depth as organic matter dissolves during its sinking (Bermin et al., 2006; Boyle et al., 2012).

Previous experiments have determined the single stage biological fractionation of Zn isotopes by organisms, including microorganisms as well as more recently evolved species such as C3 and C4 plants and mammals (Cloquet et al., 2008; Gélabert et al., 2006; John et al., 2007; Moynier et al., 2009a). From these experiments it was determined that organisms preferentially use the lighter Zn isotopes for biological functions, while retaining an “outer pool” of Zn adsorbed on the cell’s surface, causing the cell to become isotopically light while the dissolved Zn in the environment becomes isotopically heavy. This combined process allows the use of Zn as an alternate biological benchmark to the traditional carbon. This has value as organisms conventionally alter isotopes in enzymatic catalytic metabolic processes; consequently the different elements capture different segments of biologic activity, and, potentially, other organisms.

The Cryogenian glaciations have been postulated to be responsible for periods of rapid biological evolution as evidenced by increased organism complexity and diversity following the glaciations (Hoffman and Schrag, 2000). In particular the Marinoan glaciation, the final event of the Cryogenian before the Ediacaran, precedes the appearance of the first metazoans (Peterson et al., 2004), large shifts in the biogeochemical carbon cycles (Canfield et al., 2007), and an overall rise of atmospheric oxygen (Kennedy, 1996). The association between

the Marinoan glaciations and large changes in biological mass (consisting in this era of micro-organisms) makes the Zn isotopic composition an ideal test, as it is significantly modified by biological activity (metabolic) and, coupled with carbon isotopic measurements, will provide deeper insight into the cumulative process.

We performed isotopic measurements to evaluate changes in biological activity by measuring the Zn isotopic composition of cap carbonate samples in parallel to the traditional C and O isotopic ratios, which are traditionally used to detect the event by their change, especially for carbon. The Zn isotopic composition of cap carbonate samples from the Nuccaleena Formation in the Flinders Ranges, South Australia, has been measured in a recent study by Kunzmann et al. (2012), who propose a two-stage evolution of the ocean post glacial event based upon the observed variation. In the first post event stage the  $\delta^{66}\text{Zn}$  declines from 0.47 to 0.07 ‰. This is most likely due to the influx of light Zn from weathering of isotopically light source rocks. The  $\delta^{66}\text{Zn}$  subsequently increases to 0.87 ‰ in a second stage, which is attributed to the effects of the reactivation of the biosphere. Kunzmann et al. (2012) present a single profile, single site which demonstrates the potential of Zn isotopic measurements in carbonates for reconstruction of the biosphere and its recovery. They suggested the need for a more global basis observation data set to determine if the zinc isotopic excursion is local or global. In the present study we expand the study to a different location (Namibia) and include multiple sample sites.

## 5.2 Materials and Methods

Multi-isotopic analysis of boundary layer samples dated to the Marinoan glaciation event (635 Myr) in Northern Namibia was performed for C, O, and Zn isotopic compositions. These samples (Fig. 1, map of the area) were collected by one of us (F. P.) and processed at the University of Vienna. Samples are primarily from layers nearest at/above the boundary between the uppermost Ghaub glacial diamictite and the basal post-glacial cap dolomite (Keilberg Mb. of the Maieberg Fm./ basal Karibib Fm. respectively). They were collected primarily from the distal slope facies deposits abutting the Otavi platform at outcrops near Fransfontain (sample C1 / 20°11'59.06"S; 15° 0'58.68"E) and near Naraachamspos (sample C3 and profile 1/ 20°11'27.68"S"; 14°51'4.42"E). Other samples were collected from outcrops representing inner Otavi platform facies deposits; these sample sites are located within the Khowarib Fold Belt near Ongongo (profile 2 / 19° 8'35.77"S; 13°51'15.40"E), at the head of a valley extending from Entrance (near Devede village) towards the SW (sample C14 / 19°11'18.40"S; 13°56'13.39"E) and lastly at the hillside of the Khowarib valley (sample C15/ 19°18'24.52"S; 13°59'25.57"E).

Our samples from the Otavi Group's distal slope facies focus on the immediate transition layers mediating between glacial Ghaub deposits and their post-glacial Keilberg cap carbonate. The tested transition layers from both related sample sites are expected to be synchronous deposits: A) Sample C1 (eastward from C35 road cut near Fransfontain) comes from the top layer of a shift sequence composed of debrite and well-bedded, fining upward dololomite choked throughout with outsized clasts of ice-rafted debris, the lot representing the upper Ghaub Formation (Bethanis Member). Paraconformably overlying the tested transition layer, characterized by its content of marly lutite, is a cm-layered, micropeloidal Keilberg cap dolostone (basal Karibib Fm., respectively) featuring giant wave ripple-structures at its base and transitioning into limestone rhythmite in the hanging wall. B) The Fransfontain slope at Naraachamspos (Pip's rock) exhibits stratified and finally ice-rafted debris flows of the Bethanis Member (upper Ghaub Fm.) which is overlain with a sharp contact by stratified dolomicrite of the basal Keilberg Member (basal Karibib Fm.)

Our profile 1 spans the basal 20 cm of these capping dolomite strata, whereas samples C3 is a collection of samples from the direct contact of the two Formations, and are listed in Table 1. as C2, C1C, C17C and C3 samples. Our samples from the Otavi Group's inner platform facies region are also focused on Marinoan postglacial transition layers, but those are expected to be diachronous with respect to our slope facies samples: C) At Ongongo locality our profile 2 consists of 16 single samples covering a total thickness of 5.5 meters of the hanging wall fitted to the Marinoan Boundary, with the lithology constituted by a bulky brown-gray dolomite specific for the inner platform facies of the Keilberg cap carbonate (Maieberg Formation). The basal contact of the tested Keilberg cap dolostone is a glacial erosional surface on top of the Ombaatjie formation. Consequently, the Ghaub diamictite is lacking or sparse in places. Furthermore, due to Pan-African folding and thrusting, the contact is tectonically overprinted and layers are vertically dipping. The subjacent upper Ombaatjie strata display a regressive cycle of shallow-water carbonate culminating in aeolianite when running dry in some locations. At the same locality Halverson et al. (2002) realized a complete cycle of a Trezona  $\delta^{13}\text{C}$  excursion, indicating a perturbation in the carbon cycle leading to the Ghaub Glaciation in the upper Ombaatjie Formation. Consequently, the glacial erosional surface at the base of our tested Keilberg dolostone profile did not significantly erode strata from the Ombaatjie platform, but removed most of the Ghaub glacial deposits.

Within the Khowarib fold belt our samples C14 (Entrance towards SW valley) and C15 (eastern Khowarib valley) represent the Marinoan boundary contact in platform facies lithologies; thin red-green marly lutite marks the boundary between diamictite and cap dolomite, the latter being reddish stained at its base. As cap carbonates from this area are some

of the most studied samples from the Neoproterozoic, they provide ideal subjects for exploration through new isotope system measurements.

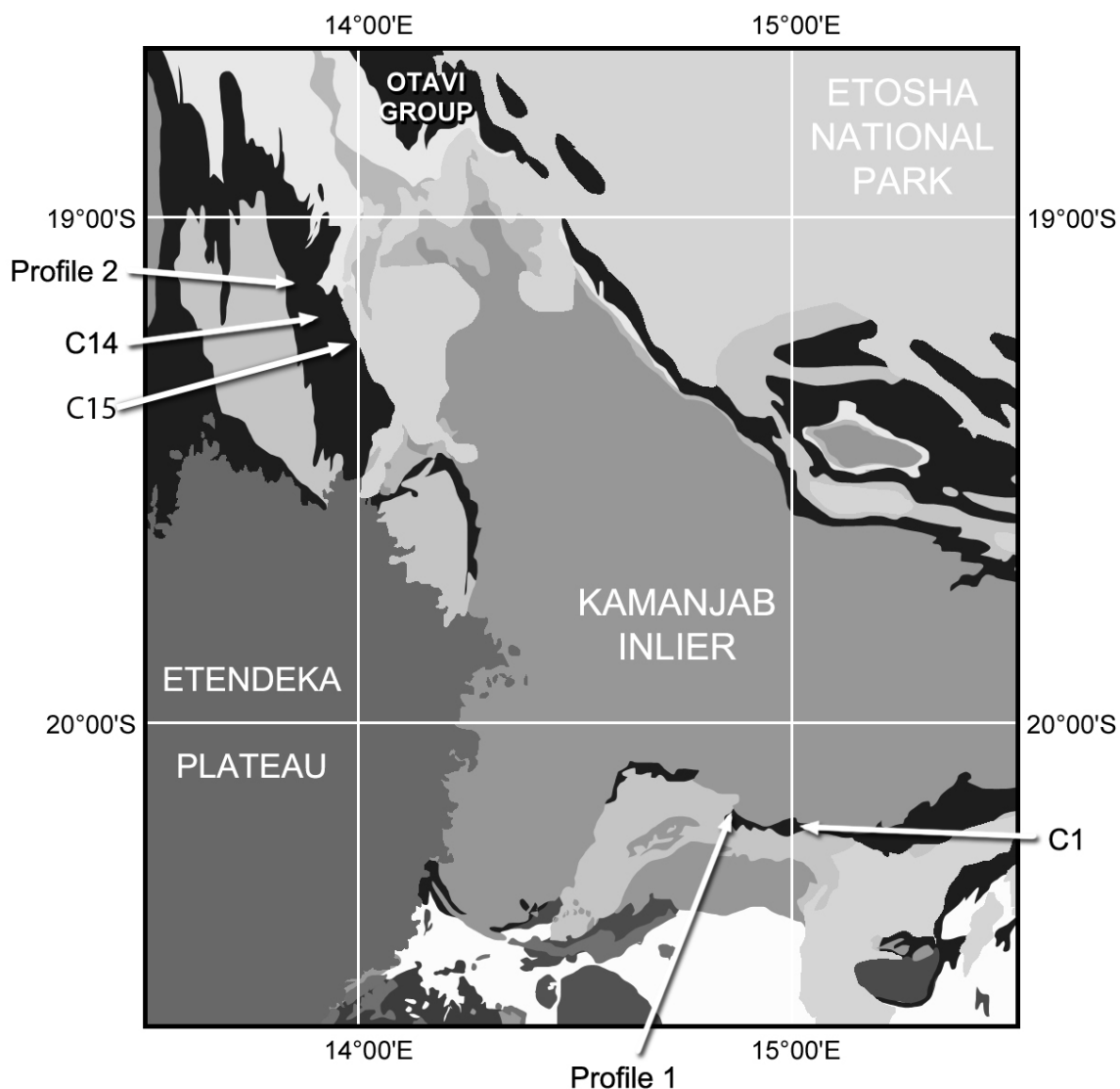


**Figure 1.** Sample collection map: Profile 1 (C3 is from this same site): Topmost diamictite from Naraachampos. Profile 2: Brown-gray dolomite from the Keilberg cap carbonates in the Maieberg Formation. C14, C15 are from the Khararib Valley, from the Maieberg Formation.

Zinc isotopic measurements were performed at Washington University in St. Louis. Powdered samples of 0.2 g were dissolved in cold 2N 10% acetic acid to extract calcite from the sediments. Samples were sonicated for two hours to ensure full dissolution. The acetic acid phase containing the carbonate fraction was centrifuged and dried under a heat lamp, then redissolved in 1.5N HBr with the addition of 0.001 %  $H_2O_2$ . Separation of the Zn from its potentially interfering chemical isobars and sample matrix is done through anion-exchange

chromatography (Moynier et al., 2006, 2009b). The total yield of the chemistry is >99% and the typical blank is 10ng. Isotopic measurements were performed on a Thermo Scientific Neptune MC-ICP-MS following the same procedure as Paniello et al. (2012). Reproducibility was typically better than 50 ppm, within the 95 % confidence interval, based on replicate analyses.

Carbon and O isotopic measurements were performed at the University of California, San Diego. Fine powdered samples were added to the reaction vessel containing 100% phosphoric acid ( $\text{H}_3\text{PO}_4$ ) in the side arm. The sample tube was pumped overnight to remove trapped air in the acid. The acid was added to the evacuated carbonate powder at room temperature and allowed to react for 8h at  $25 \pm 2^\circ\text{C}$ . The  $\text{CO}_2$  gas was cryogenically separated using two glass spiral traps (trap I at  $-65^\circ\text{C}$  to collect water and trap II at  $-196^\circ\text{C}$  to collect  $\text{CO}_2$ ) and non-condensable gas was removed from the system. The trap II was replaced with ethanol slush at  $-65^\circ\text{C}$  and  $\text{CO}_2$  was transferred to the sample tube. After  $\text{CO}_2$  extraction, the sample tube was placed in a silicone bath at  $150^\circ\text{C}$  for 4 hours and  $\text{CO}_2$  released at this temperature was collected as described above. The  $\text{CO}_2$  extraction at two different temperatures allowed to separate Ca-rich phase from the Fe-Mg-Mn rich phase (Al-Aasm et al., 1990). The C and O isotopic composition of purified  $\text{CO}_2$  gas was measured using Finnigan MAT 253 Isotope Ratio Mass Spectrometer, as described in detail by Shaheen et al. (2010). Control samples of carbonate of known isotopic composition were routinely analyzed to insure isotopic precision and accuracy. For replicate mass spectrometric analysis 1 sigma standard deviations (SD) is 0.01‰ for  $^{13}\text{C}$  and  $^{18}\text{O}$ . Overall reproducibility for acid dissolution and gas chromatography steps for  $\text{CO}_2$  gas ( $n = 5$ ) is  $\pm 0.05$  ‰ for  $^{13}\text{C}$  and  $\pm 0.1$  ‰ for  $^{18}\text{O}$ .

### 5.3 Results

The Zn, C, and O isotopic data from the cap carbonates are presented in Table 1., and Figures 2 to 5. All  $\delta^{13}\text{C}$  measurements are standardized to V-PDB. Figure 2 shows a plot of the  $\delta^{13}\text{C}$  against the  $\delta^{18}\text{O}$  compositions, where we find little correlation between the two isotopic systems. The  $\delta^{18}\text{O}$  values vary between -3 and 12 ‰ (Standardized to VPDB) (Figure 2.) and  $\delta^{13}\text{C}$  between 0 and -10 ‰.  $\delta^{13}\text{C}$  exhibits a general correlation between the chemically separated non-calcite (primarily composed of siderite; Tziperman et al., 2011) and calcite (Figure 3.). In the majority of samples the high temperature extract component has a concentration of released  $\text{CO}_2$  ~10 times larger than for calcite. At Site 1 we observe  $\delta^{13}\text{C}$  to remain constant while  $\delta^{66}\text{Zn}$  varies widely. At site 2 and C3, the  $\delta^{66}\text{Zn}$  values do not fluctuate, while the  $\delta^{13}\text{C}$  values reach the low of -6 ‰. At  $\delta^{13}\text{C}$  values of -3,  $\delta^{66}\text{Zn}$  undergoes greater variation. At C14  $\delta^{66}\text{Zn}$  reaches its heaviest ratio, while  $\delta^{13}\text{C}$  is isotopically lightest.

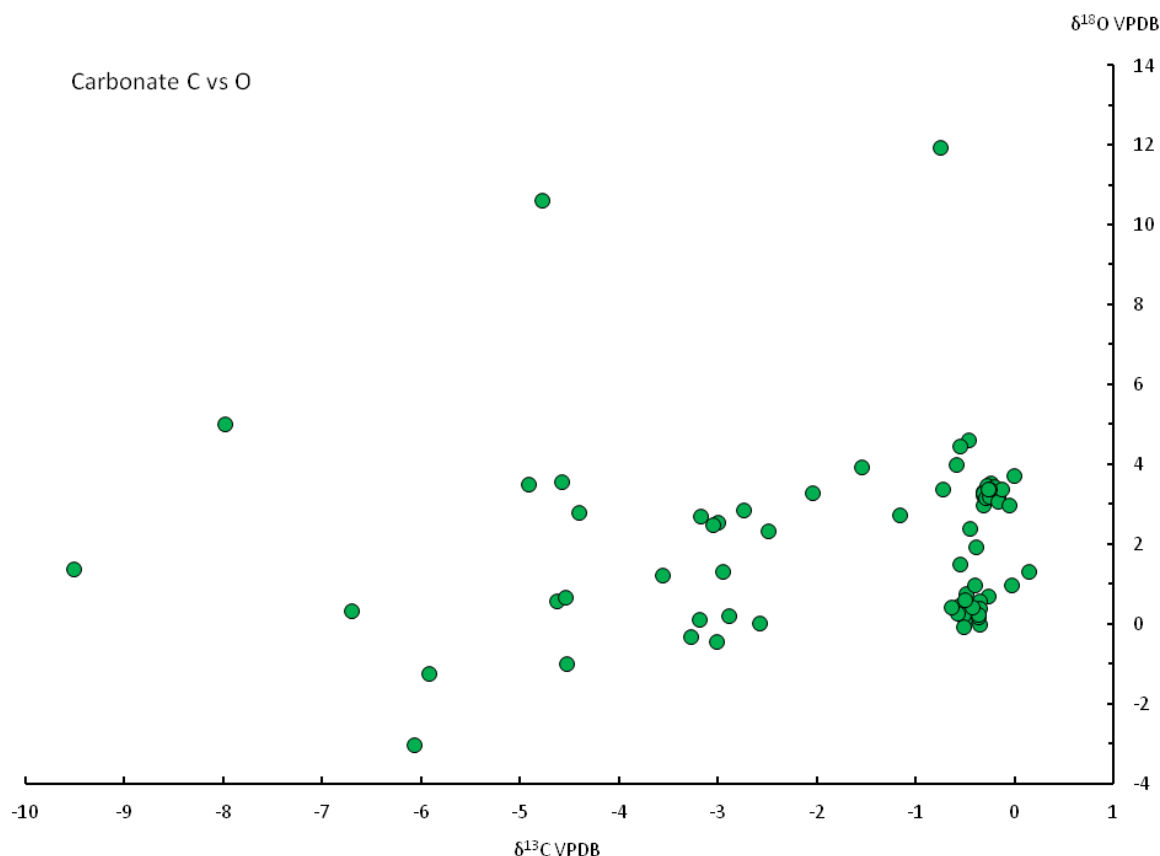


**Figure 2.**  $\delta^{13}\text{C}$  vs.  $\delta^{18}\text{O}$ : The plot of  $\delta^{13}\text{C}$  vs.  $\delta^{18}\text{O}$  shows little evidence of correlation, but the  $\delta^{18}\text{O}$  values cluster mostly between 2‰ and 5‰.

Direct comparison of the  $\delta^{66}\text{Zn}$  and  $\delta^{18}\text{O}$  (Figure 4.) finds that the variation of Zn isotopic ratios beyond standard terrestrial values occurs between  $\delta^{18}\text{O}$  values of 2 and 5 ‰. Similarly,

$\delta^{18}\text{O}$  variations occur primarily within the relatively narrow range of  $\delta^{66}\text{Zn}$  values  $0.40 \pm 0.05$  ‰.

Comparisons of the  $\delta^{66}\text{Zn}$  with  $\delta^{13}\text{C}$  (Figure 5.) shows the greatest variation of Zn isotopic ratios beyond standard terrestrial values and they correlate with  $\delta^{13}\text{C}$  values of 0 to -1 ‰. In turn, the  $\delta^{13}\text{C}$  excursions occur almost exclusively within the range of  $\delta^{66}\text{Zn}$  values of 0.3 and 0.5 ‰.

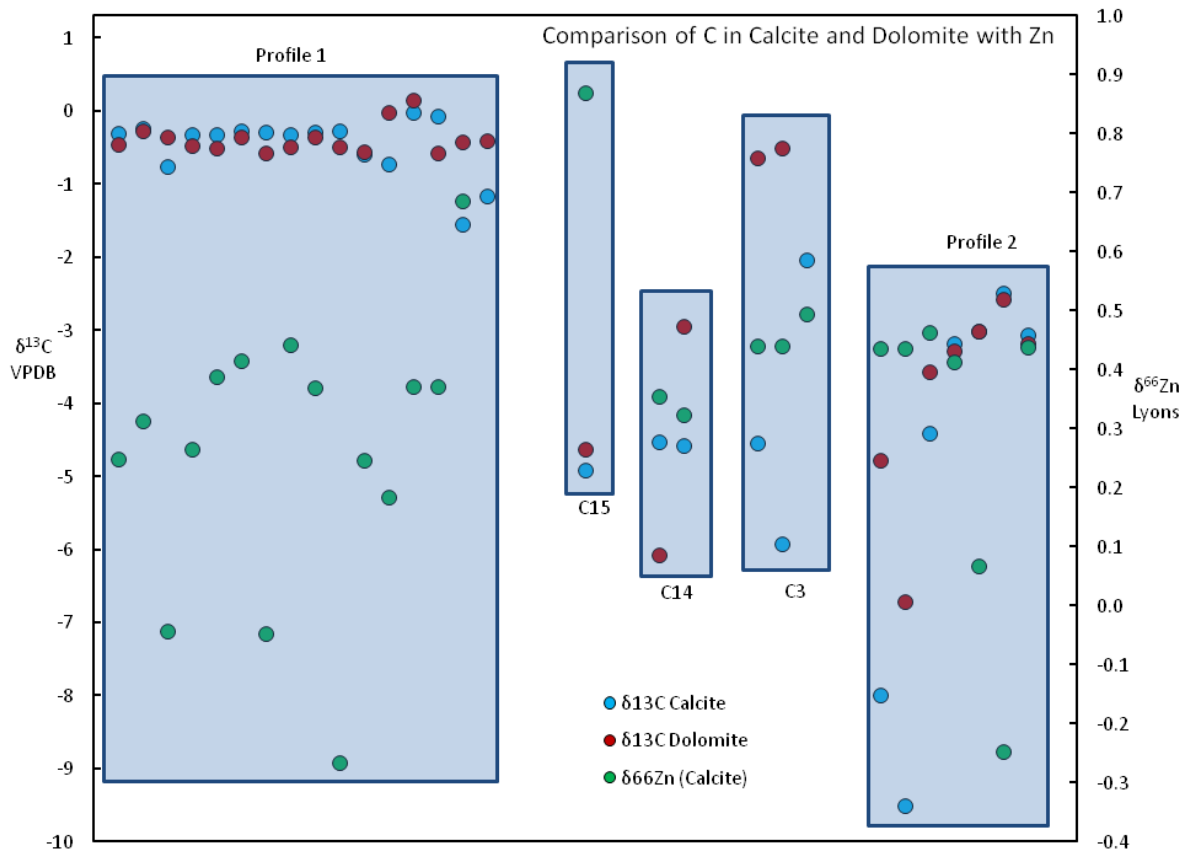


**Figure 3**  $\delta^{66}\text{Zn}$  and  $\delta^{13}\text{C}$ : Comparison of the Zn and C across multiple profiles. The x-axis is used to cluster samples from the same sites, with the samples taken from closest to the boundary layer preferentially plotted closer towards the y-axis (that is, towards 0). In profile 1 the  $\delta^{13}\text{C}$  is relatively constant, while the  $\delta^{66}\text{Zn}$  shows its widest variations. In profile 2 and C3, the  $\delta^{66}\text{Zn}$  stays relatively constant while the  $\delta^{13}\text{C}$  dips to the excursion of -6‰. At  $\delta^{13}\text{C}$  values of -3,  $\delta^{66}\text{Zn}$  undergoes greater variation. At C14 note the low C values with the highest  $\delta^{66}\text{Zn}$ , while C15 shows one of the highest  $\delta^{66}\text{Zn}$  values, of 0.9 ‰, while the  $\delta^{13}\text{C}$  are at -5 ‰.

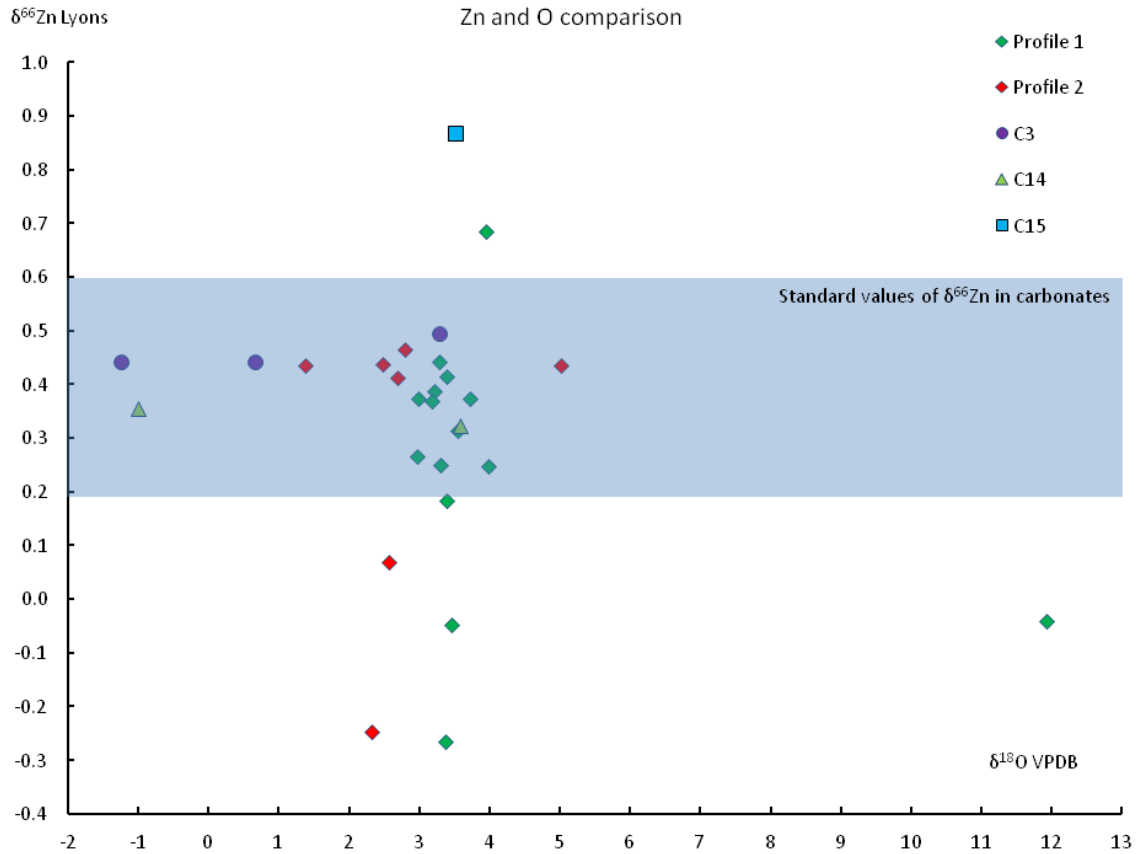


**Figure 4**  $\delta^{18}\text{O}$  vs.  $\delta^{66}\text{Zn}$ : A direct comparison of  $\delta^{18}\text{O}$  and  $\delta^{66}\text{Zn}$ , showing that the variation of Zn beyond standard terrestrial values occurs between  $\delta^{18}\text{O}$  values of 2 and 5‰.

Comparisons of the  $\delta^{66}\text{Zn}$  with  $\delta^{13}\text{C}$  (Figure 5.) shows the greatest variation of Zn isotopic ratios beyond standard terrestrial values to concentrate within  $\delta^{13}\text{C}$  values of 0 to -1‰ though other variations in Zn isotopes occur. Most notably, the  $\delta^{13}\text{C}$  excursions occur almost exclusively in the range of  $\delta^{66}\text{Zn}$  between 0.3‰ and 0.5‰.

## Comparison of C and Zn

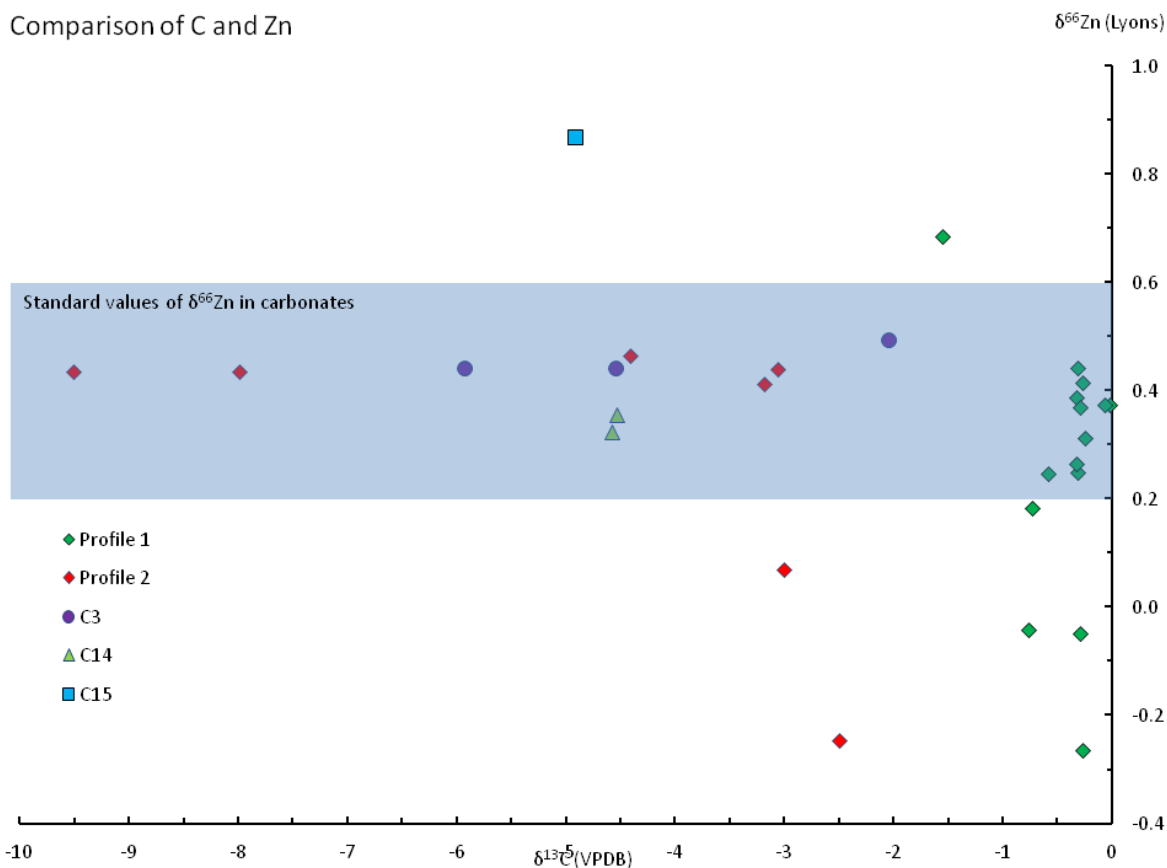


**Figure 5.**  $\delta^{13}\text{C}$  vs.  $\delta^{66}\text{Zn}$ : A plot comparing  $\delta^{13}\text{C}$  and  $\delta^{66}\text{Zn}$ , demonstrating that the variations of Zn isotope values beyond standard terrestrial values are largely concentrated within  $\delta^{13}\text{C}$  values of 0 to -1‰.

## 5.4 Discussion

An important facet in interpreting the Zn isotopic results and the potential influence of biological activity or hydrothermal activity is that all potential isotopic sources of Zn isotopic must be identified. Changes in the speciation of Zn (particularly when sulfides are involved) have been shown to be a major source of Zn isotopic variation (Fujii et al., 2011).

The relevant speciation of Zn within the ocean is controlled primarily by the ambient pH. During these specific glaciations periods the pH may fluctuate due to the high variations of dissolved  $\text{CO}_2$  as well as from the overall ocean chemistry and delivery of acidic and basic materials. The pH of standard ocean water during the Cryogenian is modeled as 8.1, the same as present, while during the post glacial periods the pH has been shown by models to have dropped to as low as 7.0 (Kasemann et al., 2005). At pH values of 7 and 8.1, the primary species of Zn in the modern ocean is  $\text{Zn}^{2+}$  (Zirino and Yamato, 1972), and little or no Zn isotopic variations are expected within this range of pH. The lifetime of Zn in the ocean is pH

dependent, and a change in pH beyond these modeled values would change Zn concentrations and speciation (Bruland et al., 1994). If the ocean is basic, it will be an insoluble Zn oxide and have a shorter lifetime, while under more acidic conditions the Zn becomes uncomplexed and more soluble with a longer lifetime. For the current models of the late Neoproterozoic oceans, we preclude the possibility of Zn being fractionated through speciation as the pH changes would not likely produce a significant isotopic variation due to changes in solubility products (Fujii et al., 2011).

Of issue is whether the Zn is representative of the carbonates or if it has been secondarily altered through diagenesis. Our oxygen isotopic measurements indicate that diagenesis was not undergone, and certainly not to a degree where the Zn isotopic record would be altered. If this had been the case, we should have observed an oxygen “reset”, where the values are all in the same band, from when the diagenetic event occurred. Given the differences in the oxygen values, we can conclude that there was not a major diagenetic event. In the modern ocean the Zn isotopic values correlate with crustal values (Bermin et al., 2006), although there are variations based on depth. These observed variations require a biological source, and if the observed Zn isotopic variations do not arise from inorganic processes then the fractionation of Zn towards heavy values observed in the carbonates must be a function of the intervention of biological processes.

Changes in the redox states of the ocean will affect the biological pool’s biochemical access to zinc as a consequence of the change in its chemical speciation and bioavailability. Zinc serves as a limiting reagent in the biosphere, which in turn modulates the zinc isotopic composition during carbonate burial as uncomplexed Zn. This Zn speciation is easier for biological organisms to utilize in metabolic processes (John et al., 2007). We postulate that the observed heavy Zn isotope ratios may be the consequence of extreme biological activity and partitioning of zinc into heavy and light reservoirs (Cloquet et al., 2008; John et al., 2007; Gelabert et al., 2006). The Zn utilized in the formation of  $\text{ZnCO}_3$  is the residual aqueous phase of Zn in the oceanic, near-shore reservoir, which should be isotopically heavy as the lighter isotopes of Zn are preferentially taken up by the biosphere.

With the large detrital flux into the ocean (or other aqueous reservoirs), plentiful nutrients (such as Zn) lift the traditionally restrictive restraints on limiting nutrients for living organisms, creating an ideal environment for reproduction. While light Zn isotopic ratios are easiest to explain as a biological component through a lack of alternate fractionation mechanisms, a heavy isotopic enrichment process is more limited and difficult to constrain. Negative  $\delta^{66}\text{Zn}$  values could be the result of sedimented light Zn removed from the biosphere during large-scale biosphere die-offs, as would be expected in the transient greenhouse following the

deglaciation, where global temperatures can oscillate between greenhouse and glacial conditions.

The heaviest  $\delta^{66}\text{Zn}$  observed values are also likely the consequence of biological activity, where Zn is removed from the biosphere by the sinking of decomposing organisms, with the “outer pool” being brought to the deep water while the light Zn remains in active use by other organisms, consequently producing two distinct isotopic zinc reservoirs. This could account for the range of  $\delta^{66}\text{Zn}$  that reaches a high value of 1.2 ‰. With a range of 0.00 to 1.04 ‰ for hydrothermal Zn, many of our observed  $\delta^{66}\text{Zn}$  values can be from the addition of hydrothermal Zn. Direct measurement of C and Zn isotopes in hydrothermal vent fluids and chimneys, expanding on the work in John et al. (2008) could provide better constraints on the potential source of the fractionation.

Comparison of the Zn isotopic variations with traditional systems finds a  $\delta^{13}\text{C}$  of  $-0.5 \pm 0.5$  with  $\delta^{66}\text{Zn}$  in the range of  $-0.30$  to  $0.45$  ‰, and, for  $\delta^{13}\text{C}$  values below  $-1$  and a  $\delta^{66}\text{Zn}$  of  $0.45$  ‰ and a second association is apparent. The lack of direct correlation between the (possible) bio-signatures in Zn and C isotope ratios indicates that the potential biological event will not be the only factor in accounting for the range in both isotopic systems, and also shows the value of simultaneous isotopic measurements.

Comparison of these results with those of Kunzmann et al. (2012) indicates that the reported  $\delta^{66}\text{Zn}$  values are slightly higher at the transition zone. The initial  $\delta^{66}\text{Zn}$  should be representative of continental values, though these values fall in the potential range of hydrothermal as well. Their results trend towards lower values, which we observe in some of the transition layers. These lower  $\delta^{66}\text{Zn}$  compositions are in the range of mantle values ( $0.2$  to  $0.4$  ‰), certainly within the range of a hydrothermally dominated system (John et al., 2008). This is expected following resumption of oceanic mixing after the deglaciation. We postulate that the biosphere’s signal would override that of the hydrothermal system, though correlation of these results with sulfur and boron isotopes could provide better evidence of hydrothermal waters modulating the carbonates isotopic signature as sulfur captures both sources and redox states with its multiplicity of available sulfur valence states. Boron records the pH, capturing another parameter for the post glacial oceans. The precipitation of sphalerite (Zn sulfide) could cause hydrothermal sources of Zn to trend towards being isotopically heavy measurement of its sulfur and zinc isotopes is anticipated and should be a future measurement.

The Zn isotopic variations are measured in diverse regions of Namibia, indicating that these may have been localized events (Site 1, C14, C15). These isotopic variations are more likely to be the result of biologically fractionated Zn, as Zn isotope ratios below the continen-

tal average are, as mentioned above, characteristic of biological processes. The variations are found in only some of our sample sites, and we conclude that these values are the result of local events. These data further support the role of local biological processes, as one would not expect a homogeneous recovery of the biosphere, and variations in a smaller local reservoir should produce an amplified signal.

The variations of Zn could also be the result of massive amounts of zinc containing sediments being deposited in the ocean by extensive continental erosion during the wet, warm period following deglaciation. However, our methods only extract Zinc from the carbonates, so the potential heterogeneities from the potential detrital rocks may not be observed. If these rocks were to have dissolved to the point that the Zn was incorporated into the carbonate phase, the seawater record should still have overprinted it. Though we do not rule this out as a potential source of interference, it is likely of negligible size.

The decoupling of the C and Zn is particularly well explained by the proposed scenario, as the massive C reservoir in the ocean system could maintain constant values, while the Zn isotope ratios remain relatively unmodified. A location where the biosphere has resumed activity will show these Zn values on a local level, as opposed to what we would observe from hydrothermal Zn input.

Our values of  $\delta^{18}\text{O}$  when compared with the  $\delta^{13}\text{C}$  compare with the range of composite carbonate data reported by Jaffres et al. (2007). Previous measurements of  $\delta^{18}\text{O}$  show that both dolomites and low calcium carbonates have undergone mild diagenesis based on the modest variability compared to the variation in carbon isotopes (Bao et al., 2008; Zhou et al., 2010). Our measurements of  $\delta^{18}\text{O}$  in calcite are similar to the measured non-calcite carbonate, but fail to mirror the  $\delta^{13}\text{C}$  perturbation. This lack of variation may indicate a partial reset in the  $\delta^{18}\text{O}$  record, the result of extreme weathering effects as one would expect following a Snowball event. This would result in the oxygen isotopic compositional record associated with the primary deposition being lost.

Global temporal correlative observations of the Marinoan  $\delta^{13}\text{C}$  excursion show depletion in  $^{13}\text{C}$  relative to the mantle value of -5 ‰ (Halverson et al., 2010). Our carbon isotopic data agree with the ranges reported in previous studies of the Marinoan (Kasemann et al., 2005; Kaufman et al., 1991; Halverson et al., 2002; Hoffman et al., 1998; Hoffman and Maloof, 1999).

Measurement of  $\delta^{13}\text{C}$  in this study was performed on chemically separated calcium-poor carbonates and a calcium-rich phase (calcite), with the objective of determining the difference in the chemical record between the two minerals. Previous studies have been done on

bulk carbonate composition measurements (combining calcite and other non calcium carbonates), while our study makes use of chemical separation, and finds that the non-calcite (dolomite) tends to exhibit a more negative  $\delta^{13}\text{C}$  value than the calcite, though at the isotopically lightest points the calcite exceeds the dolomite. This reversal could be the result of a change in the composition or formation of the dolomite, which would change the relevant isotopic fractionation factors. The difference between the carbonate and organics is likely the result of the massive input of inorganic  $\delta^{13}\text{C}$  resulting from the glaciation ending greenhouse, while dolomite formation happens in areas rich in organic matter. The decoupling suggests different sourcing of materials, with perhaps the dolomite sampling the environment more extensively in its formation, giving it the negative values in excess of one would expect of the carbon signature following deglaciation, while the calcite incorporates the atmospheric  $\text{CO}_2$  more directly. Direct comparisons of our data with the results of Hoffman et al., (2007) show the measured range of carbon values to be within the normal variations of similar samples in the same time sequence.

Future work examining the difference in  $\delta^{13}\text{C}$  composition of the calcite and dolomite, as well as the  $\delta^{13}\text{C}_{\text{org}}$  could provide greater insight into the provenance of the carbonates and the prevailing conditions that formed them. Correlation of chemically separated calcite and low calcium carbonates with previously established stratigraphic data on the  $\delta^{13}\text{C}$  could yield enhanced information on the timing of the post-glaciation events. As dolomitization is a slower process than formation of calcite (Tucker and Wright, 1990), there is a potential for production of large amounts of siderite (Tziperman et al., 2011), allowing analysis of  $\delta^{13}\text{C}$  differences in different carbonate phases. Comparison of the rate of formation of low-calcium carbonates with models of  $\text{CO}_2$  dissolution can determine the rate of atmospheric recovery from the glaciations event.

**Table 1.** Comparison of the  $\delta^{13}\text{C}$  and  $\delta^{18}\text{O}$  in the Calcite and non-calcite (dolomite) samples, as well as the  $\delta^{66}\text{Zn}$  and  $\delta^{68}\text{Zn}$ .

calcite						dolomite									
Sample ID	CO <sub>2</sub> ( $\mu$ -mole) cc	SI (mv)	$\delta^{13}\text{C}$ cc	SD	$\delta^{18}\text{O}$ cc	SD	Sample ID	SI (mv)	CO <sub>2</sub> ( $\mu$ -mole) dol	$\delta^{13}\text{C}$ dol	SD	$\delta^{18}\text{O}$ dol	SD	$\delta^{66}\text{Zn}$	$\delta^{68}\text{Zn}$
c2a01	34.6	1252	-0.32	0.01	33.6	0.02	c2a01	1285	114	-0.46	0.01	32.7	0.02	0.25	0.53
c2a02	32.5	1140	-0.24	0.02	33.8	0.01	c2a02	1259	156	-0.27	0.01	30.9	0.03	0.31	0.62
c2a03	29.3	1318	-0.76	0.01	42.5	0.02	c2a03	1099	109	-0.36	0.01	30.2	0.02	-0.04	0.05
c2a04	36.4	1161	-0.32	0.01	33.3	0.04	c2a04	1137	131	-0.48	0.01	35.0	0.02	0.26	0.54
c2a05	44.7	1298	-0.32	0.01	33.5	0.03	c2a05	1298	140	-0.51	0.01	30.3	0.02	0.39	0.78
c2a06	42.3	1180	-0.27	0.01	33.7	0.03	c2a06	1195	155	-0.36	0.02	30.8	0.02	0.41	0.84
c2a07	53.2	1231	-0.29	0.01	33.8	0.03	c2a07	1267	142	-0.57	0.01	30.7	0.01	-0.05	0.09
c2a08	52.4	1337	-0.32	0.01	33.6	0.02	c2a08	1420	142	-0.49	0.02	30.6	0.03	0.44	0.89
c2a09	39.6	1146	-0.17	0.02	33.5	0.03	c2a09	1127	105	-0.37	0.03	30.4	0.02		
c2a10	53.0	1181	-0.30	0.03	33.5	0.02	c2a10	1293	122	-0.36	0.01	30.6	0.04	0.37	0.74
c2a11	56.2	1329	-0.25	0.01	33.5	0.03	2a11	1413	133	-0.52	0.01	30.4	0.04		
c2a12	46.5	1312	-0.17	0.01	33.3	0.02	c2a12	1375	107	-0.40	0.02	32.2	0.02		
c2a13	45.9	590	-0.21	0.01	33.7	0.02	c2a13	1323	125	-0.56	0.02	34.8	0.02		
c2a14	33.3	1541	-0.13	0.01	33.7	0.02	c2a14	1295	107	-0.37	0.02	30.4	0.02		
c2a15	64.3	1211	-0.26	0.03	33.7	0.03	c2a15	1268	151	-0.52	0.02	30.1	0.02	-0.26	0.50
c2a16	86.5	1389	-0.27	0.03	33.7	0.02	c2a16	1351	113	-0.50	0.01	31.0	0.02	0.25	0.49
c2a17	81.7	1008	-0.59	0.01	34.3	0.02	c2a17	1307	165	-0.55	0.02	31.8	0.01	0.18	0.32
C2A	14.9	537	-0.02	0.01	34.0	0.03	C2A	884	95.6	0.14	0.02	31.6	0.02	0.37	0.75
C2B	9.5	727	-0.07	0.02	33.3	0.02	C2B	1041	31.1	-0.58	0.01	30.5	0.03	0.37	0.74
C2-C	13.2	1056	-0.73	0.01	33.7	0.02	C2-C	1163	247	-0.03	0.02	31.2	0.02	0.18	0.32
C1C1	18.2	1303	-1.55	0.02	34.3	0.03	C1C	1003	90.7	-0.43	0.01	30.6	0.03	0.69	1.38
C17C1	3.14	379	-1.16	0.03	33.0	0.06	C17C	1315	46.9	-0.40	0.01	31.2	0.02		
C14D	1.09	831	-4.53	0.02	29.2	0.04	C14-d	537	5.34	-6.07	0.04	27.1	0.03	0.36	0.70
C14-E1	3.39	348	-4.58	0.02	33.9	0.05	C14-E	1243	273	-2.95	0.01	31.6	0.01	0.32	0.42
C3-1-1	1.83	132	-4.55	0.03	30.9	0.07	C31-1	1108	19.8	-0.64	0.02	30.6	0.03	0.44	0.90
C3-1-2	1.40	174	-5.93	0.05	28.9	0.02	C31-2	1123	31.7	-0.51	0.02	30.8	0.03	0.44	0.90
C3-2	3.02	370	-2.05	0.02	33.6	0.05	C3_2		39.4					0.49	1.01
k2A		1123	-7.99	0.01	35.4	0.04	k2A	1090		-4.78	0.09	41.1	0.26	0.44	0.84
k2A after GC			-9.51	0.00	31.6	0.02	k2A after GC	1168		-6.71	0.02	30.5	0.03	0.44	0.84
k2b	99.8	1324	-4.41	0.02	33.1	0.04	k2b	1139	108	-3.57	0.02	31.5	0.02	0.46	0.92
k2c	157	1273	-3.18	0.01	33.0	0.04	k2c	1250	82.7	-3.28	0.02	29.9	0.02	0.41	0.82
dc5 49/4	114	1236	-3.01	0.02	32.8	0.02	dc5 49/4	1294	195	-3.02	0.01	29.8	0.01	0.07	0.20
dc5 50/4	140	1245	-2.75	0.01	33.1	0.03	dc5 50/4	1311	147	-2.89	0.01	30.4	0.01	0.44	0.85

## 5.5 Conclusions

Multi-site, multi-isotope analysis of the Marinoan cap carbonates from Namibia reveal multiple contributing reservoirs of Zn in the aftermath of the Snowball Earth glaciations. Abnormal zinc isotope ratios ( $\delta^{66}\text{Zn}$  values below 0.2 ‰ and above 0.6 ‰) provide evidence for the potential influence of hydrothermally sourced Zn, as might be expected in a global thaw from a reservoir built up of materials outgassed from volcanic sources. This record is observed at several sample sites (Sites 1, 2, and C3). Local variations in  $\delta^{66}\text{Zn}$  values are found, and isotopically light excursions are best explained as having been derived from local resumption of biological activity.

We find that the most negative  $\delta^{13}\text{C}$  values, from -4 ‰ and lower correlate with  $\delta^{66}\text{Zn}$  values of approximately 0.45 ‰, indicating a decoupling between the two isotope systems, which should not be the case if biological fractionation of carbon was the major source of the isotopic variations. The primary source of the carbon signature is likely the carbon being drawn out of the atmosphere in the post glacial melting, though this leaves the variations unaccounted for.

Correlation of the carbon and oxygen isotope ratios in chemically separated calcite and dolomite are correlated, with the calcite tending to have lower  $\delta^{13}\text{C}$  values than the non-calcite. We conclude that the dolomites' more negative  $\delta^{13}\text{C}$  signature is a function of the differences in formation of the two minerals.

Further work, involving analysis of full profiles from more geologically diverse sample sites, could provide both corroborative evidence as well as better understanding of these chemical signatures. Further segregation of chemical species of carbonates and minerals hosting zinc (e.g., sphalerite) with total isotopic measurements would further amplify understanding of the relevant processes that occur during the Snowball period.

## 5.6 Acknowledgments

This study was supported by the Austrian Academy of Sciences through a grant to C.K. We are grateful for support by the Geological Survey of Namibia and its Director Dr. G. Schneider with relation to field work organization and sample export management. N. Marzban gratefully acknowledged for travel expenses.

## 5.7 References

- Al-Aasm, I.S., Taylor, B.E., South, B., 1990. Stable isotope analysis of multiple carbonate samples using selective acid extraction. *Chemical Geology*, 80, 119–125.
- Albarede, F., 2004. The stable isotope geochemistry of copper and zinc. In: Johnson, C. M., Beard, B. L., Albarede, F., (Eds.), *Geochemistry of Non-Traditional Stable Isotopes*. Mineralogical Society of America, Washington, 55, 409-427.
- Bao, H.M., Lyons, J.R., Zhou, C. M., 2008. Triple oxygen isotope evidence for elevated CO<sub>2</sub> levels after a Neoproterozoic glaciation. *Nature*, 453, 504-506.
- Baum, S.K., Crowley, T.J., 2001. GCM response to late Precambrian (similar to 590 Ma) ice-covered continents. *Geophysical Research Letters*, 28, 583-586.
- Bermin, J., Vance, D., Archer, C., Statham, P.J., 2006. The determination of the isotopic composition of Cu and Zn in seawater. *Chemical Geology*, 226, 280-297
- Boyle, E.A., John, S., Abouchami, W., Adkins, J.F., Echevoyen-Sanz, Y., Ellwood, M., Flegal, A.R., Fornace, K., Gallon, C., Galer, S., Gault-Ringold, M., Lacan, F., Radic, A., Rehkemper, M., Rouxel, O., Sohrin, Y., Stirling, C., Thompson, C., Vance, D., Xue, Z.C., Zhao, Y., 2012. TI GEOTRACES IC1 (BATS) contamination-prone trace element isotopes Cd, Fe, Pb, Zn, Cu, and Mo intercalibration. *Limnology and Oceanography Methods*, 10, 653-665.
- Bruland, K.W., 1989. Complexation of zinc by natural organic-ligands in the central North-Pacific. *Limnology and Oceanography*, 34, 269-285.
- Bruland, K.W., Orians, K.J., Cowen, J.P., 1994. Reactive trace-metals in the stratified North-Pacific. *Geochimica et Cosmochimica, Acta* 48, 3171-3182.
- Caldeira, K., Kasting, J.F., 1992. Susceptibility of the early Earth to irreversible glaciation caused by carbon-dioxide clouds. *Nature*, 359, 226-228.
- Canfield, D. E., Poulton, S. W., Narbonne, G. M., 2007. Late-Neoproterozoic deep-ocean oxygenation and the rise of animal life. *Science*, 315, 92-95.
- Chen H., Savage, P., Teng, F-Z., Helz, R.T., Moynier, F., 2013. Zinc isotope fractionation during magmatic differentiation and the isotopic composition of the bulk Earth. *Earth and Planetary Sciences Letters*, 369-370, 34-42.
- Cloquet, C., Carignan, J., Lehmann, M.F., Vanhaecke, F., 2008. Variation in the isotopic composition of zinc in the natural environment and the use of zinc isotopes in biogeosciences: a review. *Analytical and Bioanalytical Chemistry*, 390, 451-463.
- Evans, D.A.D., 2000. Stratigraphic, geochronological, and paleomagnetic constraints upon the neoproterozoic climatic paradox. *American Journal of Science*, 300, 347-433.

- Evans, D.A.D., Li, Z. X., Kirschvink, J.L., Wingate, M.T.D., 2000. A high-quality mid-Neoproterozoic paleomagnetic pole from South China, with implications for ice ages and the breakup configuration of Rodinia. *Precambrian Research* 100, 313-334.
- Frassinetti, S., Bronzetti, G., Caltavuturo, L., Cini, M., Della Croce, C., 2006. The role of zinc in life: A review. *Journal of Environmental Pathology, Toxicology, and Oncology*, 25, 597-610.
- Fujii, T., Moynier, F., Pons, M.F., Albarede, F., 2011. The origin of Zn isotope fractionation in sulfides. *Geochimica et Cosmochimica Acta*, 75, 7632-7643.
- Gelabert, A., Pokrovsky, O.S., Viers, J., Schott, J., Boudou, A., Feurtet-Mazel, A., 2006. Interaction between zinc and freshwater and marine diatom species: Surface complexation and Zn isotope fractionation. *Geochimica et Cosmochimica Acta*, 70, 839-857.
- Halverson, G.P., Hoffman, P.F., Schrag, D.P., Kaufman, J.A., 2002. A major perturbation of the carbon cycle before the Ghaub glaciation (Neoproterozoic) in Namibia: Prelude to Snowball Earth? *Geochemistry, Geophysics, Geosystems*, on-line 10.1029/2001GC000244
- Halverson, G.P., Wade, B.P., Hurtgen, M.T., Barovich, K.M., 2010. Neoproterozoic chemostratigraphy. *Precambrian Research*, 182, 337-350.
- Herzog G., Moynier F., Albarède F., Berezhnoy A., 2009. Isotopic and elemental abundances of copper and zinc in lunar basalts, glasses, and soils, a terrestrial basalt, Pele's hair, *Geochimica et Cosmochimica Acta* 73, 5884-5904.
- Hoffman, P.F., Kaufman, A.J., Halverson, G.P., Schrag, D.P., 1998. A Neoproterozoic Snowball Earth. *Science*, 281, 1342-1346.
- Hoffman, P.F., Maloof, A.C., 1999. Glaciation: the Snowball theory still holds water. *Nature*, 397, 384-384.
- Hoffman, P.F., Schrag, D.P., 2000. Snowball Earth. *Scientific American*, 282, 68-75.
- Hoffman, P.F., Schrag, D.P., 2002. The Snowball Earth hypothesis: testing the limits of global change. *Terra Nova*, 14, 129-155.
- Hoffman, P.F., Halverson, G.P., Domack, E.W., Husson, J.M., Higgins, J.A., Schrag, D.P., 2007. Are basal Ediacaran (635 Ma) post-glacial "cap dolostones" diachronous? *Earth and Planetary Science Letters*, 258, 114-131.
- Hyde, W.T., Crowley, T.J., Baum, S.K., Peltier, W.R., 2000. Neoproterozoic 'Snowball Earth' simulations with a coupled climate/ice-sheet model. *Nature*, 405, 425-429.
- Jacobsen, S. B., Kaufman, A.J., 1999. The Sr, C and O isotopic evolution of Neoproterozoic seawater. *Chemical Geology*, 161, 37-57.

- Jaffres, J.B.D., Shields, G.A., Wallmann, K., 2007. The oxygen isotope evolution of seawater: A critical review of a long-standing controversy and an improved geological water cycle model for the past 3.4 billion years. *Earth-Science Reviews*, 83, 83-122.
- John, S.G., Geis, R.W., Saito, M.A., Boyle, E.A., 2007. Zinc isotope fractionation during high-affinity and low-affinity zinc transport by the marine diatom *Thalassiosira oceanica*. *Limnology and Oceanography*, 52, 2710-2714.
- John, S.G., Olivier J. Rouxel, O.J., Craddock, P.R., Engwall, A.M., Boyle, E.A., 2008. Zinc stable isotopes in seafloor hydrothermal vent fluids and chimneys. *Earth and Planetary Science Letters*, 269, 17–28.
- Kasemann, S.A., Hawkesworth, C.J., Prave, A.R., Fallick, A.E., Pearson, P.N., 2005. Boron and calcium isotope composition in Neoproterozoic carbonate rocks from Namibia: evidence for extreme environmental change. *Earth and Planetary Science Letters*, 231, 73-86.
- Kaufman, A.J., Hayes, J.M., Knoll, A.H., Germs, G.J.B., 1991. Isotopic compositions of carbonates and organic-carbon from upper Proterozoic successions in Namibia - Stratigraphic variation and the effects of diagenesis and metamorphism. *Precambrian Research*, 49, 301-327.
- Kaufman, A.J., Knoll, A.H., 1995. Neoproterozoic variations in the C-isotopic composition of seawater: stratigraphic and biogeochemical implications. *Precambrian Research* 73, 27-49.
- Kaufman, A.J., Knoll, A.H., Awramik, S.M., 1992. Biostratigraphic and chemostratigraphic correlation of Neoproterozoic sedimentary successions - Upper Tindir group, Northwestern Canada, as a test case. *Geology*, 20, 181-185.
- Kaufman, A.J., Knoll, A.H., Narbonne, G.M., 1997. Isotopes, ice ages, and terminal Proterozoic earth history. *Proceedings of the National Academy of Sciences*, 94, 6600-6605.
- Kennedy, M.J., 1996. Stratigraphy, sedimentology, and isotopic geochemistry of Australian Neoproterozoic postglacial cap dolostones: deglaciation,  $d^{13}C$  excursions, and carbonate precipitation. *Journal of Sedimentary Research*, 66, 1050-1064.
- Kirschvink, J.L., 1992. Late Proterozoic low-latitude glaciation: the Snowball Earth. In: Schopf, J.W.K.C. (Ed.), *The Proterozoic Biosphere*. Cambridge University Press, Cambridge, 51-52.
- Kump, L.R., Arthur, M.A., 1999. Interpreting carbon-isotope excursions: carbonates and organic matter. *Chemical Geology*, 161, 181-198.
- Kunzmann, M., Halverson, G.P., Sossi, P.A., Raub, T.D., Payne, J.L., Kirby, J., 2012. Zn isotope evidence for immediate resumption of primary productivity after Snowball Earth. *Geology*, G33422.1, doi:10.1130/G33422.1.

- Marshall, H.G., Walker, J.C.G., Kuhn, W.R., 1988. Long-term climate change and the geochemical cycle of carbon. *Journal of Geophysical Research: Atmospheres*, 93, 791-801.
- Moynier, F., Albarede, F., Herzog, G.F., 2006. Isotopic composition of zinc, copper, and iron in lunar samples. *Geochimica et Cosmochimica Acta*, 70, 6103-6117.
- Moynier, F., Fike, D., Pichat, S., 2009a. Zn isotope variations in Ediacaran carbonates. *Geochimica et Cosmochimica Acta*, 73, A910-A910.
- Moynier, F., Pichat, S., Pons, M.L., Fike, D., Balter, V., Albarede, F., 2009b. Isotopic fractionation and transport mechanisms of Zn in plants. *Chemical Geology*, 267, 125-130.
- Paniello, R. C., Moynier, F., Beck, P., Barrat, J. A., Podosek, F. A., and Pichat, S., 2012. Zinc isotopes in HEDs: Clues to the formation of 4-Vesta, and the unique composition of Pecora Escarpment 82502. *Geochimica et Cosmochimica Acta*, 86, 76-87.
- Peterson, K. J., Lyons, J. B., Nowak, K. S., Takacs, C. M., Wargo, M. J., and McPeck, M. A., 2004. Estimating metazoan divergence times with a molecular clock. *Proceedings of the National Academy of Science*, 101, 6536-654.
- Pichat, S., Douchet, C., and Albarede, F., 2003. Zinc isotope variations in deep-sea carbonates from the eastern equatorial Pacific over the last 175 ka. *Earth and Planetary Science Letters*, 210, 167-178.
- Pons, M.L., Fujii, T., Rosing, M., Quitte, G., Telouk, P., Albarede, F., 2013. A Zn isotope perspective on the rise of continents. *Geobiology*, 11, 201-214.
- Shaheen, R., Abramian, A., Horn, J., Dominguez, G., Sullivan, R., and Thiemens, M. H., 2010. Detection of oxygen isotopic anomaly in terrestrial atmospheric carbonates and its implications to Mars. *Proceedings of the National. Academy of Science*, 107, 20213-20218.
- Shields, G. A., 2005. Neoproterozoic cap carbonates: a critical appraisal of existing models and the plumeworld hypothesis. *Terra Nova*, 17, 299-310.
- Summons, R.E., Hayes, J.M., 1992. Principles of molecular and isotopic biogeochemistry. In: *The Proterozoic Biosphere, a Multidisciplinary Study* (J. W. Schopf and C. Klein, eds), pp. 83–93. Cambridge University Press, Cambridge.
- Tucker, M. E., Wright, V.P., 1990. *Carbonate Sedimentology*. Blackwell Scientific Publications, Oxford, 496 pp.
- Tziperman, E., Halevy, I., Johnston, D. T., Knoll, A. H., and Schrag, D. P., Biologically induced initiation of Neoproterozoic Snowball-Earth events. *Proceedings of the National Academy of Science*, 108, 15091-15096.
- Veizer, J., Ala, D., Azmy, K., Bruckschen, P., Buhl, D., Bruhn, F., Carden, G. A. F., Diener, A., Ebner, S., Godderis, Y., Jasper, T., Korte, C., Pawellek, F., Podlaha, O. G., and Strauss, H., 1999. Sr-87/Sr-86, delta C-13 and delta O-18 evolution of Phanerozoic seawater. *Chemical Geology*, 161, 59-88.

- Walker, J. C. G., Hays, P. B., and Kasting, J. F., 1981. A negative feedback mechanism for the long-term stabilization of Earth's surface-temperature. *Journal of Geophysical Research-Oceans and Atmospheres*, 86, 9776-9782.
- Walter, M. R., Veevers, J.J., Calver, C.R., Gorjan, P., Hill, A.C., 2000. Dating the 840-544 Ma Neoproterozoic interval by isotopes of strontium, carbon, and sulfur in seawater, and some interpretive models. *Precambrian Research*, 100, 371-433.
- Warren, S. G., Brandt, R. E., Grenfell, T. C., and McKay, C. P., 2002. Snowball Earth: Ice thickness on the tropical ocean. *Journal of Geophysical Research*, 107, 10.1029/2001JC001123
- Weiss, D. J., Mason, T. F. D., Zhao, F. J., Kirk, G. J. D., Coles, B. J., and Horstwood, M. S. A., 2005. Isotopic discrimination of zinc in higher plants. *New Phytologist*, 165, 703-710.
- Welch, R., Webb, M., and Loneragan, J., 1982. Zinc in membrane function and its role in Phosphorous toxicity. *Ninth Plant Nutrition Colloquium Commonwealth Agricultural Bureau* 710-715.
- Worseley, T.R., Kidder, D.L., 1991. First-order coupling of paleogeography and CO<sub>2</sub>, with global surface temperature and its latitudinal contrast. *Geology*, 19, 1161-1164.
- Zhou, C. M., Bao, H. M., Peng, Y. B., and Yuan, X. L., 2010. Timing the deposition of (17)O depleted barite at the aftermath of Nantuo glacial meltdown in South China. *Geology*, 38, 903-906.
- Zirino, A. and Yamamoto, S., 1972. PH-dependent model for chemical speciation of copper, zinc, cadmium, and lead in seawater. *Limnology and Oceanography*, 17, 661-671.



## 6 Paleoenvironment characterization based on microbial activity and geochemical proxies in Marinoan postglacial transition layers (NW-Namibia)

Ildikó Gyollai<sup>1,2</sup>, \*Márta Polgári<sup>2</sup>, Szabolcs Nagy<sup>3</sup>, Krisztián Fintor<sup>3</sup>, Elemér Pál-Molnár<sup>3,4</sup>  
Friedrich Popp<sup>5</sup>, Dieter Mader<sup>1</sup>, Christian Koeberl<sup>1,6</sup>

<sup>1</sup>Department of Lithospheric Research, University of Vienna, Althanstrasse 14, A-1090 Vienna, Austria; e-mail: [gyollai.ildiko@gmail.com](mailto:gyollai.ildiko@gmail.com), <sup>2</sup>Research Centre for Astronomy and Geosciences, Geobiomineralization and Astrobiological Working Group Institute for Geology and Geochemistry, Hungarian Academy of Sciences, 1112 Budapest, Budaörsi út. 45, Hungary, e-mail: [rodokrozt@gmail.com](mailto:rodokrozt@gmail.com), <sup>3</sup>Department of Mineralogy, Geochemistry and Petrology, Szeged University, 6702 Szeged, Egyetem utca 2, Hungary, <sup>4</sup>Eötvös Loránd University-Hungarian Academy of Sciences, Volcanology Research Group, H-1117 Budapest, Pázmány P. Street 1/C, Hungary, <sup>5</sup>Department of Geodynamics and Sedimentology, University of Vienna, Althanstrasse 14, A-1090 Vienna, Austria, e-mail: [friedrich.popp@univie.ac.at](mailto:friedrich.popp@univie.ac.at), <sup>6</sup>Natural History Museum, Vienna, A-1010 Burgring 7, Vienna, Austria e-mail: [christian.koeberl@univie.ac.at](mailto:christian.koeberl@univie.ac.at)

\*corresponding author

Article is prepared for “Central European Journal of Geology”.

**Abstract:** This study gives an overview about formation of microbial mats in Marinoan (Neoproterozoic) postglacial layers. These microbial mats of iron-oxidizing bacteria consume iron and phosphorous from different sources, like hydrothermal solutions, or iron-bearing minerals (pyrite, chlorite). This study examines different types of microbial mats according to their formation and provides a chance for paleoenvironmental reconstructions based on geochemical features and morphology of microbial structures. Thus, on the basis of the probed morphology of iron-biomats and geochemical signatures we consider the Marinoan postglacial transition layers formed within neutrophilic, suboxic conditions and brackish water.

**Keywords:** Snowball Earth, microbial mats of iron-oxidizing bacteria, biodegradation of minerals, basal cap carbonates, boundary layer, Otavi Group, NW-Namibia

## 6.1 Introduction

The Snowball Earth theory is based on different models: Hard Snowball Earth (Hoffmann et al., 1998a), Slushball Earth (Harland, 1964), Zipper rift Earth (Eyles and Januszczak, 2004), High-tilt Earth (Williams, 2000), which were summarized by (Fairchild and Kennedy, 2007). The hard snowball Earth postulates a completely frozen Earth caused by runaway feedback and rapid deglaciation (Hoffmann et al., 1998a). Contrarily the Slushball Earth proposes open water areas in the equatorial region assuming presence of a hydrological cycle and slow deglaciation (Hyde et al., 2000). The Zipper-rift Earth model is based on the influence of Neoproterozoic glaciations on the break-up of Rodinia. The High-tilt Earth induces initiation of Snowball Earth glaciations from equatorial regions driven by orbital obliquity higher than  $54^\circ$  (Williams, 2000).

This study gives perspectives about deglaciation of the younger Cryogenian Period (Marinoan 665-635 Ma) (Kennedy et al., 1998). Our research area is located at the Ghaub-Maieberg transition (Otavi Group) in NW-Namibia, assigned by an age of  $635 \pm 1.2$  Ma after U-Pb dating of zircon from an ash bed within the Ghaub Formation (Hoffman et al., 2004). Paleomagnetic research state that the Marinoan Ghaub Formation was formed within  $5-10^\circ$  paleolatitude (Evans, 2000).

## 6.2 Geological background

Marinoan postglacial transition layers span the uppermost / lowermost portions of the Ghaub/Maieberg Formations. The Ghaub Formation (Hoffman and Prave, 1996) is only fragmentary preserved within structural depressions of inner platform areas, suggesting the Otavi bank being one of the source areas for appreciable diamictite accumulations in slope facies areas bordering on the platform edges (Fig. 1A). The Ghaub glacial lithofacies are composed almost exclusively of carbonate debris (Hoffman and Halverson, 2008) and clasts of various size are different types of dolomite and rarely limestone, all apparently derived from the underlying Ombaatjie Formation. Stratigraphic evidence points to a single sea-level advance and retreat cycle during the Ghaub glaciation; grounded ice existed at the maximum advance leaving characteristic sedimentary features (Domack and Hoffman, 2003)

The Maieberg Formation (Hedberg, 1979; SACS, 1980) subdivided into three members, is an up to 400 m thick pile of carbonate sedimentary cycles which originated in a warm periodic platform facies environment following the Ghaub glacial period. The basal Keilberg Member (Hoffman and Prave, 1996) is a "cap dolostone" associated with the sea-level rise attending the Ghaub deglaciation (Kennedy, 1996; Hoffman and Schrag, 2002). Its characteristic feature is a uniform, 10-15 m thick, pale colored marker bed which is mechanically-laminated

on a mm-scale, with characteristic small-scale, low angle cross-stratification. Unusual sedimentary structures featuring vertical “tube-like” appearance are visible, starting about one meter above the base, in our sample sites. These tubes may have generated due to CO<sub>2</sub> oversaturation (Le Hir et al., 2008) and methane outgassing from clathrates (Kennedy et al., 2008). According to another hypothesis the tubes may have formed in close connection with the growth of stromatolites (Hoffman and Halverson, 2008).

### 6.3 Samples and methods

Samples are collected by F. Popp from layers nearest at/above the boundary between the uppermost Ghaub glacial diamictite and the basal post-glacial cap dolomite (Keilberg Mb. / Maieberg Fm.). A total of fifty-two samples from different paleogeographic regions (Fig. 1. and Table 1.); all containing microbial structures were analyzed. They originate on the one hand from distal slope facies deposits abutting against the Otavi platform at outcrops near Fransfontain (sample C1 / 20°11'59.06"S; 15° 0'58.68"E) and near Naraachamspos (sample C2a / Figs. 1b and 2/ 20°11'27.68"S"; 14°51'4.42"E) but then also from outcrops representing inner and outer Otavi platform facies deposits; these sample sites from inner platform facies are located within the Khowarib Fold Belt near Ongongo (profile K2 / Fig. 1b / 19° 8'35.77"S; 13°51'15.40"E), at the head of a valley extending from Entrance (near Devede village) towards the SW (samples K4 and C 14a / Figs. 1b and 2/ 19°11'18.40"S; 13°56'13.39"E), at the hillside of the Khowarib valley (P49-1 / 19°18'24.52"S; 13°59'25.57"E) and lastly the sample site from outer platform facies is located at the edge of the Huab ridge in farm Tweelingskop (sample C7 / 20°24'21.95"S; 14°20'35.06"E).

In general, the samples are characterized by grey-white-reddish brown color and micritic texture, but samples C14a and C2a contain layers with clastic particles. The thickness of layers holding microbial structures varies from millimeters to centimeter.

The lithology of samples was described by macroscopic observation and optical microscopy (Table 1.). The textural analysis of microbial structures were obtained by optical microscopy (Research Centre for Geology and Geochemistry, Hungarian Academy of Sciences, Budapest), and by a Thermo Scientific DXR confocal edge filter-based micro-Raman spectrometer with 10 mW, 532 nm diode-pumped solid state laser excitation system, and thermoelectrically cooled charged coupled device array detector (Department of Mineralogy, Geochemistry and Petrology, University of Szeged) for the identification of some mineral phases.

X-ray diffraction data (XRD) were collected by a Phillips-diffractometer (PW 3710, goniometer PW-1820), CuK $\alpha$  radiation (45 kV, 35 mA), step size of 0.02 degrees, and counting

time of 1 s per step (Department of Geodynamics and Sedimentology, University of Vienna). Minerals were identified using the Joint Committee on Powder Diffraction Standards (1980) database.

The contents of some major (Na, K, Fe) and trace elements including rare earth elements (REEs), were determined by instrumental neutron activation analyses (INAA) at the Department of Lithospheric Research, University of Vienna. Major element bulk analyses and some traces (Cu, Ni, Co, Sc, Cr, V) were made by a Philips PW 2400 sequential X-ray spectrometer equipped with a Rh-excitation source (Department of Lithospheric Research, University of Vienna). The carbon content and isotopic composition of carbon were measured using a Carlo Erba Element Analyzer coupled to a Micromass Optima stable isotope ratio mass spectrometer (Department of Lithospheric Research, University of Vienna).

**Table 1.** Lithology of Marinoan samples containing microbial structures and list of samples of chemical and mineralogical investigations (number of subsamples: profile K4– 8, profile K2 – 11, profile C2a – 17, \* for locality see Fig. 1).

Thin sections	Stratigraphic setting with locality	Lithology	Microbial structures
K4-3*	Maieberg Fm. Keilberg Mb – profile Entrance to the South Valley inner platform facies	kinked terrestrial layer interbedding in dolomite tectonic overprint (wurst-like detritus layers, sygmaclasts: shearing tectonics clay lenses: alteration of original biomats	filamentous iron bacteria- (colonial coccooid cells, sheath-enclosed colonial unicells and spheroidal unicells) K4-1 well preserved, K4-2 weathered, progressive weathering of biogenic structures to clay minerals in Profile K4
K4-2		terrestrial layer: wavy lamination (locally broken)	
K4-1		micritic dolomite with detrital layers cement: calcite, quartz under terrestrial layer carbonate shows flow structure, above the terrestrial layer unstratified carbonate diagenetic overprint biomats along fractures and parallel to bedding in quartz and carbonates	
K2-2	Warmquelle, slope facies	dolomite with fine-grained well-stratified structure fluidization structures (flame and ball structures) diagenetic overprint	1. primary structures: filamentous iron bacteria (coccooid spheroidal colonial cells) 2. secondary structures along fractures (Bio-weathering columnar iron-rich phosphorous collophan?)
K2-1			weathered (smectitized) microbial mat in iron rich layer and diagenetic quartz (filamentous cyanobacteria iron bacteria (coccooid colonial cells)

Thin sections	Stratigraphic setting with locality	Lithology	Microbial structures
<b>C7</b>	Tweelingskop	carbonate green-sheet facies metamorphosed <u>sedimentary structures</u> : fine plane lamination of carbonate layers, climbing lamination in iron oxide containing terrestrial layer. <u>cement</u> : sericite, micrite <u>facies</u> : slope/deep shelf margin	oscillatorian cyanobacteria filamentous iron bacteria (colonial coccoid and spheroidal cells)
<b>C1c</b>	Ghaub/Maieberg Fm. (boundary) Fransfontain	slope fine grainstone interbedding of terrigenous strata (silt, quartzarenite) ripple-lamination (quartz strata), angular cross lamination (iron-oxide and clay strata)	oscillatorian cyanobacteria (large number) filamentous iron bacteria (colonial coccoid cells and spheroidal unicells)
<b>C1b</b>		slope fine-grained grainstone with extraclasts	filamentous iron bacteria (coccoidal unicells)
<b>P49-1</b>	Khowarib Valley		bioweathering crust
<b>C14a</b>	Ghaub Fm. Entrance to the South Valley inner platform facies	top of red diamictite platform facies debris flow with large carbonate blocks and with mica among the blocks <u>cement</u> : micrite iron-oxide	filamentous iron bacteria at the boundary of clasts
<b>C2a-7</b>	Maieberg Fm. Keilberg Mb Naraachamspos slope facies	carbonate ball and flame structure – fluidization pyrite-quartz-clay sygmaclasts	weathered, filamentous iron bacteria (colonial coccoid cells, sheath-enclosed colonial unicells and spheroidal unicells)
<b>C2a-6</b>		flow structure with diagenetic quartz and carbonate rich layer sygmaclast of pyrite and quartz	moderate weathering, coccoid-forming biomat of iron bacteria filamentous cyanobacteria
<b>C2a-5</b>		carbonate with pyrite-quartz sygmaclasts – metamorphic overprint wavy lamination of iron-including and carbonate layers	weathered filamentous iron bacteria- (colonial coccoid cells, sheath-enclosed colonial unicells and spheroidal unicells) (main occurrence in pyrite - quartz lens, and in surrounding carbonate)
<b>C2a-4</b>			black and red filamentous iron bacteria (colonial coccoid cells, sheath-enclosed colonial unicells and spheroidal unicells) in pyrite lens (low weathering rate)
<b>C2a-3</b>	Ghaub/Maieberg Fm. Naraachamspos	micritic carbonate, thin terrestrial layer interbedding	no
<b>C2a-2</b> <b>C2a-1</b>	Ghaub Fm. (top) Naraachamspos	coarse terrestrial layers in carbonate micritic-coarse carbonate rhythmic bedding	

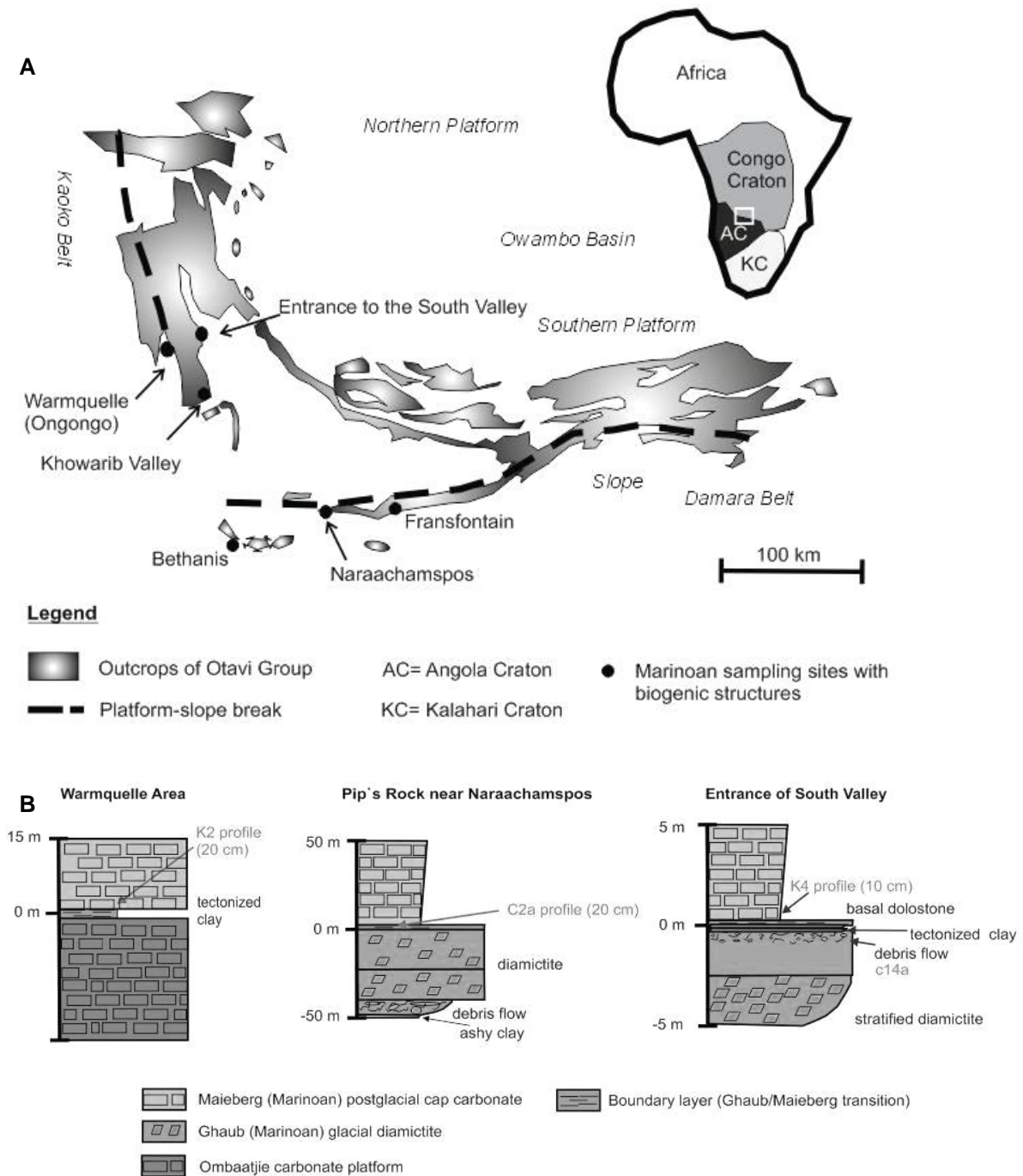


**Figure 1.** Sampling sites of Marinoan postglacial layers with map of outcrop of Otavi Group (A), and profiles (B) (modified after Hoffmann, 2002). 1A: the platform-slope facies boundary is marked by black dashed line. 1B: Stratigraphic position of profiles (Warmquelle, Entrance to the South Valley, Naraachampos) showing biogenic samples (K2, K4, C2a, C14a). Khowarib Valley (P49-1), Fransfontain (C1) and Tweelingskop (C7) there are presented at Fig. 1 A.

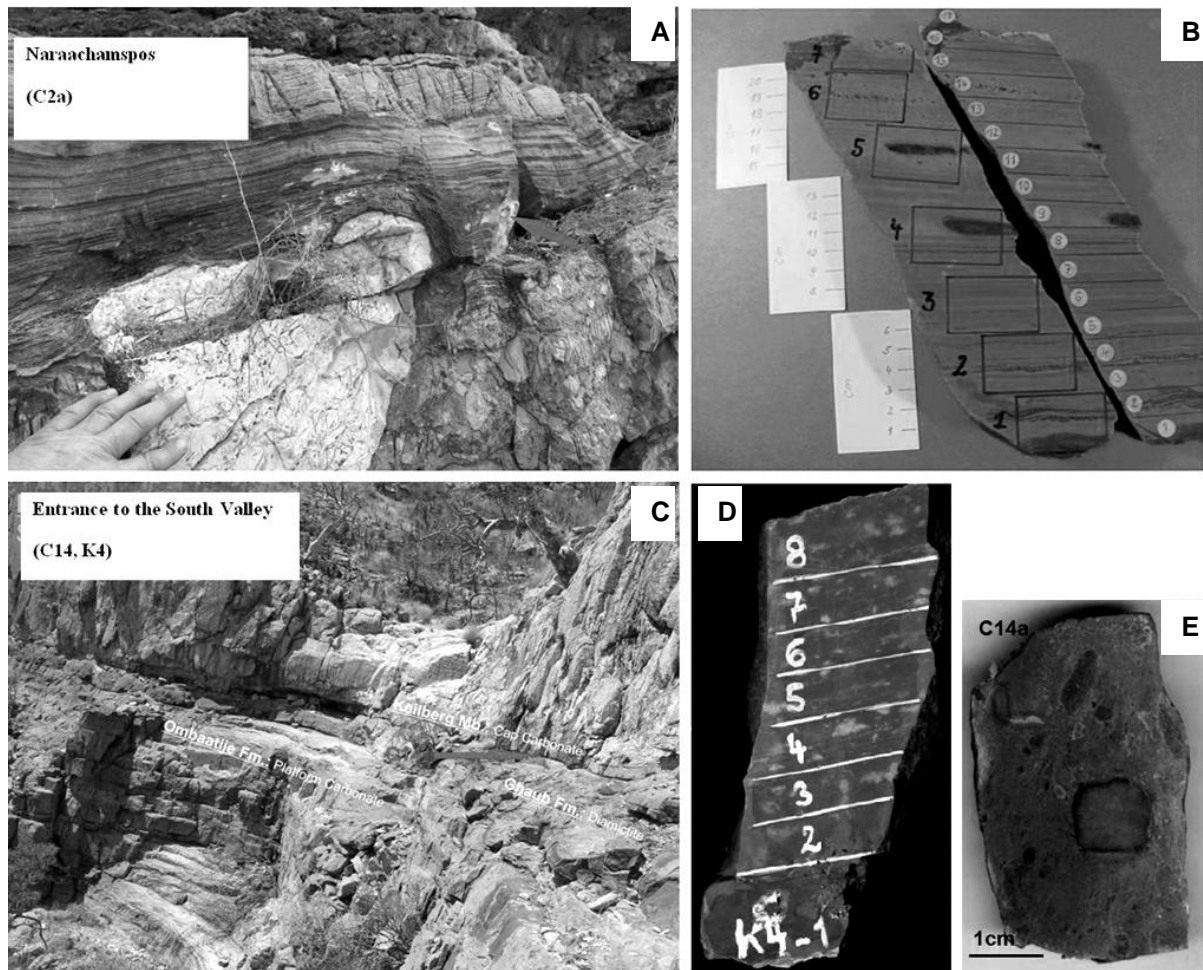


**Figure 2.** Outcrops photos and sections of selected samples at Naraachamspos (distal slope facies, C2a), and Entrance to the South Valley (inner platform facies, K4, C14a) (Photos of outcrops: F. Popp, 2009).

## 6.4 Results

### 6.4.1 Petrography of microbial structures

#### Type 1: Primary, syngedimentary biomat structures

The transition layers beneath the Maieberg Formation from the bank facies at Entrance towards the SW Valley (profile K4: Fig. 3B, D) as well as from the distal slope facies at Fransfontain (C1) enclose in-situ microbiolaminite layers. The profile K4 is wavy laminated, where well-preserved coccoidal iron bacterial colonies occur embedded in diagenetic quartz layers, whereas the iron bacterial colonies in carbonates are less preserved and strongly altered. Tiny cubic minerals might be iron-phosphorite and pyrite, which display loading

structures incising the lamination. Marinoan microbiolaminites are thin layers (1-2 cm) and besides organic material, they also contain clay minerals (smectite).

*Type 2: Secondary biomats (biodegradation of iron containing minerals)*

At Naraachamspos locality (distal slope facies), the quartz grains of sample C2a contain dense oscillatorian cyanobacteria communities. Here, the lower profile part of sample C2a (C2a-1-3) are turbiditic layers of coarse-grained carbonate, microcline and quartz. The upper part of profile C2a (C2a-4-7) likewise contains lenses with detrital content, like chlorite, pyrite and quartz (Fig. 3A, C). The quartz encloses a large amount of oscillatorian cyanobacteria, whereas pyrite and chlorite provided the nutrient source for the growth of filamentous iron bacteria. The smallish pyrite grains show concentric growth rims forming a cubic shape. The larger pyrite grains are coated with layered lepidocrocite rims. The upper part of our sample K2-2 at Ongongo locality (inner bank facies) contains pyrite-quartz lenses, which are characterized by iron-oxide rims and are decayed partly by filamentous iron bacteria (Fig. 3B). Similarly to sample C2a, the laminated structures in our sample K2 might also be formed by biodegradation of iron-rich minerals, which precursor minerals were observed as pseudomorphic grain rims. Hence, the iron-microbial communities occur as small, isolated groups inside the decayed grains, at the grain boundaries (ghosts), or along the fractures. The basal cap carbonate from the carst influenced outer bank facies at Tweelingskop (sample C7), contains several iron-containing minerals as nutrient and dense filamentous iron bacteria (coccoidal and sheet cell colonies) are observed. At this locality the iron-biomats are mostly less preserved with fine-grained hematite as weathering product. The basal cap carbonate layer from the inner bank facies at Khowarib Valley (sample P49-1) is a lutite made up of mixed clay minerals, but also contains hematite due to bio-weathering.

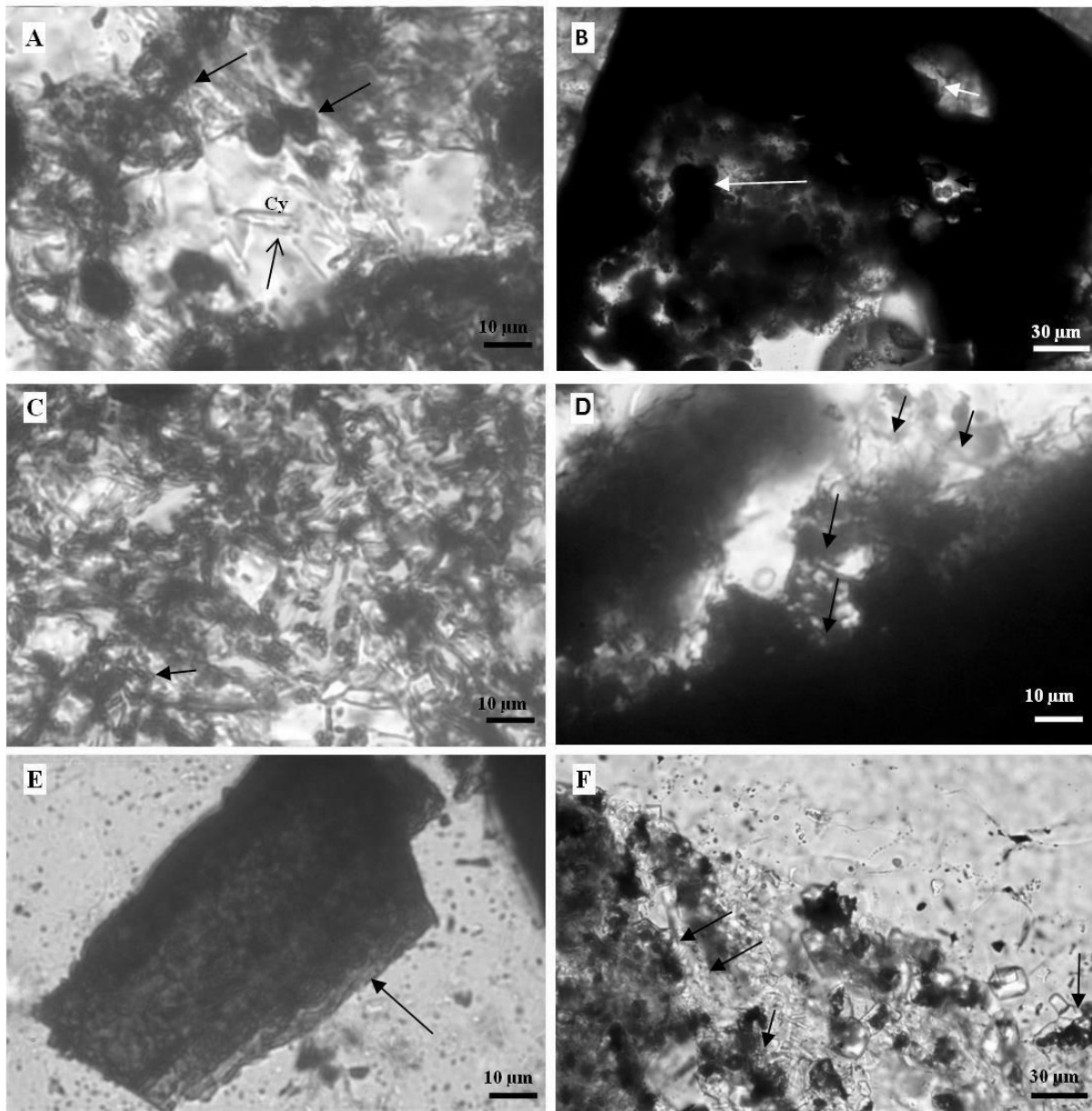


**Figure 3.** Microbial mineral decomposition and biomat formation. (A, C): Bio-weathering of chlorite and pyrite with lepidocrocite rim in profile C2a; (B): Fe biomats formed by biodegradation of pyrite (sample K2-2, Fe oxidizing bacterial colonies are shown by arrow); (D): In-situ microbialite of filamentous iron bacteria (K4-1, shown by black arrows); (E-F): Bio-weathering of pyrite altered to lepidocrocite rim in profile C2a (shown by arrows).

*Type 3: „Pseudo-secondary” structures: coating on clasts*

Filamentous iron-bacterial colonies were observed on clasts of the topmost diamictite layer at Entrance towards the SW Valley (C14a) (Fig. 4). These FeOB colonies grew on carbonate clasts which suggest short-term nutrient source or transient suboxic condition.

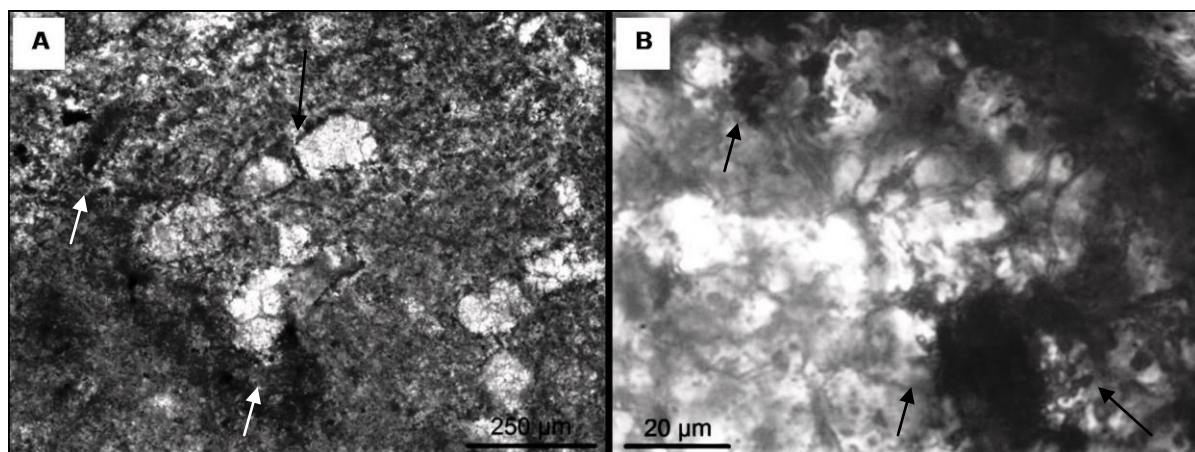


**Figure 4.** Microbial mats on the clasts in sample C14a. (FeOB-mats are shown by arrows).

#### 6.4.2 Raman-mapping measurements

According to reflectance microscopy and micro-Raman mapping measurements, the pyrite altered to variable secondary minerals such as hematite, goethite-lepidocrocite, carbonaceous material and hematite. In general the altered pyrite has a remnant phase in the core zone, which is surrounded by, a lepidocrocite-goethite-hematite alteration zone (Fig. 5.). The pyrite in sample C2a (thin sections C2a-4-7) was oxidized by microbial degradation, which is indicated by a lepidocrocite and hematite shale around a pyrite core. The microtexture of these minerals shows fine, EPS-like micro-layered appearance.

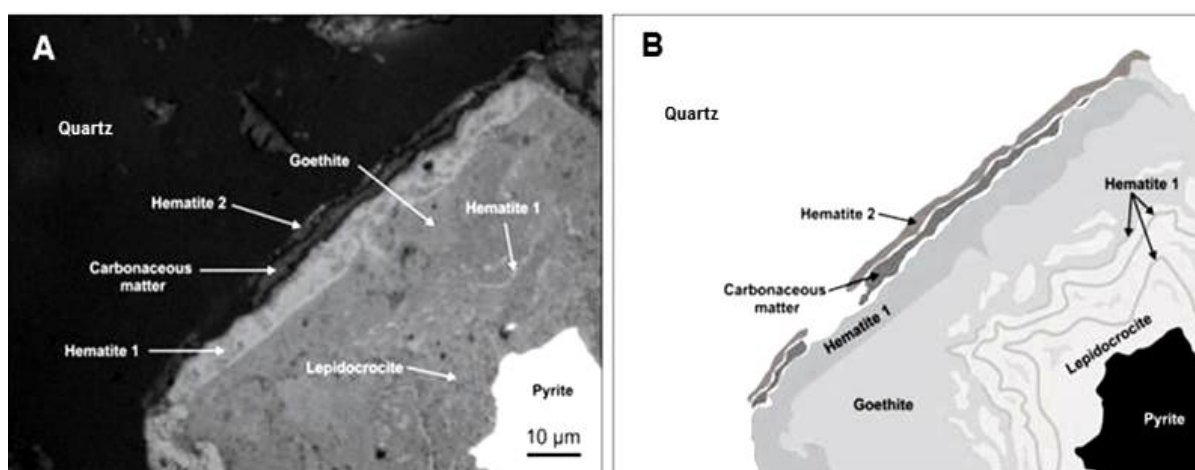


**Figure 5.** Biodegradation of a pyrite grain. (A): microphotograph in reflectance mode, and sketch of mineral zones indicated by micro-Raman spectroscopy (B).

### 6.4.3 Geochemistry

Major and trace element composition of the profiles K4, K2 and C2a are summarized in Table 2 and Chapter 10 (Appendix 2). The elevated values of Co-, Ni-, Zn (to PAAS, Post-Archean Australian Shale) with slightly negative  $\delta^{13}\text{C}$  anomalies in range of K2/5-8 and the strongly negative  $\delta^{13}\text{C}$  anomalies and elevated Ni in range of K2/2 were observed (Fig. 6.). In sample C2a within the C2a-12-15 interval, near to the visible biodegradation of detrital mineral grains accumulated in lenses, elevated trace element anomalies of Ba, Sr, Co, Ni, Zn, Ce, and As occur.

Enrichment factors (EF, biogenic elements divided by Sc, (e.g., Meyer et al., 2012) were used for determination of biogenic signatures (Table 3. for profile K2 and K4). Because of lack of Al values in most of cases, Sc was used in calculations here.

The measured iron biomat layers show high EF for Co, Ni, Zn, Fe, and U in the profiles K2 and K4, but the profile C2a has higher EF only for Ni, the other elements vary between normal marine values (0.5-2.0). The carbon isotopic ratios show negative shift between -2 and -10 ‰ in profile K2, and ranging -1 and -2 ‰ for profile K4.

**Table 2.** Main and trace element composition of profiles K4 (Entrance to the SW-Valley), K2 (Warmquelle), and C2a (Naraachamspas).

Location Strat. setting wt. %	Entrance of South Valley Profile							
	G/M* K4-1	G/M K4-2	M K4-3	M K4-4	M K4-5	M K4-6	M K4-7	M K4-8
<b>Fe<sub>2</sub>O<sub>3</sub></b>	9.05	2.22	0.48	0.44	0.45	0.47	0.50	0.45
<b>Na<sub>2</sub>O</b>	0.03	0.03	0.03	0.02	0.03	0.03	0.03	0.03
<b>K<sub>2</sub>O</b>	0.26	0.19	0.28	0.26	0.27	0.34	0.34	0.28
<b>LOI</b>	n.d.	45.4	45.9	46.0	45.8	43.6	46.0	45.8
<b>ppm</b>								
<b>Cr</b>	16.9	5.22	4.54	3.05	3.68	6.10	3.85	3.30
<b>Co</b>	38.5	6.45	2.39	2.01	1.88	2.20	2.41	2.06
<b>Ni</b>	89.1	16.5	11.1	4.88	8.93	11.9	11.8	4.75
<b>Zn</b>	50.1	26.4	22.5	21.5	22.5	29.7	23.6	20.6
<b>As</b>	28.1	6.93	0.62	0.48	0.45	0.44	0.65	0.55
<b>Rb</b>	8.61	6.74	6.35	5.55	5.58	7.5	6.73	5.71
<b>Sr</b>	60.7	56.7	68.2	62.8	64.3	64.3	67.5	62.1
<b>Zr</b>	<28	39.6	27.9	21.1	30.4	30.0	28.6	19.4
<b>Ba</b>	58.6	29.5	44.8	34.3	33.9	45.3	39.6	32.4
<b>La</b>	4.62	4.78	4.86	4.43	4.34	4.17	4.08	3.73
<b>Ce</b>	11.3	9.52	9.28	8.24	8.43	8.26	8.16	7.23
<b>U</b>	4.51	1.48	1.33	0.55	0.44	0.57	0.54	0.35
<b><math>\delta^{13}\text{C}_{\text{vs VPDB}}</math></b>	-0.95	-1.41	-1.91	-1.69	-1.87	-1.69	-1.84	-1.68

Location	Naraachamspos Profile								
Strat. setting	G	G/M	M	M	M	M	M	M	M
wt. %	C2a-1	C2a-2	C2a-3	C2a-4	C2a-5	C2a-6	C2a-7	C2a-8	C2a-9
<b>Fe<sub>2</sub>O<sub>3</sub></b>	2.27	1.54	1.94	1.63	1.97	1.95	1.73	1.82	2.16
<b>Na<sub>2</sub>O</b>	0.13	0.25	0.14	0.19	0.12	0.11	0.08	0.11	0.05
<b>K<sub>2</sub>O</b>	3.55	2.05	3.38	2.63	2.61	2.14	1.93	1.99	2.21
<b>ppm</b>									
<b>Cr</b>	120	41.6	48.1	34.8	34.1	29.7	28.0	27.7	35.5
<b>Co</b>	14.6	7.46	6.71	12.6	6.34	5.63	4.43	5.39	12.5
<b>Ni</b>	98.6	79.0	99.2	120	78.9	62.0	56.8	55.8	52.6
<b>Zn</b>	33.3	31.8	36.5	31.4	34.0	30.2	28.2	29.2	24.9
<b>As</b>	5.69	0.28	0.58	0.73	0.57	0.39	0.45	1.20	10.2
<b>Rb</b>	88.4	53.8	86.1	60.9	64.7	51.5	52.3	47.3	51.2
<b>Sr</b>	65.2	70.7	61.0	60.8	78.2	48.3	59.5	66.6	61.8
<b>Zr</b>	164	130	161	121	121	103	114	112	115
<b>Ba</b>	175	123	170	129	119	98.7	92.9	94.9	98.7
<b>La</b>	28.7	22.7	35.5	26.7	26.0	23.3	22.0	22.4	2.34
<b>Ce</b>	49.5	38.6	58.1	42.9	42.5	37.8	34.4	36.3	38.4
<b>U</b>	1.57	1.16	1.66	1.15	1.23	1.01	1.10	0.98	1.05

Location	Naraachamspos Profile							
Strat. setting	M	M	M	M	M	M	M	M
wt. %	C2a-10	C2a-11	C2a-12	C2a-13	C2a-14	C2a-15	C2a-16	C2a-17
<b>Fe<sub>2</sub>O<sub>3</sub></b>	1.85	2.09	2.17	2.97	3.45	2.00	3.07	2.40
<b>Na<sub>2</sub>O</b>	0.05	0.03	0.03	0.04	0.03	0.03	0.03	0.02
<b>K<sub>2</sub>O</b>	2.35	2.14	2.72	2.74	2.50	1.74	1.55	0.83
<b>ppm</b>								
<b>Cr</b>	30.3	30.0	36.1	34.6	31.8	23.0	24.1	16.6
<b>Co</b>	4.84	7.11	7.10	11.7	17.2	7.58	20.4	26.7
<b>Ni</b>	56.0	60.9	68.6	102	132	42.7	75.5	142
<b>Zn</b>	30.0	30.4	30.4	32.8	26.7	26.1	29.0	43.5
<b>As</b>	0.81	3.79	9.92	35.0	64.6	3.46	23.6	28.7
<b>Rb</b>	54.0	51.5	71.1	71.3	62.9	42.6	40.6	28.1
<b>Sr</b>	65.9	49.3	69.7	82.7	67.4	56.9	75.2	85.0
<b>Zr</b>	97.5	100	134	136	116	91.7	92.0	78.3
<b>Ba</b>	102	100	139	146	128	88.9	82.7	36.1
<b>La</b>	25.5	23.1	27.1	28.6	25.8	18.8	16.8	10.7
<b>Ce</b>	39.0	36.6	44.8	45.1	39.8	30.8	28.4	18.6
<b>U</b>	1.17	1.04	1.47	1.49	1.58	1.00	1.17	0.80

Location Strat. setting wt. %	Warmquelle Profile										
	M K2-1	M K2-2	M K2-3	M K2-4	M K2-5	G/M K2-6	G/M K2-7	G/M K2-8	M K2-9	M K2-10	M K2-11
<b>Fe<sub>2</sub>O<sub>3</sub></b>	1.32	1.33	1.04	0.62	4.38	3.39	3.22	1.17	0.59	0.55	0.36
<b>Na<sub>2</sub>O</b>	0.07	0.07	0.07	0.07	0.05	0.03	0.03	0.02	0.02	0.02	0.02
<b>K<sub>2</sub>O</b>	3.11	3.23	3.51	3.57	2.97	0.65	0.45	0.35	0.27	0.18	0.19
<b>LOI</b>	n.d.	5.66	4.74	2.98	5.38	39.4	42.8	44.3	45.8	46.5	46.5
<b>ppm</b>											
<b>Cr</b>	61.5	62.5	71.8	61.5	34.3	8.63	9.80	5.89	5.17	2.53	3.8
<b>Co</b>	2.31	1.29	1.02	0.57	2.84	15.1	29.3	10.6	3.02	2.72	1.73
<b>Ni</b>	17.1	23.1	15.0	8.61	35.8	45.2	80.0	28.6	12.2	7.71	7.25
<b>Zn</b>	21.5	19.7	19.2	19.8	19.8	28.1	61.6	25.5	18.1	13.3	12.9
<b>As</b>	14.9	26.4	18.7	4.21	44.7	50.3	89.5	23.1	4.30	6.21	2.43
<b>Rb</b>	79.3	81.7	87.4	86.1	75.2	17.2	14.3	8.94	7.13	3.65	5.13
<b>Sr</b>	30.6	34.3	23.0	<30	<25	55.9	63.0	72.0	72.1	68.3	70.3
<b>Zr</b>	154	129	165	158	233	<30	<34	<18	27.0	<15	10.3
<b>Ba</b>	378	420	444	422	406	94.0	63.9	48.7	35.3	25.3	26.8
<b>La</b>	17.4	17.9	20.7	21.9	9.67	3.63	4.41	3.22	2.44	2.01	2.04
<b>Ce</b>	33.6	34.7	40.9	43.1	20.2	7.58	7.63	6.16	5.60	4.60	4.81
<b>U</b>	3.89	4.24	4.52	3.96	6.32	2.38	2.89	1.19	0.59	0.53	0.44
<b>δ<sup>13</sup>C<sub>vs VPDB</sub></b>	-9.18	-7.62	-7.94	-7.80	-7.82	-3.65	-2.64	-3.54	-2.68	-2.33	-2.65

Comparison to PAAS (Post-Archean Australian shale) data as follows: Fe<sub>2</sub>O<sub>3</sub>= 7.22%, Na<sub>2</sub>O=1.2, K<sub>2</sub>O=3.7, Cr=110, Co=23, Ni=55, Zn=85, Rb=160, Sr=200, Zr=210, Ba=650, La=38, Ce=80, U=3.1 (Taylor and McLennan, 1985)

\*: M - Maieberg Fm.; G – Ghaub Fm.

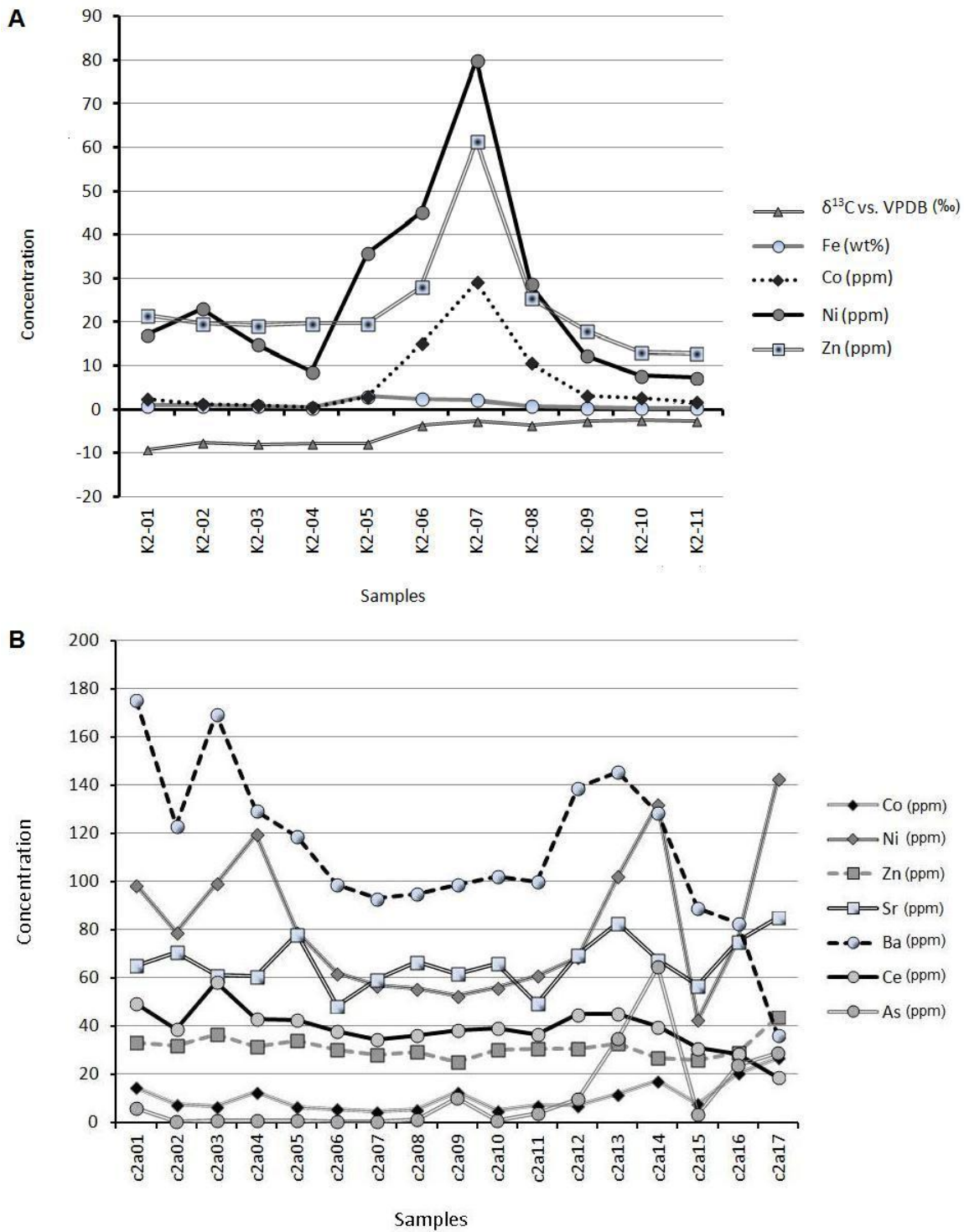


**Figure 6.** Geochemical diagrams of K2 (A) and C2a (B) profiles showing biogenic element enrichments. Fe is in wt%,  $\delta^{13}\text{C}$  is counted in permil, trace elements are added in ppm. (A): The more negative carbon isotopic anomaly correlates well with higher Ni values. The red microbialite region (K2/05-08) is enriched in biogenic elements like Zn, Ni, Co to their abiogenic values. (B): Biogenic element accumulation (Co, Ni, Zn, As, Sr, Ba, Ce) follows distribution of pyrite-chlorite-quartz rich lenses.

**Table 3.** Enrichment factors (EF) of biogenic elements for K2 (Warmquelle) and K4 (Entrance to the SW-Valley) profiles.\*

EF	K2-1	K2-2	K2-3	K2-4	K2-5	K2-6	K2-7	K2-8	K2-9	K2-10	K2-11	K4-1	K4-2	K4-3	K4-4	K4-5	K4-6	K4-7	K4-8
Cr	1.2	1.2	1.3	1.1	0.9	0.3	0.5	0.4	0.5	0.4	0.7	1.4	1.0	0.8	0.7	0.7	0.9	0.6	0.6
Co	0.2	0.1	0.1	0.0	0.3	<b>2.4</b>	<b>6.8</b>	<b>3.8</b>	<b>1.5</b>	<b>2.1</b>	1.4	<b>14.7</b>	<b>6.1</b>	<b>2.1</b>	<b>2.1</b>	1.8	1.5	1.9	1.8
Ni	0.7	0.9	0.5	0.3	1.8	<b>3.0</b>	<b>7.8</b>	<b>4.3</b>	<b>2.5</b>	<b>2.5</b>	2.5	<b>14.3</b>	<b>6.5</b>	<b>4.0</b>	<b>2.2</b>	<b>3.5</b>	<b>3.3</b>	<b>3.9</b>	1.7
Zn	0.5	0.5	0.4	0.5	0.6	1.2	<b>3.9</b>	<b>2.5</b>	<b>2.4</b>	<b>2.8</b>	<b>2.9</b>	<b>5.2</b>	<b>6.8</b>	<b>5.3</b>	<b>6.2</b>	<b>5.5</b>	<b>5.4</b>	<b>5.0</b>	<b>4.8</b>
Rb	1.1	1.1	1.1	1.0	1.3	0.4	0.5	0.5	0.5	0.4	0.6	0.5	0.9	0.8	0.8	0.8	0.7	0.8	0.7
U	<b>2.7</b>	<b>2.8</b>	<b>2.8</b>	<b>2.5</b>	<b>5.6</b>	<b>2.8</b>	<b>5.0</b>	<b>3.2</b>	<b>2.1</b>	<b>3.0</b>	<b>2.7</b>	<b>12.8</b>	<b>10.4</b>	<b>8.6</b>	<b>4.3</b>	<b>3.1</b>	<b>2.8</b>	<b>3.1</b>	<b>2.2</b>
K	1.8	1.8	1.8	1.9	<b>2.2</b>	0.6	0.6	0.8	0.8	0.8	1.0	0.6	1.1	1.5	1.7	1.6	1.4	1.7	1.5
Fe	0.4	0.4	0.3	0.2	1.7	1.7	<b>2.4</b>	1.3	0.9	1.4	1.0	<b>11.0</b>	<b>6.7</b>	1.3	1.5	1.3	1.0	1.3	1.2

EF	C2-a-1	C2a-2	C2a-3	C2a-4	C2a-5	C2a-6	C2a-7	C2a-8	C2a-9	C2a-10	C2a-11	C2a-12	C2a-13	C2a-14	C2a-15	C2a-16	C2a-17
Cr	1.2	0.6	0.6	0.5	0.5	0.5	0.5	0.5	0.6	0.5	0.5	0.5	0.5	0.5	0.5	0.6	0.6
Co	0.7	0.5	0.4	0.9	0.4	0.4	0.4	0.4	1.1	0.4	0.6	0.5	0.8	1.4	0.8	<b>2.4</b>	<b>4.3</b>
Ni	2.0	<b>2.1</b>	<b>2.3</b>	<b>3.4</b>	<b>2.2</b>	2.0	<b>2.1</b>	1.8	1.9	1.8	2.0	2.0	<b>2.9</b>	<b>4.5</b>	1.8	<b>3.7</b>	<b>9.7</b>
Zn	0.4	0.6	0.5	0.6	0.6	0.6	0.7	0.6	0.6	0.6	0.6	0.6	0.6	0.6	0.7	0.9	1.9
Rb	0.6	0.5	0.7	0.6	0.6	0.6	0.7	0.5	0.6	0.6	0.6	0.7	0.7	0.7	0.6	0.7	0.7
U	0.6	0.6	0.7	0.6	0.6	0.6	0.7	0.6	0.7	0.7	0.6	0.8	0.7	1.0	0.7	1.0	1.0
K	1.0	0.8	1.2	1.1	1.1	1.0	1.1	1.0	1.2	1.2	1.0	1.2	1.1	1.3	1.1	1.1	0.8
Fe	0.3	0.3	0.3	0.4	0.4	0.5	0.5	0.5	0.6	0.5	0.5	0.5	0.6	0.9	0.6	1.1	1.2

\* Calculation of EF was made after Meyer et al. (2012), enrichment factors to C2a samples (enrichment caused by biogenic structures is marked by bold letters).

## 6.5 Discussion

After the Neoproterozoic Oxygenation Event (NOE) (Och and Shields-Zhou 2012), the oceans were fully ventilated which resulted in the decrease of dissolved Fe<sup>2+</sup> in the water column and restricted Fe-oxidizing bacteria to the shallow water environment (Dahanayake and Krumbein, 1986) where the sources of iron were detrital minerals (Hoffman et al., 1998b, 2011). However, detrital minerals in our samples such as pyrite and chlorite were consumed as Fe-source (e.g. profile C2a). Enhanced local hydrothermal activity (Campbell and Squire, 2010; Reysenbach and Cady, 2001) could result in some cm thick 3D structure of iron-oxidizing biomat occurring in profiles K2 and K4. On account of restricted Fe and P input, mat building appeared temporary as thin laminae (C1) and coatings (C14a). Probably a short-term iron source solved the nutrient source for filamentous iron bacteria, which development ended either by suboxic conditions turned to more oxic or abrupt arrival of iron-hydrothermal fluids. During the diagenesis of Fe-biomats, the original ferrihydrite ordered to more stable minerals, such as lepidocrocite, goethite and hematite due to dissolution and dehydration processes (Konhauser, 1998; Schwertmann et al., 2007), which is well docu-

mented in our Raman map of profile C2a. Presence of sigmaclasts suggests pressure dominated metamorphism after initial bioweathering in profile C2a. Sigmaclasts of quartz and pyrite confirms formation of pyrite via precipitation from hydrothermal solutions during a shear-tectonic event. The biodegradation of pyrite is either due to surface weathering or happened earlier under low metamorphic conditions after the tectonic event.

In general, Fe-rich biomats are encrusted by dolomite and silica (Baele, 2008), which is also reported in our samples. Fe-rich biomats are better preserved in diagenetic quartz, than in carbonate host material, which is well documented in our profile C2a. Silica precipitation is derived either by the destruction of organic complexes or the transformation of ferrihydrite (Baele, 2008).

Microbial structures can be identified not only by their mineralogy and texture, but also by their geochemistry. The detected anomalies in Fe, Mn, Mg, Co, Ni, Cu, Zn and Mo can be correlated with microbial activity (Takahashi et al., 2007). It reveals that enrichment of main elements (Al, Si, Na, Ca, Mg), REE and traces (Y, Zr, Nb, Hf, Pb, Th) belong to an early phase (lag-log phase\*) of the Fe-oxidizing microbial processes via bacteria (*Gallionella*) (Heim, 2010). The Fe-oxidizing bacteria of the aged phase (log-stat phase) existed in microbial mats, enriched in Ca, Mg, Na, Cs, Sr, Se and Li (Heim, 2010).

\*Microbial population growth phases are the following: (i) *lag phase*: bacterial adaptation; (ii) *log (logarithmic) phase*: a period characterized by cell doubling with exponential growth; (iii) *stationary (stat) phase*: the growth rate slows as a result of nutrient depletion and accumulation of toxic products; (iv) *decline (dec) phase*: closes the growth period (exponential death phase), bacteria succumb to their own wastes (but endospores survive), and the cycle starts again (Novick, 1955; Zwietering et al., 1990).

The elevated values Co, -Ni, -Zn with slightly negative  $\delta^{13}\text{C}$  anomalies in the range of K2/05-08 are probably attributed to microbial metabolism (Fig. 5.). The strongly negative  $\delta^{13}\text{C}$  anomalies and elevated Ni indicate aged biomats in the basal part of our profile K2 (K2/01-03) (Fig. 5.). In our profile C2a, near to the lenses with biodegraded detritus, elevated biogenic trace element (Ba, As, Sr, Ni, Zn, Ce) anomalies occur. Within the C2a/12-15 interval, Ba, Sr, Co, Ni, Ce and As can reflect bioactivity of Fe-biomats and their weathering products, e.g. mixed smectite-iron-oxide mineral phases. The Co and As anomaly in sample C2a-9 probably indicates also the presence of bioweathering of lenses containing detrital minerals.

The measured Fe-biomaat layers show high enrichment factors for Co, Ni, Zn, Fe, and U in our profiles K2 and K4, but in our profile C2a the higher enrichment factor is restricted to Ni, the other elements vary within normal marine values (0.5-2.0). An important geochemical signature for biogenic activity in the sedimentary substrate is the enrichment in specific elements especially Fe, P, V, Co, Zn and Mo (Konhauser, 2002) and also in Mn, S, As, Mg, Ba,

Sr, Ce (Polgári et al. 2012), which are in addition associated with negative  $\delta^{13}\text{C}$  values. Our geochemical data (slightly negative Ce anomaly, less enriched HREE (heavy rare earth elements) to LREE (light rare earth elements) in PAAS (Post-Archean Australian shale) - normalized REE (rare earth element) pattern) and the presence of iron-oxidizing bacterial mats suggest suboxic sedimentary conditions, as well as (German and Elderfield, 1990).

## 6.6 Conclusions

Within the tested Marinoan postglacial layers we detected three distinct types of microbial mats with respect to their formation: synsedimentary mats, trapping sediment particles (profile K4, sample C1), secondary mats, resulting from bioweathering of iron-bearing minerals (pyrite, chlorite) (profiles C2a and K2, samples C7, P49-1), and biofilms coating on clasts surface, formed directly after their deposition in the bedrock (C14a). The synsedimentary mats formed within neutrophilic suboxic conditions, specific for starving basin environments, where the nutrient presumably came from the input of hydrothermal vents. In contrast, the nutrients of secondary microbial mats were iron-bearing minerals, like chlorite and pyrite. The coating of iron-oxidizing bacteria on clasts surface in sample C14a probably indicate transient suboxic conditions which subsequently turned to oxygenic condition. The presence of smectite in microbial mats indicates oxygenic conditions during diagenesis. The quartz sigmaclasts sheathing pyrite grains indicate tectonic shearing during diagenesis or a later low grade metamorphic process which affected the deposits of our research area due to the subsequent Panafrican Orogeny.

## 6.7 Acknowledgements

We are grateful to Peter Nagl (XRF) and Susanne Gier (XRD) for assistance in lab work and their helpful discussions. This study was supported by the Austrian Academy of Sciences through a grant to Christian Koeberl (International Geological Correlation Program IGCP No. 512. The samples were collected by Dr. Friedrich Popp, thereby supported by the Geological Survey of Namibia and Director Dr. G. Schneider which we are grateful for their important help as to field work organization and sample export management. We appreciate the help of the reactor team of the Institute of Atomic and Subatomic Physics, Vienna, with the irradiations.

## References

- Baele, J.-M., Bouvain, F., De Jong, J., Matielli, N., Papier, S., Prat, A., 2008. Iron microbial mats in modern and Phanerozoic environments. *Proc. Soc. Phot. Instr. Eng.*, 7097, 70970N–70970N–12.
- Campbell, I.H., Squire, R.J., 2010. The mountains that triggered the Late Neoproterozoic increase in oxygen: the second great oxidation event. *Geochim. Cosmochim. Acta*, 74 /15, 4187–4206.
- Dahanayake, K. and Krumbein, W.E., 1986. Microbial structures in oolitic iron formations. *Miner. Depos.*, 21, 85–94.
- Domack, E., Hoffman, P., 2003. Stratigraphic transition into and out of Snowball Glacial: Evidence from the Otavi Platform and Fransfontain slope, Namibia. - *Eos Trans. AGU*, 84/46, Fall Meet. Suppl., Abstract C11B-0819.
- Evans, D.A.D., 2000. Stratigraphic, geochronological and paleomagnetic constraints upon the Neoproterozoic climatic paradox. *Am. J. Sci.*, 300, 347–433.
- Eyles, N. and Januszczak, N., 2004. 'Zipper-rift': a tectonic model for Neoproterozoic glaciations during the breakup of Rodinia after 750 Ma. - *Earth-Sci. Rev.*, 65/1-2, 1–73.
- Fairchild I. J. and Kennedy M. J., 2007. Neoproterozoic glaciation in the Earth System. *J. of Geol. Soc. London*, 164, 895-921.
- German, C.R., Elderfield, H., 1990. Application of the Ce anomaly as a paleoredox indicator: The ground rules. *Paleoceanography*, 5, 823–833.
- Harland, W.B., 1964. Critical evidence for a great Infra-Cambrian glaciation. - *Geologische Rundschau* 54, 45–61.
- Hedberg, R.M., 1979. Stratigraphy of the Owamboland basin, South West Africa. *Bull. Precamb. Res. Unit, Cape Town*, 24, 325 pp.
- Heim, C.N., 2010. An integrated approach to the study of biosignatures in mineralizing biofilms and microbial mats. PhD thesis, Georg-August-University of Göttingen, Germany, p. 183.
- Hoffman P.F., MacDonald F.A. and Halverson G.P., 2011. Chemical sediments associated with Neoproterozoic glaciation: iron formation, cap carbonate, barite and phosphorite. - In: Arnaud E, Halverson GP, Shields-Zhou G. (Eds.) *The Geological Record of Neoproterozoic Glaciations*. *Geol. Soc., London, Mem.*, 36, 67-80.
- Hoffman, P.F. and Schrag, D.P., 2002. The snowball Earth hypothesis: testing the limits of global change. *Terra Nova*, 14, 129-155.
- Hoffman, P.F., 2002. Carbonates bounding glacial deposits: Evidence for Snowball Earth episodes and greenhouse aftermaths in the Neoproterozoic Otavi Group of northern Namibia. *Excursion*

- sion Guide, 16th International Sedimentological Conference, Auckland Park, South Africa, 39 p.
- Hoffman, P.F., Halverson, G.P., 2008. Otavi Goup of the western Northern Platform, the Eastern Kaoko Zone and the western Northern Margin Zone.-In: R.McG.Miller [Ed]: The Geology of Namibia.- Vol 2: Neoproterozoic to Lower Paleozoic.- Ministry of Mines and Energy, Geological Survey, Namibia, 69-136.
- Hoffman, P.F., Kaufman, A.J., Halverson, G.P., and Schrag, D.P., 1998a. A Neoproterozoic Snowball Earth. *Science*, 281, 1342–1346.
- Hoffman, P.F., Kaufman, J.A. and Halverson, G.P., 1998b. Comings and goings of global glaciations on a Neoproterozoic carbonate platform in Namibia. *GSA Today*, 8, 1-9.
- Hoffmann, K. H., Condon, D.J., Bowring, S.A., and Crowley J.L., 2004. U-Pb zircon date from the Neoproterozoic Ghaub Formation, Namibia: Constraints on Marinoan glaciations. *Geology*, 32, 817-820.
- Hoffmann, K.-H., and Prave, A.R., 1996. A preliminary note on a revised subdivision and regional correlation of the Otavi Group based on glaciogenic diamictites and associated cap dolostones. *Communs. Geol. Soc. Namibia*, 11, 81-86.
- Hyde, W.T., Crowley, T.J., Baum, S.K., and Peltier, W.R., 2000. Neoproterozoic 'snowball Earth' simulations with a coupled climate/ice-sheet model. *Nature*, 405, 425–429.
- Kennedy, M.J., 1996. Stratigraphy, sedimentology, and isotopic geochemistry of Australian Neoproterozoic postglacial dolostones: deglaciation,  $\delta^{13}\text{C}$  excursions, and carbonate precipitation. *J. Sed. Res.*, 66, 1050-1064.
- Kennedy, M.J., Mrofka, D. and von der Borch, C., 2008. Snowball Earth termination by destabilization of equatorial permafrost methane clathrate. *Nature*, 453, 642-645.
- Kennedy, M.J., Runnegar, B., Prave, A.R., Hoffmann, K.-H. and Arthur, M.A., 1998. Two or four Neoproterozoic glaciations? *Geology*, 1998, 26, 1059-1063.
- Konhauser, K.O., 1998. Diversity of bacterial iron mineralization. – *Earth-Sci. Revs.*, 1998, 43, 91-121.
- Konhauser K.O., Hamade T., Raiswell R., Morris R.C., Ferris F.G., Southam G. and Canfield D.E., 2002. Could bacteria have formed the Precambrian banded iron formations? *Geology*, 20, 1079-1082.
- Le Hir, G., Donnadieu, Y., Godderis, Y., Pierrehumbert, R.T., Halverson, G.P., Macouin, M., Nedelec, A., and Ramstein, G., 2008. The snowball Earth aftermath: Exploring the limits of continental weathering processes. *Earth Planet. Sci. Lett.*, 277, 453-463.
- Meyer, E. E., Quicksall, A.N., Landis, J.D., Link, P.K and Bostick, B.C., 2012. Trace and rare earth elemental investigation of a Sturtian cap carbonate, Pocatello, Idaho: Evidence for ocean redox conditions before and during carbonate deposition. *Precamb. Res.*, 192, 195, 89–106.

- Novick, A., 1955. Growth of Bacteria. *Ann. Rev. Microbiol.* 9, 97-110.
- Och, L.M. and Shields-Zhou, G.A., 2012. The Neoproterozoic oxygenation event: Environmental perturbations and biogeochemical cycling. *Earth-Sci. Revs* 110, 26–57.
- Polgári, M., Hein, J.R., Vigh, T., Szabó-Drubina, M., Fórizs, I., Bíró, L., Müller, A., Tóth, A.L., 2012. Microbial processes and the origin of the Úrkút manganese deposit, Hungary. *Ore Geol. Revs.*, 47, 87–109.
- Reysenbach, A., Cady, S., 2001. Microbiology of ancient and modern hydrothermal systems. - *Trends Microbiol.*, 9, 79-86.
- Taylor, S.R. and McLennan, S.M., 1985. *The Continental Crust: Its Composition and Evolution*. Blackwell Scientific Publications, Palo Alto, CA. 328 pp.
- SACS, South Africa Committee for Stratigraphy 1980. *Stratigraphy of South Africa*. Kent L.E. (Comp); Part 1. Lithostratigraphy of the Republic of South Africa, South West Africa / Namibia and the Republics of Bophuthatswana, Transkei and Venda. *Handb. Geol. Surv. S. Africa*, 8, 690 pp.
- Schwertmann, U., Cornell, R.M., 2007. *Iron Oxides in the Laboratory: Preparation and Characterization*. Wiley-VCH, 188 pp.
- Takahashi, Y., Hirata, T., Shimizu, H., Ozaki, T. and Fortin, D., 2007. A rare earth element signature of bacteria in natural waters? *Chem. Geol.*, 244, 569-583.
- Williams, G.E., 2000. Geological constraints on the Precambrian history of Earth's rotation and the Moon's orbit. *Rev. of Geophys.*, 38, 37-59.
- Zwietering, M.H., Jongenburger I, Rombouts F.M, van Riet T.K., 1990. Modeling of the bacterial growth curve". *Appl. Envir. Microbiol.*, 56, 1875-1881.

## 7 Paleoenvironmental reconstruction, weathering and diagenesis of Neoproterozoic postglacial transition layers: Observation from the Otavi Group/ Namibia

Ildiko Gyollai<sup>1, 3</sup>, Friedrich Popp<sup>2</sup>, Marta Polgári<sup>3</sup>, Dieter Mader<sup>1</sup>, Szabolcs Nagy<sup>4</sup>, K. Fintor<sup>4</sup>, E. Pál-Molnár<sup>4</sup>, Christian Koeberl<sup>1, 5</sup>

<sup>1</sup>Department of Lithospheric Research, University of Vienna, Althanstrasse 14, A-1090, Vienna, Austria, Tel:+431427753316, e-mail: [gyildi@gmail.com](mailto:gyildi@gmail.com), <sup>2</sup>Department of Geodynamics and Sedimentology, University of Vienna, Althanstrasse 14, A-1090, Vienna, Austria, e-mail: [friedrich.popp@univie.ac.at](mailto:friedrich.popp@univie.ac.at),

<sup>3</sup>Research Center for Astronomy and Geosciences, Institute for Geology and Geochemistry, Hungarian Academy of Sciences, Budapest, Hungary, 1112 Budapest, Budaörsi út. 45. e-mail: [rodokrozt@gmail.com](mailto:rodokrozt@gmail.com), <sup>4</sup>Department of Mineralogy, Geochemistry and Petrology, Szeged University, 6702 Szeged, Egyetem utca 2-6, email: [ringwoodite@gmail.com](mailto:ringwoodite@gmail.com), <sup>5</sup>Natural History Museum, Vienna, A-

1010, Burgring 7, Vienna, Austria e-mail: [christian.koeberl@univie.ac.at](mailto:christian.koeberl@univie.ac.at)

**Article is prepared for Austrian Journal of Earth Sciences.**

### Abstract

The Neoproterozoic “Snowball Earth” Cryogenian period exhibits two discrete world-wide glaciations: the older Sturtian (~750 Ma) and the younger Marinoan (~635 Ma) event. Their subsequent deglaciation process is currently based on two hypotheses: the one postulates rapid deglaciation of a completely frozen Earth without detrital input whereas the other claims slow deglaciation of ice sheets with open sea areas and with detrital input. This study attempts a paleoenvironmental reconstruction concerning crossover periods following cryogenic ages and provides perspectives among various deglaciation theories. Our samples were collected from directly postglacial transition layers at the boundaries of the Sturtian Chuos/Rasthof Fm.'s and the Marinoan Ghaub/Maieberg Fm.'s of the Neoproterozoic Otavi Group in NW-Namibia. The observed minor amount of detrital minerals and presence of authigenic and diagenetic minerals (dolomite, calcite, diagenetic quartz, lepidocrocite, smectite) refuses any fluvial transport from continental source areas. The participation of microbial mats suggests calm sedimentary environments with suboxic conditions. Sturtian postglacial transition layers are less influenced by secondary processes (diagenesis, weathering) than Marinoan postglacial transition layers.

**Keywords:** Neoproterozoic, Snowball Earth, weathering, diagenesis, microbial structures.

## 7.1 Introduction

Observational evidence supports the idea that the Precambrian Earth's history has episodes of total ice coverage of the planet. The Snowball Earth hypothesis states that the Sturtian (about 710 Ma) and Marinoan glaciations (about 635 Ma) were of global extent and lasted for several million years each (Hoffman et al., 1998). A variation of this hypothesis, called the Slushball Earth, requires milder conditions without substantial equatorial sea ice. The Snowball Earth glaciations would have ended abruptly in a greenhouse environment (Hoffman et al., 1998), whereas the Slushball would have experienced a slower deglaciation (Harland and Rudwick, 1964). A variety of reasons for initializing global glaciation have been discussed, including decreased solar luminosity, continental breakup, or the passage of the solar system through a molecular cloud (Hoffman and Schrag, 2002). Alternatively, the 'Zipper-rift' model emphasizes the strong linkage between the first-order reorganization of the Earth's surface created by diachronous rifting of the supercontinent Rodinia, the climatic effects of uplifted rift flanks and the resulting sediments deposited in newly formed rift basins (Eyles and Januszczak, 2004). Not only the cause of a possible glaciation is unclear, the cause and mechanism of deglaciation is also debated. The above presented authors have variety for hypotheses for runoff of glaciations, but the paleoenvironment during deglaciation in our research area (Otavi Group, NW-Namibia) is not documented. The goal of study is to give a paleoenvironmental reconstruction for Cryogenian deglaciations using mineral composition and geochemical proxies in postglacial transition layers. Our study gives perspectives for influences during sediment deposition (detrital input, mass-flow related fluidization), secondary processes (diagenesis, weathering), and biogenic influence during the sedimentation and weathering.

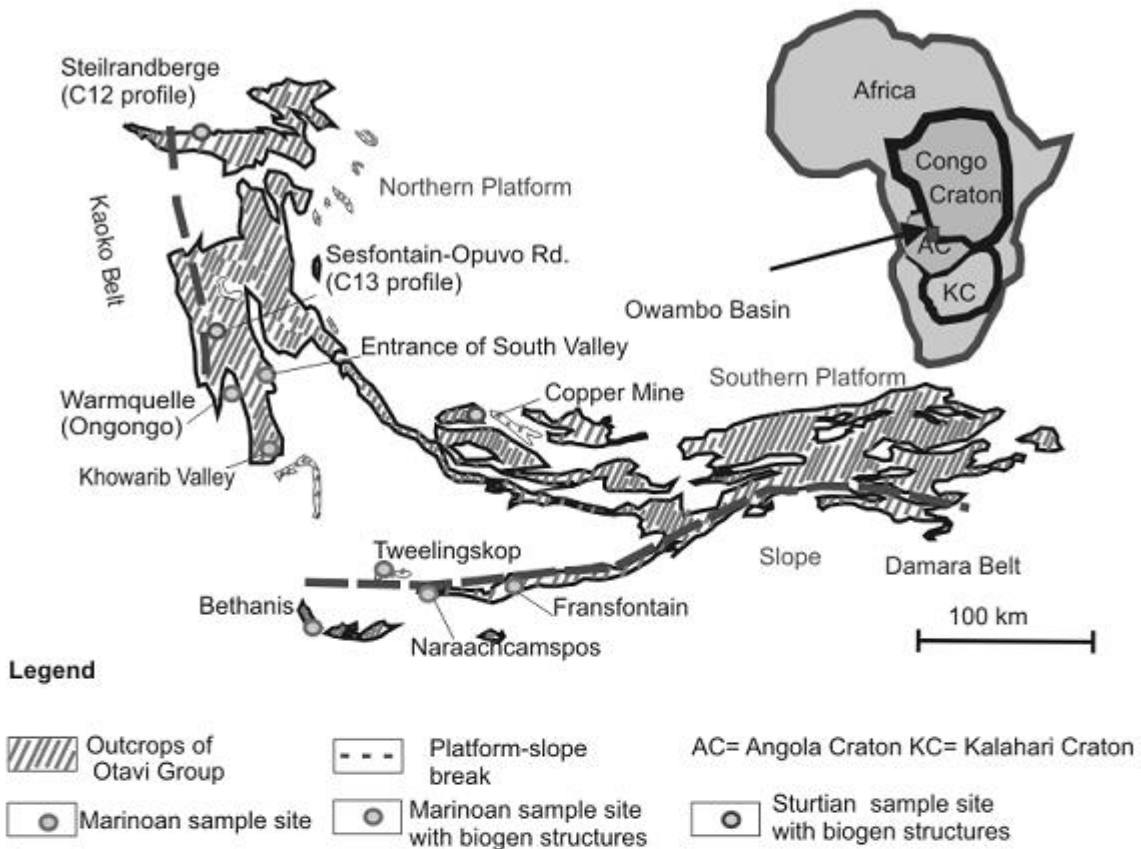
## 7.2 Geological background

Continental break-up of the Mid-Proterozoic Rodinia supercontinent produced world-widespread extensional rift systems followed by the development of passive continental margins. In Namibia the Damara Supergroup, consisting of the Nosib-, Otavi-, Mulden-, Nama-, Witvlei- and Gariiep Groups, formed during this period in response to Pan-African continental rifting with subsequent seafloor spreading, subsidence, and marine transgression on the West Gondwanaland continent (Porada, 1989). On the Congo Craton initial rifting caused deposition of the Nosib Group siliciclastic sediments (Fig. 1.); later subsidence and transgression lead to the development of a stable platform where the thick sequence of Otavi Group carbonate-dominated sediments accumulated. Subsequent uplift in the northwestern part of the Damara Orogen, caused by the collision of the Kalahari and Rio de la Plata

Cratons with the Congo Craton, resulted in deep erosion of Damaran age and older rocks (Martin, 1965; Hedberg, 1979; Miller, 1983) and the consequent deposition of the Mulden Group as a molasse.

In the late Neoproterozoic the Congo Craton was a Bahama-type sea-level carbonate platform of enormous size, accumulating the Otavi Group sediments which nowadays drape the craton's southern promontory in NW Namibia. The Otavi Group is exposed for ~700 km along strike in the external zone of the Pan-African Damara-Kaoko Belt that rims the Congo Craton (Hedberg, 1979).

A



B

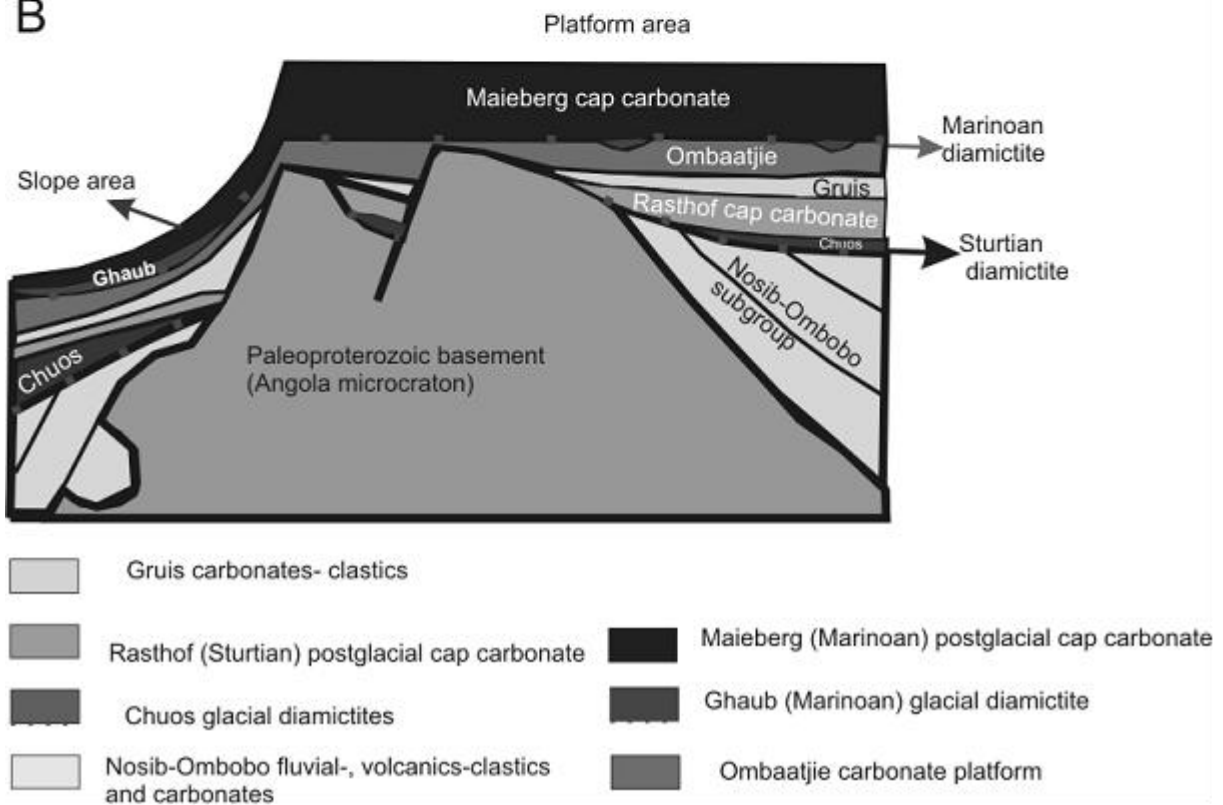


Figure 1. Geological map of sampling sites and cross sections (Modified after Hoffman, 2002).

### 7.2.1 The Congo Cratonic Sedimentary Cover Sequence

At the base is the rift-clastic Nosib Group, known to be older than  $756 \pm 2$  My (Hoffmann et al., 1996) (Fig. 1B). It consists of conglomerate, arkosic quartzite, and siltstone with minor shale and carbonate. Volcanic rocks are found sporadically within the section (Hedberg, 1979).

In the middle is the carbonate-dominated Otavi Group, a succession of Neoproterozoic age (~600-760 Ma), which constitutes a typical shelf facies and rests paraconformably or unconformably upon the Nosib Group. The Otavi Group (Fig. 1AB) spans the rift-drift transition and succeeding thermal subsidence stage of the Congo Craton's passive margin. The lower Otavi Group (Ombombo Subgroup) contains volcanics in the south dated at  $758 \pm 4$  and  $746 \pm 2$  Ma (Hoffmann et al., 1996)

The middle Otavi Group (Abeneb Subgroup) is bounded by two discrete intervals of diamictite and associated glaciomarine deposits sandwiched by thick carbonate piles. The glaciogenic origin of the older interval (Chuosi Formation) was first documented by Martin (1965) and Hedberg (1975). Later Hoffmann and Prave (1996) lined out the younger glaciogenic interval (Ghaub Formation) covering an erosional surface on top of a carbonate platform sequence (Ombaatjie Formation) (Fig. 1B). The sediments of both glaciogenic periods are overlain by distinct "cap-carbonate" layers, represented by the basal parts of the Rasthof- and Maieberg Formations.

The upper Otavi Group (Tsumeb Subgroup) is a thick and rather monotonous stack of grainstone-dominated cycles of cherty dolomite, deposited during the prolonged drift stage of the Pan-African. (Fig. 1B)

At the top of the succession follows the Mulden Group siliciclastic foreland sequence, a typical molasses facies pile related to the Congo craton's collision (~630-550 Ma) with the active margin of the Rio de la Plata Craton (Stanistreet et al., 1991; Alkmim et al., 2001). The Mulden Group rests disconformably upon the folded Otavi Group and consists of conglomerate, quartzite, siltstone and shale. Rb-Sr isotopic studies of Mulden Group shales suggest a model depositional age of 550-560 Ma followed by two distinct low-grade thermal events of regional extent at  $537 \pm 7$  and  $457 \pm 12$  Ma, respectively (Clauer and Kröner, 1979).

### 7.2.2 The Otavi Group Research Area

Our research area is located in the Neoproterozoic Otavi Group, holding a foreland position relative to the Kaoko Belt in the West and the Damara Belt in the South (Hoffman, 2005). The Otavi Group contains two glaciogenic diamictite units, the lower Chuos Formation of Sturtian age and the upper Ghaub Formation of Marinoan age (Hoffmann 2002, 2005). Each of the glacial sedimentary piles is overlain by characteristic cap-carbonate layers belonging to the Rasthof F. and the Maieberg F. respectively, both showing quite different structural and sedimentary features.

#### *Sturtian (Chuos/Rasthof) diamictite/cap carbonate deposits*

Sturtian postglacial transition layers span the uppermost / lowermost portions of the Chuos / Rasthof Formations (Fig 1-2.). Massive to poorly stratified diamictite is the characteristic lithology formed in the glaciogenic Chuos period of sedimentation. The **Chuos Formation** is widely exposed throughout the Northern Platform Area (Martin, 1965) varying both regionally and locally in thickness, being thickest (up to ~1000m) in paleodepressions and absent on paleohighs. Towards the outer platform edge and foreslope area the diamictite thins virtually to zero. Hoffmann and Halverson (2008) interpret these diamictites as originating mainly as glacial marine rain-out deposits formed close to the grounding line of warm-base ice streams. The upper Chuos Formation contact is almost invariably sharp and smooth, genetically interpreted as an abrupt flooding surface separating diamictite from deepwater dolomite rhythmite of the basal **Rasthof Formation** that on his part displays no evidence of reworking, subaerial exposure or significant hiatus. Unlike the Marinoan Maieberg cap-carbonate sequence, the Rasthof Formation has no transgressive stage: the deepest water facies are at the bottom of the sequence. This implies that carbonate sedimentation did not begin until after the glacio-eustatic rise (Hoffmann and Schrag, 2002; Hoffmann and Halverson, 2008). The Rasthof Formation, normally 200-400m thick on the Otavi Platform, has a layer-cake internal stratigraphy comprised of three members termed “abiotic”, “microbial” and “epiclastic” (Hoffmann and Halverson, 2008). The basal “abiotic” member of the Lower Rasthof Formation consists of flaggy, dark gray dolomite and dolomitic limestone, characterized by mm-scale, parallel, turbiditic lamination. Hematite, mobilized from the underlying diamictite, stains the basal few centimeters of the dolomite rhythmite (Hoffmann and Halverson, 2008).

The “microbial” member, which is one focus of this work, may rest directly upon Chuos diamictites in tectonically elevated regions (our samples C13) indicating that the mentioned terms “abiotic” and “microbial” do not represent stratigraphic but facies features. Furthermore even the “epiclastic” member can be recognized in these tectonically elevated regions, thus providing a chance for stratigraphic correlation of time equivalent facies regions.

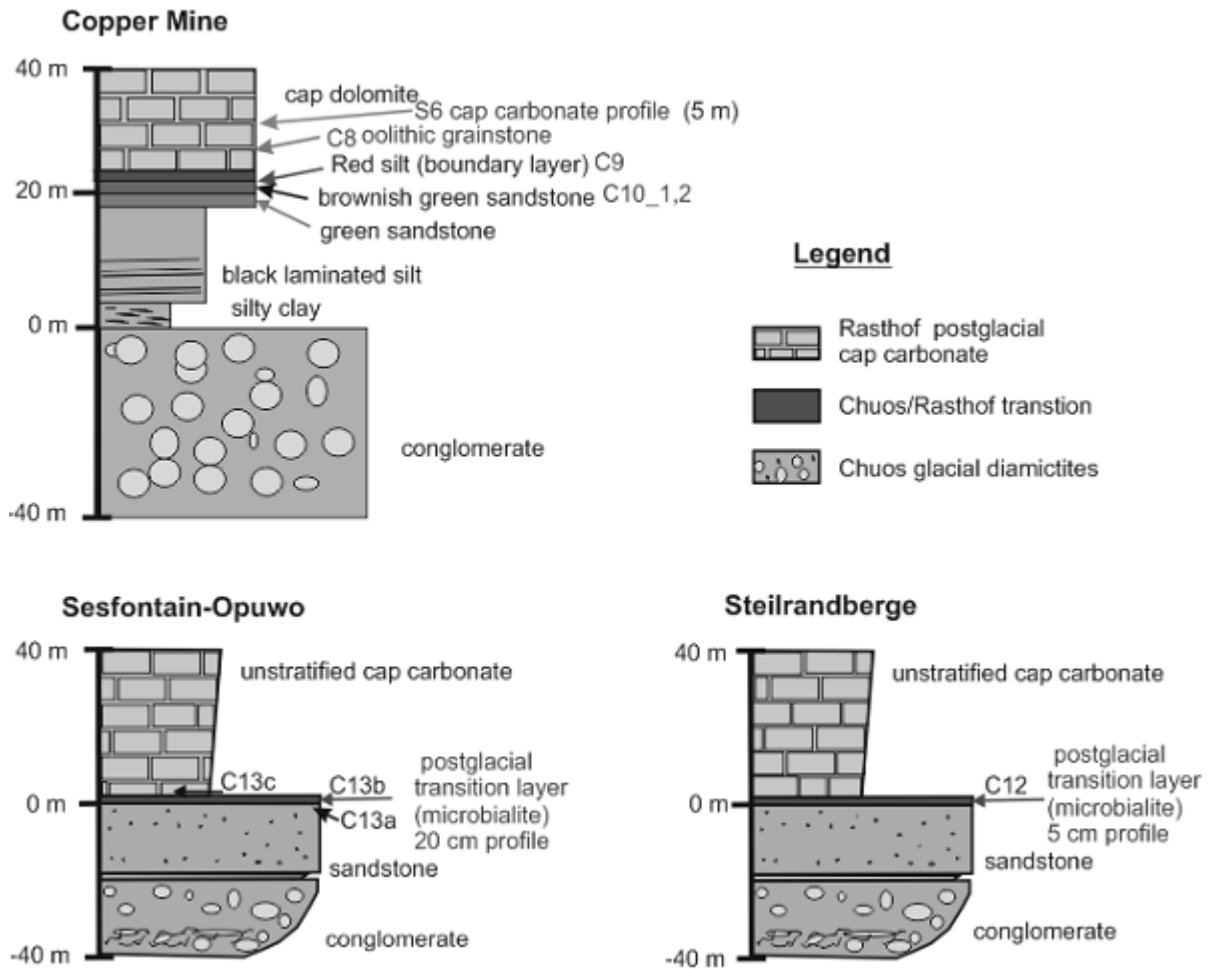


Figure 2. Profiles from Sturtian sampling sites (modified after Hoffman, 2002).

**Table 1.** Sturtian sampling sites and their facies with GPS Data

Site Nr	Sample Nr	Locality	GPS-Data	Lithology	Stratigraphic position	Facies
8	Profile S6	Copper Mine	19°25'18.43 "S; 15° 9'50.90"E	opalized carbonate	Rasthof F.	platform
8	C8	Copper Mine	"	red carbonate	Chuoss-Rasthof F.	platform
8	C9	Copper Mine	"	carbonate-quartzite	Chuoss-Rasthof F.	platform
8	C10_1	Copper Mine	"	sandstone	Chuoss-Rasthof F.	platform
8	C10_2	Copper Mine	"	sandstone compact	Chuoss-Rasthof F.	platform
8	C11_1	Copper Mine	"	black laminated sandstone	Chuoss-Rasthof F.	platform
8	C11_2	Copper Mine	"	black laminated sandstone	Chuoss-Rasthof F.	platform
9	C12	Steilrandberge	17°47'1.67" S; 13°39'54.10 "E	red-brown dolomite	Chuoss-Rasthof F.	platform
10	C13a	Sesfontain- Opuwo Rd	18°46'26.49 "S; 13°45'11.24 "E	brown sandstone unaltered	Chuoss-Rasthof F.	platform
10	C13b	Sesfontain- Opuwo Rd	"	red/green sand- stone altered	Chuoss-Rasthof F.	platform
10	C13c	Sesfontain- Opuwo Rd	"	transitionzone to carbonate	Chuoss-Rasthof F.	platform

#### *Marinoan (Ghaub/Maieberg) diamictite/cap carbonate deposits*

Marinoan postglacial transition layers span the uppermost / lowermost portions of the Ghaub / Maieberg Formations (Fig. 1-2.). The **Ghaub** Formation (Hoffmann and Prave, 1996) is only fragmentary preserved within structural depressions of inner platform areas, suggesting the western Otavi Platform being the source area for appreciable diamictite accumulations in slope facies areas bordering on the platform edges. The clasts are different types of dolomite and rarely limestones, all apparently derived from the underlying Ombaatjie Formation. The Ghaub glacial lithofacies are composed almost exclusively of carbonate debris (Hoffman and Halverson, 2008). Stratigraphic evidence is presented for a single advance and retreat cycle for the Ghaub glaciation; grounded ice existed at the maximum advance leaving characteristic sedimentary features (Domack and Hoffman, 2003).

The **Maieberg Formation** (Hedberg, 1979; SACS, 1980), subdivided into three members, is an up to 400 m thick pile of carbonate sedimentary cycles which originated in a warm periodic platform facies environment following the Ghaub glacial period (Fig. 1B). The basal **Keilberg Member** (Hoffmann and Prave, 1996) is a "cap dolostone" associated with the sea-level rise attending the Ghaub deglaciation (Kennedy, 1996; Hoffmann and Schrag, 2002). Its characteristic feature is a uniform, 10-15 m thick, pale colored marker bed which is strongly laminated from bottom to top. Unusual sedimentary textures featuring vertical "tube-like" appearance are visible, starting about one meter above the base, in our sample sites. Ac-

According to Le Hir et al. (2008) these tubes may have been generated due to CO<sub>2</sub> oversaturation and methane outgassing from clathrates (Kennedy et al., 2001). However, Hoffmann and Halverson (2008) prefer the hypothesis that the tubes formed in close connection with the growth of compound stromatolites.

**Table 2:** Marinoan sampling sites and facies

Sit e Nr	Sam- ple Nr	Locality	GPS Data	Lithology	Stratigraphic posi- tion	Facies
1	C1a	Fransfontain	20°11'59.06"S; 15° 0'58.68"E	allodapic dolostone	Ghaub-Maieberg F.	slope
1	C1b	Fransfontain	"	allodapic dolostone	Ghaub-Maieberg F.	slope
1	C1c	Fransfontain	"	allodapic dolostone	Ghaub-Maieberg F.	slope
2	C2a	Naraachamspos	20°11'27.68"S; 14°51'4.42"E	boundary layer	Ghaub-Maieberg F.	slope
2	C2b	Naraachamspos	"	boundary layer	Ghaub-Maieberg F.	slope
2	C2c	Naraachamspos	"	boundary layer	Ghaub-Maieberg F.	slope
2	Profile C2a	Naraachamspos	"	cap carbonate	Ghaub-Maieberg F.	slope
2	C3_1	Naraachamspos	20°11'28.74"S; 14°51'4.38"E	boundary layer	Ghaub-Maieberg F.	slope
2	C3_2	Naraachamspos	"	boundary layer	Ghaub-Maieberg F.	slope
2	C17a	Naraachamspos	no data	tectonic clay	Ghaub-Maieberg F.	slope
2	C17b	Naraachamspos	no data	ashy clay	Ghaub-Maieberg F.	slope
2	C17c	Naraachamspos	20°11'28.00"S; 14°51'2.76"E	boundary layer	Ghaub-Maieberg F.	slope
3	C4	Tweelingskop	20° 7'13.47"S; 14°35'1.30"E	red dolomite	Ghaub-Maieberg F.	platform edge
3	C5	Tweelingskop	20° 7'13.82"S; 14°35'1.71"E	aeolianite	Ghaub-Maieberg F.	platform edge
4	C6	Bethanis	20°24'24.00"S; 14°20'13.55"E	red silt	Ghaub-Maieberg F.	distal slope
4	C7	Bethanis	20° 7'13.47"S; 14°35'1.30"E	dolomite rhythmite	Ghaub-Maieberg F.	distal slope
5	C14a	Valley S En- trance	19°11'18.40"S; 13°56'13.39"E	red diamictite	Ghaub-Maieberg F.	platform
5	C14b	Valley S En- trance	"	red transition layer	Ghaub-Maieberg F.	platform
5	C14c	Valley S En- trance	"	tectonized clay	Ghaub-Maieberg F.	platform
5	C14d	Valley S En- trance	"	red green bounda- ry clay	Ghaub-Maieberg F.	platform
5	C14e	Valley S En- trance	"	basal dolomite	Ghaub-Maieberg F.	platform
5	Profile K4	Valley S En- trance	"	cap carbonate	Ghaub-Maieberg F.	slope
6	C 15a	Khowarib Valley	19°18'24.52"S; 13°59'25.57"E	banded cap- dolomite	Ghaub-Maieberg F.	platform
6	C 15b	Khowarib Valley	"	boundary layer	Ghaub-Maieberg F.	platform
6	C 15c	Khowarib Valley	"	red boundary Clay	Ghaub-Maieberg F.	platform
6	C 15d	Khowarib Valley	"	basal cap dolomite	Ghaub-Maieberg F.	platform
6	C 15e	Khowarib Valley	"	boundary clay	Ghaub-Maieberg F.	platform
6	Profile P49	Khowarib Valley	"	cap carbonate	Ghaub-Maieberg F.	platform
7	C 16a	Ongongo	19° 8'35.77"S; 13°51'15.40"E	sericited clay	Ghaub-Maieberg F.	platform
7	C 16b	Ongongo	"	basal mylonite	Ghaub-Maieberg F.	platform
7	C 16c	Ongongo	"	opalized layer	Ghaub-Maieberg F.	platform
7	Profile K2	Ongongo	"	cap carbonate	Ghaub-Maieberg F.	platform

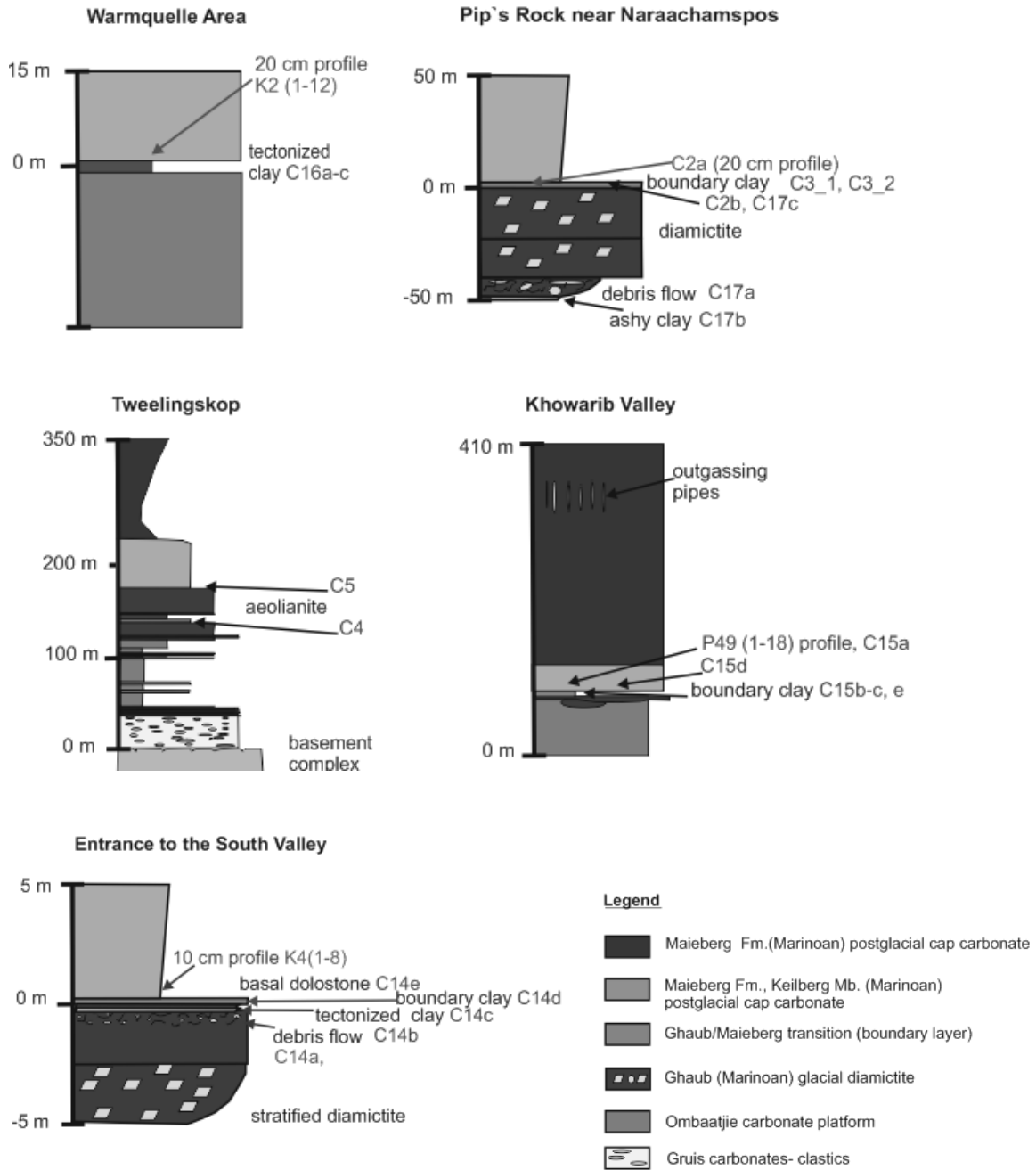


**Figure 3.** Profiles of Marinoan sampling sites (modified after Hoffman, 2002).

## 7.3 Samples and methods

### 7.3.1 Samples

We analyzed a total of 99 samples from 10 localities (Fig. 1A, Table 1-2.) encompassing the transition layers of the rift related **Sturtian Chuos-Rasthof Formations** as well as those from the platform and slope facies areas of the **Marinoan Ghaub-Maieberg Formations** (Fig. 1B): Marinoan samples were collected from the following facies regions (platform or slope): Fransfontain (slope), Naraachamspos (slope), Tweelingskop (paleokarst), Bethanis (distal slope), Entrance to SW Valley (inner platform), Warmquelle/Ongongo (inner platform) and Khowarib Valley (inner platform) (Fig. 1., Table 2.). All Sturtian samples were collected from platform facies regions (Fig. 1., Table 1.). Field work was done in the field season 2009 by one of us (F.P.) in order to retrieve well-documented sets of samples; we collected a total of 28 samples at seven locations from the Marinoan age stratigraphic horizon (Ghaub/Maieberg Fm.) and 10 samples at three locations from the Sturtian age stratigraphic horizon (Chuos/Rasthof Fm.) for further analyses (Fig. 2-4., Table 1-2.). The samples are a lithologic variety of cap carbonates, with colors ranging from pale gray to red and black, depending on their iron content.

### 7.3.2 Methods

A series of thin sections was analyzed using a polarizing microscope in order to identify the samples mineral composition and structural/textural features. The bulk sample's mineral compositions were determined by X-ray diffraction (XRD) at the Department of Geodynamics and Sedimentology, University of Vienna. Diffraction data were collected with a Phillips-diffractometer (PW 3710, goniometer PW-1820), CuK $\alpha$  radiation (45 kV, 35 mA), step size of 0.02 degrees, and counting time of 1 s per step. Minerals were identified using the Joint Committee on Powder Diffraction Standards database (JCPDS, 1980).

A Renishaw RM1000 confocal edge filter-based micro-Raman spectrometer with 20 mW, 632.8 nm He-Ne laser excitation system, and thermoelectrically cooled charged coupled device array detector was used at the Institute of Mineralogy and Crystallography, University of Vienna for the identification of some mineral phases.

For the identification of different carbonate cement and quartz grain generations a Lumic HC5-LM cathodoluminescence-microscope was used. The acceleration voltage applied on the tungsten filament in the electron gun is 14 KV; the beam current can be varied from about 0.05 to 0.4 mA, depending on the examined material.

The contents of some major elements (Na, K, Fe) and trace elements including rare earth elements (REEs), were determined by instrumental neutron activation analyses (INAA) at the Department of Lithospheric Research, University of Vienna (Austria). About 140-150 mg of

each sample powder was sealed in polyethylene capsules and irradiated, together with appropriate geological standards, at the Triga reactor of the Austrian “Atomic Institute”. Details regarding the instrumentation, standards, calculations, as well as information on precision, accuracy, and detection limits of our INAA method are given in Mader and Koeberl (2009).

The major elements and some trace elements (Cu, Ni, Co, Sc, Cr, and V) were determined by XRF (Philips 2400) at the Department of Lithospheric Research, University of Vienna. The specimens were grinded in an electric agate mill, homogenized, dried at 110 °C and fired at 950 °C. For X-ray fluorescence (XRF) analysis, fused beads were produced, consisting of a 1:5 diluted mixture of fired sample material and flux ( $\text{Li}_2\text{B}_4\text{O}_7$ ). Major element bulk analyses were made with a Philips PW 2400 sequential X-ray spectrometer equipped with a Rh-excitation source (Department of Lithospheric Research, University of Vienna). The carbon content and isotopic composition of carbon were measured in the at the Department of Geodynamics and Sedimentology, University of Vienna, using a Carlo Erba Element Analyzer coupled to a Micromass Optima stable isotope ratio mass spectrometer. For analytical details, see e.g., Maruoka et al., 2003, 2007.

Carbonate content measurements were utilized with pressure calcimeter method (“Karbonat-Bombe”) using 1 g of dried powder.

## 7.4 Lithology of Cryogenian postglacial transition layers in Otavi Group

### 7.4.1 Sturtian

Our **Chuoss Formation** samples (Table 1., Fig. 3.) were collected from Site 8 (Copper Mine C10\_1-2, Table 1.) and from Site 10 (Sesfontain Opuwo Rd., C13a, Table 1.). (See site numbers in Table 1-2.) Generally, towards the top diamictite layers decrease in grain size and the matrix is dominated by the silt fraction. The diamictite layers contain variable amounts of carbonate from different origins: a) carbonate precipitation synsedimentary structures (Site 10, Table 1.), b) detrital carbonate clasts, which are derived from older carbonate platform deposits (Site 8). Site 10 contains microbial synsedimentary structures (“iron-stromatolite” with high amount of authigenic iron-oxide (goethite, hematite) but minor amount of quartz. Compared to Site 10 (Sesfontain Opuwo Rd. Table 1.), the uppermost diamictite layer from Site 8 (Copper Mine) contains plenty of minerals from terrigenous input: chlorite, quartz with rutile needles, clay minerals (rectorite, kaolinite), chlorite, and muscovite. Here the iron-microbial structures occur at the rim of bipyramidal quartz. The synsedimentary microbial structures at Site 10 (Sesfontain Opuwo Rd. Table 1.) accumulated within a starving basin lacking terrigenous input, whereas at Site 8 (Copper Mine) layers accumulated within various mild terrigenous input from turbidite flows. The carbonate content varies between 3.4

wt% (Site 10, Table 1.) and 20 wt% (Site 8, Table 1.), but individual layers may lack carbonate at all probably caused by diagenetic segregation (for carbonate content data see Appendix 2.3).

Our samples of boundary layers of the Chuos and Rasthof Formations (Table 2., Fig. 3.) were collected at Site 8 (Copper Mine, C9), at Site 10 (Sesfontain Opuwo Rd., (C13b) and Site 9 (Steilrandberge, C12). Sites 9 and 10 enclose synsedimentary iron microbialites with authigenic mineral phases (hematite, goethite, quartz, carbonate, and albite). Boundary layers from Site 8 contain authigenic (quartz) and terrigenous (kinked mica, feldspar, and iron-oxide with climbing cross lamination) minerals. The carbonate content of boundary layers varies between 3-50 wt% (Copper Mine: 3.4 wt%, Sesfontain-Opuwo, 10.1 wt%, Steilrandberge: 50 wt%). Chlorite and smectite are minor mineral components in Site 8 samples.

The basal layers of the Sturtian cap carbonates (**Rasthof Formation**) (Table 1., Fig. 1-2.) from Site 10 contain “stromatolitic” synsedimentary structures with authigenic carbonate, quartz, and iron oxides. At Site 8 these cap carbonate layers are oolitic-oncoidic grainstones with tiny, terrigenous mineral phases included in the core of oncoids, such as feldspar, quartz, zircon, and muscovite. The rim of some oncoids consists of kaolinite (as weathering product of feldspar), and montmorillonite. Barite veins also cross the matrix material and together pebbles with up to 1 cm in diameter. The cap carbonate were collected as a 20 cm profile at Site 8 (Copper Mine, borehole profile S6) where the cap micritic carbonate is infused with coarse, diagenetic quartz cement indicating wormy intergrowth. The cavities are filled with calcite block cement. Minor minerals are zircon and mica. The carbonate content varies between 94 (C13c) and 99 wt% (S6) in the bottom cap carbonate layers (Chapter 10.3).

#### 7.4.2 Pre-Marinoan

Selected samples from the **Ombaatjie Formation** were collected from Site 3 (Tweelingskop, C4) (Table 2., Fig. 2.). Carbonatic fragments from sample C4 contain numerous synsedimentary structures: flame and ball structure (fluidization), synsedimentary faults, and convolution. The carbonate appears as peloids and rhombohedral crystals, and micritic material. Quartz is present in the form of chert lenses that are rimmed by sericite.

#### 7.4.3 Marinoan

We collected samples from the uppermost portion of the **Ghaub diamictites** from Site 2 (Naraachamspas), Site 3 (Tweelingskop), and Site 5 (Entrance of South Valley) (Table 2., Fig. 2.). The carbonate content varies between 7-70 wt% depending on the amount of trans-

ported carbonate clasts, activity of calcimicrobae in microbialites, and diagenetic reworking. The diamictite from Tweelingskop is strongly altered diagenetically, with large carbonate clasts with euhedral diagenetic quartz matrix. The diamictite from Site 5 (C14a) has a chaotic, slump-structure containing large clastic carbonate fragments (with peloids and shales, and quartz grains in the interior) with iron biomats and contains montmorillonite as clay mineral phase. The diamictite from Naraachamspos contains chlorite as sheet mineral phase.

Our Marinoan postglacial boundary (**Ghaub/Maieberg**) layer samples were collected from different localities: Fransfontain, Naraachamspos, Bethanis, Entrance of South Valley, Kowharib Valley, Warmquelle (Table 2., Fig. 1-2.). The carbonate content of the boundary layer varies between 0 and 70 wt%, depending on local composition and diagenetic reworking. The samples from Site 1 (Fransfontain, C1b-c) contain thin, synsedimentary structures of biomats ascribed to the activity of iron-oxidizing bacteria now visible as hematite and goethite minerals (Gyollai et al., 2013). These samples contain high amounts of micritic carbonate. Flame structures are signatures for fluidization, and carbonate extraclasts are also coated with these iron biomats. At Site 7 (Ongongo, profile K2) biogenic structures are interpreted as weathering product of iron-phosphorites. At Site 2 our sample (C2a1-2) contains debris diamictite layers within a micritic-wackestone carbonate matrix material. The debris layers contain coarse, twinned carbonate, kalifeldspar, albite, quartz, kinked chlorite, and muscovite. The sample C3 located within the same horizon contains organosedimentary structures (micritic spheres with tiny detritus fragments) affected by synsedimentary tectonics (with iron-oxide and micrite). Also shale fragments, with stalactitic calcite and xenomorphic symplectitic quartz cement are visible. The boundary layer at Naraachamspos contains clay minerals, pyrite, and hematite. The boundary layer from Site 4 (Bethanis, C6) contains dyke infiltrations and boudinage structures, marked by iron-oxide embedded in micritic carbonate and wackestone material. The boundary layer from Site 5 (Entrance of South Valley) has low carbonate content. From this locality two kinds of boundary layers exist: 1) synsedimentary iron- microbialites (K4-1, transition to cap carbonate), and 2) boundary clay from leaching (C14d). The boundary clay at profile C14 contains chlorite, rectorite, and montmorillonite as sheet mineral phases. The sample C14d has synsedimentary folds and ripple lamination. The transition layer from Site 7 (Ongongo - Warmquelle, C16) is a tectonized layer containing wavy laminations and lenses of coarser carbonates.

The Marinoan basal cap carbonate layer (**Maieberg Formation – Keilberg Member**) was collected from Sites 1, 4, 5, 6 and 7 (Bethanis, Khowarib Valley, Fransfontain, Entrance of South Valley, Warmquelle; see Table 2., Figs. 1-2.). Their carbonate content varies between 30 and 100 wt%. The basal cap carbonate from Site 4 (Bethanis, C7) contains chlorite, phlogopite, and quartz as detrital minerals within carbonate matrix. Here the putative microbial structure proves to be generated as weathering product of iron-containing minerals

(Gyollai et al. in prep., Chapter 6). The carbonate layers exhibit plane and climbing lamination. At Site 5 (Entrance of South Valley) the profile K4 contains synsedimentary microbial structures of thin, iron biomat layers, and rich organic material-bearing lenses with remains of cyanobacteria and calcimicrobae. The abiogenic portion of these basal cap carbonate layers, as well as from Site 5 (C14e) and from Site 6 (C15d), contain sedimentary loading structures and debris flow features. In addition, the Marinoan basal cap carbonate contains hematite, clay minerals, and quartz as minor mineral phases. At Site 2 (Naraachamspos, C2a3-8) the cap carbonate contains detrital lenses of quartz, chlorite and iron-phosphorite, which is presumably reworked by iron-oxidizing bacteria, cyanobacteria. At Site 6 (Khowarib Valley) the micritic cap carbonate contains oscillatorian cyanobacteria.

Both Sturtian and Marinoan samples are fine-grained, except Sturtian sample C8 (basal cap carbonate from Copper Mine) and several Marinoan samples C14a (Entrance to the Southern Valley), C3, C17a, C2a-1 (Naraachamspos), C15e (Khowarib Valley) are characterized by coarser less classified grain distribution.

## 7.5 Results of analyses

### 7.5.1 Raman Spectroscopy

The micro-Raman spectroscopy proved as a suitable method for the determination of organic material and hydrocarbon phases in Precambrian fossils (e.g. Marshall et al. (2005), Kempe et al. (2005), Kudryastev (2001), Mapelli et al. 1999). The abiogenic origin of the FeOB filaments incorporated in iron-stromatolite layers of our samples C12 and C13a was proved with hydrocarbon phases determined by Raman spectroscopy. A Raman profile of the organic material was taken in the C12 and C13a thin sections (Sturtian iron-stromatolite from Steilrandberge and Sesfontain-Opuwo), and the hydrocarbon phases were determined in C8 sample (Sturtian oolitic sandstone from Copper Mine, Fig. 4.). From four ooids within our sample C8 (basal Rasthof Formation, Copper Mine) the following hydrocarbon phases were determined: from four ooids in the C8 sample (basal Rasthof Formation, Copper Mine). A group of bands at 1300-1350  $\text{cm}^{-1}$  belongs to kerogen (Kempe et al., 2005). The spectral bands at 1710  $\text{cm}^{-1}$  are assigned to the C=O vibration, and a peak at 1450  $\text{cm}^{-1}$  belongs to bending and stretching of the methylen group (Marshall et al., 2005). The A broad peak at 1500-1550  $\text{cm}^{-1}$  is associated with amorphous carbon (Nikiel and Jagodzinski, 1993).

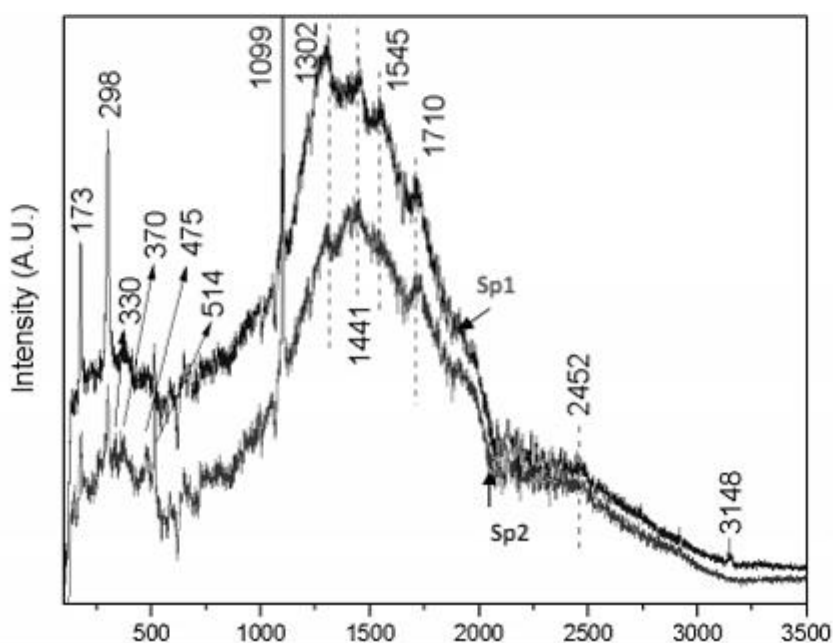
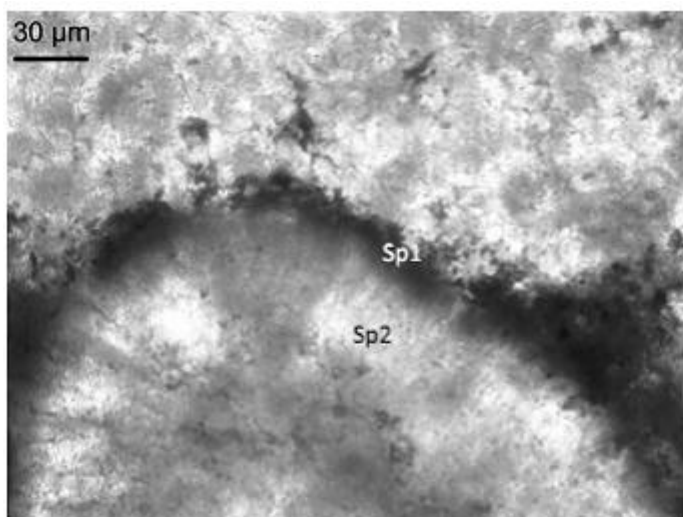


**Figure 4.** Raman spectra of an ooid in sample C8: Sp1 was taken near to iron-oxidizing bacteria bearing rim, whereas Sp2 was taken in cyanobacteria-rich area of ooids. In both of the spectra vibrations of dolomite and hydrocarbon phases appear. The peaks of dolomite appears at  $173\text{ cm}^{-1}$  (Eg),  $298\text{ cm}^{-1}$  (Eg), and  $1099\text{ cm}^{-1}$  (Ag), the peak at  $724\text{ cm}^{-1}$  disappeared because of polarization effect. The kalifeldspar (microcline) has minor peaks  $330\text{ cm}^{-1}$ ,  $364\text{ cm}^{-1}$  and strong vibration of Si-O-Si/Si-O-Al bridges at  $475\text{ cm}^{-1}$ , whereas Ag (major) vibration is centered at  $513\text{ cm}^{-1}$ . The bend vibration of  $\text{CH}_2$  groups is centered at  $1441\text{ cm}^{-1}$ , at  $1545\text{ cm}^{-1}$  the deformation bending of C=C in COOH group. The C-O stretching vibration is centered at  $1710\text{ cm}^{-1}$ , and at  $2452\text{ cm}^{-1}$  of graphite. The stretch vibration of C-H bonds is centered at  $3148\text{ cm}^{-1}$ .

The Raman vibrations of feldspars in samples C2a2 and C4 were interpreted according to Mernagh (1991). In general Si-O vibrations are centered between  $1300\text{-}600\text{ cm}^{-1}$ , and most

intense Raman bands exhibit between 450 and 600  $\text{cm}^{-1}$  Raman shift. Below 450 $^{-1}$  occur external lattice modes for feldspar, the Ag vibration modes are centered in 500-510  $\text{cm}^{-1}$  range. The mixed Si-O-Si/Si-O-Al bridge appears in 478-488  $\text{cm}^{-1}$  range. The Raman spectra of feldspars follow not only crystal structure, but chemistry as well, so the Raman spectroscopy is a powerful tool to distinguish different feldspar phases. In general, the albite has peak at 1000  $\text{cm}^{-1}$  (Si-O stretching mode), and at 513-514  $\text{cm}^{-1}$  (Ag vibration) and above 600  $\text{cm}^{-1}$  (Si-O-Si/Si-O-Al stretching). The kalifeldspars have also specific peaks (Si substitution for Al at T1 and T2 sites), which is at 455  $\text{cm}^{-1}$  for orthoclase, 1102  $\text{cm}^{-1}$  for microcline, doublets at 282-265 and 123-111  $\text{cm}^{-1}$  for sanidine. The feldspars can be identified by a characteristic Raman peak between 500 and 515  $\text{cm}^{-1}$  (503  $\text{cm}^{-1}$  in anorthite, 514  $\text{cm}^{-1}$  in sanidine). The plagioclases show two intense bands in region 450-600  $\text{cm}^{-1}$ , while a triplet is observed in alkali feldspar spectra (Table 3.).

**Table 3.** Raman shifts of feldspar in Marinoan transition layers (Legend: alb=albite, mcl=microcline, fp=feldspar, s=strong, vs=very strong, vibr=vibration).

Albite	Micro-cline	2a2 twinned feldspar Albite	2a2 kinked fp Albite	2a2 Micro-cline	2a2 feldspar with zoisite inclusions Albite	C4 feldspar in detritus Microcline	Vibration
1121	1122	1123		1121		1121 mcl	Vibration of T1 T2 positions
1097 s 1011		1097	1010	1096 alb 1000 mcl	1096 alb	1011 alb	
980	1000		980		981 alb		Si-O-Si stretching
813 s	840	812	814	814 alb	815 alb	811 alb	
763 s	804	763	763		763 alb		
647	714	647	645				Si-O-Si/Si-O-Al stretching
634	657	635	636	632 mcl	636 alb,	632 mcl	
577	624	578 alb	579	579 alb 513 mcl	576 alb	579 alb 513 mcl	A g vibr
507 vs 478 vs	513 vs 475 s	508 vs 479 vs	507 478	476 mcl	507 alb 477 alb	473 mcl	Mixed Si-O-Si/Si-O-Al stretching
414					415 alb		
408	406	408	408	406 mcl	407 alb	404 mcl	
	364						
	358	358 mcl		358 mcl		359 mcl	
351	330					332 mcl	
327		328	328	328 alb	327 alb		
302				303 alb			
290		290	289		292 alb		
267	281 s					283 alb	
249	269	264	269	269 mcl	267 alb	268 mcl	
	257		251	257 mcl	251 alb	257 mcl	
	218						
207		209	209		206 alb		
	198			200 mcl		199 mcl	
183		185	184	181 alb	185 alb		
	174					176 mcl	
163		163	162	162 alb	165 alb		
150	154 s	152	148	155 mcl	152 alb	152 mcl,	
	126			126 mcl		126 mcl	
	109			110 mcl	111 mcl	108 mcl	
87		88	87	85 alb			

### 7.5.2 Cathodoluminescence studies

Cathodoluminescence studies were utilized in those cases where partly coarser grain size and lower iron content occur. The sample C8 originates from Sturtian slope facies, including high abundance of oolites. The oolites show zoned luminescence (bright red zones in dull red material) (Fig. 5.). Between the oolites, several detrital minerals can be observed (blue luminescent quartz and feldspar). In general, the carbonate between oolites has brighter red luminescent color than the oolites themselves. Between the oolites, bright red luminescent clasts and peloids with bright red rim occur (Figs. 5AB). Sample C8 includes variable cement phases in cavities, which are bright orange luminescent calcite ( $Mn^{2+}$  rich) mixed with lower luminescent (more  $Fe^{2+}$  quenching ions) carbonate phase. Lower luminescent micritic extraclasts occur, which might have scapped from older sediments and resedimented (storm or turbidite well-moved sea water area – facies: platform slope).

Gradation is characteristic of profile C2a (Fig. 6AB). The so-called diamictite layer appears as coarse layer in fine-grained postglacial micritic material. The basal Rasthof Fm. samples show bright luminescent calcite cement with non-luminescent quartz cement interval (Fig. 6CD). The coarse carbonate grains have zoned growing (sample C5, Fig. 6EF) and bright rim (C2a), with brighter red luminescent color (Figs. 6.). The groundmass has no luminescent color (sample C5: diagenetic quartz, samples C14a, C15d, C3\_2: mixing of clay with hematite and carbonate-micritic material). The sample C2a1 thin section shows intervals of coarse and fine-grained strata. Bright orange luminescent carbonate grains are floating in non-luminescent (iron-rich) groundmass, where the larger dolomite grains have non-luminescent cores ( $Fe^{2+}$  quencher) and bright luminescent rims. The coarse layer contains a number of brown luminescent quartz grains which implies formation during slow cooling in regional deformation. The twinned feldspars have dull blue luminescence indicating magmatic origin.

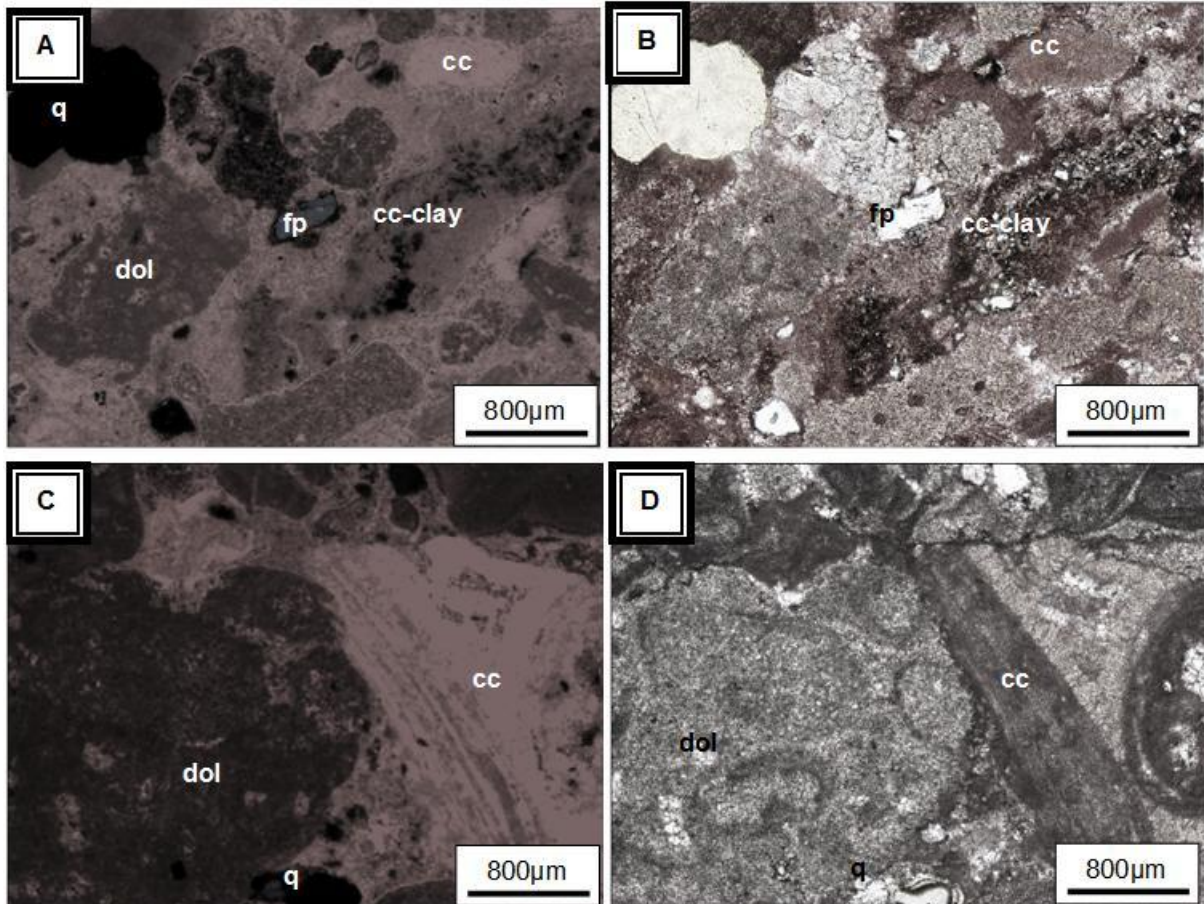


**Figure 5.** Photos of sample C8 (basal Rasthof formation, Copper Mine) in cathodoluminescence (A, C) and transmitted light (B, D). A-B: calcite cement generations in cavities among the oncoids. Among the oncoids, scrapped clasts and feldspar grains occur. C-D: Carbonate Clotted, spongiostrome micrite formed by calcification sheath-like cyanobacteria (Riding, 2000) in C8 sample. (Legend: cc=calcite, dol=dolomite, q=calcite, fp=feldspar).

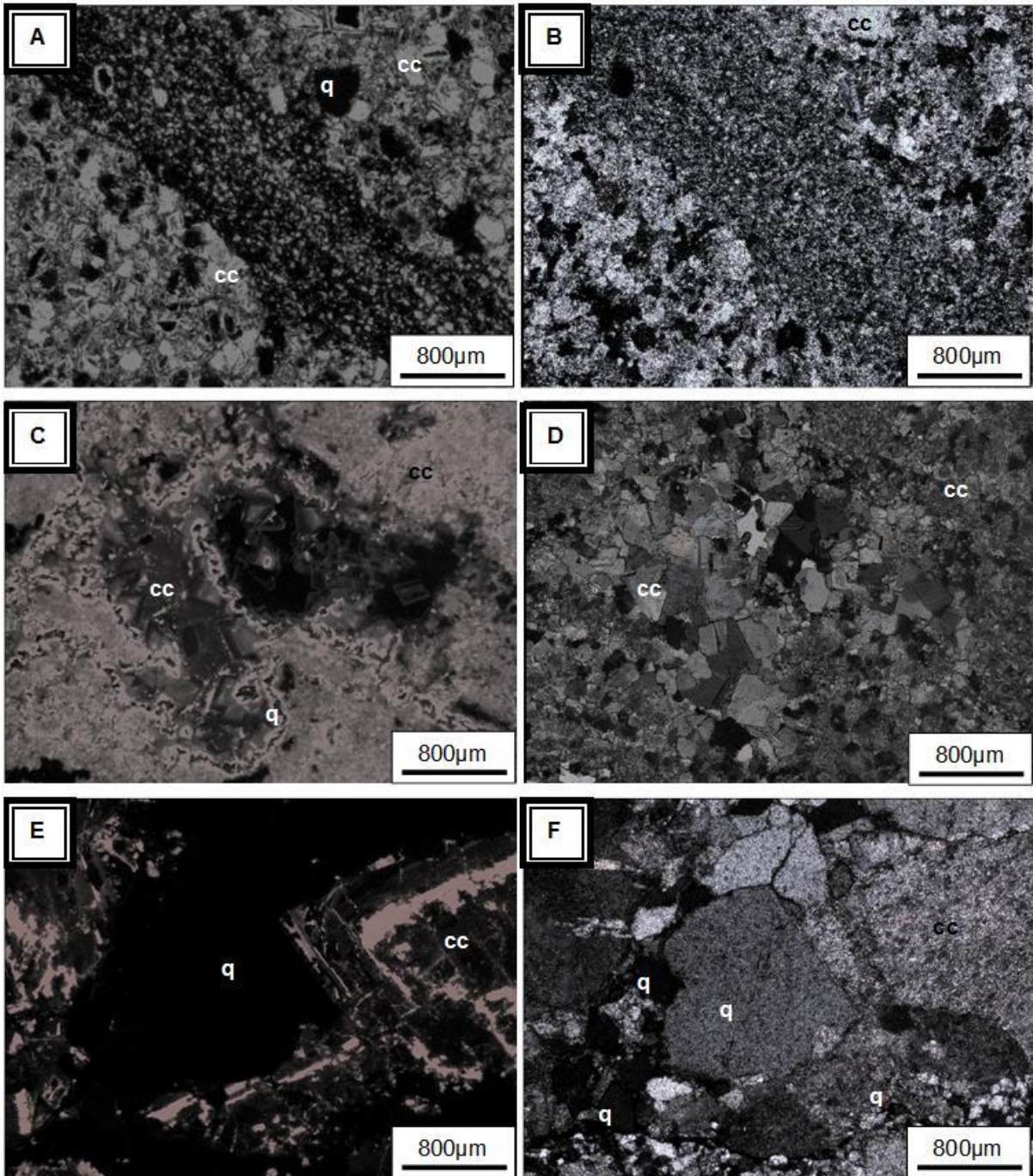


**Figure 6.** A-B: Photos of sample C2a (Ghaub/Maieberg transition, Naraachamspos) in cathodoluminescence (A) and polarized light (B) C-D Photos of sample S6-1a (Rasthof Fm., Copper Mine) in cathodoluminescence (C) and polarized light (D). Sample S6-1a: microsparite around the peloids might be calcified bacterial aggregates, whereas sparite within pores indicate precipitation of pore water within microbiolaminite (CL image, 5x). The photo under crossed polars shows cyanobacteria filaments. E-F: diagenetic quartz in sample C5: Zoned growth of mechanical twinned dolomite. The brighter luminescent zones are changing between orange and red luminescence colors. Quartz shows no luminescence indicating an authigenic origin. (E-F) (Width: 3mm, C, E: cathodoluminescence, D: plane polarized light, F: crossed polars) (Legend: cc= calcite, dol=dolomite, q=quartz).

### 7.5.3 Geochemistry

#### 7.5.3.1 Major and trace element geochemistry

The carbonate-poor Sturtian and Marinoan samples (top diamictite and boundary clay) have been analyzed for major and trace element geochemistry (listed in Table 4. and Chapter 10). The PAAS (Post-Archean Australian Shale) is used as standard of sea floor sediment, the enrichments proofs detrital (Si, Al, Ti, K) or biogenic signature (Mn, Fe, P) The top Chuos samples vary between 46-68 wt% SiO<sub>2</sub>, 0.4-0.7 wt% TiO<sub>2</sub>, 3-13wt% for Al<sub>2</sub>O<sub>3</sub>, 2-42 wt% Fe<sub>2</sub>O<sub>3</sub>, CaO 1.3-7.5 wt%, MgO 1.2-6.5 wt%, Na<sub>2</sub>O 0.1-0.3 wt%, K<sub>2</sub>O 1.3-9wt%, P<sub>2</sub>O<sub>5</sub> 0.2 wt%. The Sturtian boundary layer samples (Chuos/Rasthof transition) vary between 30-67 wt% SiO<sub>2</sub>, 0.2-0.6 wt% TiO<sub>2</sub>, 2.8- 9.3wt% for Al<sub>2</sub>O<sub>3</sub>, 2-42 wt% Fe<sub>2</sub>O<sub>3</sub>, CaO 1.3-7.5 wt%, MgO 1.2-6.5 wt%, Na<sub>2</sub>O 0.1-0.3 wt%, K<sub>2</sub>O 1.3-9wt%, P<sub>2</sub>O<sub>5</sub> 0.2 wt%. The samples from Copper Mine have SiO<sub>2</sub> and K<sub>2</sub>O concentrations near to PAAS, whereas other samples are decreased to PAAS. In general, most of the Sturtian samples (excluding boundary clay sample C9 from Copper Mine) are depleted in Al, Mn, K, Na to PAAS, but Ca and Mg, Fe are enriched. The Marinoan transition layer samples (top Ghaub, Ghaub/Maieberg boundary) vary between 19-80 wt% SiO<sub>2</sub>, 0.4-1. wt% TiO<sub>2</sub>, 2.7- 19 wt% for Al<sub>2</sub>O<sub>3</sub>, 2-7 wt% Fe<sub>2</sub>O<sub>3</sub>, CaO 3.3-44 wt%, MgO 1.6-28 wt%, Na<sub>2</sub>O 0.1-1.2 wt%, K<sub>2</sub>O 0.03-6 wt%, P<sub>2</sub>O<sub>5</sub> 0.2-0.8 wt%. The P<sub>2</sub>O<sub>5</sub> values exceed PAAS value in case of both of Sturtian and Marinoan transition layers. Most of the Marinoan transition layer samples are enriched in Ca and Mg (excluding C16c) to PAAS, but depleted in other major elements (excluding C16c from Warmquelle). Except of the boundary clays, the loss of ignition values (LOI) are higher for both of Sturtian and Marinoan top diamictite and basal cap carbonate sections (C samples), and cap carbonate profiles (K and P samples) compared to upper continental crust (UCC). The Marinoan top diamictites and boundary clay from Naraachamspos (C3\_1-2) are enriched in trace elements. The trace element concentrations in residual clays after dissolving carbonate (C2b-c-T, C3\_T, C14 a-d, C9-T samples) exceed UCC values. The As, U, Pb is enriched to UCC values for most of Sturtian and Marinoan residual clays after dissolving carbonates.

**Table 4.** Major element concentrations of Sturtian and Marinoan transition layers.

Stratigraphy	Chuoss			Chuoss/Rasthof			
Locality	SO	CM	CM	CM	SR	SO	
Sample name	C13A	C10_1	C10-2	C09	C12	C13b	PAAS
SiO <sub>2</sub>	46.5	61.9	68.1	67.3	29.7	47.4	62.8
TiO <sub>2</sub>	0.39	0.61	0.72	0.62	0.19	0.65	1
Al <sub>2</sub> O <sub>3</sub>	3.65	12.0	14.6	9.3	2.7	6.7	18.9
Fe <sub>2</sub> O <sub>3</sub>	42.1	2.02	2.56	11.7	25.4	32.3	7.22
MnO	0.01	0.00	0.00	0.00	0.00	0.04	0.11
CaO	1.28	7.48	0.53	0.98	34.3	5.60	2.2
MgO	1.16	6.47	1.78	1.53	1.32	1.30	1.3
Na <sub>2</sub> O	0.13	0.21	0.24	0.20	0.13	0.14	1.2
K <sub>2</sub> O	1.27	7.53	9.03	5.94	0.93	2.39	3.7
P <sub>2</sub> O <sub>5</sub>	0.18	0.20	0.22	0.21	0.09	0.57	0.16

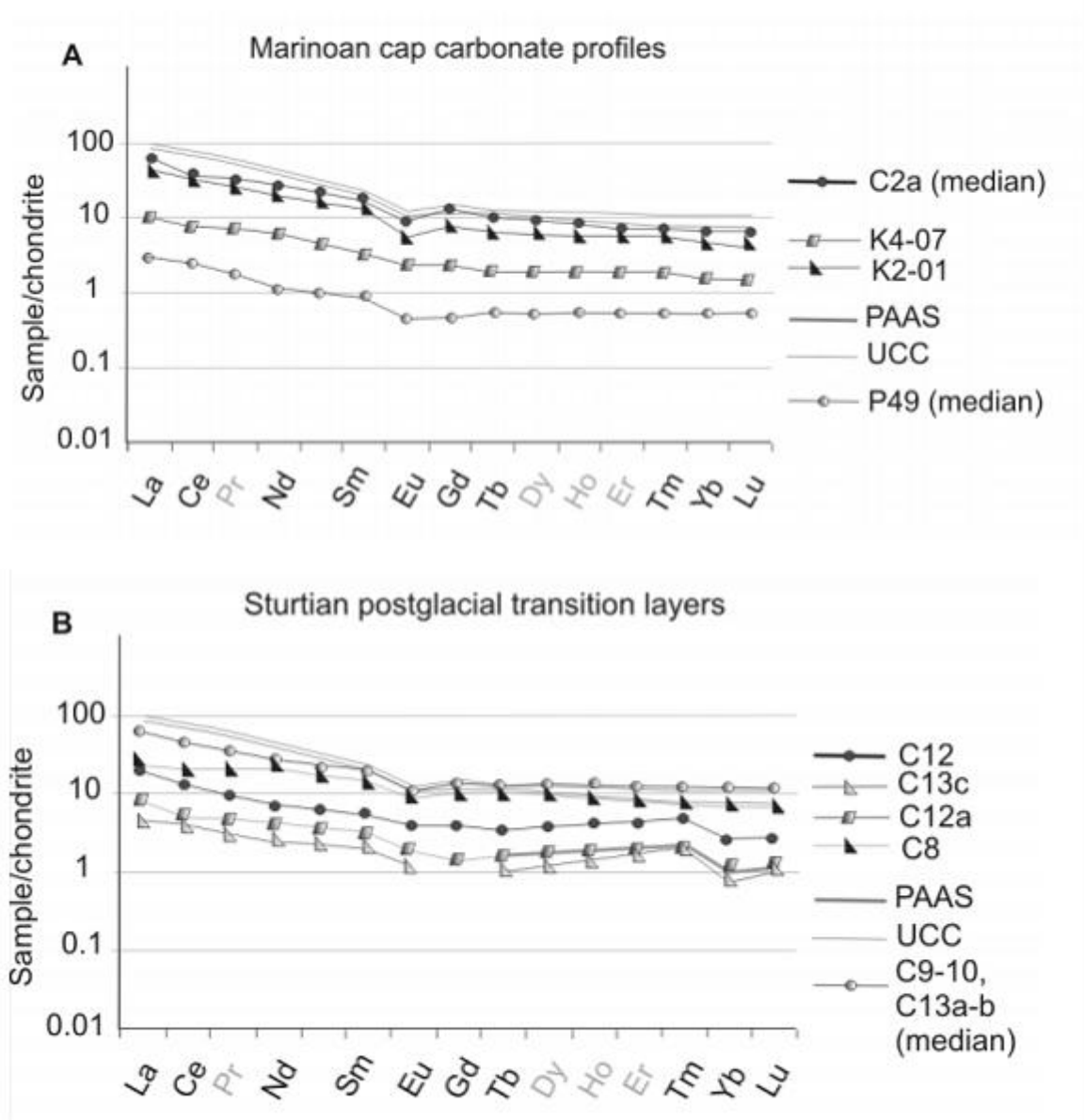
  

Stratigraphy	Ghaub			Ghaub/Maieberg					Maieberg		
Locality	NA	TW	WQ	ESV	ESV	KV	KV	FF	WQ	KV	WQ
Sample name	C17a	C5	C16a	C14b	C14c	C15b	C15c	C1c	C16b	C15d	C16c
SiO <sub>2</sub>	64.0	62.2	39.0	24.0	52.9	31.6	28.2	27.5	19.3	55.8	80.7
TiO <sub>2</sub>	0.91	0.05	1.14	0.40	0.62	0.34	0.35	0.42	0.25	0.67	0.48
Al <sub>2</sub> O <sub>3</sub>	16.2	0.37	20.6	6.9	13.5	6.44	5.97	7.00	4.36	13.4	8.68
Fe <sub>2</sub> O <sub>3</sub>	2.45	14.2	7.31	3.08	2.48	1.43	1.65	2.56	2.30	3.36	2.07
MnO	0.03	0.06	0.00	0.02	0.00	0.00	0.01	0.19	0.02	0.01	0.00
MgO	4.87	7.95	4.89	24.2	8.52	15.9	24.7	22.6	28.5	9.34	1.63
CaO	3.36	12.7	14.8	38.6	15.5	39.8	35.4	36.04	44.2	10.7	1.14
Na <sub>2</sub> O	0.19	0.09	0.23	0.22	0.16	0.16	0.19	0.15	0.11	0.14	0.14
K <sub>2</sub> O	6.18	0.03	8.46	1.82	5.11	2.29	1.98	2.55	0.42	5.73	3.29
P <sub>2</sub> O <sub>5</sub>	0.34	0.30	0.36	0.24	0.24	0.79	0.65	0.28	0.15	0.35	0.26

### 7.5.3.2 Rare earth elements

Our Sturtian boundary layer displays enrichment in HREE related to Post-Archean Australian Shale (PAAS). Sample C8 (basal Rasthof Formation/ Copper Mine) shows LREE depletion to UCC whereas HREE values are near UCC (upper continental crust) what indicates HREE fractionation (Fig. 7.). REE abundances of fine-grained cap carbonates and iron-stromatolite from sample C12 (Steilrandberge) are depleted to upper crust. All of the Sturtian samples have a negative Eu anomaly and Ce/Ce\* ratios are near or below 1. All of Marinoan basal cap carbonates show depleted REE abundances to the upper crust, however C14e (Entrance to the South Valley) and C4 (Tweelingskop) display HREE fractionation. All samples of the Marinoan postglacial transition layer have a negative Eu anomaly and the Ce/Ce\* ratios are near (C14 – Entrance to the South Valley, C15 – Khowarib Valley, C16 – Warmquelle) or below to 1. Excluding some Naraachamspos samples (C3, C17a), REE

abundances of the Marinoan transition layer are depleted to upper crust (UCC, Rudnick and Gao, 2003), and PAAS (Taylor and McLennan, 1985) (Fig. 7.)



**Figure 7.** Chondrite-normalized rare earth element patterns of Sturtian and Marinoan postglacial transition layers. A: Marinoan cap carbonate profiles B: Sturtian postglacial transition layers, C: Marinoan postglacial transition layers, D: Marinoan basal cap carbonates.

### 7.5.3.3 Carbon isotopic ratios

The Sturtian basal cap carbonate of the Warmquelle section displays strongly negative carbon isotopic values ( $-8\text{‰}$  and  $-10\text{‰}$   $\delta^{13}\text{C}_{\text{VDB}}$ ), whereas their hanging wall section (K2/6-8) features less negative values of between  $-3$  and  $-4\text{‰}$   $\delta^{13}\text{C}_{\text{VDB}}$ , and this trend is continued in the overlying cap carbonate (Fig. 8.). We also measured the bulk carbon isotopic composition of Marinoan basal cap carbonates with weathered (smectitized) iron biomats (K4/1-3)

varying between 0 and  $-2\text{‰}$   $\delta^{13}\text{C}_{\text{VPDB}}$ , whereas within their hanging wall cap carbonate the values are near  $-2\text{‰}$   $\delta^{13}\text{C}_{\text{VPDB}}$  (Fig. 8.) The Marinoan postglacial cap carbonate deposits show no variation within slightly negative ( $-2\text{‰}$   $\delta^{13}\text{C}_{\text{VPDB}}$ ) values proposing calm and rapid sedimentation of the cap carbonate layers (Fig. 8.).

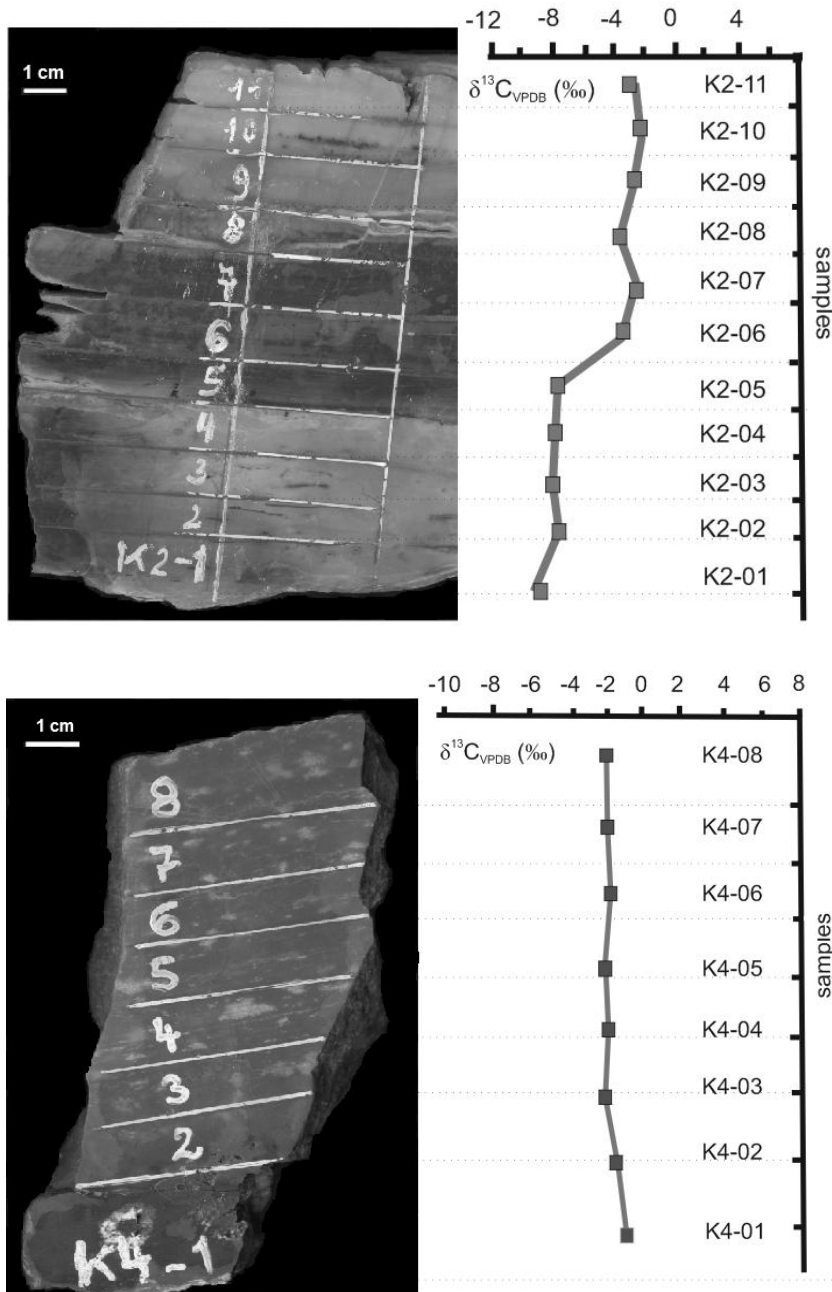


**Figure 8.** Carbon isotopic profiles of K2 and K4 samples.

## 7.6 Paleoenvironment

### 7.6.1 Paleoredox conditions

**Paleoredox proxies** are not only influenced by paleoenvironmental conditions, but also by diagenetic alteration, weathering, and detrital input (McLennan et al. 1990, 1993) and especially they are influenced by clay minerals, because these minerals easily may adsorb U, V, Cr, Ni etc. at their surface (Algeo and Maynard 2004). Thus paleoredox proxies can be used for paleoenvironmental reconstructions. Algeo and Maynard (2004) used the abundances of authigenic U and Mo and the  $V/(V+Ni)$  ratio as a paleoenvironmental proxy. Accordingly the modern oxygenated, shallow seawater is characterized by 1) LREE (light rare earth elements) depletion to HREE (heavy rare earth elements), positive shale-normalized La, Gd, Lu, Eu anomalies and negative Ce anomalies. Further, the modern fresh water patterns are distinguished by less LREE depletion with MREE (middle rare earth elements) and HREE enrichment. Microbialites are highly enriched in REE with robust REE+Y pattern providing the possibility to reconstruct ancient sea water and depositional environment (Kamber and Webb, 2011). The REE abundances depend on grain size, presence of detrital minerals in particular from clay minerals for rare earth elements can easily be adsorbed at the surface of these minerals. The paleoredox conditions of Sturtian age cap carbonate were studied by Meyer et al. (2012) revealing transient anoxia in basal layers. Arguing with Meyer et al. (2012), our mineralogical and geochemical data indicate transient suboxic conditions during the deposition of postglacial boundary layer, which change to oxygenic conditions in the cap carbonates.

An U/Th ratio between 0.75-1.5 reflects suboxic condition; a ratio above 1.5 implies anoxic condition. A  $(Cu+Mo)/Zn$  ratio between 1 and 3 indicates suboxic conditions, above 3 anoxic conditions. The V/Cr ratio can be used as a paleoredox proxy, where values below 2 indicate oxic conditions, 2-4.25 dysoxic, and above 4.25 anoxic conditions. V/Cr can be used together with other paleoredox proxies, such as Ni/Co, Ni/V, and U/Th (McLennan et al. 1990, 1993). Our results concerning geochemical proxies are listed in Table 5: The paleoredox proxies for our uppermost Chuos formation samples reveal suboxic conditions. The Sturtian boundary layers exhibit variable paleoredox values depending on sample locality. Paleoredox proxies of our microbial boundary layers (C12, C13b) exceed in suboxic range. However, higher U/Th values in our Sturtian samples altogether indicate consumption of U in their microbial structures (Table 5.). In general, following the suboxic conditions of Marinoan diamictites and its postglacial boundary layer (C 14d, clay), the paleoredox proxies of their overlying cap carbonates exceed in oxygenic range, which support the “Neoproterozoic Oxidation Event” theory (e.g., Och and Shields-Zhou, 2012). The high  $(Cu+Mo)/Zn$  for our sample C9 (Copper

Mine) and some other proxies within the suboxic range indicate Cu-Mo accumulation at clay minerals.

According to mineralogical and geochemical data (presence of diagenetic quartz and clay minerals, diagenetic proxies) the samples C5 (Tweelingskop) and C16 (Warmquelle) are strongly influenced by secondary processes, so their paleoredox proxies point to strongly reducing environmental condition after their sedimentation. According to its paleoredox proxy, the sample C5 (Tweelingskop) is influenced by reductive diagenetic fluids, whereas the sample C16 (Warmquelle) was affected by oxygenic pore water after it's tectonic deformation (Table 5.). In general the Marinoan postglacial transition layers are characterized by paleoredox proxies plotting within the oxygenic range, but only the samples C15 (Khowarib Valley) demonstrate higher Cu, Mo, V abundances.

**Table 5.** Geochemical calculations for paleoenvironmental conditions A-C Marinoan (G= Ghaub Fm., G/M= boundary, M=Maieberg Fm.), D: Sturtian(C= Chuos Fm., C/R=boundary, R=Rasthof Fm.).

**A)**

Sampling site	Fransfontain			Naraachamspos					Tweelingskop		Bethanis	
	M	G/M	G/M	G/M	G/M	G/M	G/M	G/M	O	G	G/M	M
Stratigraphy	C1a	C1b	C1c	C2a	C2b	C2c	C3_1	C3_2	C4	C5	C6	C7
ppm/ppm												
U/Th	2.38	0.61	0.50	0.22	0.20	0.31	0.32	0.40	0.66	15.8	0.53	0.24
V/Cr	0.03	3.24	1.85	1.08	0.80	1.44	2.17	2.11	1.59	6.53	1.02	1.16
V/(V+Ni)	0.03	0.51	0.41	0.19	0.28	0.28	0.54	0.47	0.76	0.74	0.30	0.40
(Cu+Mo) /Zn	0.39	1.06	0.43	0.77	1.14	0.25	3.20	2.80	1.08	2, 61	1, 22	0, 66
Eu/Eu*	0.73	0.46	0.47	0.67	0.55	0.78	0.51	0.54	0.90	0.61	0.79	0.71
Ce/Ce*	0.88	0.91	0.90	0.88	0.93	0.91	1.07	1.07	0.98	0.72	0.84	0.67
Total REE (ppm)	38.0	111	185	236	335	195	606	734	61.0	83.0	89.0	200
Total LREE (ppm)	28.0	81.0	141	177	271	159	517	622	38.0	63.0	64.0	166
Total HREE (ppm)	10.0	30.0	44.0	59.0	64.0	36.0	89.0	112	23.0	20.0	25.0	34.0
$\Sigma$ LREE/ $\Sigma$ HREE	2.69	2.71	3.21	3.00	4.23	4.47	5.84	5.54	1.67	3.09	2.62	4.87

**B)**

Sampling site Stratigraphy ppm/ppm	Entrance to the South Valley										Khowarib Valley	
	G	G/M	G	G/M	G/M	G/M	M	G/M	G/M	M	G/M	M
	C14 a	C14 b	C14 c	C14 d	C14d 1	C14d 2	C14 e	C15 b	C15 c	C15 d	C15e	C15e1
U/Th	0.74	4.79	0.62	0.45	1.36	0.39	4.27	0.57	0.80	0.41	0.45	0.44
V/Cr	1.91	0.53	1.97	2.11	n. d.	n. d.	1.95	1.15	0.94	1.64	n. d.	24.0
V/(V+Ni)	0.70	0.29	0.67	0.67	n. d.	n. d.	0.46	0.73	0.50	0.75	n. d.	n. d.
(Cu+Mo) /Zn	2.46	1.26	1.88	0.43	n. d.	n. d.	1.91	1.53	0.62	2.33	0.30	4.37
Eu/Eu*	0.59	0.67	0.56	0.44	0.28	0.52	0.58	0.54	0.55	0.40	0.40	n. d.
Ce/Ce*	0.94	1.02	0.88	0.93	0.97	0.99	1.00	1.00	0.96	0.94	1.07	0.87
Total REE (ppm)	170	67.0	252	325	n. d.	180	97.0	133	88.0	184	138	n. d.
Total LREE (ppm)	130	47.0	206	274	175	140	68.0	103	65.0	143	105	n. d.
Total HREE (ppm)	40.0	21.0	45.0	51.0	n. d.	40.0	29.0	30.0	23.0	41.0	33.0	23.0
$\Sigma$ LREE/ $\Sigma$ HREE	3.27	2.25	4.54	5.40	n. d.	3.45	2.35	3.43	2.82	3.44	3.21	n. d.

**C)**

Sampling site Stratigraphy ppm/ppm	Warmquelle			Naraachamspas		
	G/M	G/M	G/M	G	G/M	M
	C16a	C16b	C16c	C17a	C17b	C17c
U/Th	0.60	0.89	0.57	0.33	0.27	0.26
V/Cr	1.62	1.15	1.62	0.91	2.15	1.31
V/(V+Ni)	0.80	0.61	0.89	0.78	0.70	0.46
(Cu+Mo) /Zn	0.65	0.88	3.20	1.20	1.87	1.17
Eu/Eu*	0.33	0, 67	0, 48	0, 58	0.44	0.67
Ce/Ce*	0.97	0.71	0.97	0.88	0.90	0.80
Total REE (ppm)	303	89.0	246	569	595	294
Total LREE (ppm)	242	65.0	199	499	489	246
Total HREE (ppm)	61.0	24.0	47.0	70.0	106	48.0
$\Sigma$ LREE/ $\Sigma$ HREE	3.96	2.72	4.23	7.11	4.62	5.14

**D)**

Sampling site Stratigraphy ppm/ppm	Copper Mine				Steilrandberge		Sesfontain-Opuwo		
	R	C/R	C	C	C/R	R	C	C/R	R
	C8	C9	C10-1	C10-2	C12	C12a	C13a	C13b	C13c
U/Th	1.69	0.74	0.34	0.41	1.12	2.93	1.93	1.73	3.45
V/Cr	0.68	3.12	0.81	1.08	1.99	n. d.	3.32	6.16	0.03
V/(V+Ni)	0.22	0.89	0.62	0.74	0.54	n. d.	0.37	0.86	0.07
(Cu+Mo) /Zn	0.57	6.34	0.23	0.14	0.38	1.42	2.50	2.62	1.82
Eu/Eu*	0.74	0.64	0.65	0.68	0.85	0.75	0.68	0.61	0.83
Ce/Ce*	0.92	0.98	0.95	0.95	0.82	0.75	0.93	0.98	1.00
Total REE	200	395	319	325	94	48	296	335	30
Total LREE	140	305	242	236	69	33	223	251	21
Total HREE	60	90	77	89	25	15	74	84	8
$\Sigma$ LREE/ $\Sigma$ HREE	2.34	3.38	3.14	2.65	2.71	2.30	3.01	2.99	2.54

Within the marine environment, Rb substitutes K within illite structures and marine water favors higher Rb/K-ratios than brackish or fluvial water (Campbell and Williams, 1965). Thus, the Rb/K ratio is used as **paleosalinity proxy** (Campbell and Williams, 1965), where  $4 \cdot 10^{-3}$  is common for freshwater/brackish environment,  $6 \cdot 10^{-3}$  for shales (Campbell and Williams, 1965). For instance, the Rb/K value for post-Archean Australian shale (Taylor and McLennan, 1985) is  $5 \cdot 10^{-3}$ . In general, the carbonate rich samples are characterized by lower Rb/K ratios ( $1-5 \cdot 10^{-3}$ ), so the decarbonated samples are used for paleosalinity reconstruction. Most of our Sturtian and Marinoan postglacial transition layers are characterized by low Rb/K ratios ( $2-4 \cdot 10^{-3}$ ) indicating brackish environment (Table 6.). Some Marinoan basal cap carbonates (C1a – Fransfontain, C7 Bethanis) and boundary layers (Sturtian: C12 Steilrandberge, Marinoan: C14b Entrance to the South Valley) are characterized by higher Rb/K ratios indicating marine environment.

**Table 6.** Rb/K ratios as paleosalinity proxy for silt fractions of Sturtian (C8-C13) and Marinoan (C1-C7, C9-C17) postglacial transition layers (values in  $10^{-3}$ )  $Rb/K \cdot 10^{-3} = 4$ : brackish environment,  $Rb/K \cdot 10^{-3} = 6$ : marine environment (Campbell and Williams, 1965).

<b>PAAS</b>	<b>C1a_T</b>	<b>C1b-T</b>	<b>C2a_T</b>	<b>C2b-T</b>	<b>C2c_T</b>	<b>C3/1-T</b>	<b>C3/2-T</b>	<b>C17a-T</b>	<b>C17b-T</b>	<b>C17c_T</b>	
5.21	11.1	3.00	1.13	3.23	2.09	3.12	3.00	2.87	3.19	13.0	
<b>C14a_T</b>	<b>C14b_T</b>	<b>C14c_T</b>	<b>C14d_T</b>	<b>C14e-T</b>	<b>C15b-T</b>	<b>C15e_T</b>	<b>C16a-T</b>	<b>C16b-T</b>	<b>C16c-T</b>		
2.84	9.47	2.56	2.59	2.87	2.83	2.18	3.15	2.98	3.03		
<b>C4-T</b>	<b>C5B-T</b>	<b>C6-T</b>	<b>C7-T</b>	<b>C8-T</b>	<b>C9-T</b>	<b>C10/1-T</b>	<b>C10/2-T</b>	<b>C12_T</b>	<b>C13a-T</b>	<b>C13b_T</b>	<b>C13c-T</b>
4.75	5.16	3.98	5.56	2.33	2.41	2.26	3.04	9.59	4.38	1.02	2.77

Most of our samples are characterized by Mg/Ca values between 0.5 and 2.6 which is characteristic for dolomites (Veizer, 1983), but only the samples C12 (Steilrandberge, Sturtian) and C16a (Marinoan, Warmquelle) have lower Mg/Ca values.

## 7.6.2 Diagenesis

Commonly used proxies for diagenetic alteration are the Ca/Sr, Fe/Sr and Mn/Sr ratios (Veizer, 1983). Carbon isotopic ratios can also be affected by diagenesis. Sturtian glacial transition layers (**uppermost Chuos Formation**) have low values in both of Ca/Sr- and Fe/Sr proxies and the lack of clay minerals indicates the absence of diagenetic alteration. The Sturtian (microbial) boundary layers (**Chuos/Rasthof boundary**) have low Fe/Sr- and Ca/Sr ratios and no clay minerals, which is common for fresh, unaltered rocks, except C12 (FeOB biomat from Steilrandberge), which shows an elevated Ca/Sr ratio, possibly indicating

diagenetic alteration (Table 7.). The Marinoan glacial transition layers (**Ghaub Formation**) have clay minerals (kaolinite, smectite) after diagenetic alteration of primary minerals low Fe/Sr ratio, but elevated Ca/Sr ratios which indicate diagenetic alteration via non-ferruginous diagenetic fluids (Table 7.). Marinoan postglacial transition layers (**Ghaub/Maieberg boundary, basal Maieberg Formation**) and cap carbonates contain abundant iron-oxides, smectite, kaolinite, and elevated Ca/Sr- and low Fe/Sr ratios, possibly resulting from alteration by non-ferruginous diagenetic fluids.

**Table 7.** Geochemical data used for diagenesis interpretation, A: Sturtian postglacial transition layers, B: Marinoan postglacial transition layers. (G= Ghaub Fm., G/M= boundary, M=Maieberg Fm.), D: Sturtian (C= Chuos Fm., C/R=boundary, R=Rasthof Fm.).

**A)**

Sample name	C13a	C10_1	C10-2	C9	C12	C13b
Locality	SO	CM	CM	CM	SR	SO
Sample name	C	C	C	C/R	C/R	C/R
Mn/Sr	0.46	n. d	n. d	n. d.	n. d	0.25
Ca/Sr	55	331	105	128	2355	33
Fe/Sr	2.11	86	397	1, 58	1, 08	205

**B)**

Sample name	C17a	C5	C16a	C1c	C14b	C14c	C15b	C15c	C16b	C15d	C16c
Locality	NA	TW	WQ	ESV	ESV	KV	KV	FF	WQ	KV	WQ
Stratigraphy	G	G	G	G/M	G/M	G/M	G/M	G/M	G/M	M	M
Mn/Sr	0.001	5.16	0	21.8	1.22	n. d.	n. d.	1.21	1.08	2.34	n. d.
Ca/Sr	1396	1010	1682	3822	2175	2733	2488	3949	2200	2315	637
Fe/Sr	n.d.	1.42	747	129	66	337	54	157	115	576	n.d.

The sample C3 (Marinoan boundary layer) does not seem to contain dolomicrite but slightly negative Ce/Ce\* values indicate diagenetic alteration caused by suboxic pore fluids. Moreover early-diagenetic (organodiagenetic) structures in samples C3 and C4 (Fig. 9.) can be derived by soft sediment deformation via overpressure dewatering (Gammon, 2012; Gammon et al. 2012). The removal of detrital clay leads to an increased grain size in dolomicropar. Dehydration of finer-grained sediments generally occurs in two ways: 1) via diffusive bulk loss from the matrix in instances where fluid overpressure does not develop, or 2) if fluid overpressure produces brittle fracturing which followed by advective (fluid overpressure deformation-derived) dewatering (Gammon et al., 2012) (Fig. 9.). The low-energy structures (peritidal environment, e.g., filling structures, microbial lamination) occur in synsedimentary microbialites (Sturtian: samples C12, C13a, Marinoan: samples C1 and K4). High energy environment (storm facies, e.g. cross bedding or hummocky cross bedding) structures also present in several Marinoan cap carbonates, like sample C14e (E. of South Valley), sample C15e (Khowarib Valley), and diamictite (sample C14a from E. of South Valley). The cap carbonate profile of Naraachamspos shows more negative C isotopic values in the cement phase compared to the primary dolomicrite (Thiemens et al., 2014), indicating reducing diagenetic fluids. The profile K2 has similar carbon isotopic ratio in cement and dolomicrite, indicating early diagenetic alteration. In general, both of mineralogical and geochemical indicate no presence of diagenetic alteration of Sturtian microbial samples. In gen-

eral, the Marinoan transition layers are more altered, which is good agreement with Thiemens et al. (2014).

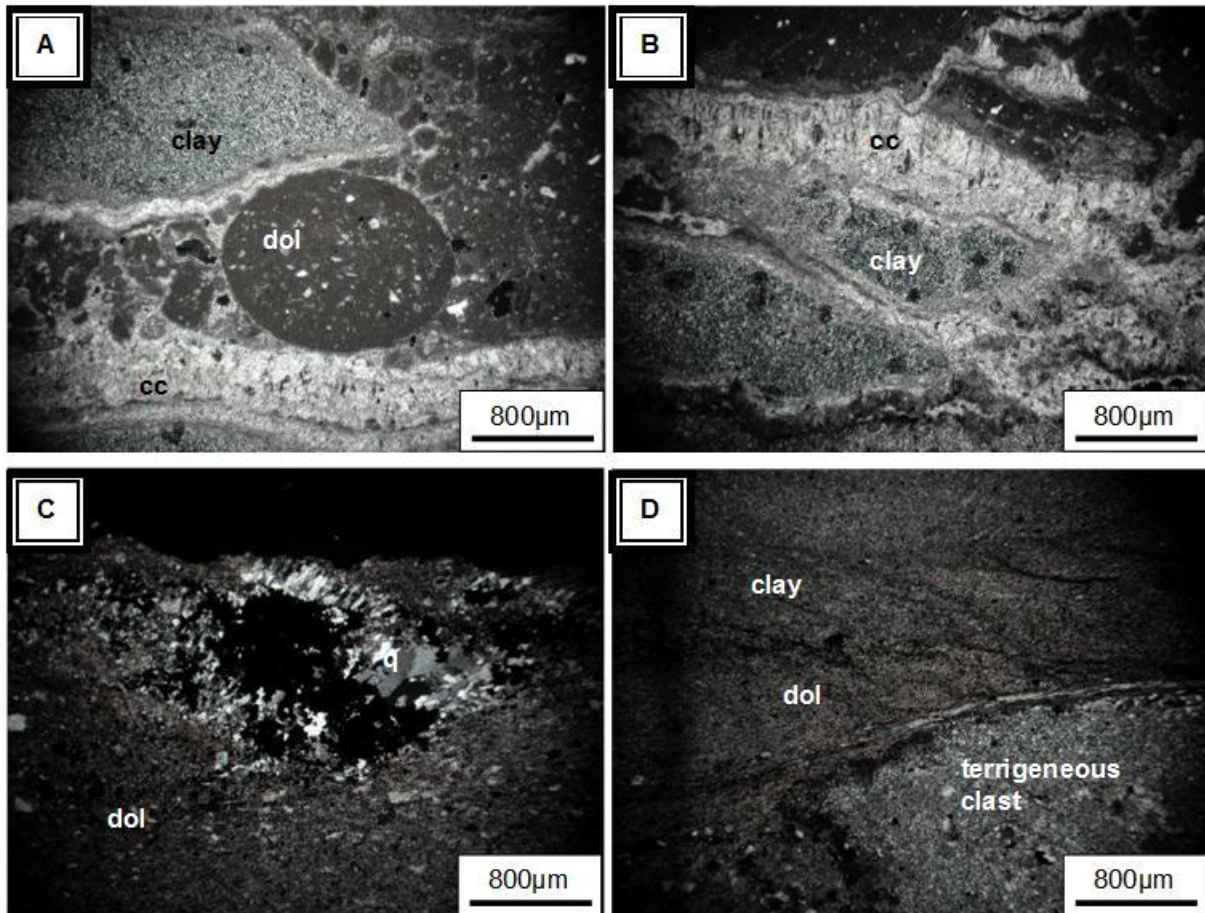


**Figure 9.** Diagenetic structures A-B: Soft-sediment deformation with early diagenetic textures of C4 (A-B) and C3\_2 (C-D) samples (width: 3mm, crossed polars). (Legend: cc= calcite, dol=dolomite, q=quartz).

### 7.6.3 Estimation of detrital input

The main elements (Na, K, Fe, P, Ca, Mg, and Mn) exhibit in authigenic and detrital minerals (Pettijohn et al., 1972, Brumsack, 1989). For estimation of amount of main elements in ancient water column, the main elements have to be normalized for Al. The ratios of elements to Al are influenced by dilution of detritus with carbonate. The elements/Al values are influenced by climatic conditions (Pettijohn et al., 1972). In general, the glacial elements/Al values are higher than the postglacial layers. The immobile element ratios, like Si/Al and Ti/Al are not influenced by climate change, but indicate variation of provenance. The substitution of Al by Ti in feldspar and clay minerals indicates strong correlation between  $Al_2O_3$  and  $TiO_2$  (Table 8.). The increase of quartz in sediments displays decrease in proportion of  $Al_2O_3$ .

The Sturtian samples from Sesfontain-Opuwo and Steilrandberge are synsedimentary microbialites, which are not affected by terrigenous input. Therefore the high major element/Al ratios from these locations belong to microbial structures. The samples from

Copper Mine contain minerals from detrital input. The high Si/Ti and Ti/Al, K/Al, Na/Al belongs to clay minerals (kaolinite, smectite) and feldspar (microcline). The Marinoan diamictites have higher main element/Al ratios which are effected by not only by terrigenous input, but also diagenetic reworking (especially sample C5, Figure 3.). The higher Ti and K/Al of diamictite from Naraachamspos is affected by terrigenous mineral from silt fractions. The variable main element/Al ratios of boundary layers are affected by weathering and diagenetic mixing. The high Ti/Al, Mg/Al, Ca/Al, K/Al belong to presence of carbonate clay minerals, especially, smectite and kaolinite. The high Si-, Ti-, K/Al ratios in Maieberg Fm. belong to feldspar and its weathering product, kaolinite.

**Table 8.** Correlation table of A) Sturtian glacial layers (C12, C13a, C10\_1-2 samples, B) of Sturtian postglacial layers (C13b-c, C8, and C9), C) glacial layers (C14a, C17a, C2a, C5, and C16a) D) Marinoan postglacial transition layers samples (C14 b-e, C15 d-e, C16b-c, C2a-c, C3\_1-2).

A)

wt%	SiO <sub>2</sub>	TiO <sub>2</sub>	Al <sub>2</sub> O <sub>3</sub>	Fe <sub>2</sub> O <sub>3</sub>	MnO	MgO	CaO	Na <sub>2</sub> O	K <sub>2</sub> O	P <sub>2</sub> O <sub>5</sub>
SiO <sub>2</sub>	1	<b>0.99</b>	<b>0.99</b>	<b>-0.95</b>	<b>-0.96</b>	0.34	0.14	<b>0.99</b>	<b>0.99</b>	<b>0.98</b>
TiO <sub>2</sub>	<b>0.99</b>	1	0.99	-0.94	<b>-0.95</b>	0.31	0.11	<b>0.99</b>	<b>0.99</b>	<b>0.98</b>
Al <sub>2</sub> O <sub>3</sub>	<b>0.99</b>	<b>0.99</b>	1	-0.97	<b>-0.97</b>	0.38	0.19	<b>0.99</b>	<b>0.99</b>	<b>0.97</b>
Fe <sub>2</sub> O <sub>3</sub>	<b>-0.95</b>	<b>-0.94</b>	<b>-0.97</b>	1	<b>0.99</b>	-0.59	-0.42	<b>-0.97</b>	<b>-0.98</b>	<b>-0.88</b>
MnO	<b>-0.96</b>	<b>-0.95</b>	<b>-0.97</b>	<b>0.99</b>	1	-0.41	-0.41	<b>-0.97</b>	<b>-0.98</b>	<b>-0.89</b>
MgO	0.34	0.31	0.38	-0.59	-0.41	1	<b>0.97</b>	0.19	0.23	-0.04
CaO	0.14	0.11	0.19	-0.42	-0.41	<b>0.97</b>	1	0.39	0.43	0.16
Na <sub>2</sub> O	<b>0.99</b>	<b>0.99</b>	<b>0.99</b>	<b>-0.97</b>	<b>-0.97</b>	0.19	0.39	1	<b>0.99</b>	<b>0.97</b>
K <sub>2</sub> O	<b>0.99</b>	<b>0.99</b>	<b>0.99</b>	<b>-0.98</b>	<b>-0.98</b>	0.23	0.43	0.99	1	<b>0.96</b>
P <sub>2</sub> O <sub>5</sub>	<b>0.98</b>	<b>0.98</b>	<b>0.97</b>	<b>-0.88</b>	<b>-0.89</b>	-0.04	0.16	<b>0.97</b>	<b>0.96</b>	1

B)

wt%	SiO <sub>2</sub>	TiO <sub>2</sub>	Al <sub>2</sub> O <sub>3</sub>	Fe <sub>2</sub> O <sub>3</sub>	MnO	MgO	CaO	Na <sub>2</sub> O	K <sub>2</sub> O	P <sub>2</sub> O <sub>5</sub>
SiO <sub>2</sub>	1	0.82	<b>0.98</b>	-0.67	-0.03	<b>-0.90</b>	0.84	<b>0.93</b>	<b>0.97</b>	0.21
TiO <sub>2</sub>	<b>0.82</b>	1	<b>0.90</b>	-0.13	0.54	<b>-0.98</b>	0.38	0.56	0.68	0.73
Al <sub>2</sub> O <sub>3</sub>	<b>0.98</b>	<b>0.90</b>	1	-0.55	0.12	<b>-0.96</b>	0.74	<b>0.86</b>	<b>0.93</b>	0.37
Fe <sub>2</sub> O <sub>3</sub>	-0.67	-0.13	-0.55	1	0.75	0.31	0.74	<b>-0.89</b>	-0.81	0.56
MnO	-0.03	0.54	0.12	0.75	1	-0.38	-0.56	-0.38	-0.23	<b>0.96</b>
MgO	<b>-0.90</b>	<b>-0.98</b>	<b>-0.96</b>	0.31	-0.38	1	-0.54	-0.70	-0.80	-0.60
CaO	<b>0.84</b>	0.38	0.74	0.74	-0.56	-0.54	1	<b>0.97</b>	<b>0.93</b>	-0.34
Na <sub>2</sub> O	<b>0.93</b>	0.56	<b>0.86</b>	<b>-0.89</b>	-0.38	-0.70	<b>0.97</b>	1	<b>0.98</b>	-0.13
K <sub>2</sub> O	<b>0.97</b>	0.68	<b>0.93</b>	<b>-0.81</b>	-0.23	<b>-0.80</b>	<b>0.93</b>	<b>0.98</b>	1	0.01
P <sub>2</sub> O <sub>5</sub>	0.21	0.73	0.37	0.56	<b>0.96</b>	-0.60	-0.34	-0.13	0.01	1

C)

	SiO <sub>2</sub>	TiO <sub>2</sub>	Al <sub>2</sub> O <sub>3</sub>	Fe <sub>2</sub> O <sub>3</sub>	MnO	MgO	CaO	Na <sub>2</sub> O	K <sub>2</sub> O	P <sub>2</sub> O <sub>5</sub>
SiO <sub>2</sub>	1	-0.61	-0.61	0.03	0.83	0.43	-0.68	-0.66	-0.66	-0.61
TiO <sub>2</sub>	-0.61	1	1	-0.80	<b>-0.95</b>	<b>-0.97</b>	-0.14	<b>0.99</b>	<b>0.99</b>	<b>0.99</b>
Al <sub>2</sub> O <sub>3</sub>	-0.61	1	1	-0.80	<b>-0.95</b>	<b>-0.97</b>	-0.14	<b>0.99</b>	<b>0.99</b>	<b>0.99</b>
Fe <sub>2</sub> O <sub>3</sub>	0.03	<b>-0.80</b>	<b>-0.80</b>	1	0.58	0.91	0.69	-0.77	-0.77	-0.81
MnO	0.83	<b>-0.95</b>	<b>-0.95</b>	0.58	1	<b>0.86</b>	-0.17	-0.62	<b>-0.96</b>	<b>-0.94</b>
MgO	0.43	<b>-0.97</b>	<b>-0.97</b>	<b>0.91</b>	<b>0.86</b>	1	0.34	<b>-0.96</b>	<b>-0.96</b>	<b>-0.97</b>
CaO	-0.68	-0.14	-0.14	0.69	-0.17	0.34	1	-0.08	<b>-0.96</b>	-0.15
Na <sub>2</sub> O	-0.66	<b>0.99</b>	<b>0.99</b>	-0.77	-0.62	<b>-0.96</b>	-0.08	1	<b>0.99</b>	<b>0.99</b>
K <sub>2</sub> O	-0.66	<b>0.99</b>	<b>0.99</b>	-0.77	<b>-0.96</b>	<b>-0.96</b>	<b>-0.96</b>	<b>0.99</b>	1	<b>0.99</b>
P <sub>2</sub> O <sub>5</sub>	-0.61	<b>0.99</b>	<b>0.99</b>	<b>-0.81</b>	<b>-0.94</b>	<b>-0.97</b>	-0.15	0.99	0.99	1

D)

	SiO <sub>2</sub>	TiO <sub>2</sub>	Al <sub>2</sub> O <sub>3</sub>	Fe <sub>2</sub> O <sub>3</sub>	MnO	MgO	CaO	Na <sub>2</sub> O	K <sub>2</sub> O	P <sub>2</sub> O <sub>5</sub>
SiO <sub>2</sub>	1	<b>0.90</b>	<b>0.95</b>	-0.03	-0.22	<b>-0.94</b>	<b>-0.95</b>	0.08	<b>0.96</b>	0.03
TiO <sub>2</sub>	<b>0.90</b>	1	<b>0.97</b>	0.33	0.03	<b>-0.82</b>	<b>-0.95</b>	0.28	<b>0.96</b>	-0.22
Al <sub>2</sub> O <sub>3</sub>	<b>0.95</b>	0.97	1	0.24	-0.13	<b>-0.88</b>	<b>-0.97</b>	0.18	<b>0.96</b>	-0.19
Fe <sub>2</sub> O <sub>3</sub>	-0.03	0.33	0.24	1	0.31	0.11	-0.16	0.25	0.09	<b>-0.86</b>
MnO	-0.22	0.03	-0.13	0.31	1	0.22	0.12	-0.16	-0.03	-0.27
MgO	<b>-0.94</b>	<b>-0.82</b>	<b>-0.88</b>	0.11	0.22	1	<b>0.83</b>	-0.09	<b>-0.92</b>	-0.17
CaO	<b>-0.95</b>	<b>-0.95</b>	<b>-0.97</b>	-0.16	0.12	<b>0.83</b>	1	-0.16	<b>-0.92</b>	0.15
Na <sub>2</sub> O	0.08	0.28	0.18	0.25	-0.16	-0.09	-0.16	1	0.21	0.22
K <sub>2</sub> O	<b>0.96</b>	<b>0.96</b>	<b>0.96</b>	0.09	-0.03	<b>-0.92</b>	<b>-0.92</b>	0.21	1	-0.01
P <sub>2</sub> O <sub>5</sub>	0.03	-0.22	-0.19	<b>-0.86</b>	-0.27	-0.17	0.15	0.22	-0.01	1

The Zr/Rb ratio depends not only on grain size distribution, but on quartz content as well (Dypvik and Harris, 2001). In general, the Zr is adsorbed on clay minerals and belongs to heavy mineral phases, such as zircon and monazite (Wedepohl, 1969; Pettijohn et al., 1972). The heavy minerals corresponds to silt fraction, hence several boundary layer samples have higher Zr/Rb ratio (Fig. 10-11.). The diamictite from Tweelingskop (sample C5) has high quartz cement resulting higher Zr/Rb ratio (Fig. 10.). The microbial Sturtian layer has low Zr/Rb ratio, while the boundary layer with clastic components (quartz, zircon, feldspar) from Copper Mine has higher Zr/Rb ratio. The Zr/Rb ratio is influenced by grain size distribution and ratio of siliciclastic material of the samples. The Zr/Rb ratio was compared with grain size distribution of samples after dissolving carbonate (Fig. 10-11.). The used formic acid probably dissolved the carbonate phase from matrix material, while the detrital dolomite grains were resistant to formic acid. Under binocular microscope large number of rounded, pale, yellow dolomite grains were observed among quartz and mica grains.

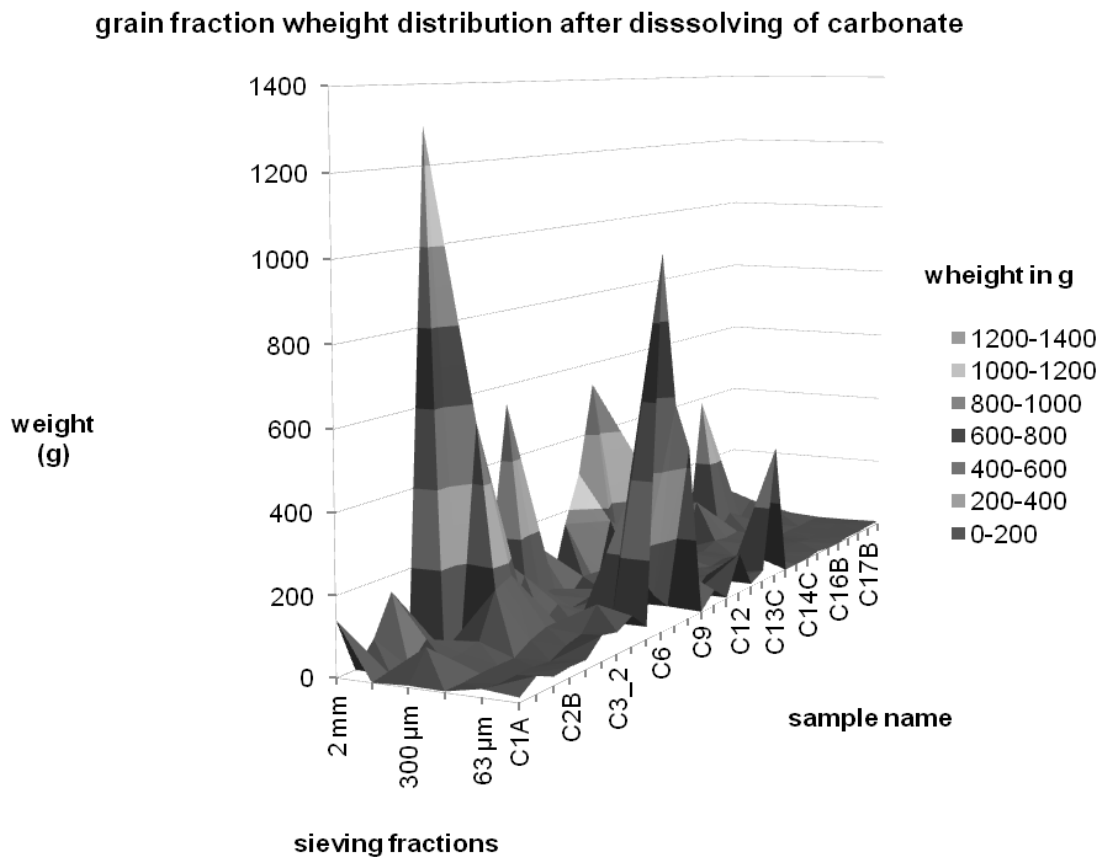


**Figure 10.** Grain-size distribution of Sturtian and Marinoan postglacial samples with weight (in grams) of sieving fractions.

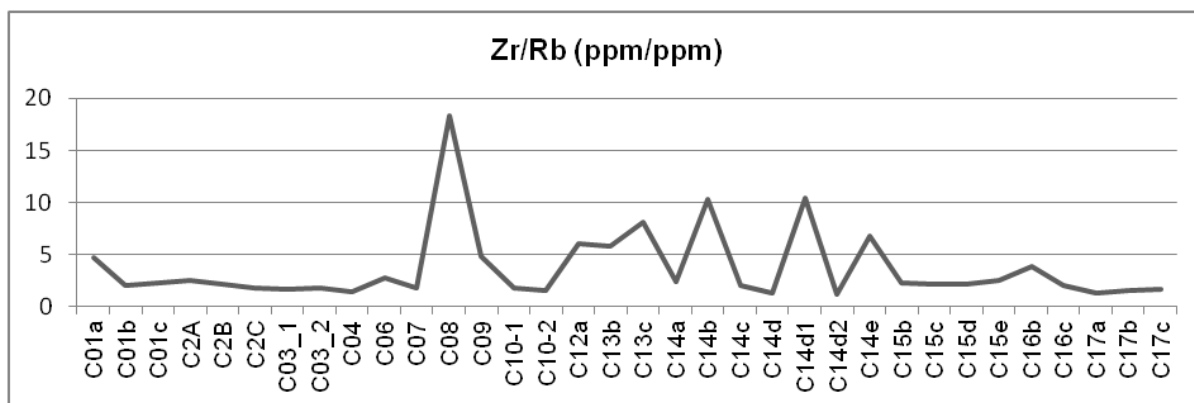


**Figure 11.** Grain-size distribution of Sturtian and Marinoan transition layers regarding Zr/Rb ratios.

#### 7.6.4 Weathering

During the warm period, the weathering rate increases which drives ratio of  $\text{Al}_2\text{O}_3$  to  $\text{SiO}_2$  (Nesbitt and Young, 1982). Hence,  $\text{SiO}_2/\text{Al}_2\text{O}_3$  can be used as climatic proxy to identify glacial and postglacial periods (Scheffler, 2004). During the cold period, the ratio of  $\text{SiO}_2$  to  $\text{Al}_2\text{O}_3$  is higher whereas, the  $\text{Al}_2\text{O}_3$  ratio to  $\text{SiO}_2$  is higher in postglacial period due to increased continental weathering (Figure 12.). Hence, within topmost diamictite layer a higher  $\text{SiO}_2$  ratio to  $\text{Al}_2\text{O}_3$  exhibits and higher  $\text{Al}_2\text{O}_3$  to  $\text{SiO}_2$  ratio is found in postglacial transition layers and basal cap carbonate. Although the  $\text{Al}_2\text{O}_3/\text{SiO}_2$  ratio can be influenced by diagenetic reworking and selective biogenic silica enrichment (e.g. quartz cement growth). In general, the Marinoan glacial layer have higher  $\text{SiO}_2$  ratio to  $\text{Al}_2\text{O}_3$  because of climatic effect and low weathering, but the C5 sample has high  $\text{SiO}_2$  because of quartz cement after diagenetic alteration (Figure 1B). During the deglaciation the  $\text{Al}_2\text{O}_3$  is higher because of increased continental weathering.

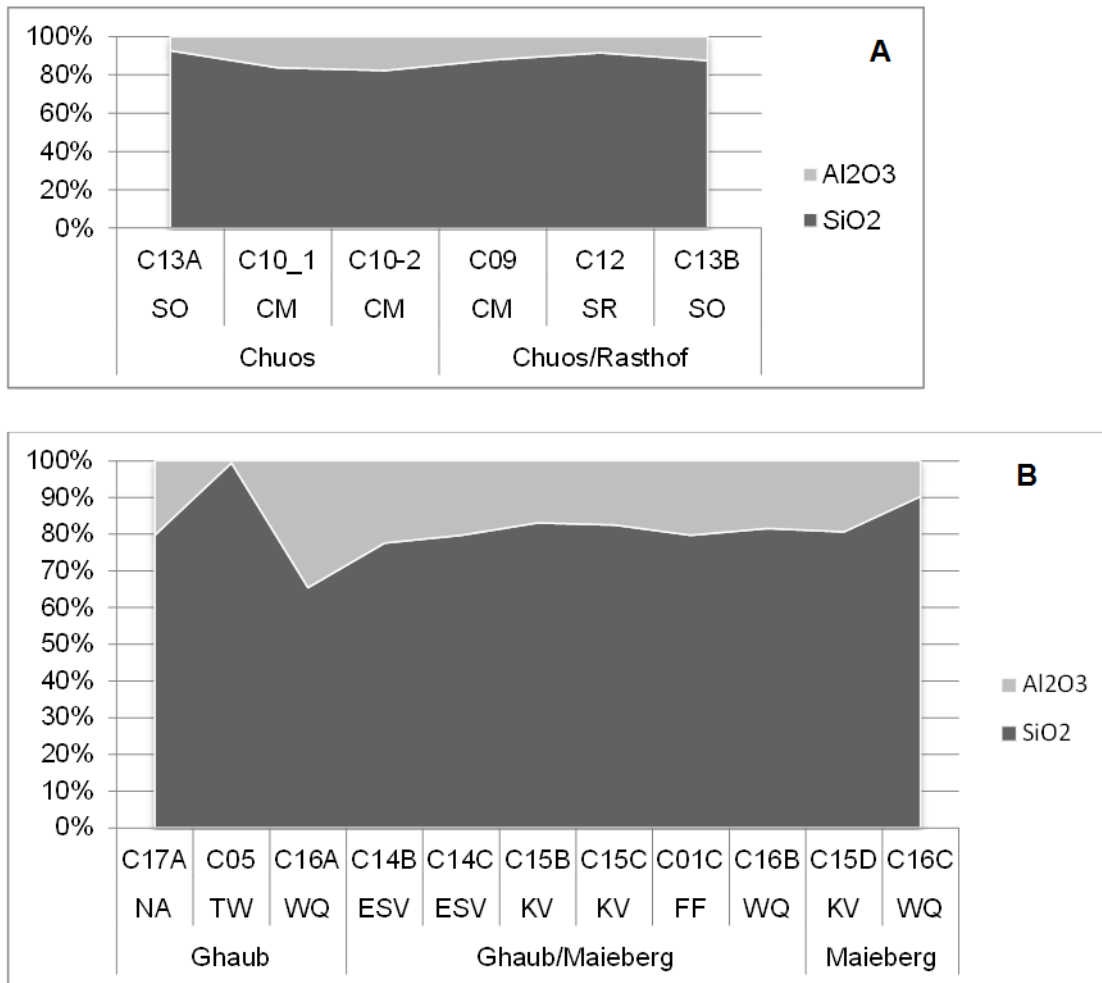


**Figure 12.** Al<sub>2</sub>O<sub>3</sub>-SiO<sub>2</sub> distribution according to stratigraphic setting and localities. The increase of Al<sub>2</sub>O<sub>3</sub> depends not only on climatic effects, but on weathering rate and biogenic character of adjacent samples. A) Sturtian: Legend: SO=Sesfontain-Opuwo, CM=Copper Mine, SR=Steilrandberge, B) Marinoan: Legend: NA=Naraachamspos, TW=Tweelingskop, ESV= Entrance of South Valley, FF=Fransfontain, WQ=Warmquelle, KV=Khowarib Valley.

Cr, Ni and V, which concentrate on surface of clay minerals, have similar ionic radii, so they behave similarly during the weathering process (Brumsack, 1989; Tribovillard et al., 2006). These elements show good correlation in Sturtian and Marinoan transition layers, indicating presence of clay minerals. The Ni and Zn can substitute MgO in chlorite structure because of similar ion radii (Brumsack, 1989; Tribovillard et al. 2006), hence the good correlation indicates presence of chlorite in Marinoan boundary layers. The good Cr-Ni-V vs Al<sub>2</sub>O<sub>3</sub> correlation (Algeo and Maynard, 2004) according to localities in Sturtian layers belong to microbial structure of iron-oxidizing bacteria. The Marinoan postglacial layers have good correlation of Cr-Ni-Zn-MgO, which indicate presence of chlorite. The Sturtian diamictite samples have wrong correlation, whereas the boundary layers have moderate correlation.

The good correlation between CaO vs Sr in Sturtian and Marinoan transition layers indicates Sr belonging to carbonate phases. The good correlation between Ba vs K<sub>2</sub>O, Al<sub>2</sub>O<sub>3</sub> and Na<sub>2</sub>O belongs feldspars especially albite and kalifeldspar. The Marinoan boundary layer samples have weak correlation between Al and Ba indicating that Ba belongs to clay minerals and not to feldspars. The SiO<sub>2</sub>/Al<sub>2</sub>O<sub>3</sub> vs Cu, Cr and Co show dilution trends of quartz. Except the diamictite from Tweelingskop (which is opalized after diagenetic alteration), show low quartz dilution. The Rb, Cs, Sr, U, Th vs. Al<sub>2</sub>O<sub>3</sub> correlation (Breit and Wanty, 1991) marks presence of phyllosilicates in Marinoan and Sturtian postglacial layers. The strong correlation between K<sub>2</sub>O-Rb-Th indicate clayey component (Pettijohn et al., 1972) for both of Marinoan and Sturtian samples.

On the basis of characteristic **mineral-element associations** from limestones and dolostones described by Barber (1974), our Sturtian postglacial layers reveal the following characteristics: A strong correlation between Al<sub>2</sub>O<sub>3</sub>-TiO<sub>2</sub>-SiO<sub>2</sub> belongs to detrital phases, in which Ti substitutes Al in feldspar and clay minerals (Table 8.). We attribute the observable strong Na-K correlation with Al-Ti-Si to feldspar and clay mineral phases (kaolinite), whereas the Ca-Mg correlation belongs to dolomite. Further the strong correlation of immobile versus alkaline earth elements indicates the presence of clay minerals and an excellent correlation of Fe-Na-K indicates the adsorbance of K and Na on iron minerals. Ti is well correlated with Al, Mg, Na, K, Si, Al determining it's substitution in silicate lattices (Table 8.). Our Marinoan age samples also show a good correlation of Ti-Al-K (Table 8.) indicating Ti substitution in feldspars and clay minerals. The correlation of Si-Ca-Mg is known as a geochemical signature of kaolinite and smectite minerals. Strong Ca-Mg correlation reveals dolomitization.

In general, the Sturtian glacial transition layers (**Chuoss Formation**) have low Al<sub>2</sub>O<sub>3</sub>/SiO<sub>2</sub> ratios and values in the ANK diagram near the upper crust, indicating low continental weathering (Fig. 9.). C10 samples have enhanced Al<sub>2</sub>O<sub>3</sub>/SiO<sub>2</sub>, Mg/Al, K/Al ratios (Fig. 12-13.) and values near the illite/muscovite line in the ANK (Al<sub>2</sub>O<sub>3</sub>- Na<sub>2</sub>O- K<sub>2</sub>O) diagram (Nesbitt and Young, 1982) because of presence of weathering products of detrital feldspars, e.g., kaolinite, and smectite.

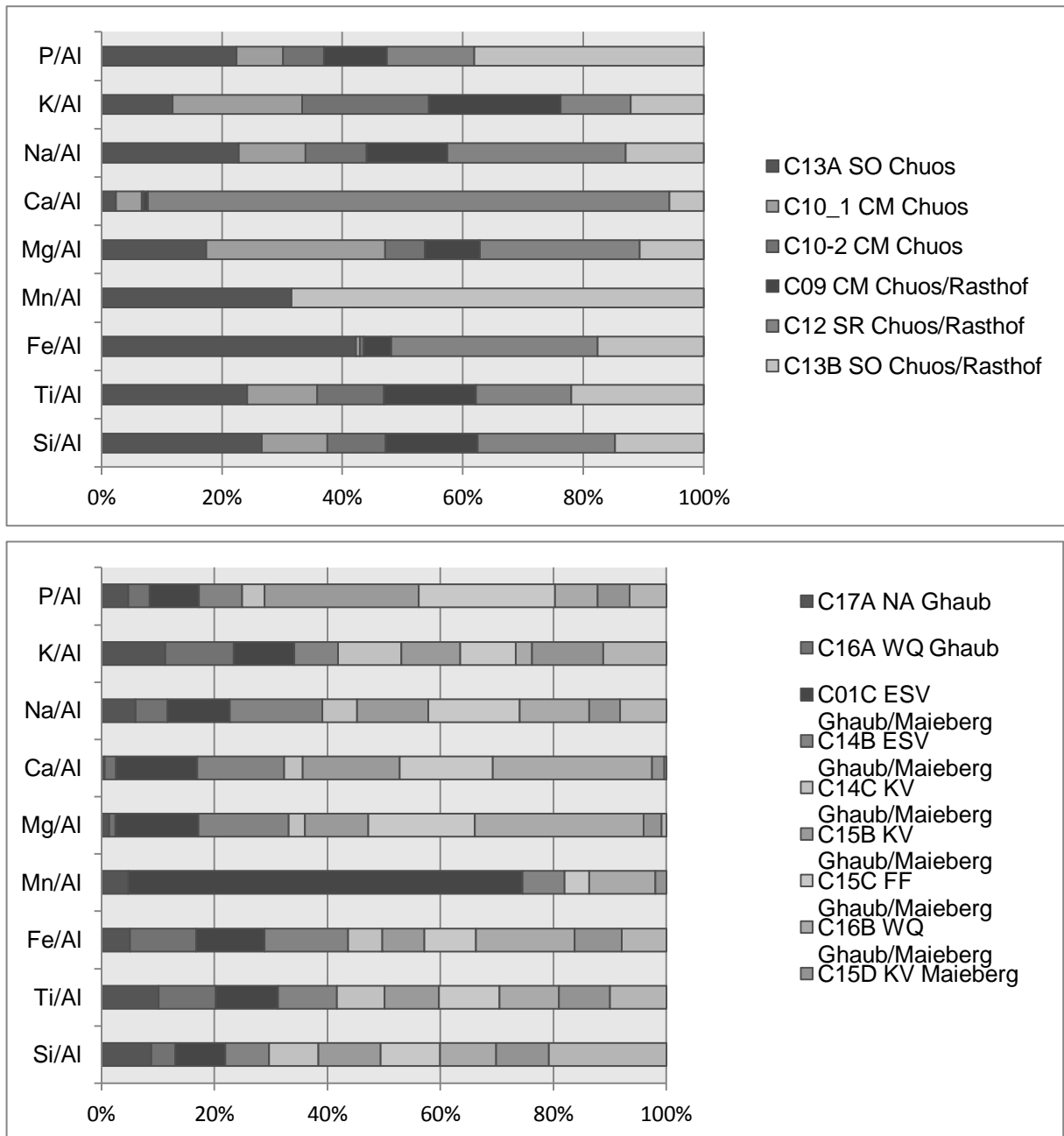


**Figure 13.** Major element/Al ratios for Sturtian and Marinoan postglacial transition layers. (Legend: Sturtian: SO=Sesfontain-Opuwo, CM=Copper Mine, SR=Steilrandberge; Marinoan: NA=Naraachamspos, TW=Tweelingskop, ESV= Entrance of South Valley, FF=Fransfontain, WQ=Warmquelle, KV=Khowarib Valley).

Sturtian postglacial transition layers (**Chuoss/Rasthof boundary, basal Rasthof Formation**), which contain synsedimentary biogenic structures, also have low  $\text{Al}_2\text{O}_3/\text{SiO}_2$  ratios, indicating lack of clay minerals from continental weathering. The abiogenic boundary layer (C9, Copper Mine) shows low  $\text{Al}_2\text{O}_3/\text{SiO}_2$ , Ti/Al, Na/Al, K/Al ratios because of the presence of clay minerals due to continental weathering (Fig. 13.).

In Marinoan glacial transition layers (**Ghaub Formation**), samples C17a (Naraachamspos) and C16a (Warmquelle) has higher  $\text{Al}_2\text{O}_3/\text{SiO}_2$  ratio and values near to kaolinite-chlorite on ANK diagram indicating higher continental weathering (Fig. 14). The opalized diamictite (C5) with low  $\text{Al}_2\text{O}_3/\text{SiO}_2$ , but high Ti/Al, Na/Al, K/Al ratios reveal moderate weathering rate.

Samples from all locations of Marinoan postglacial transition layers (**Ghaub/Maieberg boundary, basal Maieberg Formation**) show moderate enhanced  $\text{Al}_2\text{O}_3/\text{SiO}_2$ , Na/Al, K/Al, Ti/Al ratios (Fig. 12.) due to the presence of smectite and kaolinite indicating increased continental weathering due to deglaciation.

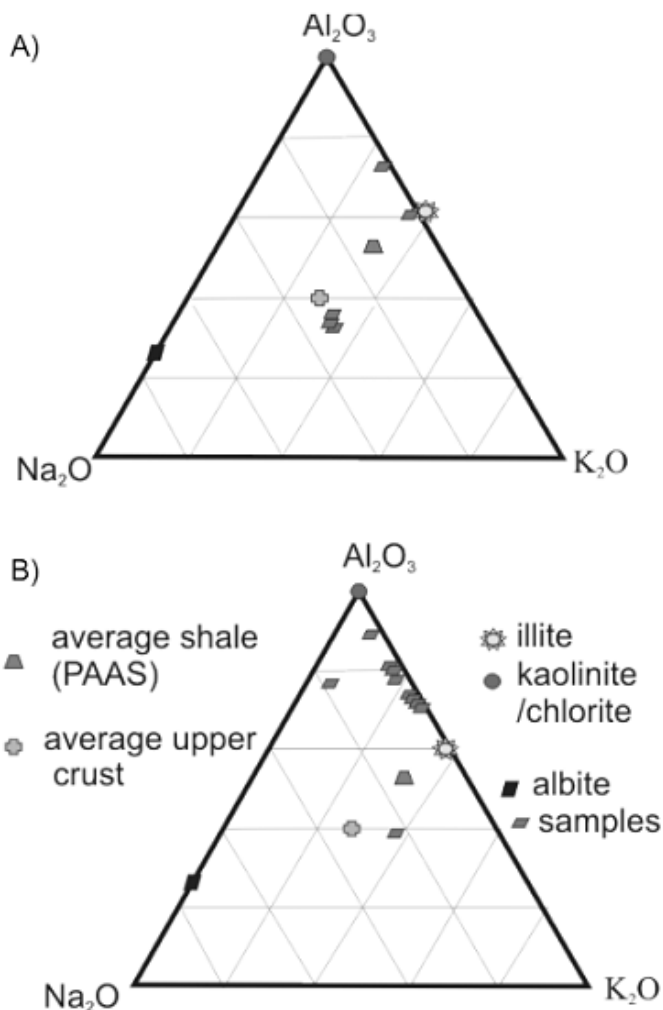


**Figure 14.** ANK diagram and major element correlations  $\text{Al}_2\text{O}_3$ - $\text{Na}_2\text{O}$ - $\text{K}_2\text{O}$  diagram with mineral standards showing weathering (Nesbitt and Young, 1982) rate: Sturtian (A: weak to moderate weathered) and Marinoan (B: strongly weathered) postglacial shift sequences (UCC (upper continental crust) (Rudnick and Gao, 2003) and PAAS (Post-Archean Australian shale (Taylor and McLennan, 1985). C-D: Correlation diagrams for the geochemical abundances of selected elements in Sturtian (C) and Marinoan (D) postglacial transition layers, where high correlation values are indicative of different mineral phases, like albite (Na-Al, Na-Si), kalifeldspar (K-Al, K-Si), sheet silicates (e.g., mica, clay minerals): (Na-K, Fe-K, Fe-Na, Fe-Al, MgO-Ti, Na-Ti, K-Ti, Ca-Si, Mg-Si), dolomite: (CaO-MgO) (after Algeo and Maynard, 2004).

### 7.6.5 Microbial structures

Iron-rich stromatolite structures were described by Pruss et al. (2010) in samples from the basal Rasthof Fm., which were identified as biogenic structure formed under anoxic conditions in a deep water environment. Le Heron et al. (2012) found thick ironstone stromatolite structures in the basal Sturtian diamictite, which were interpreted as FeOB biomats with acidophil CO<sub>2</sub>-fixing metabolism in analogy to modern acid drainage. We propose that the presence of iron-microbial structures represents the first signal of deglaciation. Also, present-day ice biota in near-shore region of Antarctica is dominated by oscillatorian cyanobacteria and iron-oxidizing bacteria, hence such ice-tolerant biomats could have existed during the Snowball Earth glaciations (Vincent and Howard-Williams, 2000). According to our mineralogical and geochemical data, the microbial community lived in suboxic near-shore environments, which occurred when anoxic conditions changed to oxygenic conditions (Hoffman et al. 1998; Och and Shields-Zhou, 2012). The morphological and geochemical data implies presence of iron-oxidizing bacteria (*Gallionella*) in Sturtian postglacial boundary layers and Marinoan basal cap carbonates (profiles K2, K4, sample C1). The nutrients (Fe and P) of synsedimentary biogenic structures were generated from hydrothermal vents active during the break-up of Rodinia (Campbell and Squire, 2010). Interpreting our data after Noffke et al. (2006) we suppose that our carbon isotope values are indicating a biogenic origin. The FeOB filaments in our samples are composed of lepidocrocite, goethite, and hematite (Fig. 15.), which formed by transformation after poorly ordered ferrihydrite via dissolution dehydration processes (Konhauser, 1998). The fossilized iron biomats are encrusted by authigenic dolomite and silica (Baele et al. 2008) (ordered to more stable quartz; Herdianata et al. 2000). In general, the synsedimentary structures of FeOB mats are thinner (layer thickness 1 mm - 1 cm) for Marinoan samples (sample C1, profiles K2, K4) than for Sturtian (20 cm), which can result from a different paleolatitude setting: Namibian Sturtian (Chuoss Fm.) diamictite was formed at 35° paleolatitude (Christie-Blick et al., 1999), whereas the Marinoan (Ghaub Fm.) was formed between 5 and 10° paleolatitude (Evans, 2000). In general, the Neoproterozoic banded iron formations (BIFs) are associated by Cryogenian glacial deposits, formed at 35° paleolatitude (Hoffman, 2011). The FeOB occur as biodegradation of iron-bearing mineral in Sturtian (C10\_1-2, top of Chuoss Fm.; profile S6, basal Rasthof Fm. at Copper Mine) and for Marinoan (profile C2a, basal cap carbonate at Naraachamspos) samples. The presence of FeOB and smectite in weathering of minerals indicate suboxic neutral conditions during the diagenesis (Douglas, 2005). Most cap carbonates formed during oxygenic conditions, except Marinoan sample C15d (Khowarib Valley), and Sturtian sample C13c (Sesfontain-Opuwo) formed during suboxic conditions.

The biomineralization of different carbonate components was summarized by Riding (2000): 1) dense micrites forms calcification of biofilms and after dying of bacteria. This dense micrite films were observed at rim of oncoids in sample C8 (basal Rasthof Fm.). 2) The peloids are granular in-situ precipitates which are silt size (20-60 micron) spherules which discussed either cement fabrics, or calcified bacterial aggregates which rimmed by euhedral calcite (Riding, 2000), which is observed in pores among the oncoids. 3) The oncoids are formed by calcification of cyanobacteria or micrite envelopes on grains were microbial coatings. The most basal cap carbonate, sample C8 contain ooids and oncoids, which formed by cyanobacterial encrusting of other carbonate components and detrital particles. Between the oncoids, spongiostrome micrite can be observed, which formed by calcification of cyanobacterial cells. The cyanobacterial encrusting reveals tidal, near-shore environment for most basal Sturtian cap carbonate from Copper Mine.

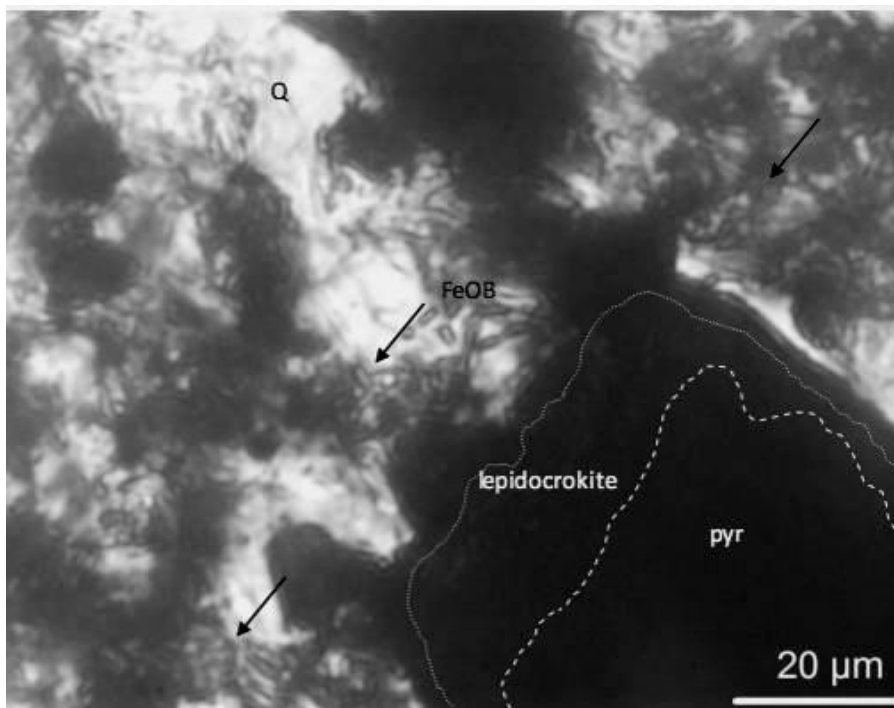


**Figure 15.** Example for biogenic structures of iron-oxidizing bacteria (FeOB, marked by black arrows) in our studied stratigraphic setting: Biodegradation of pyrite (B) in Profile C2a.

## 7.7 Conclusions

The Sturtian and Marinoan postglacial layers formed within suboxic conditions in brackish water environment except Copper Mine (Sturtian) and Naraachamspos (Marinoan) locations, the transition layers contain only authigenic minerals refusing influence of detrital input.

The geochemical proxies suggest syngedimentary formation of iron biomats in both of Sturtian iron-stromatolites (C12, C13) and Marinoan iron biomats in basal cap carbonate (K2, K4).

## 7.8 Acknowledgements

We are grateful to Peter Nagl (XRF), Miklos Veres (micro-Raman Spectroscopy), and Susanne Gier (XRD), Lidia Pittarello and Ludovic Ferriere (SEM) for help in lab work and helpful discussions. This study was supported by the Austrian Academy of Sciences (grant to C.K.). We are grateful the Geological Survey of Namibia and Director Dr. G. Schneider for their important help as to field work organization and sample export management. We appreciate the help of the reactor team of the Institute of Atomic and Subatomic Physics, Vienna, with the irradiations.

## 7.9 References

- Algeo, T.J., Maynard, J.B., 2004. Trace-element behavior and redox facies in core shales of Upper Pennsylvanian Kansas-type cyclothems. *Chemical Geology*, 206/3–4, 289–318.
- Alkmim, F.F., Marshak, S. and Fonseca, M.A., 2001. Assembling West Gondwana in the Neoproterozoic: Clues from the Sao Francisco craton region. *Braz. Geol.*, 29, 319-322.
- Barber, C., 1974. Major and trace element associations in limestones and dolomites. *Chem. Geol.*, 14/4, 273-280.
- Baele, J.-M., Bouvain, F., De Jong, J., Matielli, N., Papier, S., Prat, A., 2008. Iron microbial mats in modern and Phanerozoic environments. *Proc. Soc. Phot. Instr. Eng.* 7097, 70970N–70970N–12.
- Breit, G.N. and Wanty, R.B., 1991. Vanadium accumulation in carbonaceous rocks: a review of geochemical controls during deposition and diagenesis. *Chem. Geol.* 91, 83–97.
- Brumsack, H.-J., 1989. Geochemistry of recent TOC-rich sediments from the Gulf of California and the black Sea. *Geol. Rundsch.*, 78/3, 851-882.
- Campbell, F.A. and Williams, G.D., 1965. Chemical composition of shales of Mannville Group (Lower Cretaceous) of Central Alberta, Canada. *AAPG Bull.*, 49/1, 81-87.
- Campbell, I.H. and Squire, R.J., 2010. The mountains that triggered the Late Neoproterozoic increase in oxygen: the second great oxidation event. *Geochim. et Cosmochim. Acta* 74 /15, 4187–4206.
- Christie-Blick, N., Sohl, L. E., and Kennedy, M.J., 1999. Considering a Neoproterozoic Snowball Earth. *Science*, 284, 1084a
- Clauer, N. and Kröner, A., 1979. Strontium and argon isotopic homogenization of pelitic sediments during low-grade regional metamorphism: The Pan-African upper Damara sequence of northern Namibia (South West Africa). *Earth Planet. Sci. Lett.*, 43, 117-131.
- Dahanayake, K. and Krumbein, W.E., 1986. Microbial structures in oolitic iron formations. *Miner. Depos.* 21, 85–94.
- Domack, E. and Hoffman, P., 2003. Stratigraphic transition into and out of Snowball glaciations: evidence from the Otavi platform and Fransfontain slope, Namibia. *Am. Geophys. Union, Ann. Fall Mtng. Abs.* C11B–0819.
- Douglas S., 2005. Mineralogical footprints of microbial life. – *Am. J. Sci.*, 305, 503-525.
- Dypvik, H., Hams, N.B, 2001. Geochemical facies analysis of fine-grained siliciclastics using Th/U, Zr/Rb and (Zr+Rb) /Sr ratios. *Chem. Geol.*, 181, 131-146
- Evans, D.A.D., 2000. Stratigraphic, geochronological and paleomagnetic constraints upon the Neoproterozoic climatic paradox. *Am. J. Sci.*, 300, 347–433.
- Eyles, N. and Januszczak, N. 2004. Zipper-rift: a tectonic model for Neoproterozoic glaciations during the breakup Rodinia after 750 Ma. *Earth-Sci. Revs.*, 65/1-2, 1-73.

- Gammon, P.R., 2012. An organodiagenetic model for Marinoan-age cap carbonates. *Sed. Geol.*, 243-244, 17–32.
- Gammon, P.R., McKirdy, D.M. and Smith, H.D., 2012. The paragenetic history of a Marinoan cap carbonate. *Sed. Geol.*, 243–244, 1–16.
- Gyollai, I., Polgári, M., Fintor, K., Popp, F., Mader, M., Pál-Molnár, E., Nagy, N., Koeberl, C., 2013. Microbially mediated deposition of postglacial transition layers from the Neoproterozoic Otavi Group, Namibia: evidence of rapid deglaciation after the Sturtian cryogenic period. Submitted to *Carp. J. of Earth and Env. Sci.*, 2013.
- Harland, W.B., Rudwick, M.J.S., 1964. The great Infra-Cambrian glaciation. *Scientific American*, 211, 28-36.
- Hedberg, R.M., 1975. Stratigraphy of the Owamboland basin, South West Africa. Ph.D. thesis, Harvard Univ., Cambridge, Mass., 1975.
- Hedberg, R.M., 1979. Stratigraphy of the Owamboland basin, South West Africa. – *Bull. of Precamb. Res. Unit, Cape Town*, 24, 325 pp.
- Herdianita, N.R., Browne, P.R.L., Rodgers, K.A. and Campbell, K.A., 2000. Mineralogical and textural changes accompanying ageing of silica sinter. *Miner. Depos.*, 35, 48-62.
- Hoffman, P.F., Hawkins, D.P., Isachsen, C.E., and Bowring, S.A., 1996. Precise U-Pb zircon ages for early Damaran magmatism in the Summas Mountains and Welwitschia Inlier, northern Damara belt, Namibia. *Comm.of Geol. Surv. Nam.*, 11, 47-52.
- Hoffman, P.F., Kaufman, A.J., Halverson, G.P. and Schrag, D.P., 1998. A Neoproterozoic Snowball Earth. *Science*, 281, 1342–1346.
- Hoffman, P.F., 2002. Carbonates bounding glacial deposits: Evidence for Snowball Earth episodes and greenhouse aftermaths in the Neoproterozoic Otavi Group of northern Namibia. - IAS Field Excursion Guidebook, 16th Int. Geol. Congress, Rand Africaans Univ., Johannesburg, S-Africa.
- Hoffman, P.F. and Schrag, D.P., 2002. The snowball Earth hypothesis: testing the limits of global change. *Terra Nova* 14, 129-155.
- Hoffman, P.F., 2005. 28th DeBeers - Alex. Du Toit Memorial Lecture, 2004. On Cryogenian (Neoproterozoic) ice-sheet dynamics and the limitations of the glacial sedimentary record. *South Afr. J. of Geol.*, 108, 557-576.
- Hoffman, P.F. and Halverson, G.P., 2008. Otavi Group of the western Northern Platform, the Eastern Kaoko Zone and the western Northern Margin Zone.-In: R. McG. Miller [Ed]: *The Geology of Namibia. Vol 2: Neoproterozoic to Lower Paleozoic.* - Ministry of Mines and Energy, Geological Survey, Namibia 2008.
- Hoffman, P.F., 2011. Strange bedfollows: glacial diamictite and cap carbonate from the Marinoan (635 Ma) glaciations in Namibia. *Sedimentology*, 58, 57-119.

- Hoffmann, K.-H., and Prave, A.R., 1996. A preliminary note on a revised subdivision and regional correlation of the Otavi Group based on glaciogenic diamictites and associated cap dolostones. – *Comm. of Geol. Soc. Nam.* 11, 81-86.
- Kamber, B. S. and Webb, G.E., 2007. Transition metal abundances in microbial carbonate: a pilot study based on in situ LA-ICP-MS analysis. *Geomicrobiology*, 5/4, 375–389.
- Kempe, A., Wirth, R., Altermann, W., Stark, R.W., Schopf, J.W. and Heck, W.M., 2005. Focused ion beam preparation and in situ nanoscopic study of Precambrian acritarchs. *Precambr. Res.*, 140, 36–54.
- Kennedy, M.J., 1996. Stratigraphy, sedimentology and isotopic geochemistry of Australian Neoproterozoic postglacial cap dolostones: deglaciation,  $\delta^{13}\text{C}$  excursions and carbonate precipitation. *J. of Sedim. Res.*, 66, 1050-1064.
- Kennedy, M.J., Christie-Blick, N., and Sohl, L.E., 2001. Are Proterozoic cap carbonates and isotopic excursions a record of gas hydrate destabilization following Earth's coldest intervals? *Geology*, 29, 443-446.
- Konhauser, K.O., 1998. Diversity of bacterial iron mineralization. *Earth-Sci. Revs.*, 43/ 3–4, 91-121.
- Kudryavtsev, A.B., Schopf, J.W., Agresty, D.G., and Wdowiak T.J., 2001. In situ laser-Raman imagery of Precambrian microscopic fossils. *Proc. Nat. Acad. of Sci.*, 98/ 3, 823–826.
- Le Heron, D.P., Busfield, M.E., Le Ber, E., and Kamona, A.F., 2013. Neoproterozoic ironstones in northern Namibia: Biogenic precipitation and Cryogenian glaciation. *Palaeogeogr., Palaeoclimat., Palaeoecol.* 369, 48–57.
- Le Hir, G., Donnadieu, Y., Godderis, Y., Pierrehumbert, R.T., Halverson, G.P., Macouin, M., Nedelec, A., and Ramstein, G., 2008. The snowball Earth aftermath: Exploring the limits of continental weathering processes. *Earth and Plan. Sci. Lett.*, 277, 453-463.
- Mader, D. and Koeberl, C., 2009. Using Instrumental Neutron Activation Analysis for geochemical analyses of terrestrial impact structures: Current analytical procedures at the University of Vienna Geochemistry Activation Analysis Laboratory. *Appl. Rad. and Isot.*, 67, 2100–2103.
- Mapelli, C., Castiglioni, C., Zerbi, G. and Mullen, K., 1999. Common force field for graphite and polycyclic aromatic hydrocarbons. *Phys. Rev. B*, 60, 12710–12725
- Marshall, C.P., Javaux, E.J., Knoll, A.H. and Walter, A.M., 2005. Combined micro-Fourier-transform infrared (FTIR) spectroscopy and micro-Raman spectroscopy of Proterozoic acritarchs: A new approach to Palaeobiology. *Precambr. Res.* 138, 208–224.
- Martin, H., 1965. The Precambrian geology of South West Africa and Namaqualand. *Bull. Precambr. Res. Unit, Univ. Cape Town*, 159 pp.

- Maruoka, T., Koeberl, C., Matsuda, J. and Syono, Y., 2003. Carbon isotope fractionation between graphite and diamond during shock experiments. *Met. and Planet. Sci.*, 38, 1255–1262.
- Maruoka, T., Koeberl, C. and Bohor, B.F., 2007. Carbon isotopic compositions of organic matter across continental Cretaceous–Tertiary (K–T) boundary sections: Implications for paleoenvironment after the K–T impact event. *Earth and Planet. Sci. Lett.*, 253, 226–238.
- Marshall, C.P., Javaux, E.J., Knoll, A.H. and Walter, A.M., 2005. Combined micro-Fouriertransform infrared (FTIR) spectroscopy and micro-Raman spectroscopy of Proterozoic acritarchs: A new approach to Palaeobiology. *Precamb. Res.*, 138, 208–224.
- McLennan S.M., Taylor, S.R., McCulloch, M.T. and Maynard, J.B., 1990. Geochemical and Nd-Sr isotopic composition of deep-sea turbidites - Crustal evolution and plate tectonic associations. *Geochim. et Cosmochim. Acta*, 54, 2015–2050.
- McLennan, S.M., Hemming, S., McDaniel, D.K. and Hanson, G.N., 1993. Geochemical approaches to sedimentation, provenance and tectonics. In: Johnsson, M.J. and Basu, A. (eds.), *Processes controlling the composition of clastic sediments*. *Geol. Soc. of Am. Spec. Paper*, 285, 21-40.
- Mernagh, T.P., 1991. Use of the laser Raman microprobe for discrimination amongst feldspar minerals. *J. of Raman Spectr.*, 22/8, 453–45.
- Meyer, E. E., Quicksall, A.N., Landis, J.D., Link, P.K and Bostick, B.C., 2012. Trace and rare earth elemental investigation of a Sturtian cap carbonate, Pocatello, Idaho: Evidence for ocean redox conditions before and during carbonate deposition. *Precamb. Res.*, 192-195, 89-106
- Miller, R. McG., 1983. The Pan-African Damara Orogen of South West Africa / Namibia. *Geol. Soc. South Afr. Spec. Publ.*, 11, 431-515.
- Nesbitt, H.W. and Young, G.M., 1982. Early Proterozoic climates and plate motions inferred from major element chemistry of lutites. *Nature*, 199, 715-717.
- Nikiel, L. and Jagodzinski, P.W., 1993. Raman spectroscopic characterization of graphites: a re-evaluation of spectra/structure correlation. *Carbon*, 31, 1313–1317.
- Noffke, N., Eriksson, K. A. Hazen, R.M., and Simpson, E.L., 2006. A new window into Early Archean life: Microbial mats in Earth's oldest siliciclastic tidal deposits (3.2 Ga Moodies Group, South Africa). *Geology*, 34, 253-256.
- Och, L.M. and Shields-Zhou, G.A., 2012. The Neoproterozoic oxygenation event: Environmental perturbations and biogeochemical cycling. *Earth-Science Revs.*, 110, 26–57.
- Porada, H.R., 1989. Pan-African Rifting and orogenesis in southern to equatorial Africa and eastern Brazilian. *Precamb. Res.*, 44, 103-136.

- Pruss S.B., Bosak, T., McDonald, F. A., McLane, M. and Hoffman, P.F., 2010. Microbial facies in a Sturtian cap carbonate, the Rasthof Formation, Otavi Group, northern Namibia. *Precamb. Res.*, 181, 187–198.
- Pettijohn, F.J., Potter, P.E. and Siever, R., 1972. *Sand and sandstone*. 618 pp.; Springer, New York, Heidelberg, Berlin.
- Reysenbach, A. and Cady, S., 2001. Microbiology of ancient and modern hydrothermal systems. *Trends Microbiol.* 9, 79–86.
- Riding, R., 2000. Microbial carbonates: the geological record of calcified bacterial-algal mats and biofilms. *Sedimentology*, 47, 179-214.
- Rudnick, R.L., and Gao, S., 2003. Composition of the Continental Crust. *Treatise on Geochemistry*, Volume 3. Editor: Rudnick, R.L. Executive Editors: Holland, H.D. and Turekian, K.K. pp. 659, Elsevier, 2003, p.1-64.
- SACS, South Africa Committee for Stratigraphy, 1980. *Stratigraphy of South Africa*. Kent L.E. (Comp); Part 1. Lithostratigraphy of the Republic of South Africa, South West Africa / Namibia and the Republics of Bophuthatswana, Transkei and Venda. *Handbook of Geology Survey South Africa*, 8, 690 pp.
- Scheffler, K., 2004. Reconstruction of sedimentary environment and climate conditions by multi-geochemical investigations of Late Palaeozoic glacial to postglacial sedimentary sequences from SW-Gondwana. PhD Thesis, Rheinischen Friedrich-Wilhelms-Universität Bonn, Wuppertal, Bonn, Germany, pp.243.
- Stanistreet, I.G., Kukla, P.A., and Henry, G. 1991. Sedimentary basinal response to a Late Precambrian Wilson Cycle: The Damara Orogen and Nama Foreland, Namibia. – *J. of Afr. Earth Sci.*, 13, 41-156
- Taylor, S.R. and McLennan, S.M., 1985. *The Continental Crust: Its Composition and Evolution*. Blackwell Scientific Publications, Palo Alto, CA. 328 pp
- Thiemens, M.M. Shaheen, R., Gyollai, I. Chong, K., Popp, F., Koeberl, C., Thiemens, -M.H., Moynier, F., 2014. Zn, C, and O Isotopic Variations Associated with Neoproterozoic Marinoan Glaciations. submitted to *Precamb. Res.*
- Tribovillard, N., Algeo, J.T., Lyons, T. and Riboulleau, A., 2006. Trace metals as paleoredox and paleoproductivity proxies: An update. *Chem. Geol.*, 232, 12–32.
- Veizer, J., 1983. Chemical diagenesis of carbonates: Theory and application of trace element technique. - In: Arthur et al (Eds.), *Stable Isotopes in Sedimentary Geology*. Society of Economic Paleontologists and Mineralogists, Short Course, 10/3-1, 3-100.
- Vincent, W.F. and Howard-Williams, C., 2000. Life on Snowball Earth. *Science* 287, 2421–2421
- Wedepohl, K.H, 1969. Composition and abundance of common sedimentary rocks, Chapter 8, In: *handbook of geochemistry*, Vol. 1. Geol. Surv. Prof. Pap., 1969, 250-271.



## 8 RECAPITULATION

Three research projects, which were performed as a part of the PhD studies at the Department of Lithospheric Research, University of Vienna, allowed to further improve our understanding deglaciation of Neoproterozoic Snowball Earth and improve further research ideas both of search for impact signatures and paleoenvironmental reconstruction of microbial aspect.

### ***Topic 1 Search for extraterrestrial signature in Cryogenic transition layer as signature of meteorite impact.***

Detailed mineralogical and geochemical studies were utilized to find mineralogical (shock induced deformation in minerals, high pressure phases, meteorite mineral fragments (Cr spinels), tektites and geochemical signatures (Cr, Co, Ni, Au, Ir enrichment, Cr isotopic anomaly). The investigated samples were highly diluted in carbonate, hence detrital components occur as minor components (mainly mica and feldspar), the samples consist of mostly authigenic minerals (dolomite, calcite, diagenetic quartz). The impact marker mineral can be altered to clay minerals (smectite chlorite, rectorite – which occur in the investigated material), but these are unable to confirm impact event. Neither separated clay fraction does not show geochemical signature for meteorite impact, nor separated minerals contains mineralogical signature for meteorite impact for both of Sturtian and Marinoan postglacial transition layer. However, the weathering of meteorite minerals is a rapid process in marine environment, hence the geochemical signatures can be changed due to diagenesis and weathering. Hence, later it is advisable to collect samples from continental paleoenvironment of outcrops Sturtian and Marinoan postglacial transition layers, where the possible meteorite impact signature are better preserved, and more detrital minerals would be selected from material driven to better chance to find mineralogical signature for meteorite impact.

### ***Topic 2: Biomineralization:***

- Raman spectroscopy was introduced as a new identifying method of biomarkers (trace of hydrocarbons) in biogenic structures. The microbial structures can be proofed by morphology of microbial structures (petrographic studies), enrichment of biogenic elements (Zn, Fe, Rb, Cr, Co, Ni, U, K), and negative  $\delta^{13}\text{C}$  excursions.

Geomicrobiology is a powerful tool for paleoenvironmental reconstruction, which correlates well with geochemistry interpretation. Presence of iron oxidizing bacteria suggests suboxic

conditions in brackish shallow water environment, which correlates well with paleoredox proxies.

- The clay minerals in biogenic structures identify paleoredox condition during the diagenesis. Presence of smectite in biomineralized structures suggests suboxic condition during the diagenesis.

- The biomats of iron-oxidizing bacteria can be classified to 1) primary, synsedimentary microbial layers (nutrient source: hydrothermal vents) (Sturtian Chuos/Rasthof boundary: C13 – Sesfontain-Opuwo, C12 - Steilrandberge, Marinoan basal Maieberg Fm.: K4-1 – Entrance to the South Valley, C1 -Fransfontain) secondary, weathering products (source: iron-bearing minerals: pyrite, chlorite) (Marinoan basal Maieberg Fm.: C2a -Naraachamspos, K2-1-2 -Warmquelle), 3) pseudosecondary, bacterial growth, encrusting on clasts (Marinoan: C14a, oncoids, and ooids (Sturtian: C8 – basal Rasthof Fm., Copper Mine.

- The sedimentation time synsedimentary biomats can be calculated by taking account of life cycle (up 1 day to 3 weeks) of neutrophilic photosynthetic iron-oxidizing bacteria and length of day (22 hrs) and year (400 days) of earth historic time. After extrapolation of studied 200 µm section, the whole Sturtian postglacial transition layer (1.45 m) contains 7250 laminae. The sedimentation time estimated up 18 yrs (7250 days) to 381 yrs (152, 200 days). The synsedimentary iron biomats formed during initial phase of deglaciation, hence calculated time of sedimentation rate postulates duration of initial state of deglaciation of Sturtian Snowball Earth: melting of floating ice.

### ***Topic 3 Paleoenvironmental reconstruction***

- Zn isotopic variations suggests hydrothermal alteration for Marinoan postglacial transition layer, which slightly modified by microbial alteration.

- Cathodoluminescence microscopy is powerful tool to study of different carbonate cement generations, and to distinguish from primary carbonate conditions, and estimate local paleoredox condition, incorporating elements in crystal structure ( $\text{Fe}^{2+}$ : quencher,  $\text{Mn}^{2+}$ : activator), as well as source area of minerals (non-luminescent quartz has authigenic origin) by investigating cathodoluminescence color.

- The minor role of detrital mineral and major role of authigenic minerals suggests a hard Snowball Earth (completely frozen oceans with lack of fluvial input). The occurrence of detrital minerals for Sturtian Copper Mine (mica, chlorite, feldspar, quartz), and Marinoan Naraachampos (mica, feldspar) locations suggests this locations might be near to glacier flow from continental area.

- The geochemical proxies imply that Marinoan postglacial transition layers are affected by diagenesis and weathering, whereas Sturtian transition layers are least altered by diagenesis

and weathering. The Marinoan postglacial transition layers (C3: Naraachamspos, C4: Tweelingskop) are altered by early diagenetic texture (infiltration, synsedimentary tectonics, coarse, rapid calcite cement flow.)

- Several outcrops of Marinoan basal Maieberg formation were affected by tectonic events (mylonite from Warmquelle – C16 samples, sigmaclasts around the pyrite –Profile C2a, Naraachamspos.



## 9 Appendix 1: Mineralogy tables

### 9.1 Sturtian

**Table 1.** Mineralogical composition and sedimentary petrology of Copper Mine profile

Stratigraphic setting	Sample	Lithology	Mineralogical composition	Microbial structure
Rasthof Fm.	S6/4	Variable texture (mudstone-grainstone)	80wt% carbonate (several blocky cement), 15wt% feldspar with variable weathering rate (fresh, with mechanical twins; zoitized; strongly weathered to kaolinite and sericite), 2wt% hematite pseudomorphosed after pyrite.	Organosedimentation: ooids, peloids
	S6/3a	Wackestone, with variable grainsize of carbonate (micritic, blocky-mechanical twins) and quartz (fine-grained: probably diagenetic, pebbles: detrital (?) origin; large wormy-intergrowth).	Mineral composition: 70wt% carbonate, 15% quartz, 10wt% mica and clay minerals, 5wt% feldspar (weathered: zoisite and kaolinite inclusions).	
	S6/3	Mudstone-wackestone	80% carbonate (fine grains and large aggregates), 10% quartz (euhedral), 10% fresh and weathered (zoitized) kalifeldspars	Calcification bacteria (fan like structures, circular structure 800 µm) Green algae
	S6/2	Dolomite Block cement in cavities	95wt% carbonate (mostly micritic, but blocky near to large euhedral quartz aggregates), 5wt% mica (1 large grain with detrital origin, sericite derived by diagenetic alteration) and clay minerals	Calcification bacteria (few ooid, zoned growth 100-200 µm) Green algae (dark elongated striated particles)
	S6/ 1b	Mudstone (1 layer wackestone, redeposited, large carbonate grain), block cement in cavities	dolomite	no

Stratigraphic setting	Sample	Lithology	Mineralogical composition	Microbial structure
	S6/1a	wackestone	70wt% carbonate (micritic, large grains), 25% quartz (fine euhedral; large wormy-intergrowth; large euhedral) 5% mica, clay minerals	Circle-like structures (100 µm) with aragonite pseudomorph Eosphere
Rasthof Fm. Basal region	C8	Oolitic sandstone Cement: micrite, clay cement around ooids Early organosedimentation: peloids, oncoids Centre of oncoids: kalifeldspar, mica, carbonate clasts	carbonate: 75wt%, mica: 8wt%, kalifeldspar: 7wt% quartz: 10wt%, 5wt% clay, iron-oxide, zircon, barite	Calcification bacterial communities around ooids and oncoids
Chuoss/Rasthof boundary	C9	Carbonate-quartzite silt -climbing cross-lamination (iron oxide) , plane lamination -Cement: micrite, iron-oxide; sericite among quartz grains	Carbonate: 70wt%, iron-oxide: 15wt%, quartz: 10wt%, mica: 5wt%; Quartz appears as elongated microcrystalline form. Among the microcrystalline quartz, feldspar and kinked mica assemblages occur.	no
Chuoss Fm. (top region)	C10_2	-Sandstone, -segregated terrestrial components in mudstone with later fluidization related mixing influence	Carbonate: 40-70wt%, Quartz: 10-20wt%, iron-oxide: 10%, mica (sericite), chlorite: 5-9wt%, clay: 6wt%, feldspar: 5wt%	-Raspberry structures of bacteria in recrystallized quartz -thready iron-bacteria in iron oxide
	C10_1	iron-oxide formed by weathering of feldspar -Euhedral quartz started recrystallize Green-sheet facies metamorphosis		

**Table 2.** Mineralogical composition and sedimentary petrology of Sturtian transition layers from Sesfontain-Opuwo and Steilrandberge.

Stratigraphic setting	Sample	Location	Lithology	Mineral composition	Microbial structures
<b>Basal Rasthof Fm.</b>	<b>C13c</b>	Sesfontain-Opuwo	Fe-rich microbialite Strong weathering of biogenic structures (smectite)	70 wt.% dolomite 30 wt.% clay (smectite), goethite, hematite, quartz	filamentous (tubular) forms unnamed colonial coccoid cells, and spherical unicells
<b>Chuoss/Rasthof Fm. boundary</b>	<b>C12</b>	Steilrandberge	silt Fe-rich microbialite	70 wt.% goethite, hematite, 20 wt.% quartz, 10 wt.% clay (smectite)	filamentous (tubular) forms sheath-enclosed colonial unicells
	<b>C13b 2</b>	Sesfontain-Opuwo	Fe-rich microbialite	60-70 wt.% goethite, hematite, 5-10 wt.% dolomite, 15 wt.% quartz, 10 wt.% mica, clay (smectite)	filamentous (tubular) forms unnamed colonial coccoid cells, diatomae (Navicula), filamentous cyanobacteria
	<b>C13b 1</b>				
<b>Chuoss Fm. (top)</b>	<b>C13a 2</b>		Fe-rich microbialite	50-60 wt.% goethite, hematite, 20-30 wt.% dolomite, 10 wt.% quartz, 5-10 wt.% mica, 5 wt.% clay (smectite)	filamentous (tubular) forms unnamed colonial coccoid cells, sheath-enclosed colonial unicells

**Table 3.** Magnetic separation data of Sturtian transition layers.

	<b>0.2A</b>	<b>0.4 A</b>	<b>0.8 A</b>	<b>1.2 A</b>	<b>rest</b>
<b>C8 300- 160µm Cap car- bonate (Copper Mine)</b>	90wt% hematite 5wt% siderite 3wt% muscovite 2wt% Q	hematite	50wt% hematitized carbonate 50wt% non- hematitized car- bonate	Hematitized carbonate	50wt% Q 50wt% car- bonate
<b>C9 300-160 Boundary (Copper Mine)</b>	Carbonate fil- tered with ionic solution (hema- tite, limonite, pyrite) With more ionic component	Carbonate filtered with ionic solution (hematite, limonite, py- rite)	Carbonate filtered with ionic solution (hematite, limonite, pyrite)	Pigmented carbonate	Carbonate
<b>C10_1 300-160 µm Diamictite (Copper Mine)</b>	Layered pyrite in carbonate	Layered pyrite in carbonate 10% pebbles from pyrite- carbonate- hematite- quartz	80wt% hematitized carbonate 20wt% normal car- bonate	Carbonate 1wt% hem- atite	Carbonate
<b>C12 300-160 Boundary (Steilrand berge)</b>	Hematite magnetite	Hematite limonite	80wt% hematitized carbonate 19% pyrite 1% Q	Ironic car- bonate with iron-pyrite infiltration Pyrite 5% Q 1%	80wt% hematitized carbonate 15 % Q and muscovite 5% pyrite

*After magnetic separation, the minerals were separated under binocular microscope*

<i>Copper Mine</i>	91wt% carbonate, 5wt% quartz, 1wt% hematite, 1wt% pyrite, 1wt% mica
<b>C10_2 160-63 µm (diamictite) :</b>	
<i>Sesfontain-Opuwo Rd</i>	85wt% iron-oxide, 10wt% pyrite, 4wt% car- bonate, 1wt% quartz, <1wt% chlorite
<b>C13a 160-63 µm (diamictite) :</b>	
<b>C13b (300-160) (boundary) :</b>	90wt% iron-oxide, 5wt% pyrite, 4wt% ionic car- bonate, 1wt% quartz
<b>C13c (160-63µm) (basal cap carbonate):</b>	48wt% carbonate, 40wt% diagenetic quartz, 10wt% pyrite, 2wt% hematite

## 9.2 Marinoan

**Table 4.** Mineralogical composition and sedimentary petrology of Marinoan postglacial transition layers.

Stratigraphic setting	Sample	Locality	Lithology	Mineral composition	Microbial structures
<b>Maieberg Fm. Keilberg Mb - profile</b>	<b>K4-3</b>	Entrance of South Valley	Kinked terrestrial layer interbedding in dolomite Tectonic overprint (wurst-like detritus layers, sigmaclasts: shearing tectonics Clay lenses: alteration of original biomats	90wt% dolomite 10wt% clay	filamentous iron bacteria- (colonial coccoid cells, sheath-enclosed colonial unicells and spherical unicells) K4-1 well preserved, K4-2 weathered, progressive weathering of biogenic structures to clay minerals in Profile K4
	<b>K4-2</b>		Terrestrial layer: wavy lamination (locally broken)	90wt% dolomite 10wt% clay, mica, quartz	
	<b>K4-1</b>		Micritic dolomite with detrital layers Cement: calcite, quartz Under terrestrial layer carbonate shows flow structure, above the terrestrial layer unstratified carbonate Diagenetic overprint Biomats along fractures and parallel to bedding in quartz and carbonates	80wt% dolomite (amoeboid, penetrated shape) 15wt% hematite and limonite 5wt% quartz, calcite (more set 1µm thin and with 1µm distance lamellae set) and mica (kink-bands)	
	<b>K2-2</b>	Warmquelle/Ongongo	Dolomite with fine-grained well-stratified structure Fluidization structures (flame and ball structures) Diagenetic overprint	90wt% dolomite 10wt% hematite, clay mineral, pyrite (microbial, from sulfate reduction), mica Calcite (block cement)	1. primary structures: filamentous iron bacteria (coccoidal spherical colonial cells) 2. secondary structures along fractures. (2. bio-weathering columnar iron-rich phosphorous collophane (?))
	<b>K2-1</b>				Weathered (smectitized) secondary microbial mat in iron rich layer and diagenetic quartz (filamentous cyanobacteria iron bacteria (coccoidal colonial cells),

Stratigraphic setting	Sample	Locality	Lithology	Mineral composition	Microbial structures
Basal Maieberg Fm. – Keilberg Mb.	C17c	Naraachampos, Pip` Rock a` vis	silt, mud, clay intervals, terrestrial blocks -Sedimentary structures: plane bedding, fluidization mixing, loading structure Facies: "slope" basin: ritmithic bedding Cement: iron oxide	clay 40wt%, carbonate 35wt%, quartz 5wt%, mica 15wt% iron-oxide 5wt%	-
	C15d	Kho-warib Valley	silty mudstone with iron-oxide strata, loading, mixing <u>Sedimentary structures</u> : sediment dike infiltration; Mixing and loading structure Facies: Restricted platform	clay: 40wt%, mica: 30wt%, iron-oxide: 20wt%, carbonate: 10wt%	-
	C15a		Mudstone, banded cap dolomite <u>Sedimentary structures</u> : plane-bedding, ball-structure as signature of fluidization-related mixing Facies: Open platform	carbonate: 80wt%, iron-oxide: 10wt%, mica: 10wt%	-
	C14e	Entrance of South Valley	fine grainstone with silty strata and some extraclasts <u>Sedimentary structures</u> : loading structures involved by fluidization Facies: open platform Cement: sericite, micrite	carbonate: 70wt%, quartz: 15wt%, mica: 10wt%, clay: 5wt%	Organosedimentation
C7	Bethanis	Carbonate Green-sheet facies metamorphosed <u>Sedimentary structures</u> : fine plane lamination of carbonate layers, climbing lamination in iron oxide containing terrestrial layer. Cement: sericite, micrite Facies: Slope/ deep shelf margin	carbonate: 80wt%, quartz: 15wt%, mica: 5wt%	oscillatorian cyanobacteria secondary biomat of filamentous iron bacteria (colonial coccoid and spheroid cells) diatomae	
C1a	Fransfontain	Dolomite 30 cm above the boundary			synsedimentary filamentous iron bacteria

Stratigraphic setting	Sample	Locality	Lithology	Mineral composition	Microbial structures
Ghaub/Maieberg Fm. (boundary)	C16c	Warm- quelle/O n-gongo	Opalized layer in milonite, silty mud- stone with terrestrial strata, but diagenetic overprint fluidization) <u>Sedimentary struc- tures:</u> infiltration, <u>Facies:</u> Open platform, <u>Cement:</u> sericite, zoned quartz	carbonate: 15wt%, quartz: 10wt%, mica: 20wt%, clay: 50wt%, iron- oxide: 5wt%	-
	C16b		Basal zone of milonite fine grainstone with thin terrestrial layers <u>Mineral composition:</u> carbonate: 80%, iron- oxide: 10%, quartz: 5%, mica: 5% <u>Sedi- mentary structures:</u> plane bed; wavy lami- nation; convolution, <u>Facies:</u> Open platform <u>Cement:</u> micrite	carbonate: 80wt%, iron- oxide: 10wt%, quartz: 5wt%, mica: 5wt%	-
	C16a		Sericitized layer in milonite		-
	C15e	Kho- warib Valley	-mudstone with terres- trial strata <u>Sedimentary struc- tures:</u> loading and mixing structure; plane bedding; ripple lamina- tion; wurst structure <u>Facies:</u> Open platform <u>Cement:</u> stalactite cement, fine-grained iron-oxide, stalactite- cement, block-cement	carbonate: 50wt%, Clay: 30wt%, iron- oxide: 10wt%, quartz: 10wt%	Organosedimentation
C15c		Red clay			-
C15b		Brecciated, red			-
C14d	En- trance of South Valley	silty mudstone with resedimentation of terrestrial strata (de- bris flow), <u>Facies:</u> Plat- form/land, <u>Cement:</u> micrite, calcite block cement, mica, <u>Sedi- mentary structures:</u> syndimentary listric faults, microfolds, rip- ple lamination	quartz: 30wt%, iron- oxide: 30wt%, mica: 10wt%, clay: 10wt%, car- bonate: 10wt%	-	

Stratigraphic setting	Sample	Locality	Lithology	Mineral composition	Microbial structures
Ghaub/ Maieberg	C17b	Naraachams-			-
	C3_2	pos Pip`s Rock in situ	wackestone/silt - slump structure with exotic blocks <u>Cement:</u> Iron-oxide growth on exotic blocks <u>Facies:</u> slope/ fore slope: instable sedi- mentation of debris	carbonate: 50wt%, mica: 19wt%, clay: 16wt%, iron- oxide: 7wt%, quartz: 5wt% feldspar: 3wt%	Organosedimentation
	C3_1		resedimented silt- stone/shale with exotic terrigenous blocks (quartzarenite) mixing structure, micro faults <u>Cement:</u> ironoxide growth on exotic blocks	Carbonate: 50wt%, Clay: 25wt%, iron- oxide: 15wt%, mica: 5wt%, quartz: 3wt% (xenomor- phic, symplectitic), feldspar: 2wt%	Organosedimentation
	C2c		Slope facies		-
	C2b		Slope facies		-
	C2a		coarse diamictite interbedding in mud- stone plane lamination of diamictite layers _wurst deformation in of diamictite layers Slope facies	carbonate: 60wt%, feld- spar: 20wt%, quartz: 10wt%, mica: 5wt%, chlo- rite: 3wt%, clay: 2wt%	-
	C1c	Frans- fontain	Slope fine grainstone interbedding of terrigenous strata (silt, quartzarenite) Ripple-lamination (quartz strata), angular cross lamination (iron- oxide and clay strata)	70wt%, quartz: 10wt%, mica: 5wt%, iron oxide: 5wt%, clay: 5wt%, feldspar: 2wt%, chlo- rite (kinked); 2wt%, zircon: 1wt%	oscillatorian cyanobacteria (large number) filamentous iron bacteria (colonial coccoid cells and spherical unicells)

Stratigraphic setting	Sample	Locality	Lithology	Mineral composition	Microbial structures
Ghaub/Maieberg	C1b	Fransfontain	Slope fine-grained grainstone with extraclasts	Carbonate: 80wt%, Quartz: 10wt%, iron-oxide: 5wt%, mica: 3wt%, clay: 1, 5wt%, feldspar: 0.5wt%, few grains in clasts	filamentous iron bacteria (coccolidal unicells) diatomae
Ghaub Fm.	C17a	Naraachampspos	Tectonic silt 5cm below the boundary Slope facies		-
	C14c	Entrance	Tectonized clay Platform facies		-
	C14a	of South Valley	Top of red diamictite Platform facies debris flow with large carbonate blocks and with mica among the blocks  <u>Cement</u> : micrite iron-oxide	Carbonate: 50wt% iron-oxide: 30wt%, clay: 10wt%, mica: 5wt%, quartz: 5wt%	Filamentous iron bacteria at the boundary of clasts
	C6	Bethanis	Red silt Slope facies mixing of micrite and wackestone, fluidization  <u>Sedimentary structures</u> : interrupted plane bedding (wurst deformation of iron-oxide strata) <u>Facies</u> : slope/ fore slope In-stable sedimentation of debris, <u>Cement</u> : micrite	carbonate: 60wt%, iron-oxide: 15wt%, mica: 10wt%, clay: 10wt%, quartz: 5wt%	-
	C5	Tweelingskop	Top of Åoleanit, slope facies, <u>Cement</u> : calcite block cement, quartz cement	carbonate: 45wt%, quartz: 45wt%, mica:	-

Stratigraphic setting	Sample	Locality	Lithology	Mineral composition	Microbial structures
Ombaatjie Fm.	C4	Tweelin gskopkop	Red dolomite silty shale blocks, lenses in wackestone (wackestone contains detrital minerals), fluidization slump structure, <u>Facies:</u> slope/fore slope: instable sedimentation of debris <u>Cement:</u> clay/sericite cement, mud cement (dolomite), stalactite cement (calcite)	diagenetic reworking 10wt% carbonate: 80wt%, mica (sericite): 15wt%, quartz: 5wt%	Organosedimentation

**Table 5.** Mineralogical composition and sedimentary petrology of Marinoan cap carbonate profile from Naraachamspos.

Sample name	Stratigraphic setting	Lithology	Mineral composition	Microbial structures
<b>C2a-7</b>	Maieberg Fm. Keilberg Mb	-Carbonate -Ball and flame structure – fluidization Pyrite-quartz-clay sigmaclasts	80wt% carbonate 10wt% pyrite (zoned) 10wt% quartz (diagenetic), clay and iron oxide (derived from weathering of pyrite)	Weathered, filamentous iron bacteria- (colonial coccoid cells, sheath-enclosed colonial unicells and spherical unicells) diatomae
<b>C2a-6</b>		Flow structure with diagenetic quartz and carbonate rich layer Sigmaclasts of pyrite and quartz	30-70wt% carbonate 30-50wt% quartz (diagenetic, worm-growth) 10-25wt% pyrite (zoned, framboidal (sulfate reducing bacteria) and cubic (metamorphic))	Moderate weathering coccoid-forming biomat of iron bacteria Filamentous cyanobacteria diatomae
<b>C2a-5</b>		Carbonate with pyrite-quartz sigmaclasts – metamorphic overprint Wavy lamination of iron-including and carbonate layers	5-10wt% clay and mica	Weathered filamentous iron bacteria- (colonial coccoid cells, sheath-enclosed colonial unicells and spherical unicells) (main occurrence in iron-pyrite -Q lens, but in surrounding carbonate
<b>C2a-4</b>				black and red filamentous iron bacteria- (colonial coccoid cells, sheath-enclosed colonial unicells and spherical unicells) in pyrite lens (low weathering rate)
<b>C2a-3</b>	Ghaub/Maieberg Fm.	Micritic carbonate, thin terrestrial layer interbedding	70-80wt% carbonate (micritic; and coarse grain in detritus) 20-30w% kalifeldspar (zoisitized, twinned, break down to clay kaolinite), quartz	-
<b>C2a-2</b>	Ghaub Fm. (top)	-Coarse terrestrial layers in carbonate		-
<b>C2a-1</b>		-micritic-coarse carbonate rhythmic bedding		-

**Table 6.** Mineralogical composition and sedimentary petrology of Marinoan cap carbonate profile from Khowarib Valley.

Sample name	Lithology	Mineral composition	microbial signatures
P49-5	Unstratified micritic carbonate stylolith	dolomite	presence of calcimicrobae and cyanobacteria
P49-4	Unstratified micritic carbonate with coarse bed	Carbonate (with fluid inclusions)	
P49-3	Unstratified dolomite clay: wavy lamination	99% dolomite (dark fluid inclusions) 1% clay, hematite	
P49-2	Unstratified dolomite Pressure solution	Dolomite(decorated twins)	
P49-1	mudstone Bottom part: fine laminated colloform outwashed texture (clay-iron-oxide rich) 1. Unstratified dolomite with mica	95% carbonate 5% iron-oxide, clay, mica	

**Table 7.** Magnetic separation data of Marinoan transition layers.

	0.2A	0.4 A	0.8 A	1.2 A	rest
<b>C2a-1</b> <b>300-160 µm</b> <b>(Naraachamspos, Boundary layer)</b>	30wt% pyrite 70wt% Q with pyrite	50wt% pyrite 50wt% Q	Carbonate with pyrite Carbonate with hematite Q (20wt%)	Hematitized carbonate	50wt% Carbonate (partly hematitized) 50wt% Q
<b>C2b</b> <b>300-160 µm</b> <b>Naraachamspos, Boundary layer)</b>	Pyrite, magnetite	Limonite, hematite	50wt% Q 50wt% hematitized carbonate	95wt% hematitized carbonate with pyrite 4% Q 1% pyrite	50wt% Q 50wt% hematitized carbonate
<b>C3_1</b> <b>(160-63 µm)</b> <b>Naraachamspos, boundary layer)</b>	80wt% Pyrite 20wt% Muscovite Carbonate Q	90wt% pyrite 10wt% carbonate, hematite	40wt% carbonate 40wt% pyrite 10wt% Q Hematite, muscovite	Locally hematitized carbonate 1wt% Q	95wt% carbonate 5wt% quartz
<b>C3_1</b> <b>(300-160 µm)</b> <b>Naraachamspos, boundary layer)</b>	95wt% pyrite 4wt% magnetite 1wt% quartz	90wt% pyrite 10% carbonate, Q, hematite	Pyritized carbonate pyrite	Layered carbonate with hematite	98wt% carbonate 2% Q

	<b>0.2A</b>	<b>0.4 A</b>	<b>0.8 A</b>	<b>1.2 A</b>	<b>rest</b>
<b>C3_2</b> <b>300-160µm</b> <b>Naraachamspos,</b> <b>boundary layer</b>	Pyrite 10wt% quartz carbonate	90wt% pyrite 10wt% car- bonate	Pyritized car- bonate pyrite	Carbonate with more pyrite limonite	Pyritized carbonate – layered
<b>C5 bright</b> <b>300-160 µm</b> <b>Tweelingskop,</b> <b>Top of Äolianit</b> <b>/Ghaub eq.</b>	30wt% magnetite 30wt% pyrite 30wt% hematite 9wt% Q	90wt% iron- oxide 10wt% Q and green mica (chlorite) <1% spar- kling black particles	80wt% pyritized car- bonate 15wt% Q	80wt% pyritized car- bonate and pyrite 20wt% quartz	98wt% Q 2wt% hema- tite
<b>C5 dark</b> <b>300-160 µm</b> <b>Tweelingskop,</b> <b>Top of Äolianit</b> <b>/Ghaub eq.</b>	Magnetite hematite	95wt% hematite 4wt% mag- netite and pyrite 1wt% Q and mica	Hematite Limonite quartz	Pyritized car- bonate 5wt% Q	50wt% Q 50wt% hematitized carbonate
<b>C6</b> <b>(300-160 µm)</b> <b>Bethanis, boundary</b>	Magnetite Siderite Carbonate with iron- oxide	Limonite Quartz Pyrite	Siderite Hematitized dolomite Few quartz	Carbonate hematite	0.5wt% mica 1-2wt% prim Q 97wt% diagenetic Q, Carbonate
<b>C7</b> <b>300-160 µm</b> <b>Green-sheet f.</b> <b>Bethanis, basal cap</b> <b>carbonate</b>	magnetite	Chlorite Q hematite	Q Magnetite muscovite	80wt% car- bonate 15wt% Q 5wt% musco- vite	70wt% Q (60wt% pri- mary) 30wt% car- bonate
<b>C14a</b> <b>300-160 µm</b> <b>Entrance of South</b> <b>Valley. Top of red</b> <b>diamictite</b>	Pyrite limonite	70% limonite 20% Q <1% pyrite	Limonite and Q	70wt% car- bonate 18wt% Q 2wt% pyrite and limonite	70wt% car- bonate 30% Q
<b>C14d</b> <b>300-160 µm</b> <b>Entrance of South</b> <b>Valley.</b> <b>boundary</b>	Hematite pyrite	60% siderite 30% hema- tite 10% Q with hematite	80 % siderite 20%quartz	85% car- bonate with hematite 15 % diagenetic quartz	85% car- bonate 15% quartz diagenetic
<b>C14e</b> <b>300-160 µm</b> <b>Entrance of South</b> <b>Valley.</b> <b>Basal cap car- bonate</b>	Limonite- magnetite	Limonite, Q	Hematitized carbonate and Q grains	90wt% car- bonate 10wt% hema- tite and diagenetic Q	30wt% diagenetic Q with hematite 70wt% car- bonate
	<b>0.2A</b>	<b>0.4 A</b>	<b>0.8 A</b>	<b>1.2 A</b>	<b>rest</b>

<b>C15b</b> <b>300-160 µm</b> <b>Khovarib Valley,</b> <b>boundary</b>	Pyrite magnetite	30wt% pyrite 30wt% limo- nite 30wt% car- bonate	70wt% Peb- bles from hematite- pyrite- carbonate layers 30wt% diagenetic Q <1wt% pyrite	Hematitized carbonate	50wt% hematitized carbonate 50wt% quartz
<b>C17a</b> <b>300-160 µm</b> <b>Naraachamspos,</b> <b>diamictite</b>	95wt% pyrite 5wt% car- bonate	80wt% pyrite 10wt% Q 2wt% car- bonate Hematitized pyrite	Carbonate with pyrite 10wt% diagenetic quartz	carbonate	99wt% car- bonate 1wt% Q
<b>C17c</b> <b>300-160 µm</b> <b>Naraachamspos,</b> <b>boundary</b>		Magnetite Hematite carbonate	Hematite carbonate	95wt% car- bonate 5wt% hema- tite	90wt% car- bonate 10wt% Q

After magnetic separation, the mineral fractions were separated under binocular microscope:

*Fransfontain*

**C1a 160-63 µm (basal dolomite):** 50wt% carbonate, 48wt% quartz, 2wt% pyrite  
**C1b 160-63µm (boundary) :** 50wt% carbonate, 49wt% quartz, 1wt% pyrite

*Naraachamspos*

**C2c 160-63 µm (boundary)** 50wt% carbonate, 50wt% quartz, <1wt% hematite, pyrite  
**C2c 300-160 µm (boundary)** 99wt% carbonate, 1wt% pyrite, iron-oxide  
**C17b 160-63µm (top of diamictite** 97wt% carbonate, 1wt% pyrite, 1wt% hematite,  
**C17c 160-63µm (boundary) :** 89wt% carbonate, 5wt% pyrite, ) <1wt% mica and quartz  
5wt% quartz, 1wt% hematite

*Tweelingskop*

**C4 160-63 µm (platform carbonate** 45wt% quartz, 45wt% carbonate, 4wt% pyrite (framboidal),  
**(Ombaatjie Fm.):** 1wt% hematite

*Entrance of South Valley*

**C14b 160-63µm (transition layer):** 80wt% carbonate, 7wt% quartz, 2wt% iron-oxide, 1wt% pyrite

*Khovarib Valley*

**C15e 300-160 µm (boundary):** 45wt% pyrite 45wt% quartz, 9wt% carbonate, 1wt% iron-oxide

*Warmquelle*

*C16: tectonized layer*

**C16b 160-63 µm (boundary):** 10wt% pyrite, 1wt% mica (chlorite) 88wt% Q, 1wt% hematite

**C16c 160-63µm (basal cap carbonate):** 97wt% carbonate, 1wt% hematite, 1wt% Q, 1wt% pyrite

### 9.3 Raman spectroscopy results

**Table 8.** Raman shifts of calcites in K4 and K2 samples.

standard Raman shift $\text{cm}^{-1}$	mechanical twins (K4-1 sample)	dense mechanical twins (K2-1 sample)	dense mechanical twins (K4-1 sample)	between twin lamellae (K2-1 sample)
152	157			157
278	280	280	280	278
712				711
1086	1084	1084	1084	1086

**Table 9.** Raman shifts of dolomite in K2 and K4 samples.

1. standard (Raman shifts in $\text{cm}^{-1}$ )	2. dolomite with mechanical twins	3. dolomite with inclusions
174	176	174
299	299	297
720	725	
1096	1098	1096

**Table 10.** Raman shifts of quartz and dolomite in K2-1 and K4-1 samples

standard 1 dolomite (Raman shift in $\text{cm}^{-1}$ )	standard2 quartz (Raman shift $\text{cm}^{-1}$ )	spectrum 1. quartz in iron-oxide rich layer (K4-1 sample)	spectrum 2. quartz in vein (K2-1 sample)	spectrum 3. quartz with inclusion (K4-1 sample)
	124	126	126	126
176				175
	204	207	202 256	204
299				299
	357	353	355	
	392		391 399	
	462	462 601	463	462
724				724
1099				1097

**Table 11.** Raman shifts of quartz in Sturtian (C10, C13) and Marinoan transition layers (C4) and vibrations (Vib).

Vib	References				Samples										
	standards (RUFF database)				C4 sample		C10_1		C13a1 deflam		C13a1 detriens		c13b2 sympl		
					Pea k	FW HM	Pea k	FW HM	Pea k	FW HM	Pea k	FW HM	Pea k	FW HM	
<b>A1</b>	194	239	219	207	202	25	207	23	207	21	203.	22	205	14	
											5				
	355.0	339	358	356	351	8	353	7	356	8	355	9	355	10	
	460.	462	469	464	463	8	466	11	466	11	466	12	465	12	
	1123.	1061	1082	1085											
<b>ET</b>	121	133	133	128	128	7	130	9	130	10	129	8	130	4	
	257	261	269	265	266	8	264	8	264	7	264	7	-		
	390	378	393	394	-		-		395		-		394		
	703.3	690.8	698	697	-		698	3	695	8	697	5	695	9	
	810	792	799	795	-		-		795	9	-		-		
	1109	1045	1066	1072	-		-		1066	11	-		-		
	1191	1128	1158	1162	1159	7	1159	14	1160	9	1160	13	1160	12	
<b>EL</b>	399	389	402	401	401	12	401	11	-		399	18	-		
	824	804	812	807	-		806	8	-		806	9	807	5	

**Table 2.** Raman vibrations of quartz of Sturtian and Marinoan transition layers.

standard	Q in C4	C10_1 PF Q	C13a1 deflam	C13a1 detrlens	c13b2 symp1	Vibration
128	130	130	130	129.2	129.8	ET
207	202	207	207	203.5	204.8	A1
265	266	264	264	264		ET
353	351	353	356	355	355.4	A1
394			395		393.7	ET
398.6				399		EL
401	401	401		399		EL
464	463.3	465.5	465.5	465.6	465	A1
697		698	695	697	695	ET
795			795.5			ET
807		805.5		806	807	EL
1066			1066.7			ET
1158	1159	1159			1159.7	ET
1162			1160.2	1160.3		ET

**Table 3.** Raman vibrations of carbonate phase in transition layers.

calcite (RUFF Database)		Dolomite (RUFF Database)		Sample cc cement (C12)		lim+cc (C12)		Dolomite stal-actite cement (C4)		Vibration type
Peak	FWHM	Peak	FWHM	Peak	FWHM	Peak	FWHM	Peak	FWHM	Herman et al 1987 Appl. Spectr. 43 437-450
155	7			157	10	153	35			Eg (ext)
		176	9					177	17	
282	13			282	13	282	30			Eg (ext)
		299	11					296	14	
712	7			711	8	713	8			v4 -Eg (int) vibration planar bending of carbonate ion
		725	20			-	-			
1085	4			1086	9	1087	13			A1g (int) internal stretching of carbonate ion
		1098	7					1097	9	

**Table 4.** Raman shifts of iron oxid phases in Sturtian boundary layers.

RUFF Data-base		RUFF Data-base		RUFF Data-base		C13b2 sample		C13b2 sample		C12 sample	
Goethite		Hematite		Lepidocrocite		Goethite (boundary of calcite cement)		Iron oxide matrix		iron oxide-carbonate micrite	
Peak	FWHM	Peak	FWHM	Peak	FWHM	Peak	FWHM	Peak	FWHM	Peak	FWHM
				148	21					150	30
				215	20					217	21
		225	11					225	7		
<b>244</b>	11	245				246	10				
<b>299</b>	12	292	15			300	13	292	16		
				279	30					278	30
<b>385</b>	25			395	36	386	27			397	38
		410	15					410	15		
<b>480</b>	22					482	26				
		499	25					500	23		
<b>548</b>	21			523	19						
						550	20			537-638	broad
				588	34						
		611	18					613	20		
		658	24	668	69			-	-		
<b>681</b>	30					679	49				
		818	32					-	-		
		958	23	910-1150	broad			957	35		
		1050	23					1050	14		
		1090	4					1090	26		
		1195	38	1170-1417	broad			1193	38		
		1267									

## **10 Appendix II: Geochemical tables of Sturtian and Marinoan samples following sampling sites**

The main element oxides are added in weight-percents, the transition and rare earth elements are measured in ppm, whereas Au and Ir are detected in ppb. The main elements of 19 samples and V, Cu, Y, Mo, Nb of "C" samples were measured with X-ray fluorescence spectroscopy, whereas Na-, K-, Fe oxides of other samples and transition elements were determined with Instrumental Neutron Activation Analysis. (Legend: Marinoan: G= Ghaub Fm., G/M= Ghaub/Maieberg boundary, M=Maieberg Fm., C=Chuosi Fm., C/R=Chuosi/Rasthof boundary, R=Rasthof Fm., n.d=no data, b.d.l=below the detection limit)

## 10.1 Major and rare earth elements

## A) Marinoan transition layers

Location Strat. setting wt. %	Fransfontain			Tweelingskop		Bethanis	
	M C1a	G/M C1b	G/M C1c	O C4	G C5	G/M C6	M C7
SiO <sub>2</sub>	<i>n.d.</i>	<i>n.d.</i>	27.5	<i>n.d.</i>	62.2	<i>n.d.</i>	<i>n.d.</i>
TiO <sub>2</sub>	<i>n.d.</i>	<i>n.d.</i>	0.43	<i>n.d.</i>	0.05	<i>n.d.</i>	<i>n.d.</i>
Al <sub>2</sub> O <sub>3</sub>	<i>n.d.</i>	<i>n.d.</i>	7.00	<i>n.d.</i>	0.37	<i>n.d.</i>	<i>n.d.</i>
Fe <sub>2</sub> O <sub>3</sub>	0.38	1.42	2.56	1.33	14.2	0.94	3.48
MnO	<i>n.d.</i>	<i>n.d.</i>	0.19	<i>n.d.</i>	0.06	<i>n.d.</i>	<i>n.d.</i>
MgO	<i>n.d.</i>	<i>n.d.</i>	22.6	<i>n.d.</i>	7.95	<i>n.d.</i>	<i>n.d.</i>
CaO	<i>n.d.</i>	<i>n.d.</i>	36.0	<i>n.d.</i>	12.7	<i>n.d.</i>	<i>n.d.</i>
Na <sub>2</sub> O	0.02	0.02	0.03	0.02	0.09	0.06	0.37
K <sub>2</sub> O	0.18	1.02	1.74	0.74	0.03	0.75	1.81
P <sub>2</sub> O <sub>5</sub>	<i>n.d.</i>	<i>n.d.</i>	0.28	<i>n.d.</i>	0.30	<i>n.d.</i>	<i>n.d.</i>
Total	-	-	99.3	-	98.0	-	-
LOI ppm	45.9	40.4	35.3	45.4	17.0	41.3	29.4
Sc	1.22	4.49	6.45	2.63	0.88	2.42	6.42
V	0.20	48.5	47.8	22.9	60.5	14.4	35.7
Cr	7.22	15.0	25.8	14.4	9.27	14.1	30.8
Co	1.32	5.43	7.20	2.14	3.50	4.03	6.82
Ni	7.13	47.1	67.7	7.11	20.9	34.3	53.9
Cu	3.9	18.6	10.1	14.9	81.8	36.4	22.1
Zn	12.7	18.1	24.2	14.1	32.8	30.3	34.8
As	2.34	13.8	10.2	3.82	99.4	8.1	4.36
Se	<0.4	0.2	<2.1	<1.5	<0.6	<0.6	<1.3
Br	0.30	0.38	0.86	0.50	0.47	2.03	2.00
Rb	4.14	26.2	49.0	23.4	3.60	21.2	58.7
Sr	73.5	69.1	96.4	62.6	50.0	96.4	286
Y	4.50	10.2	12.4	7.60	19.7	9.10	12.2
Zr	19.5	54.8	113	34.1	<21	58.7	110
Nb	0.30	2.30	5.10	1.10	b.d.l.	1.00	4.90
Mo	1.10	0.60	0.30	0.40	3.60	0.60	0.90
Sb	0.10	0.51	1.26	0.22	6.36	0.69	0.17
Cs	0.23	2.06	3.36	1.50	0.08	1.16	6.55
Ba	21.8	104	185	48.1	38.2	171	376
La	2.25	6.99	12.9	2.37	4.74	5.61	20.3
Ce	4.46	13.9	25.3	5.56	8.00	10.2	27.4
Nd	2.52	6.99	12.5	3.46	6.37	5.40	13.0
Sm	0.65	1.77	2.94	1.07	1.71	1.39	2.60
Eu	0.15	0.27	0.41	0.28	0.31	0.37	0.60
Gd	0.58	1.90	2.43	0.86	1.40	1.45	2.56
Tb	0.10	0.27	0.39	0.19	0.25	0.24	0.34
Tm	0.05	0.15	0.23	0.15	0.08	0.12	0.15
Yb	0.31	0.92	1.29	0.54	0.50	0.73	1.07
Lu	0.06	0.15	0.22	0.07	0.08	0.11	0.18
Hf	0.15	0.82	2.00	0.52	0.71	0.53	2.18
Ta	0.02	0.20	0.48	0.12	<0.01	0.14	0.53
Au (ppb)	<0.2	0.2	0.2	<0.5	<0.4	<0.2	0.1
Pb	1.40	1.40	2.30	5.80	39.2	7.50	7.30
Th	0.39	2.27	5.42	1.18	0.28	1.44	4.55
U	0.92	1.39	2.70	0.77	4.45	0.76	1.10

Location Strat. setting wt. %	Naraachamspos							
	G C2a	G/M C2b	G/M C2c	G/M C3_1	G/M C3_2	G C17a	G/M C17b	M C17c
SiO <sub>2</sub>	<i>n.d.</i>	<i>n.d.</i>	<i>n.d.</i>	<i>n.d.</i>	<i>n.d.</i>	64.0	<i>n.d.</i>	<i>n.d.</i>
TiO <sub>2</sub>	<i>n.d.</i>	<i>n.d.</i>	<i>n.d.</i>	<i>n.d.</i>	<i>n.d.</i>	0.91	<i>n.d.</i>	<i>n.d.</i>
Al <sub>2</sub> O <sub>3</sub>	<i>n.d.</i>	<i>n.d.</i>	<i>n.d.</i>	<i>n.d.</i>	<i>n.d.</i>	16.2	<i>n.d.</i>	<i>n.d.</i>
Fe <sub>2</sub> O <sub>3</sub>	1.90	2.66	1.68	3.76	14.21	2.5	2.33	2.19
MnO	<i>n.d.</i>	<i>n.d.</i>	<i>n.d.</i>	<i>n.d.</i>	<i>n.d.</i>	0.03	<i>n.d.</i>	<i>n.d.</i>
MgO	<i>n.d.</i>	<i>n.d.</i>	<i>n.d.</i>	<i>n.d.</i>	<i>n.d.</i>	4.87	<i>n.d.</i>	<i>n.d.</i>
CaO	<i>n.d.</i>	<i>n.d.</i>	<i>n.d.</i>	<i>n.d.</i>	<i>n.d.</i>	3.36	<i>n.d.</i>	<i>n.d.</i>
Na <sub>2</sub> O	0.42	0.13	0.20	0.06	0.07	0.19	0.07	0.07
K <sub>2</sub> O	1.60	2.76	1.75	6.33	7.23	6.18	5.25	3.61
P <sub>2</sub> O <sub>5</sub>	<i>n.d.</i>	<i>n.d.</i>	<i>n.d.</i>	<i>n.d.</i>	<i>n.d.</i>	0.34	<i>n.d.</i>	<i>n.d.</i>
Total	-	-	-	-	-	98.6	-	-
LOI	35.9	27.6	34.1	11.7	9.38	6.80	11.7	24.8
ppm								
Sc	8.77	10.7	7.03	22.2	24.3	19.5	13.7	11.8
V	21.7	52.2	51.0	205	231	174	191	54.2
Cr	20.2	65.4	35.4	94.1	110	191	88.5	41.4
Co	18.2	32.7	16.9	40.7	56.9	2.93	7.04	14.0
Ni	93.0	132	128	172	257	48.2	82.1	63.6
Cu	21.1	48.4	19.3	169	184	55.5	84.0	53.1
Zn	27.9	42.7	78.0	53.0	65.8	46.3	45.2	46.0
As	10.3	21.4	8.61	21.5	56.9	2.58	17.3	5.96
Se	<2.3	<2.2	<3.5	<1.8	<1.8	<1.5	<2	<1.8
Br	0.53	0.51	0.62	<0.2	<0.6	0.14	0.77	0.51
Rb	37.6	73.3	47.7	160	180	175	160	83.1
Sr	53.0	56.4	59.8	<40	<40	<30	62.0	46.3
Y	20.3	21.5	11.4	25.1	29.8	20.4	30.5	17.2
Zr	95.4	157	85.3	267	327	226	261	146
Nb	4.70	8.00	3.80	17.2	19.0	15.1	16.4	9.30
Mo	0.50	0.30	0.30	0.50	0.60	0.20	0.50	0.50
Sb	0.61	2.02	0.71	0.57	1.88	0.49	0.74	1.49
Cs	2.84	5.69	3.71	12.9	14.7	21.4	17.8	5.40
Ba	107	173	111	303	367	331	292	203
La	16.7	27.2	16.2	52.1	63.9	53.5	51.4	28.0
Ce	31.3	52.5	30.9	117	142	98.4	95.7	45.6
Nd	14.8	21	13.3	42.1	48.8	42.5	39.2	19.4
Sm	3.69	4.99	2.61	7.67	9.31	8.40	8.51	3.86
Eu	0.70	0.88	0.60	1.12	1.35	1.20	1.15	0.79
Gd	2.78	4.76	2.10	5.79	6.41	4.71	7.57	3.45
Tb	0.58	0.67	0.34	0.79	1.04	0.62	0.92	0.42
Tm	0.29	0.29	0.19	0.41	0.51	0.35	0.53	0.24
Yb	1.90	1.98	0.98	3.02	3.78	2.24	3.63	1.63
Lu	0.24	0.27	0.14	0.52	0.63	0.38	0.55	0.23
Hf	1.56	2.77	1.62	5.36	6.31	4.70	7.46	3.10
Ta	0.31	0.69	0.32	1.46	1.71	1.27	1.80	0.75
Au (ppb)	<1.0	<1.1	<0.9	0.5	<0.9	<0.7	0.3	<0.9
Pb	6.40	12.1	27.2	7.80	9.50	4.00	4.70	31.7
Th	4.05	7.19	3.84	15.7	16.4	13.2	16.9	7.27
U	0.88	1.43	1.20	5.06	6.54	4.40	4.63	1.86

Location Strat. setting wt. %	Entrance of South Valley						
	G C14a	G/M C14b	G/M C14c	G/M C14d	G/M C14d1	G/M C14d2	M C14e
SiO <sub>2</sub>	<i>n.d.</i>	24.0	52.9	<i>n.d.</i>	<i>n.d.</i>	<i>n.d.</i>	<i>n.d.</i>
TiO <sub>2</sub>	<i>n.d.</i>	0.40	0.63	<i>n.d.</i>	<i>n.d.</i>	<i>n.d.</i>	<i>n.d.</i>
Al <sub>2</sub> O <sub>3</sub>	<i>n.d.</i>	6.93	13.5	<i>n.d.</i>	<i>n.d.</i>	<i>n.d.</i>	<i>n.d.</i>
Fe <sub>2</sub> O <sub>3</sub>	1.86	3.08	2.48	2.35	17.1	1.55	2.98
MnO	<i>n.d.</i>	0.02	<i>n.d.</i>	<i>n.d.</i>	<i>n.d.</i>	<i>n.d.</i>	<i>n.d.</i>
MgO	<i>n.d.</i>	24.2	8.52	<i>n.d.</i>	<i>n.d.</i>	<i>n.d.</i>	<i>n.d.</i>
CaO	<i>n.d.</i>	38.6	15.5	<i>n.d.</i>	<i>n.d.</i>	<i>n.d.</i>	<i>n.d.</i>
Na <sub>2</sub> O	0.04	0.22	0.16	0.09	0.03	0.09	0.04
K <sub>2</sub> O	1.53	1.81	5.11	8.65	1.64	8.89	0.50
P <sub>2</sub> O <sub>5</sub>	<i>n.d.</i>	0.24	0.24	<i>n.d.</i>	<i>n.d.</i>	<i>n.d.</i>	<i>n.d.</i>
Total	-	99.4	98.9	-	-	-	-
LOI	36.3	43.9	17.4	4.3	<i>n.d.</i>	<i>n.d.</i>	42.6
<b>ppm</b>							
Sc	6.30	1.41	11.4	22.2	4.62	20.7	2.18
V	62.0	2.7	88.2	151	<i>n.d.</i>	<i>n.d.</i>	23.7
Cr	32.4	5.08	44.8	71.3	26.2	71.7	12.2
Co	3.79	3.28	5.93	4.83	62.2	4.87	12.2
Ni	26.7	6.5	43.2	75.0	139	51.8	27.8
Cu	186	25.5	126	22.9	<i>n.d.</i>	<i>n.d.</i>	92.0
Zn	75.8	20.8	67.3	53.8	77.3	69.6	48.9
As	10.2	3.78	9.65	7.72	87.6	6.59	13.0
Se	<1.2	0.31	2.48	<4.5	13.6	<1.6	8.26
Br	0.61	0.72	0.51	0.57	0.82	<0.3	0.88
Rb	40.7	4.70	69.9	176	38.6	179	13.1
Sr	58.4	119	38.2	<48	<31	<40	52.2
Y	13.4	5.5	13.9	14.3	<i>n.d.</i>	<i>n.d.</i>	7.6
Zr	97.1	48.6	142	243	402	220	89.8
Nb	10.7	0.10	9.60	16.1	<i>n.d.</i>	<i>n.d.</i>	0.90
Mo	0.40	0.60	0.20	0.50	<i>n.d.</i>	<i>n.d.</i>	1.40
Sb	0.57	0.75	0.95	1.42	7.32	0.61	2.15
Cs	3.45	0.43	6.35	14.4	3.20	14.9	1.17
Ba	184	40.4	323	958	222	910	58.9
La	11.7	3.97	23.1	30.7	18.5	14.2	5.58
Ce	23.7	8.75	42.1	58.8	37.2	29.1	12.3
Nd	10.9	3.70	16.7	21.6	13.8	11.0	5.83
Sm	2.67	1.06	3.11	3.65	2.70	2.39	1.55
Eu	0.49	0.21	0.48	0.52	0.25	0.36	0.27
Gd	2.43	0.85	2.15	3.54	2.76	1.91	1.35
Tb	0.39	0.13	0.33	0.35	<0.03	0.27	0.19
Tm	0.19	0.17	0.27	0.30	0.09	0.20	0.22
Yb	1.21	0.45	1.44	1.71	0.57	1.65	0.68
Lu	0.19	0.07	0.26	0.29	0.11	0.31	0.12
Hf	1.33	0.23	2.73	5.85	1.72	4.99	0.46
Ta	0.32	0.05	0.57	1.17	0.32	1.16	0.09
Au	0.5	<0.3	<0.5	1.1	0.8	<0.6	0.3
Pb	5.90	8.20	8.60	15.5	<i>n.d.</i>	<i>n.d.</i>	12.7
Th	3.82	0.67	6.96	13.9	10.8	12.0	1.28
U	2.82	3.20	4.31	6.26	14.7	4.72	5.44

Location Strat. setting wt. %	Khowarib Valley					Warmquelle		
	G/M C15b	G/M C15c	M C15d	G/M C15e	M C15e1	G C16a	G/M C16b	M C16c
SiO <sub>2</sub>	31.6	28.2	55.8	<i>n.d.</i>	<i>n.d.</i>	39.0	19.3	80.7
TiO <sub>2</sub>	0.34	0.35	0.67	<i>n.d.</i>	<i>n.d.</i>	1.14	0.25	0.48
Al <sub>2</sub> O <sub>3</sub>	6.44	5.97	13.4	<i>n.d.</i>	<i>n.d.</i>	20.6	4.36	8.68
Fe <sub>2</sub> O <sub>3</sub>	1.43	1.65	3.36	2.06	0.47	7.31	2.30	2.07
MnO	<i>n.d.</i>	0.01	0.01	<i>n.d.</i>	<i>n.d.</i>	<i>n.d.</i>	0.02	<i>n.d.</i>
MgO	15.9	24.7	9.34	<i>n.d.</i>	<i>n.d.</i>	4.89	28.5	1.63
CaO	39.8	35.36	10.7	<i>n.d.</i>	<i>n.d.</i>	14.8	44.2	1.14
Na <sub>2</sub> O	0.16	0.19	0.14	0.03	0.02	0.23	0.11	0.14
K <sub>2</sub> O	2.29	1.98	5.73	3.81	0.35	8.46	0.42	3.29
P <sub>2</sub> O <sub>5</sub>	0.79	0.65	0.35	<i>n.d.</i>	<i>n.d.</i>	0.36	0.15	0.26
Total	98.8	99.0	99.5	-	-	96.9	99.7	98.4
LOI ppm	32.6	35.6	15.4	27.4	44.8	14.4	39.9	2.95
Sc	4.78	3.85	9.03	9.70	2.35	18.9	3.53	8.12
V	30.9	23.2	121	<1	82.0	245	29.2	97.2
Cr	26.9	24.6	73.7	40.0	3.42	151	25.3	59.8
Co	3.38	2.60	6.69	11.6	2.68	9.68	3.49	0.75
Ni	11.3	23.1	40.2	34.6	<19	62.9	18.3	11.7
Cu	40.2	20.5	89.6	14.3	60.7	57.2	30.6	72.3
Zn	26.8	34.3	38.7	47.5	14.1	95.2	35.7	22.6
As	3.07	7.83	26.3	29.7	1.74	58.5	11.6	14.2
Se	<1.6	3.03	1.79	1.10	<2.3	1.56	0.30	<1.4
Br	0.74	0.12	0.07	1.20	0.56	0.34	0.15	0.73
Rb	35.1	33.0	92.5	72.0	7.18	176	22.5	83.5
Sr	107	46.1	32.7	93.4	69.5	59.5	81.1	<23
Y	11.2	8.70	14.6	5.5	11.0	16.0	8.7	14.5
Zr	78.7	71.9	205	187	<29	<13	87.6	174
Nb	2.90	3.50	11.3	0.10	9.10	16.6	2.00	8.60
Mo	0.70	0.60	0.60	0.10	1.10	4.70	1.00	0.20
Sb	0.66	0.41	1.29	1.96	0.14	21.8	2.72	3.41
Cs	1.72	1.49	3.99	3.12	0.33	3.97	0.78	4.23
Ba	281	446	550	748	57.8	580	143	475
La	9.09	5.17	15.1	9.78	3.13	24.7	6.19	19.4
Ce	19.7	11.3	29.4	22.1	5.7	50.3	9.36	39.8
Nd	8.71	6.30	11.0	8.27	2.46	20.0	5.61	16.4
Sm	2.02	1.46	2.45	1.92	0.6	4.23	1.59	3.83
Eu	0.35	0.23	0.29	0.26	0.14	0.39	0.31	0.50
Gd	1.95	1.12	2.02	2.0	<3.3	3.06	1.23	2.66
Tb	0.27	0.19	0.27	0.21	0.10	0.47	0.22	0.42
Tm	0.17	0.12	0.22	0.20	0.25	0.33	0.12	0.24
Yb	0.79	0.73	1.62	1.19	0.47	1.93	0.72	1.47
Lu	0.13	0.13	0.3	0.19	0.07	0.38	0.11	0.23
Hf	1.17	1.25	4.12	3.3	0.28	5.00	0.69	2.86
Ta	0.24	0.33	0.91	0.62	0.05	1.35	0.16	0.68
Au	<0.3	<0.4	<0.6	<0.9	<0.4	<0.9	0.6	0.2
Pb	10.3	22.6	21.9	3.4	29.0	43.6	6.9	5.8
Th	2.77	3.48	12.5	8.88	0.76	11.9	1.80	6.79
U	1.57	2.77	5.08	4.01	0.33	7.08	1.59	3.88

## B) Sturtian transition layers

wt.%	Copper Mine				Steilrandberge		Sesfontain-Opuwo		R
	R C08	C/R C09	C C10-1	C C10-2	C/R C12	R C12a	C C13a	C/R C13b	
SiO <sub>2</sub>	<i>n.d.</i>	67.3	61.9	68.1	29.7	<i>n.d.</i>	46.5	47.4	<i>n.d.</i>
TiO <sub>2</sub>	<i>n.d.</i>	0.62	0.61	0.72	0.19	<i>n.d.</i>	0.39	0.65	<i>n.d.</i>
Al <sub>2</sub> O <sub>3</sub>	<i>n.d.</i>	9.26	12.0	14.6	2.72	<i>n.d.</i>	3.65	6.72	<i>n.d.</i>
Fe <sub>2</sub> O <sub>3</sub>	1.74	12.0	2.02	2.56	25.4	0.62	42.1	32.3	1.61
MnO	<i>n.d.</i>	<i>b.d.l.</i>	<i>b.d.l.</i>	<i>b.d.l.</i>	<i>b.d.l.</i>	<i>n.d.</i>	0.01	0.04	<i>n.d.</i>
MgO	<i>n.d.</i>	0.98	7.48	0.53	34.3	<i>n.d.</i>	1.28	5.60	<i>n.d.</i>
CaO	<i>n.d.</i>	1.53	6.47	1.78	1.32	<i>n.d.</i>	1.16	1.30	<i>n.d.</i>
Na <sub>2</sub> O	0.05	0.20	0.21	0.24	0.13	0.05	0.13	0.14	0.01
K <sub>2</sub> O	<0.4	5.94	7.53	9.03	0.93	0.16	1.27	2.39	0.10
P <sub>2</sub> O <sub>5</sub>	<i>n.d.</i>	0.21	0.20	0.22	0.09	<i>n.d.</i>	0.18	0.57	<i>n.d.</i>
Total	<i>n.d.</i>	97.8	98.4	97.8	94.8	<i>n.d.</i>	96.7	97.1	<i>n.d.</i>
LOI	35.8	2.93	11.1	1.68	25.2	42.9	7.28	7.23	45.7
ppm									
Sc	2.64	7.27	11.2	14.7	4.22	0.87	9.96	9.32	0.55
V	5.80	207	49.0	80.0	30.0	<1	88.0	232	0.30
Cr	8.52	66.2	61.0	74.3	15.2	4.57	26.4	37.6	11.3
Co	4.42	5.96	3.16	3.75	4.90	1.72	17.4	34.4	1.65
Ni	21.2	25.9	30.2	28.0	25.4	3.3	147	38.7	4.2
Cu	36.9	290	11.6	9.00	45.2	14.4	181	81.6	11.4
Zn	66.2	46.2	53.1	63.6	162	10.8	148	48.4	7.71
As	2.53	12.1	1.03	0.43	80.7	2.56	203	67.3	5.53
Se	<1.2	2.63	<1.9	<1.7	1.17	<0.8	17.0	4.25	0.87
Br	0.87	0.51	0.97	0.50	0.87	4.73	0.78	0.79	0.60
Rb	5.18	102	143	184	40.8	5.91	42.3	63.0	2.53
Sr	129	46.6	152	42.8	127	472	139	1000	93.6
Y	17.1	32.2	22.2	29.3	7.00	3.90	25.4	39.6	4.2
Zr	94.9	489	257	285	<12	35.5	<19	364	20.4
Nb	0.60	10.8	8.10	10.9	3.20	<i>b.d.l.</i>	13.5	22.7	<1
Mo	1.00	3.20	0.70	0.10	16.7	1.00	190	45.3	2.60
Sb	0.12	2.42	0.42	0.42	8.92	0.33	16.7	7.45	0.28
Cs	0.21	4.65	8.12	10.1	0.75	0.22	0.40	0.73	0.11
Ba	65.3	490	557	645	85.5	73.9	292	511	45.4
La	8.40	28.6	22.2	21.8	7.42	3.04	23.1	23.5	1.79
Ce	19.7	59.4	45.0	44.1	12.4	5.02	44.8	49.0	3.92
Nd	15.2	24.3	19.6	18.6	5.03	3.11	17.7	20.4	1.77
Sm	3.47	5.86	5.02	4.81	1.23	0.75	3.46	4.74	0.48
Eu	0.85	1.13	0.96	1.00	0.33	0.16	0.75	0.90	0.11
Gd	3.53	5.03	4.11	4.25	1.16	0.57	3.28	4.31	0.34
Tb	0.64	0.8	0.70	0.81	0.20	0.09	0.51	0.75	0.07
Tm	0.27	0.45	0.38	0.44	0.17	0.13	0.39	0.43	0.05
Yb	1.67	2.92	2.47	2.88	0.63	0.26	3.01	2.69	0.21
Lu	0.26	0.47	0.38	0.44	0.10	0.04	0.47	0.41	0.04
Hf	0.83	11.0	6.2	7.25	0.82	0.46	2.45	3.53	0.13
Ta	0.11	0.90	0.83	0.93	0.18	0.06	0.75	1.29	0.04
Au	<0.5	0.4	0.4	<0.7	16.7	0.9	1.7	0.9	0.2
Pb	10.9	68.8	9.90	12.3	86.7	4.80	117	87.8	3.90
Th	1.97	11.0	8.58	9.73	1.71	0.60	4.38	7.20	0.32
U	3.31	8.17	2.92	3.95	1.92	1.75	8.48	12.5	1.11

## C) Marinoan cap carbonates – profile

Location Strat. setting wt. %	Warmquelle profile										
	M K2-1	M K2-2	M K2-3	M K2-4	M K2-5	G/M K2-6	G/M K2-7	G/M K2-8	M K2-9	M K2-10	M K2-11
<b>Fe<sub>2</sub>O<sub>3</sub></b>	1.32	1.33	1.04	0.62	4.38	3.39	3.22	1.17	0.59	0.55	0.36
<b>Na<sub>2</sub>O</b>	0.07	0.07	0.07	0.07	0.05	0.03	0.03	0.02	0.02	0.02	0.02
<b>K<sub>2</sub>O</b>	3.11	3.23	3.51	3.57	2.97	0.65	0.45	0.35	0.27	0.18	0.19
<b>LOI</b>	n.d.	5.66	4.74	2.98	5.38	39.4	42.8	44.3	45.8	46.5	46.5
<b>ppm</b>											
<b>Sc</b>	7.52	7.75	8.3	8.21	5.86	4.45	2.99	1.93	1.44	0.9	0.84
<b>Cr</b>	61.5	62.5	71.8	61.5	34.3	8.63	9.80	5.89	5.17	2.53	3.8
<b>Co</b>	2.31	1.29	1.02	0.57	2.84	15.1	29.3	10.6	3.02	2.72	1.73
<b>Ni</b>	17.1	23.1	15.0	8.6	35.8	45.2	80.0	28.6	12.2	7.7	7.3
<b>Zn</b>	21.5	19.7	19.2	19.8	19.8	28.1	61.6	25.5	18.1	13.3	12.9
<b>As</b>	14.9	26.4	18.7	4.21	44.7	50.3	89.5	23.1	4.30	6.21	2.43
<b>Se</b>	0.70	0.13	<1	<1.4	<1.2	<1.1	<1.2	0.55	0.43	0.19	<0.7
<b>Br</b>	0.63	0.51	0.51	0.48	0.51	0.49	0.61	0.55	0.57	0.53	0.59
<b>Rb</b>	79.3	81.7	87.4	86.1	75.2	17.2	14.3	8.94	7.13	3.65	5.13
<b>Sr</b>	30.6	34.3	23.0	<30	<25	55.9	63.0	72.0	72.1	68.3	70.3
<b>Zr</b>	154	129	165	158	233	<30	<34	<18	27.0	<15	10.3
<b>Sb</b>	2.36	0.90	0.53	0.56	7.95	7.61	8.22	1.91	0.29	0.97	0.17
<b>Cs</b>	3.45	3.66	3.96	3.89	3.70	0.90	2.77	0.76	0.47	0.33	0.37
<b>Ba</b>	378	420	444	422	406	94.0	63.9	48.7	35.3	25.3	26.8
<b>La</b>	17.4	17.9	20.7	21.9	9.67	3.63	4.41	3.22	2.44	2.01	2.04
<b>Ce</b>	33.6	34.7	40.9	43.1	20.2	7.58	7.63	6.16	5.60	4.60	4.81
<b>Nd</b>	14.6	16.5	17.1	20.3	8.55	3.91	3.44	2.21	2.77	1.81	1.97
<b>Sm</b>	3.25	3.45	3.94	3.82	2.19	1.02	0.89	0.7	0.57	0.47	0.46
<b>Eu</b>	0.49	0.50	0.57	0.57	0.31	0.21	0.22	0.19	0.18	0.11	0.11
<b>Gd</b>	2.47	2.39	2.72	2.45	1.83	1.07	<1.1	0.68	0.56	<0.8	0.37
<b>Tb</b>	0.38	0.39	0.43	0.41	0.28	0.17	0.12	0.11	0.09	0.08	0.07
<b>Tm</b>	0.21	0.19	0.22	0.24	0.23	0.15	0.16	0.11	0.13	0.12	0.11
<b>Yb</b>	1.17	1.18	1.32	1.41	1.31	0.65	0.54	0.42	0.38	0.29	0.29
<b>Lu</b>	0.16	0.16	0.17	0.18	0.21	0.09	0.08	0.06	0.05	0.04	0.04
<b>Hf</b>	2.54	2.60	2.95	2.99	2.91	0.52	0.39	0.32	0.23	0.12	0.14
<b>Ta</b>	0.63	0.65	0.68	0.69	0.83	0.09	0.06	0.09	0.06	0.02	0.02
<b>Au</b>	0.3	<0.4	<0.4	<0.3	0.2	<0.4	<0.4	<0.2	<0.2	0.1	0.1
<b>Th</b>	5.93	6.35	6.89	6.52	7.18	1.61	1.15	0.95	0.71	0.43	0.47
<b>U</b>	3.89	4.24	4.52	3.96	6.32	2.38	2.89	1.19	0.59	0.53	0.44

Location Strat. setting wt%	Entrance of South Valley Profile							
	G/M K4-1	G/M K4-2	M K4-3	M K4-4	M K4-5	M K4-6	M K4-7	M K4-8
<b>Fe<sub>2</sub>O<sub>3</sub></b>	9.05	2.22	0.48	0.44	0.45	0.47	0.50	0.45
<b>Na<sub>2</sub>O</b>	0.03	0.03	0.03	0.02	0.03	0.03	0.03	0.03
<b>K<sub>2</sub>O</b>	0.26	0.19	0.28	0.26	0.27	0.34	0.34	0.28
<b>LOI</b>	n.d.	45.4	45.9	46.0	45.8	43.6	46.0	45.8
<b>ppm</b>								
<b>Sc</b>	1.82	0.73	0.8	0.65	0.73	1.04	0.88	0.82
<b>Cr</b>	16.9	5.22	4.54	3.05	3.68	6.10	3.85	3.30
<b>Co</b>	38.5	6.45	2.39	2.01	1.88	2.20	2.41	2.06
<b>Ni</b>	89.1	16.5	11.1	4.9	8.9	11.9	11.8	4.8
<b>Zn</b>	50.1	26.4	22.5	21.5	22.5	29.7	23.6	20.6
<b>As</b>	28.1	6.93	0.62	0.48	0.45	0.44	0.65	0.55
<b>Se</b>	1.60	0.29	0.44	<0.7	<0.7	<0.5	<0.5	<0.6
<b>Br</b>	0.64	0.63	0.60	0.56	0.55	0.49	0.51	0.58
<b>Rb</b>	8.61	6.74	6.35	5.55	5.58	7.5	6.73	5.71
<b>Sr</b>	60.7	56.7	68.2	62.8	64.3	64.3	67.5	62.1
<b>Zr</b>	<28	39.6	27.9	21.1	30.4	30.0	28.6	19.4
<b>Sb</b>	4.60	1.09	0.10	0.07	0.07	0.13	0.09	0.08
<b>Cs</b>	0.47	0.27	0.41	0.32	0.37	0.48	0.41	0.39
<b>Ba</b>	58.6	29.5	44.8	34.3	33.9	45.3	39.6	32.4
<b>La</b>	4.62	4.78	4.86	4.43	4.34	4.17	4.08	3.73
<b>Ce</b>	11.3	9.52	9.28	8.24	8.43	8.26	8.16	7.23
<b>Nd</b>	5.11	4.87	4.44	3.82	3.65	2.92	4.57	3.20
<b>Sm</b>	1.41	1.00	0.99	0.78	0.72	0.82	0.77	0.61
<b>Eu</b>	0.23	0.22	0.23	0.21	0.22	0.21	0.21	0.19
<b>Gd</b>	0.93	0.91	0.93	0.74	0.64	0.66	0.75	0.55
<b>Tb</b>	0.20	0.15	0.15	0.12	0.11	0.12	0.11	0.09
<b>Tm</b>	0.16	0.14	0.13	0.11	0.13	0.09	0.07	0.11
<b>Yb</b>	0.56	0.49	0.47	0.38	0.38	0.51	0.4	0.33
<b>Lu</b>	0.07	0.05	0.06	0.05	0.05	0.08	0.06	0.04
<b>Hf</b>	0.34	0.18	0.28	0.20	0.24	0.36	0.31	0.22
<b>Ta</b>	0.06	0.04	0.08	0.04	0.05	0.1	0.08	0.05
<b>Au</b>	0.4	2.3	0.3	<0.2	0.1	<0.2	<0.2	<0.2
<b>Th</b>	1.54	0.47	0.78	0.56	0.64	1.08	0.84	0.63
<b>U</b>	4.51	1.48	1.33	0.55	0.44	0.57	0.54	0.35

Location Strat. setting wt%	Khowarib Valley profile						
	M P49-1	M P49-2	M P49-3	M P49-4	M P49-5	M P49-6	M P49-7
<b>Fe<sub>2</sub>O<sub>3</sub></b>	0.21	0.16	0.15	0.15	0.19	0.19	0.15
<b>Na<sub>2</sub>O</b>	0.02	0.01	0.02	0.02	0.02	0.02	0.01
<b>K<sub>2</sub>O</b>	0.22	0.21	0.17	0.11	0.16	0.12	0.14
<b>LOI</b>	n.d.	46.4	46.5	46.6	46.6	46.6	46.5
<b>ppm</b>							
<b>Sc</b>	1.57	1.08	0.76	0.61	0.53	0.47	0.40
<b>Cr</b>	3.40	2.22	1.89	1.93	1.74	2.05	1.52
<b>Co</b>	1.56	1.37	1.32	1.44	1.62	1.61	1.24
<b>Ni</b>	5.8	3.5	5.4	6.8	6.6	7.3	3.7
<b>Zn</b>	13.1	12.1	11.5	23.6	12.0	19.4	9.87
<b>As</b>	0.80	0.54	0.47	0.48	0.94	0.79	0.48
<b>Se</b>	<0.2	<0.4	<0.3	<0.4	<0.2	<0.2	<0.3
<b>Br</b>	0.40	0.40	0.42	0.43	0.46	0.40	0.41
<b>Rb</b>	3.85	3.88	3.01	2.39	3.54	2.89	2.02
<b>Sr</b>	57.4	44.2	42.6	52.3	51.6	43.8	44.3
<b>Zr</b>	12.1	<11	<10	11.7	6.57	9.34	6.46
<b>Sb</b>	0.08	<0.03	0.03	0.02	0.03	<0.03	0.02
<b>Cs</b>	0.18	0.21	0.13	0.11	0.11	0.10	0.07
<b>Ba</b>	37.6	32.8	23.7	25.7	41.3	30.4	35.5
<b>La</b>	1.75	1.72	1.43	1.33	1.42	1.22	1.06
<b>Ce</b>	3.60	3.57	3.09	2.99	2.96	2.76	2.41
<b>Nd</b>	1.05	1.14	0.78	1.59	0.85	1.65	<2.7
<b>Sm</b>	0.32	0.29	0.26	0.23	0.27	0.23	0.20
<b>Eu</b>	0.06	0.06	0.05	0.05	0.05	0.05	0.04
<b>Gd</b>	0.25	<0.3	<0.3	<0.3	0.26	0.22	0.1
<b>Tb</b>	0.05	0.04	0.04	0.03	0.04	0.03	0.03
<b>Tm</b>	0.03	0.03	0.03	0.02	0.03	0.02	0.02
<b>Yb</b>	0.20	0.2	0.17	0.16	0.17	0.15	0.14
<b>Lu</b>	0.03	0.03	0.03	0.03	0.03	0.02	0.02
<b>Hf</b>	0.14	0.10	0.09	0.09	0.09	0.10	0.08
<b>Ta</b>	0.03	0.02	0.02	0.02	0.03	0.02	0.02
<b>Au</b>	<0.2	<0.2	<0.2	<0.2	<0.2	<0.2	<0.1
<b>Th</b>	0.38	0.32	0.28	0.27	0.31	0.26	0.25
<b>U</b>	0.48	0.41	0.46	0.35	0.47	0.35	0.30

Location Strat. setting wt%	Khowarib Valley profile							
	M P49-8	M P49-9	M P49-11	M P49-12	M P49-13	M P49-14	M P49-16	M P49-18
<b>Fe<sub>2</sub>O<sub>3</sub></b>	0.16	0.16	0.15	0.18	0.19	0.17	0.18	0.18
<b>Na<sub>2</sub>O</b>	0.02	0.02	0.01	0.01	0.01	0.01	0.02	0.01
<b>K<sub>2</sub>O</b>	0.19	0.16	0.14	0.13	0.13	0.13	0.13	0.13
<b>LOI</b>	46.4	46.4	46.3	46.4	46.5	46.3	46.5	46.5
<b>ppm</b>								
<b>Sc</b>	0.43	0.39	0.34	0.31	0.30	0.27	0.29	0.49
<b>Cr</b>	1.80	1.68	1.59	1.63	1.58	1.57	2.50	1.54
<b>Co</b>	1.11	1.08	1.10	1.21	1.21	1.12	1.38	1.14
<b>Ni</b>	4.8	5.1	3.3	4.4	3.4	4.9	4.9	3.4
<b>Zn</b>	8.62	8.60	7.36	7.59	8.06	7.68	10.5	9.16
<b>As</b>	0.62	0.55	0.48	0.51	0.51	0.7	0.38	0.56
<b>Se</b>	<0.3	<0.2	<0.3	<0.3	<0.2	<0.3	<0.3	<0.3
<b>Br</b>	0.39	0.37	0.40	0.40	0.39	0.39	0.48	0.39
<b>Rb</b>	2.89	2.74	2.06	2.17	2.25	2.21	2.66	1.62
<b>Sr</b>	27.0	42.4	38.9	42.7	37.0	32.9	43.8	35.9
<b>Zr</b>	11.2	7.16	5.83	6.90	7.33	6.84	7.21	9.39
<b>Sb</b>	0.02	0.03	0.02	0.02	0.02	0.02	0.04	0.02
<b>Cs</b>	0.08	0.08	0.07	0.05	0.05	0.06	0.07	0.06
<b>Ba</b>	32.4	29.1	52.6	31.7	38.5	33.0	31.0	32.8
<b>La</b>	1.16	1.09	0.96	0.94	0.97	0.91	1.03	1.02
<b>Ce</b>	2.50	2.37	2.02	2.24	2.22	1.95	2.11	2.16
<b>Nd</b>	1.05	1.43	<2.5	0.63	<2.7	<2.5	0.84	0.53
<b>Sm</b>	0.21	0.21	0.19	0.18	0.19	0.17	0.20	0.20
<b>Eu</b>	0.04	0.04	0.04	0.04	0.04	0.04	0.04	0.04
<b>Gd</b>	0.17	0.20	<0.2	<0.2	0.20	<0.2	0.17	<0.3
<b>Tb</b>	0.03	0.03	0.03	0.03	0.03	0.02	0.03	0.03
<b>Tm</b>	0.02	0.02	0.02	0.02	0.02	0.02	0.02	0.02
<b>Yb</b>	0.15	0.14	0.12	0.13	0.13	0.12	0.12	0.12
<b>Lu</b>	0.02	0.02	0.02	0.02	0.02	0.02	0.02	0.02
<b>Hf</b>	0.11	0.1	0.11	0.09	0.09	0.08	0.08	0.08
<b>Ta</b>	0.02	0.03	0.02	0.01	0.02	0.02	0.02	0.02
<b>Au</b>	<0.2	0.05	<0.1	<0.1	<0.1	<0.2	<0.2	<0.2
<b>Th</b>	0.30	0.27	0.27	0.25	0.25	0.23	0.26	0.29
<b>U</b>	0.41	0.4	0.34	0.33	0.30	0.30	0.38	0.33

Location Strat. setting	Naraachamspos profile								
	G	G/M	M	M	M	M	M	M	M
wt. %	C2a-1	C2a-2	C2a-3	C2a-4	C2a-5	C2a-6	C2a-7	C2a-8	C2a-9
<b>Fe<sub>2</sub>O<sub>3</sub></b>	2.27	1.54	1.94	1.63	1.97	1.95	1.73	1.82	2.16
<b>Na<sub>2</sub>O</b>	0.13	0.25	0.14	0.19	0.12	0.11	0.08	0.11	0.05
<b>K<sub>2</sub>O</b>	3.55	2.05	3.38	2.63	2.61	2.14	1.93	1.99	2.21
<b>ppm</b>									
<b>Sc</b>	14.6	10.9	12.6	10.1	10.2	8.92	7.80	8.76	8.2
<b>Cr</b>	120	41.6	48.1	34.8	34.1	29.7	28.0	27.7	35.5
<b>Co</b>	14.6	7.46	6.71	12.6	6.34	5.63	4.43	5.39	12.5
<b>Ni</b>	98.6	79.0	99.2	120	78.9	62.0	56.8	55.8	52.6
<b>Zn</b>	33.3	31.8	36.5	31.4	34.0	30.2	28.2	29.2	24.9
<b>As</b>	5.69	0.28	0.58	0.73	0.57	0.39	0.45	1.20	10.2
<b>Se</b>	<1.7	<1.1	<1.6	<1.5	<1.5	<1.4	<1.4	<1.7	<1.3
<b>Br</b>	0.32	0.20	<0.3	<0.4	<0.3	0.16	0.18	0.18	<0.2
<b>Rb</b>	88.4	53.8	86.1	60.9	64.7	51.5	52.3	47.3	51.2
<b>Sr</b>	65.2	70.7	61.0	60.8	78.2	48.3	59.5	66.6	61.8
<b>Zr</b>	164	130	161	121	121	103	114	112	115
<b>Sb</b>	0.62	0.17	0.25	0.19	0.17	0.12	0.11	0.12	0.13
<b>Cs</b>	6.54	4.21	6.88	4.82	5.17	4.28	4.16	3.94	4.31
<b>Ba</b>	175	123	170	129	119	98.7	92.9	94.9	98.7
<b>La</b>	28.7	22.7	35.5	26.7	26.0	23.3	22.0	22.4	2.34
<b>Ce</b>	49.5	38.6	58.1	42.9	42.5	37.8	34.4	36.3	38.4
<b>Nd</b>	26.5	19.9	28.8	21.3	21.7	21.3	17.7	20.7	19.0
<b>Sm</b>	5.24	3.62	5.90	4.44	4.84	4.42	4.14	4.12	4.10
<b>Eu</b>	1.00	0.85	1.07	0.88	0.96	0.92	0.86	0.88	0.81
<b>Gd</b>	4.88	3.85	5.48	4.06	4.58	3.68	3.34	3.80	3.35
<b>Tb</b>	0.75	0.69	0.78	0.62	0.74	0.69	0.68	0.63	0.54
<b>Tm</b>	0.38	0.34	0.32	0.26	0.31	0.32	0.25	0.26	0.23
<b>Yb</b>	2.43	2.03	2.25	1.96	2.13	1.97	1.64	1.86	1.55
<b>Lu</b>	0.38	0.32	0.35	0.30	0.33	0.30	0.26	0.28	0.24
<b>Hf</b>	3.38	2.50	3.40	2.57	2.5	2.09	1.93	2.02	2.16
<b>Ta</b>	0.87	0.66	0.94	0.64	0.64	0.52	0.53	0.51	0.58
<b>Au</b>	<1.8	<1	<1.5	<1.4	<1.4	<1.3	<1.3	<1.6	<1.3
<b>Th</b>	9.22	6.72	9.88	7.03	7.22	6.16	5.78	5.72	6.09
<b>U</b>	1.57	1.16	1.66	1.15	1.23	1.01	1.10	0.98	1.05

Location Strat. setting wt. %	Naraachamspos profile							
	M C2a-10	M C2a-11	M C2a-12	M C2a-13	M C2a-14	M C2a-15	M C2a-16	M C2a-17
<b>Fe<sub>2</sub>O<sub>3</sub></b>	1.85	2.09	2.17	2.97	3.45	2.00	3.07	2.40
<b>Na<sub>2</sub>O</b>	0.05	0.03	0.03	0.04	0.03	0.03	0.03	0.02
<b>K<sub>2</sub>O</b>	2.35	2.14	2.72	2.74	2.50	1.74	1.55	0.83
<b>ppm</b>								
<b>Sc</b>	8.8	8.95	9.86	10.4	8.56	6.98	6.03	4.28
<b>Cr</b>	30.3	30.0	36.1	34.6	31.8	23.0	24.1	16.6
<b>Co</b>	4.84	7.11	7.10	11.7	17.2	7.58	20.4	26.7
<b>Ni</b>	56.0	60.9	68.6	102	132	42.7	75.5	142
<b>Zn</b>	30.0	30.4	30.4	32.8	26.7	26.1	29.0	43.5
<b>As</b>	0.81	3.79	9.92	35.0	64.6	3.46	23.6	28.7
<b>Se</b>	<1.4	<1.5	<1.4	<1.7	<1.5	<1.3	3.10	1.18
<b>Br</b>	<0.3	0.19	0.14	<0.5	0.21	0.19	0.23	0.26
<b>Rb</b>	54.0	51.5	71.1	71.3	62.9	42.6	40.6	28.1
<b>Sr</b>	65.9	49.3	69.7	82.7	67.4	56.9	75.2	85.0
<b>Zr</b>	97.5	100	134	136	116	91.7	92.0	78.3
<b>Sb</b>	0.12	0.09	0.16	0.19	0.23	0.10	0.2	0.39
<b>Cs</b>	4.61	4.25	5.83	5.65	5.13	3.47	3.81	4.81
<b>Ba</b>	102	100	139	146	128	88.9	82.7	36.1
<b>La</b>	25.5	23.1	27.1	28.6	25.8	18.8	16.8	10.7
<b>Ce</b>	39.0	36.6	44.8	45.1	39.8	30.8	28.4	18.6
<b>Nd</b>	19.2	18.2	23.10	24.5	20.9	17.0	14.9	11.3
<b>Sm</b>	4.46	4.39	4.76	5.02	6.19	3.66	3.46	2.50
<b>Eu</b>	0.93	0.90	0.94	1.01	0.83	0.80	0.74	0.64
<b>Gd</b>	3.85	3.87	4.29	4.06	3.40	2.90	3.04	2.88
<b>Tb</b>	0.65	0.64	0.69	0.72	0.60	0.54	0.52	0.49
<b>Tm</b>	0.26	0.25	0.27	0.29	0.26	0.21	0.21	0.19
<b>Yb</b>	1.70	1.74	1.80	1.87	1.61	1.49	1.47	1.39
<b>Lu</b>	0.25	0.27	0.27	0.28	0.23	0.23	0.23	0.22
<b>Hf</b>	2.17	1.97	2.57	2.60	2.26	1.62	1.50	0.74
<b>Ta</b>	0.61	0.52	0.82	0.74	0.71	0.38	0.41	0.16
<b>Au</b>	<1.4	<1.4	<1.4	<1.6	<1.4	<1.3	<1.3	<1.1
<b>Th</b>	6.35	5.88	7.89	7.79	6.82	4.70	4.08	2.18
<b>U</b>	1.17	1.04	1.47	1.49	1.58	1.00	1.17	0.80

## D) Clay fractions of Sturtian transition layers

Location Strat. setting wt. %	Copper Mine				Steilrandberge	Sesfontain-Opuwo		
	R C8-T	C/R C9-T	C C10/1-T	C C10/2-T	C/R C12_T	C C13a-T	C/R C13b_T	R C13c-T
<b>Fe<sub>2</sub>O<sub>3</sub></b>	11.9	11.8	2.35	5.15	48.1	36.7	30.1	20.7
<b>Na<sub>2</sub>O</b>	0.04	0.10	0.12	0.11	0.08	0.24	0.03	0.03
<b>K<sub>2</sub>O</b>	2.04	7.04	8.93	9.69	3.04	2.05	2.81	3.29
<b>ppm</b>								
<b>Sc</b>	3.39	17.7	13.0	28.5	13.9	12.3	11.8	3.86
<b>Cr</b>	47.4	114	73.0	150	61.1	46.9	50.8	53.8
<b>Co</b>	18.8	6.31	3.85	9.37	12.78	16.5	24.4	23.5
<b>Ni</b>	59.4	95.4	40.2	63.2	67.8	146	72.5	173
<b>Zn</b>	180	129	66.2	146	318	153	55.3	59.6
<b>As</b>	27.2	16.9	1.24	1.67	313	162	80.4	89.6
<b>Se</b>	1.42	2.17	1.69	1.65	3.81	10.2	3.80	2.20
<b>Br</b>	<0.4	1.98	0.29	0.48	<1.1	<1.3	<0.9	<0.7
<b>Rb</b>	39.5	141	168	245	143	74.7	86.7	75.9
<b>Sr</b>	40.8	<75	32.8	<71	<77	733	840	<55
<b>Zr</b>	225	266	177	200	<104	<121	422	178
<b>Sb</b>	0.92	3.27	0.48	0.71	15.3	12.2	5.60	6.06
<b>Cs</b>	1.48	7.88	9.13	18.7	2.99	2.28	0.88	0.76
<b>Ba</b>	422	945	706	573	271	379	719	988
<b>La</b>	36.4	18.8	16.7	15.7	23.3	37.8	31.8	3.34
<b>Ce</b>	74.0	37.6	32.5	32.1	42.0	65.4	63.6	7.71
<b>Nd</b>	29.6	14.5	14.1	12.5	15.2	23.1	23.0	2.16
<b>Sm</b>	6.74	3.80	3.49	3.22	3.27	4.32	4.95	1.03
<b>Eu</b>	1.52	0.77	0.72	0.74	0.77	0.86	0.88	0.17
<b>Gd</b>	7.10	3.66	3.91	<2.1	3.22	5.38	3.91	1.42
<b>Tb</b>	1.26	0.57	0.84	0.73	0.42	0.83	0.64	0.29
<b>Tm</b>	0.41	0.34	0.43	0.48	0.33	0.57	0.51	0.23
<b>Yb</b>	2.01	2.23	2.01	2.29	1.71	2.78	2.77	1.20
<b>Lu</b>	0.31	0.37	0.30	0.38	0.28	0.44	0.49	0.21
<b>Hf</b>	2.98	5.59	4.07	4.66	2.93	3.16	4.15	1.55
<b>Ta</b>	0.60	1.05	0.87	0.85	1.02	1.07	1.90	0.68
<b>Au</b>	0.7	0.6	<0.6	0.6	36.7	3.2	1.0	2.9
<b>Th</b>	8.24	9.61	6.17	9.40	6.86	7.18	9.13	3.22
<b>U</b>	5.84	8.05	2.18	3.16	4.11	7.01	10.8	5.87

## E) Clay fractions of Marinoan transition layers

Location Strat. setting wt. %	Naraachamspos							
	G C2a1_T	G/M C2B-T	G/M C2c_T	G/M C3/1-T	G/M C3/2-T	G C17a-T	G/M C17b-T	M C17c_T
Fe <sub>2</sub> O <sub>3</sub>	1.55	3.74	1.62	2.61	3.04	2.88	2.28	2.23
Na <sub>2</sub> O	0.41	0.14	0.79	0.07	0.07	0.09	0.07	0.09
K <sub>2</sub> O	3.83	7.71	6.64	7.89	6.91	8.48	7.22	7.82
ppm								
Sc	13.1	23.5	18.0	28.5	24.1	22.6	21.0	19.6
Cr	56.0	232	120	131.	93.0	129	98.3	89.1
Co	15.8	33.2	17.0	16.4	26.9	2.11	1.64	6.98
Ni	115	250	184	241	192	112	131	98.2
Zn	30.8	74.3	121	54.9	49.0	60.7	57.5	63.0
As	20.4	34.7	14.2	19.9	28.5	10.6	11.0	10.6
Se	<1.2	3.40	0.17	3.35	2.30	0.74	3.4	<1.7
Br	<56	<0.84	<0.5	<0.51	<0.4	<0.43	0.44	<0.41
Rb	95.3	207	177	204	172	202	192	195
Sr	<53.1	<72	<60	<84	<73	<86	<67	<66
Zr	132	324	254	247	262	213	224	276
Sb	0.85	4.95	1.07	1.75	2.02	0.79	0.70	2.22
Cs	7.83	15.8	14.8	16.3	13.7	24.3	21.4	13.4
Ba	180	440	367	450	374	513	558	394
La	28.5	57.7	38.2	55.4	49.0	63.7	52.2	48.0
Ce	52.3	107	73.4	119.2	105	108	95.9	80.5
Nd	20.4	42.8	26.9	38.8	33.5	42.1	38.4	31.6
Sm	3.57	8.41	4.23	7.63	6.75	8.04	7.12	4.00
Eu	0.54	1.11	0.75	1.00	0.89	1.09	0.94	0.79
Gd	1.92	5.06	4.16	4.60	4.73	7.07	4.55	4.78
Tb	0.24	0.64	0.53	0.62	0.55	1.04	0.65	0.52
Tm	0.16	0.38	0.37	0.36	0.34	0.65	0.39	0.42
Yb	1.32	2.54	1.67	2.60	2.38	2.96	2.93	1.83
Lu	0.23	0.41	0.30	0.45	0.39	0.45	0.45	0.33
Hf	3.42	6.07	5.27	5.40	5.07	6.21	6.51	5.51
Ta	0.95	1.87	1.44	1.74	1.60	1.81	1.79	1.92
Au	0.4	<1.4	<0.7	<1.1	<1	<1.1	<0.9	<0.6
Th	8.62	15.9	11.5	16.5	14.1	16.9	17.4	13.9
U	1.40	3.92	3.29	5.8	5.12	4.20	3.57	2.97

Location Strat. setting wt. %	Fransfontain		Tweelingskop		Bethanis		Khowarib Valley		Warmquelle	
	M C1a-T	G/M C1b-T	O C4-T	G C5b-T	G/M C6-T	M C7-T	G/M C15b-T	G/M C15e-T	G/M C16b-T	M C16c-T
<b>Fe<sub>2</sub>O<sub>3</sub></b>	1.85	3.31	3.77	3.62	5.70	7.95	3.04	14.2	2.57	4.48
<b>Na<sub>2</sub>O</b>	0.10	0.13	0.21	0.03	0.29	0.80	0.07	0.07	0.08	0.06
<b>K<sub>2</sub>O</b>	6.61	8.14	3.98	0.21	1.34	2.98	7.78	10.2	5.19	3.57
<b>ppm</b>										
<b>Sc</b>	8.10	24.6	13.6	1.58	4.04	11.1	18.6	18.5	13.3	10.8
<b>Cr</b>	95.9	84.4	110	16.8	23.1	86.7	127	68.1	87.0	70.3
<b>Co</b>	13.0	12.5	5.39	2.19	7.95	21.0	7.54	9.30	4.37	2.00
<b>Ni</b>	147	288	55.1	16.1	78.1	275	49.5	81.2	96.2	48.8
<b>Zn</b>	86.7	67.7	90.1	51.2	65.2	141	56.6	108	70.6	35.7
<b>As</b>	68.9	87.3	12.1	24.8	40.9	27.4	14.2	51.6	20.1	40.3
<b>Se</b>	0.91	3.02	2.49	<0.8	1.27	2.15	2.73	1.02	2.21	1.89
<b>Br</b>	<0.5	<0.54	0.80	0.21	0.48	0.26	0.16	0.82	0.69	<0.56
<b>Rb</b>	166	203	157	8.95	44	137	183	155	128	89.9
<b>Sr</b>	<30	<70	<54	36.0	50	<62	<44	<73	<58	<38
<b>Zr</b>	370	275	233	<45	<58	157	336	372	225	256
<b>Sb</b>	3.40	4.70	2.13	15.9	6.55	1.38	6.72	6.02	5.87	8.24
<b>Cs</b>	9.75	21.3	13.2	1.14	2.72	17.3	8.05	7.47	5.06	4.95
<b>Ba</b>	783	619	337	55.1	395	646	1530	1437	668	536
<b>La</b>	6.69	32.7	22.3	2.21	16.3	18.9	21.1	15.9	22.9	21.2
<b>Ce</b>	17.0	53.7	42.7	5.36	27.5	29.8	44.9	35.9	43.3	42.4
<b>Nd</b>	6.01	18.9	17.9	2.49	10.6	12.5	13.6	13.7	13.6	16.2
<b>Sm</b>	2.16	3.56	3.83	0.75	2.42	2.98	2.42	3.22	2.70	3.54
<b>Eu</b>	0.34	0.48	0.70	0.14	0.44	0.56	0.31	0.42	0.39	0.43
<b>Gd</b>	2.14	2.69	<1.6	1.08	2.20	2.96	2.27	3.18	2.00	<0.74
<b>Tb</b>	0.36	0.37	0.64	0.22	0.42	0.56	0.40	0.37	0.29	0.34
<b>Tm</b>	0.26	0.33	0.58	0.18	0.20	0.26	0.32	0.38	0.25	0.31
<b>Yb</b>	2.34	2.22	1.97	0.97	0.82	1.09	2.14	1.97	1.56	1.35
<b>Lu</b>	0.40	0.36	0.34	0.10	0.13	0.19	0.39	0.36	0.26	0.23
<b>Hf</b>	5.95	5.75	4.82	0.80	1.61	3.83	5.58	5.38	4.02	3.06
<b>Ta</b>	1.42	1.52	1.08	0.09	0.44	1.00	1.34	1.17	1.09	0.78
<b>Au</b>	2.29	<1	0.43	0.20	<0.80	<0.97	<0.95	0.80	1.64	0.56
<b>Th</b>	9.75	15.6	8.91	0.91	4.31	9.40	10.8	15.4	7.81	7.41
<b>U</b>	9.88	5.82	4.86	3.26	1.85	2.28	6.49	6.45	3.56	4.35

Location Strat. setting wt. %	Entrance of S Valley				
	G C14a-T	G/M C14b-T	G/M C14c-T	G/M C14d-T	M C14e-T
<b>Fe<sub>2</sub>O<sub>3</sub></b>	3.04	2.80	2.00	18.3	11.5
<b>Na<sub>2</sub>O</b>	0.10	0.08	0.09	0.08	0.06
<b>K<sub>2</sub>O</b>	8.78	5.93	8.54	6.89	1.73
<b>ppm</b>					
<b>Sc</b>	22.4	20.2	26.4	18.2	4.91
<b>Cr</b>	158	133	111	65.4	32.4
<b>Co</b>	4.39	7.80	6.47	49.2	22.5
<b>Ni</b>	122	97.5	128	206	109
<b>Zn</b>	134	151	115	109	104
<b>As</b>	26.1	19.4	7.71	75.1	52.9
<b>Se</b>	<2	0.46	1.35	11.2	31.9
<b>Br</b>	<0.8	0.46	<0.8	<0.9	0.58
<b>Rb</b>	207	142	182	148	41.4
<b>Sr</b>	<72	<44	<70	<80	<34
<b>Zr</b>	286	320	279	554	346
<b>Sb</b>	1.54	1.74	1.15	11.3	10.3
<b>Cs</b>	18.9	13.6	17.1	11.3	3.65
<b>Ba</b>	1000	627	924	804	258
<b>La</b>	39.5	53.2	37.3	32.6	5.39
<b>Ce</b>	76.7	99.4	69.7	62.6	15.7
<b>Nd</b>	27.9	33.4	22.4	21.4	7.56
<b>Sm</b>	5.22	5.48	4.25	4.36	2.57
<b>Eu</b>	0.65	0.76	0.53	0.45	0.31
<b>Gd</b>	5.02	3.09	2.58	2.69	2.19
<b>Tb</b>	0.76	0.41	0.51	0.42	0.31
<b>Tm</b>	0.42	0.26	0.41	0.32	0.28
<b>Yb</b>	2.37	2.10	2.06	1.52	1.48
<b>Lu</b>	0.46	0.42	0.39	0.27	0.25
<b>Hf</b>	5.48	5.98	5.46	4.50	1.60
<b>Ta</b>	1.84	1.62	1.60	1.14	0.36
<b>Au</b>	<0.8	0.7	<0.8	1.0	0.7
<b>Th</b>	11.7	11.8	13.3	15.6	3.16
<b>U</b>	7.59	8.44	6.17	18.6	20.6

## 10.2 Carbon-isotopy

(Legend: Marinoan: K2=Ongongo. K4=Entrance of South Valley, P49= Khowarib Valley, C1= Fransfontain, C6= Bethanis, Sturtian: C12= Steilrandberge, C13= Sesfontain-Opuwo, - measured at University of Vienna)

### A) Cap carbonate profiles

Samples	$\delta^{13}\text{C}_{\text{vs VPDB}}$		C	
		Error	[wt.%]	Error
K4-8	-1.68	0.27	12.35	0.06
K4-7	-1.84	0.28	12.36	0.02
K4-6	-1.69	0.28	11.72	0.06
K4-5	-1.87	0.34	12.29	0.09
K4-4	-1.69	0.28	12.40	0.02
K4-3	-1.91	0.28	12.36	0.01
K4-2	-1.41	0.29	12.26	0.02
K4-1	-0.95	0.30	10.94	0.06
K2-11	-2.65	0.29	11.68	0.79
K2-10	-2.33	0.29	15.18	4.63
K2-9	-2.68	0.33	12.24	0.07
K2-8	-3.54	0.29	11.85	0.06
K2-7	-2.64	0.37	11.55	0.11
K2-6	-3.65	0.32	10.35	0.40
K2-5	-7.82	0.27	1.16	0.03
K2-4	-7.80	1.85	2.61	3.61
K2-3	-7.94	0.42	0.97	0.02
K2-2	-7.62	0.36	1.15	0.03
K2-11	-9.18	0.29	2.48	0.05

Samples	$\delta^{13}\text{C}_{\text{vs VPDB}}$	Error	C [wt%]	Error
P49-18	-3.30	0.18	12.65	0.04
P49-17	-3.49	0.17	12.57	0.03
P49-16	-3.38	0.18	12.74	0.35
P49-15	-3.33	0.17	12.61	0.08
P49-14	-3.24	0.19	12.43	0.40
P49-13	-3.29	0.17	12.54	0.04
P49-12	-3.33	0.20	12.35	0.29
P49-11	-3.33	0.18	12.48	0.04
P49-10	-3.20	0.17	12.63	0.09
P49-9	-3.26	0.18	11.19	2.26
P49-8	-3.26	0.17	12.52	0.06
P49-7	-3.25	0.18	12.57	0.02
P49-6	-3.25	0.18	12.55	0.09
P49-5	-3.25	0.17	12.50	0.10
P49-4	-3.25	0.24	12.55	0.05
P49-3	-3.14	0.17	12.78	0.19
P49-2	-3.28	0.18	12.57	0.15
P49-1	-3.10	0.18	12.65	0.13

### B) Marinoan and Sturtian transition layers

Samples	$\delta^{13}\text{C}_{\text{vs VPDB}}$	Error	C [wt%]	Error
C1a	-0.18	0.23	12.4	0.2
C1b	-0.36	0.26	11.1	0.2
C1c	-0.73	0.24	9.3	0.1
C2c	-0.32	0.19	8.9	0.1
C6	-1.40	0.19	10.8	0.0
C12	-5.36	0.20	6.6	0.3
C12a	-7.29	0.21	11.5	0.2
C13c	-0.70	0.20	12.2	0.1

### 10.3 Table of CaCO<sub>3</sub> values

(Data obtained by "Carbonate bomb" at University of Vienna)

<b>Sample</b>	<b>Carbonate content</b>
C1a	32.2
C1b	3.8
C1c	99.7
C2a	88.7
C2b	75.9
C2c	73.9
C3_1	54.9
C3_2	73.2
C4	19.4
C5	10.9
C6	97.2
C7	25.4
C8	81.6
C9	61.6
C10_1	97.5
C10_2	3.4
C12	20.1
C13a	0.0
C13b	50.0
C13c	3.4
C12a	10.1
C14a	99.4
C14b	94.4
C14c	77.4
C14d	87.8
C14e	30.1
C15b	0.0
C15c	93.5
C15d	70.3
C15e	77.0
C15e1	28.3
C16a	56.8
C16b	97.0
C16c	21.4
C17a	87.3
C17b	3.4
C17c	7.5



---

## 11 CURRICULUM VITAE

---

### Ildikó Gyollai

**Department of Litospheric Research  
University Vienna**

Address: Althanstrasse 14., A-1090, Vienna, Austria

Office: 2C182

Phone: +43-1-4277-53316

E-mail: [gyollai.ildiko@gmail.com](mailto:gyollai.ildiko@gmail.com)

---

#### EDUCATIONAL BACKGROUND:

- **2009-2014: PhD student at University of Vienna:** Search for extraterrestrial signature on triggering of global warming after Snowball Earth glaciation, supervisors: Prof. Christian Koeberl, and Dr. Friedrich Popp

#### **Collaboration with research groups related to PhD topic:**

- Geology Survey of Namibia (Dr. G. Schneider): field trips of F. Popp in 2009, 2012, 2013
- Department of Earth and Planetary Sciences, Washington University in St. Louis (Fred Moynier's group: Zn, C, O isotopy of Marinoan postglacial boundary layers)
- Scripps Institute of Oceanography, University of California, San Diego, California 92093-0212, USA (G. W. Lugmair and A. Shulyokov) - Cr isotopy of Marinoan postglacial transition layers (search for extraterrestrial component)
- Research Center for Astronomy and Geosciences, Institute for Geology and Geochemistry, Hungarian Academy of Sciences, Astrobiology Group (M. Polgári) - iron-oxidizing bacteria in Sturtian and Marinoan postglacial transition layer – topic: estimation duration of sedimentation of Sturtian microbial postglacial transition layer - duration of initiation of deglaciation. (optical microscopy by 100x objectives)
  - University of Szeged, Department of Mineralogy, Petrology and Geochemistry: micro-Raman spectroscopy (C12, C13 Sturtian postglacial boundary layer- iron stromatolites) and micro-Raman mapping (C2a-4 sample) (K. Fintor's laboratory), scanning electron microscopy (C2a-4 sample) (E. Pál-Molnár's laboratory)

- Research Institute for Solid State Physics and Optics of Hungarian Academy of Sciences, Budapest, Hungary (M. Veres's laboratory) Micro-Raman Spectroscopy of C8 sample (Sturtian oolitic packstone)
- Eötvös University, Department of Mineralogy and Petrology electron microprobe of C8-sample (Zs. Bendő's laboratory)
  
- **2004-2009: University of Loránd Eötvös, MSc in geology**, Thesis: Evidences of thermal and shock metamorphism in evolution of a little planetary body comparison of Hungarian and Antarctic meteorites using Raman and Infrared spectroscopy. (*in Hungarian*), supervisor: Prof. Szaniszló Bérczi

#### **PRACTICE IN ANALYTICAL METHODS:**

- micro-Raman spectroscopy (University of Vienna, KFKI-SZFKI, Budapest, University of Szeged)
- infrared-spectroscopy (KFKI-SZFKI, Budapest)
- Instrumental neutronactivation analysis (University of Vienna)
- X-Ray fluorescence spectrometry (University of Vienna)
- X-Ray diffraction (University of Vienna, Eötvös University, Budapest)
- optical microscopy (University of Vienna, Eötvös University, Budapest)
- optical cathodoluminescence microscopy (University of Vienna)
- scanning electron microscope (Eötvös University, Budapest)
- isotope ratio mass spectrometry (University of Vienna)

#### **MEMBERSHIP:**

- 2004-: Hungarian Geological Society
- 2006-: Eötvös Loránd Student Chapter of the Society of Economic Geologist
- 2008-: Cosmic Material Spece Research Group of Academy of Hungarian Sciences
- 2012- :Geobiomineralization and Astrobiological Research Group of Academy of Hungarian Sciences

#### **IT-SKILLS:**

- MS Office Word, Excel, Power Point
- Corel Draw
- Geochemistry Software: Geochemical DataToolkit, GeoPlot

**LANGUAGE SKILLS:**

- Hungarian (mother tongue)
- German (professional intermediate level)
- English (intermediate level)
- Japanese (entry level)

**AWARDS:**

- 2<sup>nd</sup> place at Geology Heritage Competition for Students in Budapest, (Hungary), (2004)
- 4<sup>th</sup> place at the AAPG European Region Conference of students held in Prague (Czech Republic), (2008)
- 2<sup>nd</sup> place at National Conference of the Young Hungarian Environment Scientists, held in College of Nyíregyháza (Hungary), 2008
- Woman in Hungarian Space Science Award 2013- co-awarded

**PUBLICATIONS AND PRESENTATIONS****MANUSCRIPTS:**

- Gyollai, I.** (2002): Caves of outskirts Buda Rose Hill (Hungary) - (in Hungarian) Thesis for Geology Heritage Competition for Students
- Gyollai, I.** (2003): Caves in Bükk Mountain (Hungary) – (in Hungarian) Thesis for Geology Heritage Competition for Students
- Gyollai, I.** (2003): Exhibition of Gánt bauxite mine characteristics by way of analysis Harasztos and East-Újfeltárás (in Hungarian) - Thesis for National Competition for Hungarian Secondary School Students - Geography category
- Gyollai, I.** (2004): In the wake of secrets of a wonderful Martian-like landscape (Gánt bauxite mine) (in Hungarian) – Thesis for Geology Heritage Competition for Students
- Gyollai, I.,** Simó Zs. and Marosvölgyi, K. (2007, 2008) Radon in the Great Hungarian Plain. (in Hungarian) Department of Petrology and Geochemistry, Eötvös University, Budapest (Hungary), pp. 35. (Thesis of Conference of the Young Hungarian Environment Scientists)

- Gyollai, I., Fűrj, J.** (2008, 2009): Thermic and shock metamorphism in Hungarian L-chondrites (Mezőmadaras, Knyahinya, Mócs).(in Hungarian) Department of Material Physics, Eötvös University, Budapest, Hungary pp. 63 (Thesis of Conference of the Young Geologist of Eötvös University, Budapest)
- Gyollai, I.** (2009): Evidences of thermal and shock metamorphism in evolution of a little planetary body comparison of Hungarian and Antarctic meteorites using Raman and infrared spectroscopy.(in Hungarian) – M. Sc. Thesis, Eötvös University

### PEER-REVIEWED PAPERS

- Gyollai, I.** (2005) Egy csodálatos „marsbéli táj” titkainak nyomában. Természet Világa 136/2, Földtani Örökségünk diákpályázat melléklet, XIX-XXIII
- Gyollai, I., Nagy, Sz., Fűrj, J., Bérczi, Sz., Gucsik, A., Veres, M.** (2009) Petrographic and Micro-Raman Study of Thermal and Shock Metamorphism in Mezőmadaras, Knyahinya and Mócs L-Chondrites. MICRO-RAMAN SPECTROSCOPY AND LUMINESCENCE STUDIES IN THE EARTH AND PLANETARY SCIENCES: Proceedings of the International Conference Spectroscopy, Mainz (Germany), 2–4 April 2009. AIP Conference Proceedings Volume 1163. (Editor: Arnold Gucsik). pp. 75-85. (ISBN: 978-0-7354-0700-8)
- Gyollai I., Gucsik A., Veres M., Nagy Sz., Bérczi Sz.** (2012): Petrographic and micro-Raman spectrometry of two diamond rich meteorite (ALH 77257 ureilite and ALH-78113 aubrite) – Spectroscopy Letters, 45:1-5 DOI: 10.1080/00387010.2011.627527
- Nagy Sz., Józsa S., **Gyollai I.**, Bérczi Sz., Bendő Zs., Stehlik H. (2011): Ringwoodite microstructures in L-chondrite NWA 5011: implications for transformation mechanism and source region in L parent body. Central European Geology, Vol. 54/3:233–248 (2011) DOI: 10.1556/CEuGeol.54.2011.3.2
- Gyollai, I., Gucsik, A., Nagy, Sz. Bérczi, Sz., Veres M.** (2012): Petrographic and Mid-Infrared Spectroscopy Study of Shocked feldspar in Asuka-881757 lunar gabbro meteorite sample. – Central European Geology 55/1 23-32
- Gucsik, A., T. Endo, H. Nishido, K. Ninagawa, M. Kayama, Sz. Bérczi, Sz. Nagy, P. Ábrahám, Y. Kimura, H. Miura, **I. Gyollai, I.** Simonia, P. Rózsa, J. Posta, D. Apai, K. Mihályi, M. Nagy, U. Ott: Cathodoluminescence microscopy and spectroscopy of forsterite from Kaba meteorite: An application to the study of hydrothermal alteration of parent body, Meteoritics and Planetary Science, 48/12, 2577–2596, December 2013 DOI: 10.1111/maps.12238

**In review:**

**Gyollai, I.**, M. Polgári, K. Fintor, F. Popp, D. Mader, Sz. Nagy, E. Pál-Molnár, C. Koeberl: Microbially mediated Sturtian formations of rapid deglaciation after the Neoproterozoic Snowball Earth, Namibia. (submitted to *Carp. J. of Earth and Env. Sci.*, 2013)

**Gyollai, I.**, F. Popp, M. Polgári, D. Mader, C. Koeberl: Search for impact ejecta in Chuos/Rasthof (Sturtian) and Ghaub/Maieberg(Marinoan) transition (submitted to *Austrian Earth Sci.*, 2013 December)

Thiemens, M. M., R. Shaheen; **I. Gyollai**; K. Chong; F. Popp; C. Koeberl; M. H. Thiemens; F. Moynier: Zn, C, and O Isotopic Variations Associated with Neoproterozoic Marinoan Glaciations. (submitted to *Precamb. Res.* February 2014)

**Gyollai, I.**, M. Polgári, M. Veres, Sz. Nagy, F. Popp, D. Mader, C. Koeberl, 2013. Evidence of microbial activity involved with Neoproterozoic postglacial sediments from the Otavi Group, Namibia: a study of Sturtian oolitic carbonate sandstone with spectroscopic methods (revised version submitted to *Comm. Nam. Geol. Surv.*, November 2013)

**In preparation:**

**Gyollai, I.**, M. Polgári, F. Popp, D. Mader, Sz. Nagy, C. Koeberl: Paleoenvironmental reconstruction, weathering and diagenesis of Neoproterozoic postglacial transition layers: Observation from the Otavi Group/ Namibia (in preparation to *Austrian. J. of Earth Sci.*)

**Gyollai, I.**, M. Polgári, Sz. Nagy, K. Fintor, F. Popp, E. Pál-Molnár, , D. Mader, C. Koeberl, 2013. Paleoenvironment characterization based on microbial activity and geochemical proxies in Marinoan postglacial transition layers (NW-Namibia) (in preparation to *Central Eur. J. of Geology*)

**CONFERENCE CONTRIBUTIONS AND PRESENTATIONS****Conference participations related PhD topic:**

- Gyollai, I.**, F. Popp, C. Koeberl, 2011. Global warming after the Snowball Earth glaciation: The search for an extraterrestrial component. EGU, 03-08 April 2011. Poster Presentation, presented by Ildiko Gyollai
- Gyollai, I.** F. Popp, D. Mader, C. Koeberl, 2011. Search for extraterrestrial signatures of a possible impact event in the diamictite/cap carbonate transition after Snowball Earth glaciations (Sturtian, Marinoan), Otavi Group, NW-Namibia. GSA Annual Meeting in Mineapolis, 9-12 October, 2011. – Poster Presentation, presented by Christian Koeberl
- Gyollai, I.**, Nagy Sz., Popp F., Koeberl C.: Globális fölmelegedés okainak keresése a Snowball Earth eljegesedés után. (English title: Search for causes of global warming after Snowball Earth glaciation). II. Kőzettani és Geokémiai Vándorgyűlés (2<sup>nd</sup> Meeting for Geochemistry and Petrology), Szatymaz, Hungary (abstract).
- Gyollai, I.**, F. Popp, D. Mader, and Ch. Koeberl, 2012. Diagenesis, weathering and paleoenvironmental conditions from postglacial diamictite/cap carbonate transition layers of the Otavi Group (NW-Namibia) EGU2012-9318
- Gyollai, I.**, Nagy Sz., Veres M., Mader D., Popp F., Köberl C. (2012) Élet a sturti globális jégkorszak után. III. Kőzettani és Geokémiai Vándorgyűlés (3<sup>rd</sup> Meeting for Petrology and Geochemistry), 4-6 September, Telkibánya, Hungary (abstract, in Hungarian) (English title: Life after Sturtian Snowball Earth) – Oral presentation, presented by Ildiko Gyollai
- Thiemens, M. M., F. Moynier, Ch. Koeberl, M. H. Thiemens, R. Shaheen, **I. Gyollai**, F. Popp, K. Chong: Zn and C isotopic evidence of climatic change during the Marinoan. - 5-9 December AGU Fall Meeting, San Francisco, USA. Oral presentation, presented by M. M. Thiemens
- Thiemens, M.M., F. Moynier, M.H. Thiemens, R. Shaheen, K. Chong, C. Koeberl, F. Popp, **I. Gyollai** (2012): Zn and C isotopic variations associated with Neoproterozoic Ice Ages. 43. LPSC, #2499, LPI, Houston. Oral presentation, presented by M. M. Thiemens
- Gyollai, I.**, F. Popp, D. Mader and C. Koeberl (2013): Diagenesis, weathering, and paleoenvironmental conditions from postglacial diamictite/cap carbonate transition layers of the Otavi Group (NW-Namibia) 24th Colloquium of African Geology 8-14 January, Ethiopia. Poster presentation, presented by C. Koeberl.
- Gyollai, I.** (2013): Meteoritbecsapódás okozta a kriogén globális jégkorszakok utáni gyors felmelegedést? - avagy becsapódási üledék kutatása geológiai módszerekkel. (English title: Meteorite impact triggered deglaciation of Cryogenian Snowball Earth?- or search for geological signature of impact ejecta). IV. Kőzettani Vándorgyűlés (4<sup>th</sup> Meeting for Petrology and Geochemistry), Orfű, Hungary 12-14<sup>th</sup> September. Oral presentation, presented by Ildiko Gyollai.

## CONFERENCE PRESENTATIONS

### Poster presentations:

- Gyollai, I.**, Simó, Zs. and Marosvölgyi, K. (2008): The environmental geochemistic and environmental physic investigation of Kunszentmiklosian adobe. (*in Hungarian*) – (The Conference of Young Earth Scientists), 28-29 March, 2008, Baja, Hungary
- Gyollai I.**, Bérczi Sz, Józsa S., Nagy Sz., Gucsik A. (2010): Review study of shock metamorphism on specimens of the Antarctic Meteorite Educational Thin Section Set of the National Institute of Polar Research, Tokyo, Japan. - The 20<sup>th</sup> General Meeting of The International Mineralogical Association 21-27August 2010 Budapest, Hungary
- Gyollai, I.**, F. Popp, C. Koeberl (2011): Global warming after the Snowball Earth glaciation: The search for an extraterrestrial component – European Geoscience Conference, 3-8 April 2011, Vienna
- Gyollai, I.**, F. Popp, D. Mader, and Ch. Koeberl. Diagenesis, weathering and paleoenvironmental conditions from postglacial diamictite/cap carbonate transition layers of the Otavi Group (NW-Namibia) EGU2012-9318
- Gyollai, I.**, Sz. Nagy, A. Gucsik, Sz. Bérczi, M. Veres (2012) Magmatic and Impact metamorphic processes in ALH-77005 Martian meteorite (shergottite). The ESA and Hungarian Academy of Sciences sponsored Workshop on Mars.
- Gyollai, I.**, Sz. Nagy, Sz. Bérczi (2013): Comparison studies of shock vein formation in Tenham (L6) NWA-5011 (L6), NWA-4353 (L4), ALH-77005 (shergottite) and Mócs (L6) meteorites. Workshop on Planetesimal Formation and Differentiation, Washington D.C., USA, 27-29th October.

### Oral presentations:

- Gyollai, I.**, Simó Zs. and Marosvölgyi, K. (2007, 2008) :Radon in the Great Hungarian Plain. Conference of the Young Hungarian Environment Scientists, 25-26 March, 2008, Nyíregyháza
- Gärtner, D., **Gyollai, I.**, Horti, A., Lengyel, T., Uhrin, A.: Evaluation of the ELTE Block: North Viking Graben, offshore Norway. (*in English*) – AAPG Conference of European Region, Prague, Czech Republic, 14-16 March, 2008
- Gyollai, I.**, Fűrj, J. (2008, 2009): Thermic and shock metamorphism in Hungarian L-chondrites (Mezőmadaras, Knyahinya, Mócs).(*in Hungarian*) Department of Material

Physics, Eötvös University, Budapest, Hungary (Thesis of Conference of the Young Geologist of Eötvös University, Budapest 13th Dec. 2008.)

- Gyollai, I.** (2009): Evidences of thermal and shock metamorphism in evolution of a little planetary body comparison of Hungarian and Antarctic meteorites using Raman and infrared spectroscopy. (*in Hungarian*) – M. Sc. Defensio, 14.06.2009, Eötvös University
- Gyollai, I.** (2009): Evidences of thermal and shock metamorphism in evolution of a little planetary body comparison of Hungarian and Antarctic meteorites using Raman and infrared spectroscopy. (*in Hungarian*) Meeting of Geonomic Committee, Konkoly Thege Institute for Astronomists, Budapest, 05.05 May, 2010
- Gyollai, I.** (2010): Geochemical, petrographical, and mineralogical studies of Namibian Snowball Earth diamictite/cap carbonate deposits. – 07.06.2011., University of Vienna
- Gyollai, I., Sz. Nagy, A. Gucsik, Sz. Bérczi, S. Józsa, Gy. Szakmány** (2010): Petrographical and micro-Raman study of microdiamonds in ALH-77257 (ureilite) and ALH-78113 (aubrite) - samples From Dust to Rocky Planets, Workshop, Aug 28, 2010 Konkoly Observatory
- Gyollai I., Nagy Sz.** (2011): Sokkmetamorfózis – (*in Hungarian*) oral presentation, 9th February 2011, Cultural Centre, Kecskemét, Hungary
- Gyollai, I., Szabolcs Nagy, S. Józsa, Sz. Bérczi, K. Havancsák, G. Varga:** Shock metamorphic effects in olivine (Mócs meteorite): possible phase transformation. 49th EHPRG International Conference, Budapest (Hungary), 28 August-2 September 2011
- Gyollai I., Nagy Sz.** (2011) Termikus és sokkmetamorf jelenségek a magyarországi és antarktisi meteoritokban. II. Közletani és Geokémiai Vándorgyűlés, Szatymaz
- Gyollai I., Nagy Sz., Veres M., Mader D., Popp F., Köberl C.** (2012) Élet a sturti globális jégkorszak után. III. Közletani és Geokémiai Vándorgyűlés, Telkibánya
- Gyollai I.** (2013) Meteoritbecsapódás okozta a kriogén globális jégkorszakok utáni gyors felmelegedést? - avagy becsapódási üledék kutatása geológiai módszerekkel. (English title: Meteorite impact triggered deglaciation of Cryogenian Snowball Earth?- or search for geological signature of impact ejecta). IV. Közletani Vándorgyűlés (4th Meeting for Petrology and Geochemistry), Orfű, Hungary 12-14th September.
- Gyollai, I., Sz. Nagy, Sz. Bérczi, H. Nishido** (2013): Petrology and mineralogy of ALH-77005 shergottite. 4th Symposium on Polar Science, Tokyo, Japan 12-15th November.
- Gyollai, I., K. Fintor, Sz. Nagy, Sz. Bérczi, H. Nishido, A. Gucsik** (2013) Characteristic features shock-induced on Mócs chondrite (L6). Symposium on Polar Science, Tokyo, Japan 12-15th November.